São Paulo State University
Materials Science and Technology
Doctoral Dissertation

Concepts of Nanoscale Electrochemistry: Understanding Electron Transfer in Biological Systems

PhD Dissertation

Edgar Fabian Pinzón Nieto

Araraquara, SP
2025

São Paulo State University
Materials Science and Technology
Doctoral Dissertation

Concepts of Nanoscale Electrochemistry: Understanding Electron Transfer in Biological Systems

Edgar Fabian Pinzón Nieto

PhD Dissertation submitted in partial fulfillment of the requirements for the degree of Doctor of Philosophy in Materials Science and Technology Program.

Advisor:
Prof. Paulo Roberto Bueno, PhD.

Co-advisor:
Prof. Adriano Santos, PhD

Araraquara, SP
2025

Universidade Estadual Paulista "Julio de Mesquita Filho"
Ciência y Tecnologia de Materiais
Tese de Doutorado

Conceitos de Eletroquímica na Nano-escala: Entendendo a Tranferência Eletrônica em Sistemas Biológicos

Tese de Doutorado

Edgar Fabian Pinzón Nieto

Araraquara, SP
2024

Universidade Estadual Paulista "Julho mesquita Filho"
Ciência y Tecnologia de Materiales
Tese de Doutorado

Conceitos de Eletroquímica na Nano-escala: Entendendo a Tranferência Eletrônica em Sistemas Biológicos

Edgar Fabian Pinzón Nieto

Tese submetida como parte dos requisitos para a obtenção do grau de Doutor em Filosofia em Ciência e Tecnologia de Materiais.

Orientador:
Prof. Paulo Roberto Bueno, PhD.

Co-Orientador:
Prof. Adriano Santos, PhD

Araraquara, SP
2024

UNIVERSIDADE ESTADUAL PAULISTA

Câmpus de Bauru

MINUTES OF THE PUBLIC DEFENSE OF THE DOCTORAL THESIS OF EDGAR FABIAN PINZÓN NIETO, STUDENT OF THE GRADUATE PROGRAM IN MATERIALS SCIENCE AND TECHNOLOGY, SCHOOL OF SCIENCES - BAURU CAMPUS.

On the 30th day of January 2025, at 9:00 am, through Videoconference, the defense of EDGAR FABIAN PINZÓN NIETO's DOCTORAL THESIS was held, entitled **Concepts of Nanoscale Electrochemistry: Understanding Electron transfer in Biological systems**. The Examining Committee was composed of the following members: Prof. Dr. PAULO ROBERTO BUENO (Virtual Participation) from the Department of Physics and Mathematics and Engineering / Institute of Chemistry - Unesp/ Araraquara Campus, Prof. Dr. DAVID ALEJANDRO MIRANDA MERCADO (Virtual Participation) from the Escuela de Física / Universidad Industrial de Santander, Colombia, Prof. Dr. SALVO MIRABELLA (Virtual Participation) from the Department of Physics and Astronomy / Università di Catania, Prof. Dr. CARLOS FREDERICO DE OLIVEIRA GRAEFF (Virtual Participation) from the Department of Physics and Meteorology / School of Sciences - Unesp / Bauru Campus, Prof. Dr. NELSON RAMOS STRADIOTTO (Virtual Participation) from the Department of Analytical, Physical-Chemical and Inorganic Chemistry / Institute of Chemistry - UNESP - Araraquara. After the presentation by the student and questioning by the members of the Examining Committee who participated in the act virtually, the student received the final concept: APPROVED. If there was nothing else, these minutes were drawn up and signed by the President of the Examining Committee after being read and approved by all members.

Prof. Dr. PAULO ROBERTO BUENO

Documento assinado digitalmente
gov.br PAULO ROBERTO BUENO
Data: 25/02/2025 13:15:20-0300
Verifique em https://validar.iti.gov.br

Pinzón, Edgar
Concepts of Nanoscale Electrochemistry: Understanding Electron Transfer in Biological Systems / Edgar Fabian Pinzón Nieto. -- 2025.
193 f.

Advisor: Paulo Roberto Bueno, PhD.

PhD Dissertation () - São Paulo State University, Baurú, Science Department 2025.

velocidade quântica, capacitância quântica, densidade de estados, eletrólito, espectroscopia impedância eletroquímica, eletrônica molecular. I. São Paulo State University, Baurú, Science Department. II. Santos, Adriano., coorient. III. PhD.

Acknowledgements

When I embarked on this academic journey, I never imagined that I would one day be able to submit my PhD thesis in a foreign language. Therefore, I am deeply proud to present this dissertation in English. However, I am even more proud of my Colombian heritage and my native language, which, in my humble and modest opinion, is the most beautiful language in existence. For this reason, I feel compelled to write this section in my mother tongue, Spanish. I apologize in advance to any readers who may find this choice unconventional.

Primero, y como me enseñó mi madre, deseo agradecer y dedicar esta tesis doctoral a Dios, en quien creo profundamente y cuyo amor y protección he sentido a lo largo de toda mi vida, especialmente durante mi formación doctoral.

En segundo lugar, deseo compartir con todos que esta tesis, está dedicada a mi abuelo, Luis Alejandro Pinzón, y a mi prima Nubia Corzo, a quienes Dios llamó a su descanso hace algunos años. Ambos me amaron profundamente y siempre me instaron a cumplir mis sueños.

Deseo dedicar esta tesis a mi familia: mis padres, mi hermana y mi sobrino. Su apoyo incondicional y su confianza en mis capacidades hicieron posible la realización de mi investigación doctoral. Ellos han sido una fuente invaluable de motivación y parte esencial de todos mis logros.

Quiero expresar mi gratitud a todos los miembros del grupo de investigación Nanobionics por su trabajo en equipo, sus orientaciones y las valiosas discusiones compartidas. Cada espacio académico contribuyó de manera fundamental a mi crecimiento tanto científico como personal. De manera especial, deseo agradecer al Profesor Paulo Roberto Bueno, mi orientador, por asumir con generosidad y dedicación la ardua tarea de transmitirme su experiencia y su visión sobre la construcción de la ciencia y su impacto en la sociedad. Asimismo, extiendo mi agradecimiento a los doctores Adriano dos Santos y Olivia Carr, con quienes, además de disfrutar de una experiencia profesional enriquecedora, encontré un apoyo clave en mi proceso de desarrollo personal.

Quiero expresar mi agradecimiento a mis amigos Francis Rivas, Daniela Remonatto Andrés Felipe Torres, Saidy Cristina Ayala y Hernan Dario Rojas, por su sincera y genuina amistad. Su compañía, sus palabras y sus gestos de cariño fueron siempre una fuente de fortaleza y motivación a lo largo de este proceso.

Deseo expresar mi profundo agradecimiento a las diversas instituciones, unidades y secciones que invirtieron su capital financiero, material, intelectual y humano en mi formación doctoral. En particular, extiendo mi gratitud a la FAPESP, la UNESP, el Programa de Posgrado POSMAT de la UNESP en Baurú y al Instituto de Química de la UNESP en Araraquara.

Resumo

A busca pela compreensão da dinâmica dos elétrons dentro da matéria tem cativado a investigação científica desde as origens da ciência. Ao longo do tempo, várias teorias e modelos — que vão desde a descoberta do elétron por Thomson até as teorias de transferência de elétrons de Marcus-Gerischer — contribuíram significativamente para nossa compreensão atual da eletrodinâmica e impulsionaram o desenvolvimento de aplicações eletrônicas críticas na sociedade moderna. No entanto, este capítulo da ciência permanece em aberto, com muitas questões sem resposta em torno dos princípios físicos que regem a dinâmica dos elétrons entre estados de energia quantizados dentro de nanomateriais. Por exemplo, o avanço de dispositivos optoeletrônicos baseados nas propriedades quânticas de estruturas em escala nanométrica é restringido por uma compreensão incompleta dos fenômenos de transferência e transporte de elétrons, uma vez que esses processos seguem os princípios da eletrodinâmica quântica em vez das leis da física clássica. O controle das propriedades elétricas e eletrônicas na escala nanométrica continua a ser um desafio considerável. Portanto, modelos fundamentados nas leis da mecânica quântica, juntamente com abordagens experimentais versáteis e acessíveis, são essenciais para avançar nossa compreensão da dinâmica dos elétrons nessa escala. Neste contexto, a presente pesquisa de doutorado investiga a eletrodinâmica de estruturas semicondutoras orgânicas e inorgânicas com diferentes tipos de confinamento quântico, incluindo nanofilmes de óxido de cobre, arranjos de pontos quânticos de telureto de cádmio, grafeno monocamada e arranjos de moléculas heterocíclicas do tipo push-pull, sob a perspectiva da *Teoria da velocidade Quântica*. Esta teoria, derivada dos princípios da eletrodinâmica quântica, é baseada no conceito eletrodinâmico de velocidade quântica $\nu = e^2/hC_q$, que se funda na propriedade de capacitância quântica C_q — uma característica associada à estrutura eletrônica que pode ser medida experimentalmente utilizando metodologias eletroquímicas dependentes do tempo. Através de medições de espectroscopia de impedância eletroquímica em um meio eletrolítico, interpretadas sob a perspectiva desse marco teórico, tornou-se possível medir diretamente a densidade de estados eletrônicos à temperatura ambiente de estrutura á nano-escala, e elucidar as regras quânticas que governam a eletrodinâmica nessas estruturas. Este estudo abriu novas avenidas para a pesquisa científica em um campo emergente conhecido como *Eletrônica em Escala Nanométrica em Meios Eletrolíticos*.

Palavras chaves: velocidade quântica, capacitância quântica, densidade de estados, eletrólito, espectroscopia impedância eletroquímica, eletrônica molecular

Abstract

The quest to understand electron dynamics within matter has captivated scientific inquiry since the origins of science. Over time, various theories and models—ranging from Thomson's discovery of the electron to the Marcus-Gerischer electron transfer theories—have significantly contributed to our current understanding of electrodynamics and have driven the development of critical electronic applications in modern society. Nevertheless, this chapter of science remains open, with many unanswered questions surrounding the physical principles that govern electron dynamics between quantized energy states within nanomaterials. For example, the advancement of optoelectronic devices based on the quantum properties of nanoscale structures is constrained by an incomplete understanding of electron transfer and transport phenomena, as these processes follow quantum electrodynamic principles rather than the laws of classical physics. Controlling electrical and electron properties at the nanoscale remains a considerable challenge. Therefore, models grounded in quantum mechanics laws, alongside versatile and accessible experimental approaches, are essential for advancing our understanding of electron dynamics at this scale. In this context, the present PhD research explores the electrodynamics of organic and inorganic semiconductor structures with varying types of quantum confinement, including copper oxide nanofilms, one assembly of cadmium tellurium quantum, single layer graphene and one assembly of push-pull heterocyclic molecules, from the perspective of *Quantum Rate Theory*. This theory, derived from quantum electrodynamics principles, is based on the electrodynamic concept of quantum rate $\nu = e^2/hC_q$, which is founded on the quantum capacitance property C_q—a feature associated with the electronic structure that can be experimentally measured using time-dependent electrochemical methodologies. Through electrochemical impedance spectroscopy measurements in an electrolytic medium, interpreted from the perspective of this theoretical framework, it became possible to directly measure the electron density of states of nanoscale structures at room temperature and to elucidate the quantum rules governing electrodynamics in these structures. This study opened new avenues for scientific research in an emerging field known as *Nanoscale Electronics in Electrolytic Media.*

Keywords: quantum rate, quantum capacitance, density of state, electrolyte, electrochemical impedance spectroscopy, molecular electronics

Contents

List of Figures

Figure 7.7 (a) The traditional Randle equivalent circuit models the direct electric contact of electro-active molecules or compounds, whether undergoing electrochemical reactions or not, within an electrolyte medium, with a conducting electron reservoir (a probe electrode). The series combination of charge transfer resistance R_{ct} and Warburg W circuit elements in the equivalent circuit branch (depicted in green) signifies electron transfer kinetics governed by diffusion. The presence of the W element accounts for electrodynamics controlled by the transport of mass of reacting species toward the electrode. The parallel capacitance C_{dl} corresponds to double-layer capacitance. (b) This equivalent circuit models the electrodynamics of molecularly modified electrodes within an electrolyte environment. The non-faradaic charging dynamics (illustrated in gray) refers to dynamics that do not follow quantum RC dynamics (depicted in red), which involve a series combination of quantum resistive R_q and capacitive C_q elements. The quantum RC dynamics obey the quantum rate dynamics predicted by the quantum rate model, where $\tau = R_q C_q$ corresponds directly to $\nu = 1/\tau \propto e^2/hC_q$ rate. 145

Figure 7.8 Nyquist capacitive diagrams measured at the OCP for the cysteamine (denoted in red as Cys SAM) and **TPC** (indicated in blue as **TPC**)-Au junctions in 20 mmol L^{-1} of $TBAClO_4$. The **TPC** junction comprises **TPC** molecules chemically attached to the surface of the electrode employing the cysteamine film. The C_q of the interfaces is accessible as the measurement of the real component of the complex capacitance obtained as the diameter of the Nyquist capacitive diagram. The corresponding frequency for this value of C_q corresponds to the charge equilibrium frequency indicated as ω_0. 147

Chapter 1

Resumo Expandido em Português

A Espectroscopia de Velocidade Quântica (Quantum Rate Spectroscopy - QRS), baseada no princípio da eletrodinâmica quântica $E = h\nu = e^2/C_q$ é uma ferramenta poderosa para obter insights quânticos experimentais sobre estruturas em escala nanométrica. Essa abordagem inovadora envolve a realização de medições de capacitância derivadas da impedância em um meio eletrolítico à temperatura ambiente, utilizando uma célula eletroquímica de três eletrodos e um potenciostato com analisador de frequência como equipamento de medição. Nesse contexto, com base nos fundamentos da Teoria da Velocidade Quântica (Quantum Rate Theory - QRT) discutidos em estudos anteriores (LOPES et al., 2021; BUENO; DAVIS, 2014b; SANCHEZ et al., 2022), a QRS não apenas permite explorar a eletrodinâmica intrínseca dessas estruturas, mas também oferece acesso direto às suas propriedades eletrônicas, como a densidade de estados eletrônicos (Density of States - DOS), por meio da medição da resposta de C_q,

Dadas as atuais dificuldades na fabricação de dispositivos optoeletrônicos em escala nanométrica com estruturas semicondutoras menores que 10 nm — onde as propriedades elétricas se desviam da física clássica, dificultando seu controle (BUENO, 2018a; DHILLON; KANT, 2017) — esta pesquisa de doutorado explorou a eletrodinâmica e a DOS em quatro estruturas nanométricas com diferentes tipos de confinamento quântico e naturezas químicas. Essa investigação partiu do princípio de que as propriedades eletrônicas do material central governam o desempenho do dispositivo, tornando essencial o acesso à sua estrutura eletrônica. Nesse contexto, o estudo examinou essas estruturas sob a ótica da Teoria da QRT e utilizou medições de impedância eletroquímica dependentes do tempo. A exploração de cada uma dessas estruturas contribuiu progressivamente para estabelecer os fundamentos da QRS como uma metodologia espectroscópica eletrônica. Os parágrafos

a seguir apresentam uma síntese dos principais resultados e conclusões obtidos nos estudos dessas estruturas semicondutoras. O autor, admitidamente influenciado por tendências românticas, convida os leitores a verem essa síntese como a narrativa de uma jornada em busca de um objetivo que transcende os limites acadêmicos, pois é assim que este trabalho foi percebido por ele.

Nesse contexto, a jornada começou com o estudo de uma estrutura de óxido de metal de transição redox-ativa: nanofilmes mistos de Cu_2O/CuO. Essas estruturas semicondutoras foram fabricadas na superfície de um eletrodo de ouro utilizando técnicas eletroquímicas, incluindo voltametria cíclica, voltametria de varredura linear e cronoamperometria (Figura 4.1a). A caracterização eletroquímica e morfológica indicou que os nanofilmes de óxido de cobre continham uma mistura equimolar de Cu_2O e CuO, com espessura de aproximadamente 3,0 nm. Sua morfologia apresentava uma distribuição de partículas maiores e heterogêneas, em contraste com a morfologia observada no filme de cobre metálico, caracterizado por partículas de tamanho uniforme. Consequentemente, esses nanofilmes mistos de Cu_2O/CuO representaram uma estrutura inorgânica intrigante, com potencial confinamento quântico em uma dimensão. As medições de impedância eletroquímica realizadas nesses nanofilmes revelaram a resposta de capacitância quântica (C_q) em função do potencial (no regime de baixa frequência). Essa resposta mostrou dois domínios distintos: um máximo em forma de gaussiana centrado em 0 V versus o eletrodo de referência Ag/AgCl e uma resposta exponencial em potenciais mais altos, com a capacitância aumentando com o potencial (Figura 4.2b).

Embora C_q seja definido, a partir da perspectiva da QRT e com base em princípios fundamentais da mecânica quântica, como sendo proporcional à DOS, $\frac{\partial n}{\partial \mu}$, tal que $C_q = e^2 \frac{\partial n}{\partial \mu}$, desafios permanecem na interpretação dessa resposta de C_q ou DOS. Considerando que a definição anterior de C_q foi derivada a temperatura zero absoluto, uma abordagem estatística pode ser aplicada ao incluir o efeito de alargamento térmico nos níveis de energia da estrutura semicondutora. Assim, assumindo que o sistema representa um grande ensemble canônico e que a ocupação eletrônica segue a função de distribuição de Fermi-Dirac, obtém-se uma expressão termalizada para C_q: $C_q = \left(\frac{e^2 N}{k_B T}\right) f(1-f)$, que descreve uma distribuição gaussiana de estados de energia discretos. Além disso, ao examinar energias eletrônicas mais altas, onde $eV \gg k_B T$, e assim $f \ll 1$ e $f \sim \exp\left(-\frac{eV}{k_B T}\right)$, uma nova expressão para C_q foi derivada: $C_q = \left(\frac{e^2 N}{k_B T}\right) \exp\left(-\frac{eV}{k_B T}\right)$, que

segue um comportamento exponencial que aumenta com o potencial.

Consequentemente, ambas as equações de C_q descrevem duas funções distintas de ocupação eletrônica. A resposta de C_q, conforme registrada experimentalmente por espectroscopia de impedância eletroquímica (EIS), foi analisada usando essas equações, revelando ajustes excelentes com parâmetros de $R^2 \sim 0,999$. Isso demonstra que os resultados experimentais estão alinhados com os comportamentos previstos pela Teoria da Taxa Quântica (QRT). Nesse contexto, a primeira equação, $C_q = \frac{e^2 N}{k_B T} f(1-f)$, descreve uma distribuição em forma de gaussiana de estados discretos localizados no band gap do nanofilme semicondutor. Esses estados no band gap correspondem a estados redox associados à reação eletroquímica entre os estados de oxidação do cobre, especificamente a transição eletrônica entre íons Cu^{+1} e Cu^{+2}, e vice-versa. Adicionalmente, a presença de defeitos na rede atômica do óxido de cobre — como vacâncias, impurezas e defeitos intersticiais — introduz esses estados no band gap na estrutura eletrônica. Em contraste, a segunda equação, $C_q = \frac{e^2 N}{k_B T} \exp\left(-\frac{eV}{k_B T}\right)$, representa uma resposta exponencial correspondente a uma distribuição de estados contínuos na banda de condução do nanofilme de óxido de cobre (Figura 4.1b).

Assim, a DOS dos nanofilmes semicondutores mistos Cu_2O/CuO, conforme medida por EIS à temperatura ambiente e utilizando uma solução tampão de fosfato como meio eletrolítico, meio no qual o nanofilme é quimicamente estável, foi resolvida com base nos fundamentos da QRT. Essa caracterização revelou uma distribuição semelhante a uma gaussiana de estados discretos localizados no band gap do semicondutor, bem como uma distribuição exponencial de estados eletrônicos correspondentes ao contínuo de estados na banda de condução. A resolução da DOS para esse nanofilme semicondutor, determinada pela medição da resposta C_q em um meio eletrolítico, sugeriu duas direções principais para a próxima etapa da pesquisa de doutorado: primeiro, o desenvolvimento de uma nova metodologia in situ para acessar a estrutura eletrônica, que, embora em andamento, requer um entendimento mais profundo de seus princípios físicos subjacentes; e segundo, a observação de que a distribuição exponencial de estados na banda de condução, que não envolve reações eletroquímicas, indica que o acesso à DOS de nanomateriais por medições de EIS não está restrito a estruturas com comportamento redox reversível, como monocamadas de peptídeos marcados com ferroceno, previamente estudadas (ALARCÓN et al., 2021a; SANCHEZ et al., 2022), e óxidos de metais de transição.

Nesse contexto, uma montagem de estruturas semicondutoras 0D foi eletronicamente acoplada à superfície de um eletrodo de ouro por meio de uma monocamada molecular. Especificamente, pontos quânticos (QDs) de telureto de cádmio (CdTe) foram quimicamente imobilizados em um eletrodo de ouro modificado com L-cisteína. Uma ligação química foi formada via uma ligação amídica entre os grupos carboxílicos presentes na superfície dos QDs e os grupos amina terminais das moléculas de L-cisteína (Figura 5.3). É importante notar que os QDs são nanopartículas semicondutoras que exibem efeitos de confinamento quântico em todas as três dimensões. Esses nanomateriais são frequentemente chamados de "átomos artificiais", pois o confinamento de seus portadores de carga resulta em níveis de energia discretos dentro das estruturas, análogos aos estados atômicos (identificados como s, p, d, etc.) (Figura 5.1). A DOS eletrônica de um conjunto de QDs é comumente medida experimentalmente por espectroscopia de tunelamento por varredura (STS), que permite uma caracterização abrangente da estrutura eletrônica, capturando distribuições em forma de gaussiana dos estados de valência, condução e band gap do conjunto. Essa técnica envolve a aplicação de uma diferença de potencial (V) entre o substrato que suporta o conjunto de QDs e uma ponta de microscópio posicionada acima dele, medindo a corrente de ressonância (I) associada à injeção ou remoção de elétrons entre a ponta e os estados eletrônicos dos QDs. A partir dessa corrente de ressonância, a condutância eletrônica (dI/dV) é calculada em função do potencial aplicado, que é proporcional à DOS.

Embora as medições por espectroscopia de tunelamento por varredura (STS) permitam a resolução experimental da DOS em montagens de pontos quânticos (QDs), seu funcionamento exige temperaturas ultra-baixas, condições de vácuo e pessoal altamente treinado para operar o equipamento. Esses requisitos tornam essa abordagem impraticável para a caracterização eletrônica rotineira de nanomateriais. Consequentemente, a necessidade de um método rápido e direto para acessar estruturas eletrônicas em escala nanométrica continua sendo um desafio em nanociência e nanotecnologia. Assim, ao registrar a resposta de C_q para a montagem de QDs de CdTe em função do potencial do eletrodo de ouro, que atua como uma sonda, utilizando uma solução tampão de fosfato (pH 7,4) à temperatura ambiente, foi obtido um perfil de distribuição semelhante a uma gaussiana dos estados dos QDs, comparável ao obtido por STS (Figura 5.5). Nesse caso, o conjunto de respostas em forma de gaussiana observadas em potenciais negativos corresponde aos estados de valência s_h e p_h, onde os subscritos indicam estados de lacunas.

Por outro lado, os comportamentos gaussianos identificados em potenciais positivos correspondem aos estados de condução s_e e p_e, com e indicando estados de elétrons. Cada uma dessas respostas gaussianas foi ajustada usando a expressão termalizada de C_q aplicada aos estados no band gap de nanofilmes de óxido de cobre, apresentando um excelente parâmetro de ajuste ($R^2 = 0,999$), o que confirmou que essas respostas correspondem aos estados eletrônicos dos QDs.

Dessa forma, a medição da DOS de montagens de pontos quânticos de CdTe por EIS eletroquímica à temperatura ambiente, utilizando um meio eletrolítico, foi demonstrada, representando uma grande contribuição para a área de caracterização de nanomateriais e levando ao desenvolvimento de uma nova abordagem espectroscópica eletrônica para exame in situ da estrutura eletrônica de nanomateriais, denominada Quantum Rate Spectroscopy (QRS). Contudo, é necessário um esclarecimento adicional sobre o mecanismo espectroscópico subjacente a essa metodologia. Na ausência de reações eletroquímicas, a QRT prevê uma comunicação do tipo antena eletromagnética entre os estados do eletrodo sonda e os estados de energia discretos da montagem de QDs. Esse mecanismo eletrônico pode ser entendido da seguinte forma: quando uma perturbação sinusoidal de baixa frequência e dependente do tempo é aplicada ao eletrodo sonda, os elétrons oscilantes geram uma onda eletromagnética associada ao elétron, que se propaga pela junção. Essa onda eletromagnética ressoa com a estrutura eletrônica dos QDs, gerando um sinal de corrente como resposta. Essa resposta não envolve fluxo líquido de elétrons, pois não há transporte eletrônico; em vez disso, corresponde a uma corrente de deslocamento. No entanto, essa resposta de corrente fornece informações sobre a estrutura eletrônica da montagem. O potenciostato, equipado com um analisador de frequência, captura tanto os sinais de perturbação quanto de resposta e os converte em uma função de impedância.

Portanto, o mecanismo espectroscópico da QRS baseia-se na ressonância de energia entre a onda eletromagnética de perturbação e os estados eletrônicos dos QDs. Com base nesse mecanismo proposto e considerando os resultados obtidos para as estruturas inorgânicas — nanofilmes de óxidos de cobre e QDs de CdTe — o foco da pesquisa foi direcionado para estruturas orgânicas, a fim de demonstrar a generalidade da velocidade quântica como marco teórico e metodologia experimental. Nesse sentido, explorou-se a eletrodinâmica em grafeno de camada única (SLG), uma monocamada de átomos de carbono organizados em uma rede hexagonal altamente simétrica, utilizando medições

de EIS. Como resultado, a DOS em forma de V, característica dessa estrutura orgânica 2D, foi medida por EIS à temperatura ambiente, utilizando um líquido iônico como meio eletrolítico (Figura 6.3b). Além de sua alta estabilidade química e eletroquímica, a elevada concentração iônica deste tipo de meio permite a formação de uma dupla camada elétrica mais compacta, tornando mais eficiente o fenômeno de blindagem do campo elétrico associado aos estados do grafeno (NOVOSELOV et al., 2005a; LOPES et al., 2021). Além disso, aplicando a análise de circuito RC quântico ao espectro de capacitância, foi identificada uma resposta em forma de semicirculo, registrada no nível de Fermi ou ponto de Dirac do SLG. Essa análise demonstrou que a eletrodinâmica do grafeno segue os princípios da eletrodinâmica quântica, revelando um valor de resistência equivalente, dentro do erro experimental, ao limite quântico de resistência, $R_q = 12,99\,k\Omega$. Assim, a eletrodinâmica do SLG sem transferência eletrônica, conforme explorada por EIS, segue um mecanismo de eletrodinâmica dada pela condição de acoplamento adiabático de estados.

Com cada estrutura estudada, avanços significativos na compreensão e aplicação das extensões da QRT foram alcançados. Nesse contexto, ao calcular a energia $E = \frac{g_e g_s N e^2}{C_q}$, associada à estrutura eletrônica a partir da resposta da capacitância quântica C_q em função do potencial, e empregando cálculos de Tight-Binding como modelo de resolução espacial, a estrutura de bandas do SLG no espaço energia-vetor de onda foi experimentalmente resolvida. A estrutura de bandas determinada por medições de EIS em meio eletrolítico mostrou excelente concordância com a estrutura eletrônica medida por outras técnicas espectroscópicas, como espectroscopia de fotoemissão resolvida em ângulo (ARPES), que requer temperaturas baixas e condições de ultravioleta para operação. Além disso, este resultado também esteve alinhado com a estrutura de bandas computada para o SLG através de cálculos de teoria do funcional da densidade (DFT) (Figura 6.5). Assim, a QRS, baseada em medições de EIS, constitui uma ferramenta experimental in situ poderosa para caracterizar a estrutura eletrônica do SLG.

Os resultados obtidos para o SLG revelaram o potencial para explorar tipos alternativos de eletrodinâmica dentro de estruturas orgânicas. Assim, a atenção foi voltada para o estudo dos princípios físicos que regem a eletrodinâmica em uma classe especial de sistemas moleculares: moléculas heterocíclicas π-conjugadas Push-Pull. Essas moléculas possuem uma estrutura química em que grupos doadores e aceitadores de elétrons estão eletronicamente acoplados através de pontes π-conjugadas, permitindo a comunicação de

elétrons entre os grupos doadores e aceitadores (RAPOSO et al., 2006). Tipicamente, essa comunicação é facilitada por transferência de elétrons induzida por luz, quando a luz visível irradia a molécula, resultando em uma transição eletrônica do HOMO (órbita molecular mais alta ocupada) para o LUMO (órbita molecular mais baixa desocupada), um processo conhecido como transferência de carga intramolecular (PIGOT et al., 2020). Consequentemente, as características eletrônicas dessas estruturas ofereceram a possibilidade de sondar a comunicação intermolecular entre os estados doador e aceitador sob a perspectiva da QRT por meio de medições EIS.

Nesse contexto, uma montagem de moléculas de 4*H*-tieno[3,2-*b*]pirrole-5-carboxílico (TPC) foi quimicamente ligada a uma superfície de ouro através de uma monocamada de cisteamina (Figura 7.5). A molécula de TPC contém grupos de tiofeno e ácido carboxílico, que atuam como grupos doadores e aceitadores de elétrons, respectivamente, conectados por um grupo pirrol. É importante notar que o grupo aceitador foi quimicamente modificado para facilitar a ligação à monocamada de cisteamina, estabelecendo ressonância entre os estados do eletrodo e os estados do grupo doador. Eletroquimicamente, essa molécula não exibe comportamento redox reversível, e, portanto, a comunicação intermolecular entre os grupos doadores e aceitadores não está associada a reações de oxidação e redução. Ao explorar a junção molecular de TPC utilizando medições EIS em dimetilformamida (DMF) e perclorato de tetrabutilamônio ($TBAClO_4$), um meio no qual a molécula é quimicamente estável e exibe excelente solubilidade, observou-se uma resposta semelhante a uma gaussiana de C_q, correspondente a uma DOS de elétrons acessada por meio de perturbações dependentes do tempo (Figura 7.9b). Essa resposta gaussiana está, portanto, associada à comunicação de elétrons entre os estados do eletrodo e os estados do grupo tiofeno. No entanto, assim como no caso dos QDs de CdTe e SLG, essa comunicação não corresponde a um processo de transferência de elétrons, mas sim a uma ressonância eletromagnética entre os estados eletrônicos, seguindo o mecanismo discutido anteriormente. Sob perturbação dependente do tempo em condições de equilíbrio, uma onda eletromagnética associada ao elétron propaga-se pelas junções moleculares, ressoando com a estrutura eletrônica da molécula. Em resposta, gera-se uma corrente de deslocamento, fornecendo insights sobre o comportamento eletrônico.

Além disso, a análise do espectro de capacitância e dos gráficos de Nyquist registrados no potencial correspondente ao máximo da resposta gaussiana, utilizando um mod-

elo de circuito RC quântico derivado da QRT, revelou que a resistência associada a essa dinâmica de elétrons entre os estados é aproximadamente 12,92 KΩ. Esse valor, dentro do erro experimental, corresponde ao $R_q = 12,99\,k\Omega$, o limite quântico de resistência. Consequentemente, a comunicação de elétrons entre os estados do eletrodo e o grupo doador da molécula ocorre com máxima eficiência quântica, consistente com os princípios da eletrodinâmica quântica. Esse resultado também revelou que esse tipo de eletrodinâmica, que não envolve reações eletroquímicas, ocorre sob uma condição de acoplamento adiabático dos estados eletrônicos, como observado no SLG. Portanto, este trabalho pioneiro com moléculas heterocíclicas π-conjugadas sob a perspectiva da QRT demonstrou o potencial de caracterizar e ajustar as estruturas eletrônicas das junções moleculares formadas por essas moléculas em condições de temperatura ambiente e pressão ambiental, o que é crucial para o design e desenvolvimento de dispositivos moleculares eletrônicos.

Em resumo, cada avanço na compreensão da dinâmica dos elétrons traz novas perspectivas e introduz ideias desafiadoras e disruptivas. Com base nos resultados obtidos nesta pesquisa de doutorado nas quatro estruturas estudadas, pode-se afirmar que a estrutura teórica QRT — fundamentada no princípio da eletrodinâmica quântica $E = h\nu$ e sua metodologia experimental, a QRS, representam uma ferramenta versátil para explorar a eletrodinâmica em estruturas químicas em escala nanométrica. Esta pesquisa demonstrou a aplicabilidade geral dessa abordagem para estudar a eletrodinâmica em estruturas de diversas naturezas químicas e tipos de confinamento quântico. No entanto, esses encontros são apenas o começo de um novo campo na nanociência, Eletrônica em Escala Nanométrica em Meios Eletrolíticos, baseado em uma eletrodinâmica de baixa energia e com potenciais aplicações que vão desde o estudo de fenômenos intrigantes, como entrelaçamento quântico e acoplamento mecânico-eletromagnético de elétrons, até o desenvolvimento de dispositivos cujos princípios operacionais são governados por fenômenos não-clássicos. Assim, este trabalho de doutorado serve como um prefácio para possibilidades impressionantes.

Chapter 2

State of the Art: Historical and Theoretical Review of Electron Dynamics

As discernible throughout the exposition of this doctoral thesis, the protagonist of this narrative, drawing an analogy between a narrative and a Ph.D. research, is the electron and its dynamic characteristics. Hence, with the aim of underscoring the significance of comprehending electron dynamics at matter for the technological and scientific progress of contemporary society, this section delineates a historical and theoretical review of this topic. It follows a chronological and analytical -line, contemplating the diverse scientific models proposed by bright minds to explicate the captivating phenomena of the electron movement in nanoscale chemical systems. It is imperative to note that this review is conducted in a concise and non-exhaustive manner, serving as an introduction to the ongoing Ph.D. thesis. Thus, only models and contributions of notable significance to the advancement of the thesis are explicitly referenced herein. Nonetheless, the omission of certain models and contributions in this context does not diminish their importance in the broader study of electron dynamics. Accordingly, this review will commence with a brief description of the atomic models that laid the foundations of modern chemistry. Subsequently, the quantum mechanical interpretation of electron dynamics will be revisited, with a special focus on the probabilistic interpretation given by Max Born. Following this, the primary models of electron transfer and transport, proposed for various physical settings, will be described, particularly those related to diffusion-limited processes in solution and the diffusionless regime. Finally, a recent model, grounded in quantum electrodynamics foundations, will be presented herein. This model, named *Quantum Rate*

Theory (QRT), predicts a quantum rate principle associated with the electron dynamics events (BUENO, 2023b; BUENO; MERCADO, 2022; BUENO, 2024), and serves as the theoretical framework for this Ph.D. thesis. Throughout its development, this thesis demonstrates the generality of the QRT for exploring electron dynamics at the nanoscale and establishing a new nanoscale electronics approach, *electronics in electrolytic medium*. Therefore, without further ado, our narrative will commence.

2.1 Atomic Models and the Discovery of the Electron

The nanoworld, the realm of atoms and molecules, has captivated the curiosity and attention of human minds since the earliest civilizations. Dating back to the 5th century BC, the Greek philosopher Democritus proposed pioneering ideas about the composition of matter (ROBINSON, 1958; ZALTA et al., 1995). According to his thinking, Democritus posited that matter is constituted by extremely small particles called atoms, which means "indestructible and indivisible" (PULLMAN, 2001; BERGMAN, 1998). Nevertheless, the idea of indivisible particles as primary components of matter was not reconciled by other important contemporaneous philosophers such as Plato and Aristotle. Thus, during many centuries, under the dominance of Aristotelian philosophy in Western culture, the notion of the atom seemed to fade over time (CHANG; OVERBY, 1986).

Notwithstanding, with the advance in the observation of the properties of gases and other materials, the idea of the atom reappeared in the 17^{th} century. In this context, the English professor John Dalton (SMITH, 1856), based on detailed macroscopic observations concerning chemical reactions, published in 1808 his postulates, which are considered the foundation of modern chemistry. In a summarized manner, these postulates defined the atom as the structural and indivisible unity of matter. Furthermore, they stated that chemical elements are constituted by identical atoms, while chemical compounds are combinations of atoms of different elements in specific proportions (CHANG; OVERBY, 1986; BROWN, 2009). Although the above ideas may seem obvious to contemporary readers, these postulated marked the origin of modern chemistry and spectroscopy and were considered completely correct for around fifty years. According to Dalton's postulates, the atom was described as a tiny, indivisible particle without structure. However, multiple research endeavors conducted from 1850 onward demonstrated that atoms possessed an

internal structure. In other words, atoms were found to be constituted by even smaller particles known as subatomic particles (PETRUCCI et al., 2022; PAULING, 1988). These investigations led to the discovery of three fundamental subatomic particles: the proton, the neutron, and the electron. Consequently, it is at this juncture that the protagonist of this narrative, the electron, makes its entrance, and its discovery and physical features will be the focal point in the upcoming paragraphs.

In the 1890s, physicists were deeply interested in comprehending the phenomena of electrical discharge in vacuum tubes containing metallic plates. In these experiments, the air was nearly completely evacuated from the vacuum tube by pumping. Subsequently, two metallic plates were placed within the evacuated tube (CHANG; OVERBY, 1986; BROWN, 2009). By applying a potential difference between the plates, the negatively charged plate, known as the cathode, emitted an invisible beam toward the positive plate or anode. This invisible beam was revealed upon impact with materials possessing fluorescence properties (MARTIN, 1986; GOLDSTEIN, 1876). Because these beams emanated from the cathode, they were termed cathodic rays, and understanding their nature puzzled physicists of the time. –Were cathodic rays a new type of radiation or a stream of particles? If the latter was correct, what type of particles did these rays consist of?- These were the questions that plagued the minds of scientists during that decade.

In this scenario, the British physicist J.J. Thomson utilized his extensive knowledge of electromagnetic theory to provide answers to these perplexities, marking the beginning of the electrodynamic field and the raison d'être of this narrative(CHANG; OVERBY, 1986). Thomson conducted experiments on cathodic rays in vacuum tubes, enhancing the setup with additional elements as depicted in Figure 2.1. In this configuration, cathodic rays traveled towards the anode, which possessed a central aperture allowing the ray to continue its trajectory to the opposite end of the tube, where it impacted a glassy surface covered with fluorescent material, indicating the precise point of impact. Additionally, two metallic plates and an electromagnet were positioned outside the vacuum tube (ATKINS; JONES, 2007; KEITHLEY, 1999). Utilizing this setup, Thomson observed three significant results that elucidated the nature of cathodic rays. Firstly, when external magnetic and electric fields were applied, the cathodic rays deviated from their initial trajectory (see Figure 2.1), indicating an interaction of these rays with the fields. According to electromagnetic theory, charged bodies or particles in motion can interact

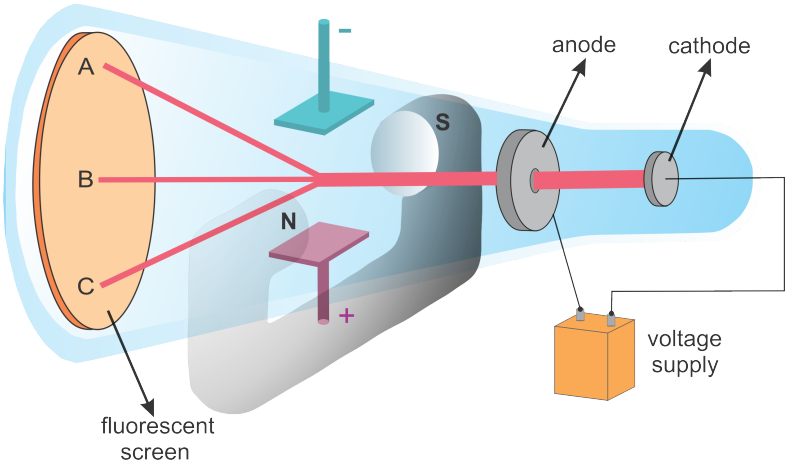

FIGURE 2.1. The vacuum tube setup used by Thomson for studying the effects of external electrical and magnetic fields on the trajectory of cathode rays. The experiments conducted with this setup led to the discovery of the electron. Source: Adapted from Chang et al. 2010, p.44.

with magnetic and electric fields. Secondly, by applying a potential difference between the external plates, the cathodic ray was repelled by the negatively charged plate, indicating that these charged bodies possessed a negative charge. Finally, Thomson observed that when cathodic rays impacted a metal material, the material became negatively charged, confirming the negative charge of the particles constituting these rays (BROWN, 2009; TRO et al., 2017). Accordingly, these observations led Thomson to conclude that cathodic rays consisted of a flux of negatively charged particles ejected from cathode atoms. Currently, these particles are known as electrons, the protagonists of this story and the reason for the existence of electrodynamics as a scientific field (THOMSON, 1901; THOMSON; REID, 1927). J.J. Thomson received the Nobel Prize in Physics in 1906 for discovering the electron. Who would have thought that our main character is approximately 130 years old since its discovery?"

Furthermore, experiments conducted by Thomson on the effect of magnetic and electric fields on cathode rays enabled him to compute the charge (q)/mass (m) ratio of the electron, revealing a value of $-1{,}76\times10^{8}$ C/g (CHANG; OVERBY, 1986; BROWN, 2009). These properties—mass and charge—are pivotal in the modern interpretation of the dynamics and nature of the electron because they dictate its mechanical-electromagnetic characteristics. Afterward, R.A. Millikan, in 1909, began a series of experiments to de-

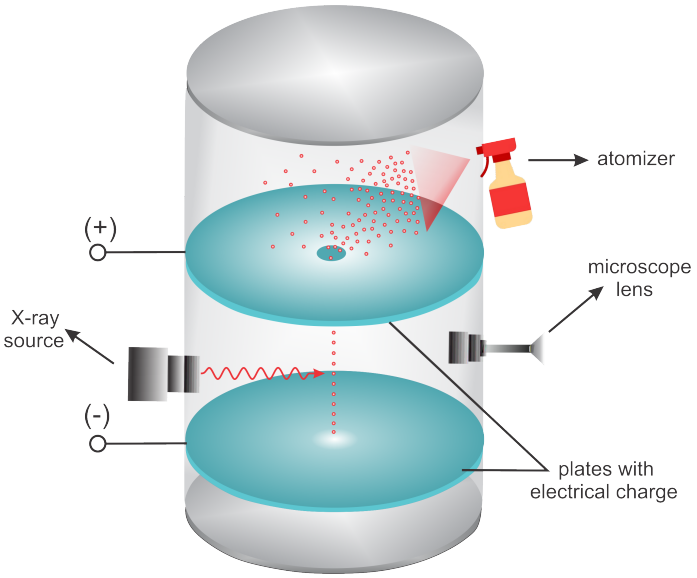

FIGURE 2.2. Schematic diagram of the Millikan oil drop experiment.The experiment involves releasing small oil droplets, which had captured excess electrons, between two electrically charged plates. Millikan observed the droplets, measuring how the voltage of the plates affected their rate of descent. Source: Adapted from Brown et al. 2004, p.38.

termine the charge of the electron (MILLIKAN, 1911; FLETCHER, 1982). In his famous experiment, known as the "Millikan oil drop experiment," he analyzed the movement of small oil drops that acquired charge due to ions present in the air, through an electric field, as depicted in Figure 2.2. By applying his extensive knowledge of electrostatics to the movement of the charged oil drops, Millikan determined that the charge of an electron accurately corresponds to $e = -1{,}6022 \times 10^{-19}$ C (MILLIKAN, 1913). From this electron charge value and using the Thomson's relation, Millikan also calculated the value of the electron mass to be $m = 9{,}10 \times 10^{-28}$ g (MILLIKAN, 1911; ATKINS; JONES, 2007). It is interesting to note that Thomson's and Millikan's experiments constituted the first characterizations of the electron in history. Thanks to their work, the protagonist of this narrative—the electron—gained an identity, a name, and two fundamental properties with accurate values: mass and charge. Millikan was awarded the Nobel Prize in Physics in 1923 for determining the electron charge (GOODSTEIN, 2000).

Until that time, two characteristics of atoms were known: the existence of electrons within their structures and their neutral electrical nature. Based on these features, Thomson proposed the first atomic model. In Thomson's model, the atom comprised a uniformly charged sphere with a positive charge, which compensated for the negative charge of the electrons, thereby ensuring atomic electroneutrality (HON; GOLDSTEIN,

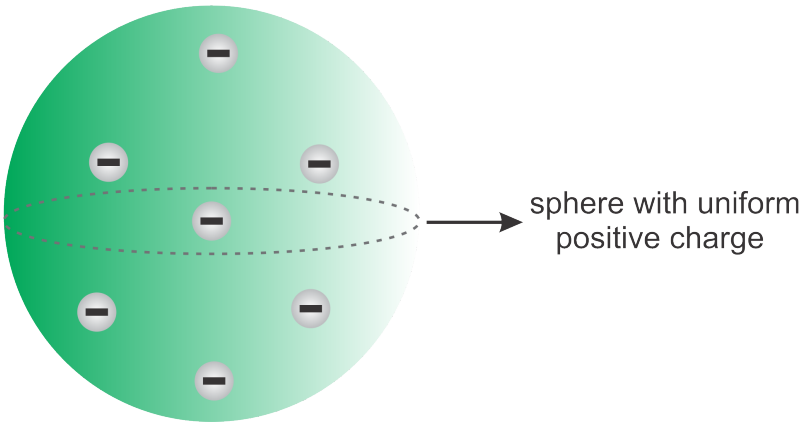

FIGURE 2.3. Thomson's atomic model, known as the "plum pudding model," due to its resemblance to a traditional English dessert made with raisins. Source: Adapted from Chang et al. 2010, p.46.

2013; HEILBRON, 1977) (see Figure 2.3). The electrons were described as particles embedded within the sphere of diffuse positive charge. This model was named the "plum pudding model" due to the similarity between the description of the atomic structure and this English dessert (FALCONER, 1987; FERGUSSON, 2011). Nonetheless, this model remained accepted only for a few years because the discovery of radioactivity by Henri Becquerel, along with Marie and Pierre Curie, introduced new experimental possibilities for exploring atomic structure (BROWN, 2009; CHANG; OVERBY, 1986). In-depth studies on radioactivity, the spontaneous emission of high-energy radiation by certain materials such as uranium, allowed to conclude that during the decomposition process of radioactive material, three types of radiation are emitted: α-rays, consisting of positively charged particles; β-rays, consisting of high-velocity electrons; and γ-rays, which are high-energy electromagnetic radiation (SEARS et al., 2014).

In 1910, Ernest Rutherford, a New Zealand physicist, along with his collaborators, conducted revealing experiments using radioactive material as a source of α-particles (CAMPBELL, 2013). Their aim was to impact a thin gold foil with these particles, which was surrounded by a fluorescent material plate, as represented in Figure 2.4a. In their observations, Rutherford and his colleagues found that the majority of α-particles passed through the gold foil, continuing along their initial trajectory. However, they also observed that a small percentage of α particles were scattered at large angles upon passing through the gold foil, and even more surprisingly, some particles were reflected back towards the radioactive source (RUTHERFORD, 1919; SEARS et al., 2014). These findings puzzled

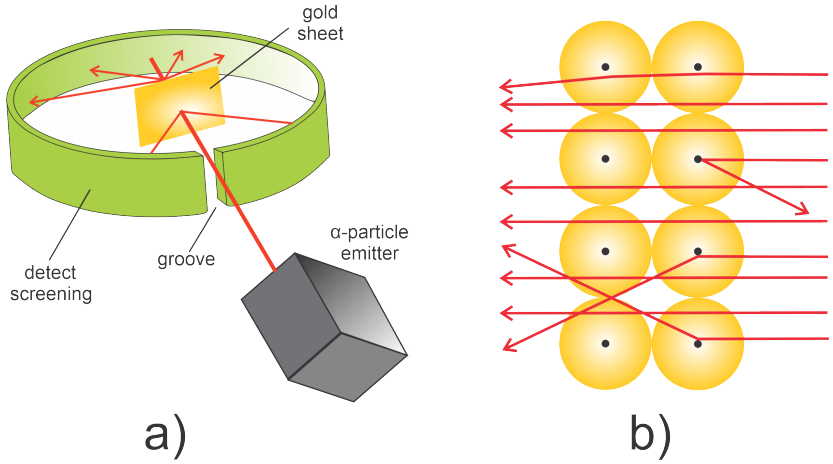

FIGURE 2.4. (a) Rutherford's experimental setup used to measure the scattering of α-particles by atoms in a gold foil. (b) Schematic representation of the trajectories followed by α-particles as they either pass through or are deflected by the atomic nucleus. Source: Adapted from Chang et al. 2010, p.47.

Rutherford for some time, as he did not have a clear interpretation. He was convinced that these results would revolutionize the understanding of the structure of matter, but he also knew he needed to be cautious with his interpretations. Therefore, he took his time before sharing the conclusions of his findings.

About a year later, Rutherford managed to explain his findings through the postulation of a new atomic model. This model stated that most of the volume of an atom consists of empty space, and the majority of the atom's mass is concentrated in a small, central, and dense region called the nuclei as depicted in Figure 2.5 (RUTHERFORD, 2012). According to Rutherford, the positive charge is concentrated in the nucleus of the atom, which occupies only $1/10^{13}$ of the atomic volume, while the negative charge, carried by electrons, randomly moves around the nucleus. This atomic structure proposal aligned with the experimental results. The majority of α particles did not suffer dispersion because they traveled through the empty space within the gold atoms. However, when some α particles passed close to the nucleus, the electrostatic repulsion force between positive charges caused their dispersion at large angles. Finally, for certain α particles that directly impacted the nuclei, the repulsion force was sufficiently strong to cause a complete reversal of their trajectory (see Figure 2.4b) (CHANG; OVERBY, 1986; BROWN, 2009). Additional studies conducted by Rutherford led to the conclusion that the positive charge localized within atomic nuclei consisted of positively charged particles called protons, whose charge magnitude was equivalent to that of electrons, but whose mass was 1840

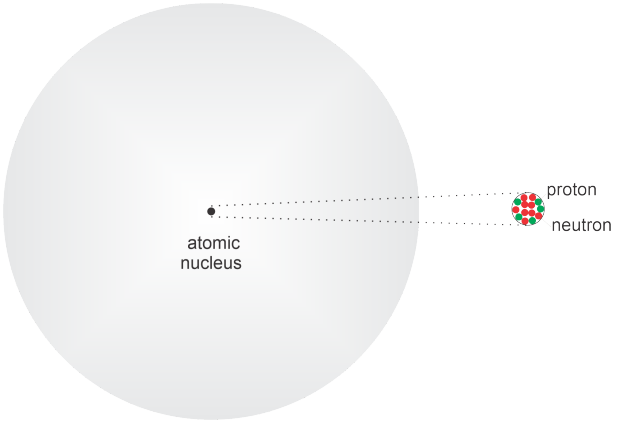

FIGURE 2.5. Rutherford's atomic model describes protons and neutrons as being confined to a small region known as the nucleus, while electrons are depicted as clouds orbiting around it. Source: Adapted from Chang et al. 2010, p.48.

times greater than the mass of an electron ($m_p = 1{,}67 \times 10^{-24}$ g) (SERWAY; JEWETT, 2021; PETRUCCI et al., 2022; DEVONS, 1991).

Nevertheless, Rutherford's model left an unresolved issue: the mass relationship between atoms of different elements. To address this problem, Rutherford and other researchers predicted the existence of another atomic particle. In such scenario, it was the British physicist James Chadwick who conducted experiments similar to Rutherford's and discovered the neutrons, charge-neutral particles with a mass slightly greater than that of protons, located in the nucleus along with the protons (BROWN, 2009). The discovery of neutrons in atomic nuclei resolved the issue of mass relationships, for instance, explaining the 4:1 mass ratio between helium and hydrogen atoms (CHADWICK, 1932; CHADWICK et al., 1931). It is important to mention at this point in the narrative that the discovery of the three subatomic particles and their properties constituted wonderful breakthroughs for both chemistry and physics, revolutionizing the understanding and manipulation of matter. Nonetheless, in the previous paragraph, as throughout this chapter, the focus was directed toward the electron, the subatomic particle directly involved in chemical and electrochemical reactions, resonance between energy levels, and overall electrodynamic processes. In other words, although approximately 2000 times heavier, the proton and neutron play a secondary role in this text, and the spotlight will continue to focus on the electron.

Therefore, until 1932, the most accepted atomic model in the scientific community described protons and neutrons as confined to a diminutive region of the atomic volume,

with electrons depicted as electron clouds surrounding the nucleus. However, this story does not end here; it only begins. Although the previous atomic model seemed consistent with the electroneutrality of the atom, the relationship between masses and electrostatic observations; the random and simple representation of the electrons surrounding the nuclei as a cloud, it did not leave physicists entirely at ease. Questions regarding the stability of electron movement around the nuclei, the true nature of the electron, and its possible probabilistic interpretation now captivated human reason. Hence, electrons deserved more attention to unveil their secrets. In the next chapter, it will be evidenced how a new field of physics emerged from the interest in understanding the unconventional behavior of the electrons.

2.2 The Electron and the Origins of Quantum Mechanics

Although Rutherford's atomic model appeared consistent with experimental observations and the principles of electromagnetism, a vast number of questions remained unsolved regarding the movement of electrons around the nucleus and the interaction mechanisms between matter—electrons, atoms, and molecules—and electromagnetic radiation, waves described as electric and magnetic fields that are perpendicular to each other and exhibit self-induction properties (SERWAY; JEWETT, 2021; SEARS et al., 2014). However, advancing to the next stage in the history of electrodynamics faced a significant obstacle: the inertia of human reasoning. Specifically, there was a belief that natural phenomena could be completely understood through certain proposed physical models.

At the end of the 17th century, physics could be summarized by three significant scientific contributions: Newton's mechanics, Maxwell's laws of electromagnetism, and thermodynamics, which together constitute what is known today as classical physics (ZETTILI, 2009; BRANSDEN; JOACHAIN, 2000). Although it is now understood that only a minuscule number of phenomena in the universe are comprehended through human science, the fascinating aspect of this historical period is that physicists of the late 1800s believed that all phenomena could and must be explained by the principles of classical models. They saw no need for additional scientific descriptions or models. However, during this period, a great number of experimental results were obtained through inge-

nious experiments designed by brilliant minds to explore the nanoworld—the realm of atoms and electrons—that could not be explained by the postulates of classical physics (ZETTILI, 2009). These experiments were based on intriguing observations of the interaction between matter and electromagnetic radiation, in other words, the phenomena of absorption and emission of radiation by matter. Among these fascinating phenomena were the continuous thermal radiation emitted by a solid object and the ejection of electrons from a metal surface when impacted by electromagnetic radiation of a specific frequency (BROWN, 2009; SCHWABL, 2007). The explanation of these two phenomena led to the origin of a new and revolutionary area of physics, the quantum mechanics (ZETTILI, 2009; SERWAY; JEWETT, 2021), as described below.

In the mid-1800s, a significant amount of experimental data regarding the thermal radiation of various solid materials had been collected. This data demonstrated that, regardless of the chemical composition and shape of the material, the thermal radiation emitted by heated solid exhibited a continuous distribution over the entire range of frequencies comprising the electromagnetic spectrum (BRANSDEN; JOACHAIN, 2000; GRIFFITHS; SCHROETER, 2018), as depicted in Figure 2.6b. For each temperature, there was a maximum energy intensity at a certain frequency, which increases with temperature. This relationship explained the change in color of objects, from red to yellow to white, as they are heated. However, although the experimental observations were reproducible for all materials, there was no theoretical model that explained this continuous spectral behavior. All attempts to provide an explanation based on classical thermodynamics and electromagnetism failed miserably, tormenting the minds of physicists at the time (ZETTILI, 2009).

Nonetheless, when current ideas fail, the mind may be willing to consider new and entirely revolutionary proposals. Thus, in 1900, Max Planck, a German physicist, succeeded in providing an accurate explanation for the continuous emission spectrum of heated solids, which shook the foundations of classical physics (HOFFMANN, 2008; EVANS; THORNDIKE, 2006). According to classical physics, matter and radiation could exchange any amount of energy (continuously), as stated by the equipartition theorem. However, Planck's proposal contradicted this principle (ZETTILI, 2009; BROWN, 2009). Building on previous attempts by Wien and Rayleigh, Planck analyzed the radiation within a hollow metal cavity with a small hole in its surface as illustrated in Figure 2.6a.

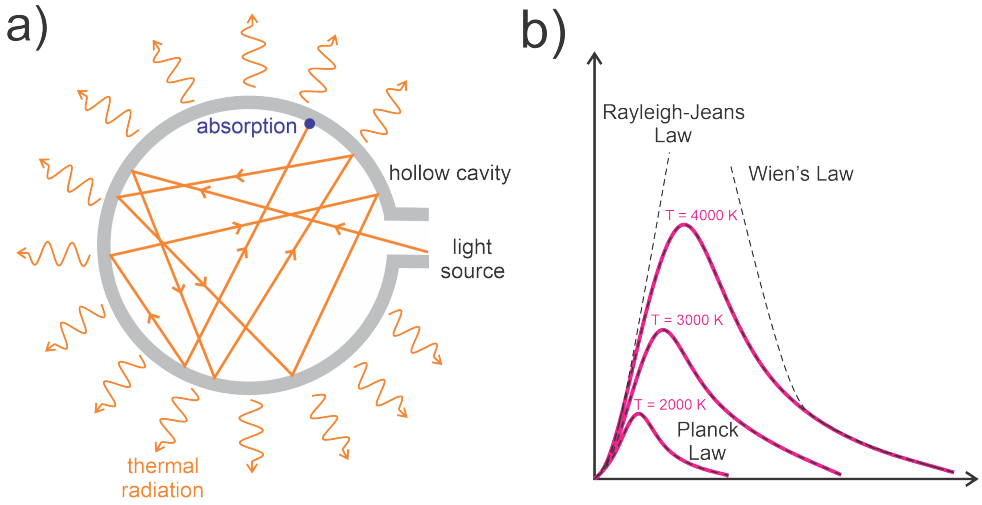

FIGURE 2.6. (a) A hollow metal cavity that serves as a physical model of a blackbody, which is a perfect absorber and emitter of electromagnetic radiation. (b) The energy density spectrum of blackbody radiation at various temperatures as a function of frequency (represented by pink curves). Additionally, the spectrum models proposed by Rayleigh-Jeans and Wien are also presented. Source: Author's own work.

When this cavity was heated and reached thermal equilibrium, Planck observed that the radiation behaved as stationary electromagnetic waves with nodes on the internal walls of the cavity. These waves were generated by the thermal agitation of the electrons on its surface—indeed, electrons, the protagonists of this story, had not been forgotten. Under thermal agitation, the electrons acted as harmonic oscillators, emitting electromagnetic radiation. Consequently, the energy density associated with these oscillating electrons corresponded to the energy density of the stationary electromagnetic waves within the cavity, as well as the thermal radiation emitted from the hole in the hollow cavity (PLANCK, 1900; PLANCK, 1978; GRIFFITHS; SCHROETER, 2018).

In this context, Planck concluded that the energy density associated with the thermal radiation leaving the hole could be calculated as the product of the number of oscillation modes of the electrons (frequencies) and their average energy $\langle E \rangle$. However, the revolutionary contribution of Planck lay precisely in the method he used to calculate this energy. In opposition to classical physics, Planck considered that matter and radiation could exchange energy only in discrete quantities, using discrete sums in his energy calculations. In other words, Planck's proposal stated that electrons could absorb and emit energy only in integer multiples of a certain amount (PLANCK, 1900; ZETTILI, 2009), which was given by:

$$E = nh\nu \tag{2.1}$$

Eq. 2.1 represents the quantum of energy, where h is a constant introduced by Planck, describing the quantization condition of the matter-radiation interaction. ν is the frequency of absorbed or emitted radiation, and n takes integer values such as $n = 1, 2, 3, \ldots$. Although these novel ideas caused the heads of physicists of the time to explode, Planck's model of thermal radiation of solids proved to adjust quite well to the experimental spectrum across the entire range of frequencies. It revealed a new and astonishing feature of electrons: they only exchange energy with radiation in discrete amounts (CANIOU, 2013; PLANCK, 1978; SEARS et al., 2014). How demanding the main character of this narrative turned out to be! Hence, Eq. 2.1 and the consequences derived from it marked the beginning of a new era in physics — quantum mechanics — and helped explain distinct phenomena in the nanoworld that were previously unresolved (ZETTILI, 2009).

In 1887, Heinrich Hertz, a German physicist, experimentally discovered the photoelectric effect —the ejection of electrons from a metal surface when electromagnetic radiation falls on it (HERTZ, 1887b; HERTZ, 1887a). A schematic representation of this effect is depicted in Figure 2.7. From his observations, Hertz concluded several empirical postulates about this phenomenon. Electrons are only ejected from the metal surface when the light reaches a threshold frequency, ν_0, regardless of the light's intensity. No electrons are ejected for frequencies below ν_0. This threshold frequency varies from material to material. For any frequency above ν_0, the number of ejected electrons depends on the light's intensity but not its frequency. Finally, the kinetic energy of the ejected electrons increases linearly with the frequency of the radiation and is independent of the light's intensity. These observations are astonishing! Electrons can not only interact with radiation but also use this interaction to be ejected from the metal that contains them (BRANSDEN; JOACHAIN, 2000; GRIFFITHS; SCHROETER, 2018). It seems that every time we delve deeper into this narrative, its protagonist reveals an even more intriguing characteristic than before.

Although Hertz's results were indisputable, there was no theoretical model to explain them, as the dependency of the photoelectric effect on frequency could not be ac-

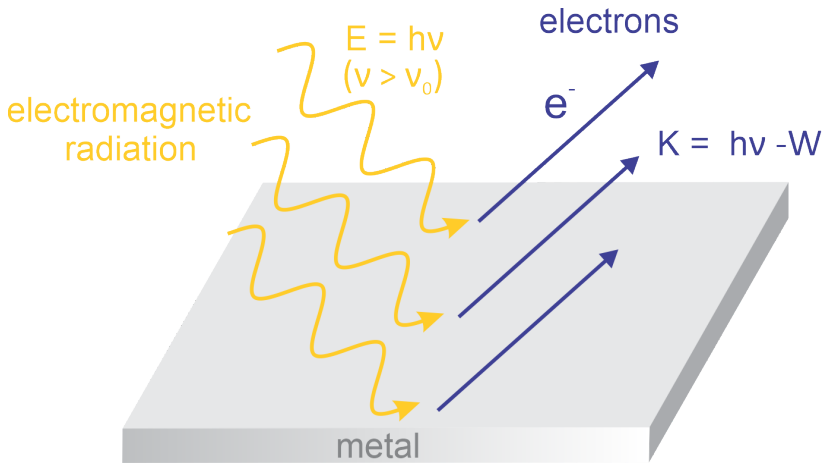

FIGURE 2.7. Schematic representation of the photoelectric effect: when a metal is irradiated with electromagnetic radiation with certain threshold frequency, electrons may get emitted from the metal surface. Source: Author's own work.

counted for within the framework of classical physics (GRIFFITHS; SCHROETER, 2018; ZETTILI, 2009). In this context, in 1905, Albert Einstein, also of German nationality, utilized Planck's concept of quantized electromagnetic radiation to provide an accurate explanation for the photoelectric effect. Einstein proposed that radiation could be modeled as fields of quanta or packets of energy $E = h\nu$, now known as photons (EINSTEIN, 1905). When radiation strikes a metal surface, a quantum of energy is completely absorbed by an electron. However, the electron will only be ejected if the energy of the absorbed quantum matches the metal's work function $W = h\nu_0$. This function describes the energy required to free an electron from the metal and is linked to the threshold frequency ν_0. Therefore, the photoelectric effect occurs only when an electron absorbs a quantum of energy with a frequency ν equal to or greater than ν_0, irrespective of the radiation's intensity. If the metal is irradiated with a frequency equal to or greater than ν_0, the number of ejected electrons depends on the intensity of the radiation, not the frequency, since this characteristic is related to the number of quanta in the radiation beam. Lastly, when the frequency of irradiation exceeds ν_0, the excess energy is converted into the kinetic energy K of the electrons ejected from the metal (BROWN, 2009; ZETTILI, 2009; GRIFFITHS; SCHROETER, 2018). The preceding arguments derived from Einstein's work can be expressed as:

$$h\nu = W + K \tag{2.2}$$

This relation represents the principle of conservation of energy in Einstein's photoelectric effect model. It describes how the radiation energy, $h\nu$, falling on the surface of a metal compensates for the work function energy, W, enabling the ejection of an electron. The excess energy is transformed into the kinetic energy of the electron, ensuring that the sum of both energies equals the initial $h\nu$ energy (BRANSDEN; JOACHAIN, 2000; CHANG; OVERBY, 1986). Einstein was awarded the Nobel Prize in Physics in 1921 for his explanation of the photoelectric effect.

As will become clear below, each proposal aimed at understanding electron phenomena paved the way for subsequent advancements in electrodynamics. In 1913, Niels Bohr, a Danish physicist, made a groundbreaking proposal for an atomic model that addressed two significant mysteries unresolved by classical physics: the discrete emission spectrum of atoms and molecules, and the stability of electrons around nuclei (BOHR, 1913; KRAGH, 1979). According to Rutherford's atomic model, the atom consists of a diminutive nucleus containing protons, with electrons traveling around this nucleus in an accelerated manner (CHANG; OVERBY, 1986). However, analyzing this electron movement from the standpoint of classical physics predicted that as electrons moved around the nucleus, they, being accelerated charged particles, would emit electromagnetic radiation, lose energy, decelerate, and eventually spiral into the nucleus, resulting in the destruction of both electrons and protons (SEARS et al., 2014; SERWAY; JEWETT, 2021). But this does not occur in nature! Drawing on the works of Planck and Einstein, Bohr proposed that in the hydrogen atom, the electron can only occupy certain orbits with specific energies E_n and angular momentum $L = n\hbar$, where $\hbar = h/2\pi$, and n corresponds to the principal quantum number, representing the energy level and taking on positive integer values. For instance, level $n = 1$ represents the state of lowest energy, or ground state, while levels $n > 1$ represent excited states, as illustrated in Figure 2.8. A key consequence of Bohr's model is that an electron in any of the allowed orbits will not spiral toward the nucleus and, therefore, will not radiate energy. Thus, the quantization of the electron's energy accounts for the stability of electrons in the atomic structure (BROWN, 2009; ATKINS; JONES, 2007).

Furthermore, Bohr also succeeded in explaining the discrete emission spectrum of atoms and molecules using his model. He proposed that when electrons are energized through thermal energy, electric discharge, or radiation, they transition from a lower

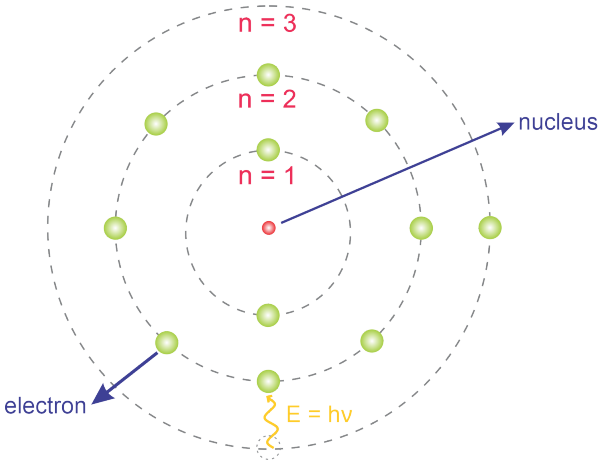

FIGURE 2.8. Bohr atomic model, in which the electrons can only occupy certain certain orbits with specific energies E_n and angular momentum $L = n\hbar$, where $\hbar = h/2\pi$, and n corresponds to the principal quantum number, representing the energy level and taking on positive integer values. Source: Author's own work.

energy state (E_1) to a higher energy state (E_2). During the relaxation process, in which the electron returns to the lower energy initial state, electromagnetic radiation is emitted with energy equal to the difference between the two levels, represented as $E = h\nu = E_2 - E_1$. Consequently, because electron transitions occur only between the allowed energy orbits, only certain spectral lines corresponding to these transitions are observed in the spectrum of atoms and molecules (ATKINS; FRIEDMAN, 2011; MCQUARRIE, 1997).

While the Bohr atomic model revolutionized the physical thinking of the time by describing the quantized nature of electron energy, the subsequent proposals would challenge the very foundations of classical physics. Although Bohr's model explained electron stability and the atomic emission spectra, two significant questions remained unresolved: Why were the energies of the hydrogen electron quantized? Why was the electron in the Bohr model restricted to orbits around the nucleus at fixed distances? Bohr did not have the answers to these questions, and approximately a decade passed without resolution (PETRUCCI et al., 2022; CHANG; OVERBY, 1986). In 1924, Louis de Broglie, a French physicist, presented a groundbreaking proposal to the scientific community. He suggested that if electromagnetic radiation, composed of energy quanta, exhibited particle-like behavior when interacting with matter, then material particles, such as electrons, could exhibit wave-like behavior within atoms (BROGLIE, 1924; BROGLIE, 1930). This proposal was revolutionary: could a particle with mass and velocity truly present wave properties? Were the ideas of Planck, Einstein, and Bohr not sufficient for classical physics? It seemed

that the challenges to the principles of physics were relentless. The protagonist of this narrative, the electron, now demonstrated a dual wave-particle behavior.

According to de Broglie, an electron bound to the nucleus of an atom behaves as a standing wave whose wavelength ν must fit the circumference of the orbital as depicted in Figure 2.9, $(2\pi r)$ so that, it does not cancel out with successive orbits. Hence, the relation between the electron wave length and circumference of orbit was described by:

$$2\pi r = n\lambda \tag{2.3}$$

where n is the principal quantum number (BROWN, 2009; CHANG; OVERBY, 1986).Furthermore, because the energy of the electron is quantized (E_n), the radius r of the orbit can only assume certain values as n increases, indicating that the radius is also quantized. Nevertheless, De Broglie went even further, starting from the relativistic momentum relation of the photon (quantum of energy), $p = E/c$, and considering the Planck's relation $E = h\nu$, he derived the fundamental relation:

$$\lambda = h/p = h/mV \tag{2.4}$$

where m and V correspond to the mass and velocity of the wave-particle with nonzero rest mass or matter wave. This expression relating the wave (μ) and particle (p) properties, led to the conclusion stating that: *each material particle of momentum p behaves as a group of waves (matter waves) whose wavelength μ are governed by the velocity and mass of the particle.*(BRANSDEN; JOACHAIN, 2000; ZETTILI, 2009) The wave behavior of electrons proposed by De Broglie was experimentally confirmed in 1927 by Davisson and Germer, and later by Thomson, who obtained interference patterns, a characteristic of waves, from beams of electrons. Although these experiments are not described in this text, they are among the most famous experimental evidences of the wave-particle duality of material particles. Thus, it is interesting to revisit them using the references provided herein (DAVISSON; GERMER, 1927b; DAVISSON; GERMER, 1927a).

The De Broglie theory and its experimental confirmation marked the beginning of a new era for physicists and chemists. Electrons, central to chemical reactions and crucial in

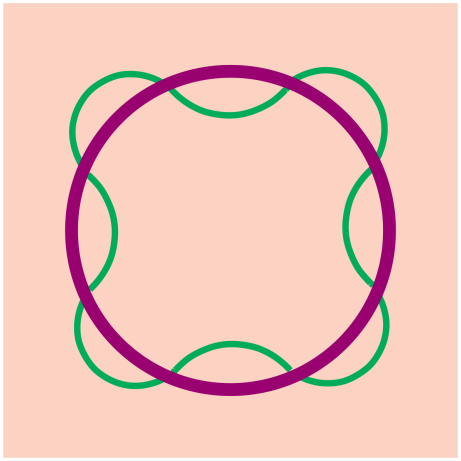

FIGURE 2.9. De Broglie's model: The circumference of the orbit is equal to an integer number of wavelengths. This is an allowed orbit. Source: Adapted from Chang et al. 2010, p.290.

determining the electrical and mechanical properties of materials based on their behavior within atomic structures, exhibit a dual nature, showing complementary wave-particle behavior. De Broglie was awarded the Nobel Prize in Physics in 1929 for his doctoral work that presented the idea of wave-particle duality of matter (CHANG; OVERBY, 1986; ZETTILI, 2009) Nonetheless, each advance in understanding the dynamic properties of the electron opens the door to new and pivotal issues. Although the proposal of the electron's dual behavior accounts for a vast array of experimental observations, important questions still arise. If the electron is a wave that extends throughout space, how can its position be accurately described? In response to this scenario, Werner Heisenberg postulated the uncertainty principle for the electron: *It is not possible to know both the momentum and the position of a particle with certainty simultaneously* (HEISENBERG, 1927; HEISENBERG, 1989). Mathematically, this postulate is expressed as:

$$\Delta x \Delta p \geq h \tag{2.5}$$

Where Δx and Δp correspond to the uncertainties in position and momentum, respectively. Hence, according to Heisenberg, accurately measuring the electron's position (i.e., making Δx very small) leads to a highly inaccurate measurement of its momentum, with Δp becoming very large, and vice versa (CHANG; OVERBY, 1986). Applying these principles to the Bohr model revealed that the electron does not move in a circular orbit, but instead, there is a probabilistic nature to determining its position within the

atom. Heisenberg received the Nobel Prize in Physics in 1932 by the uncertainly principle (BRANSDEN; JOACHAIN, 2000).

Was it not enough that our protagonist exhibited a dual nature? Must the electron also manifest probabilistic character? Well, it seems that the electron is a particular character in nature. In this sense, it was necessary a formal theory that comprised the great contributions and founds conducted so far to the electron dynamics. In 1926, Erwin Schrödinger, an Austrian physicist and philosopher, building on De Broglie's postulates, applied a rigorous mathematical formalism to develop a new theory that allowed for the resolution of the dynamics of quantum particles under potential energies (BRANSDEN; JOACHAIN, 2000; GRIFFITHS; SCHROETER, 2018; ZETTILI, 2009). This theory was named wave mechanics, and its greatest contribution was the proposal of a differential equation, known as Schrödinger's equation, which describes the dynamics of the electron and incorporates both particle and wave properties (ATKINS; JONES, 2007).

The solution to this equation is the wave function, $\Psi(r,t)$, of the electron within a given potential energy. Although, physically, this function has no direct significance, it allows for the determination of all properties of the electron system. Schrödinger was awarded the Nobel Prize in 1933 for the development of this equation (BRANSDEN; JOACHAIN, 2000; GRIFFITHS; SCHROETER, 2018). However, it is important to note that Schrödinger's equation does not account for relativistic and electromagnetic effects in its description of the electron's dynamics in matter. Thus, like all physical models, its application is limited to certain types of systems. In this context, an interesting question arises here: if the electron is a particle with mass and charge, exhibiting particle-wave duality, is it possible to describe its movement between quantum states without considering its magnetic and relativistic properties? This is a question the author leaves open for the readers to ponder.

In 1927, Max Born, a German physicist, proposed a probabilistic interpretation of wave mechanics. Born asserted that the square modulus of the wave function, which are the solutions to Schrödinger's equation, corresponds to the probability density (BORN, 1909). This probability density represents the likelihood of finding the electron within a particular region of space with volume V. Thus, according to Born's interpretation, the localization of the electron within an atom cannot be described from a deterministic per-

spective but must be understood in terms of probabilistic nature (ATKINS; FRIEDMAN, 2011; BRANSDEN; JOACHAIN, 2000). It's truly fascinating—much like a futuristic or science fiction Hollywood movie—the electron, an entity exhibiting both wave and particle duality, whose physical behavior can only be comprehended in terms of probability.

Finally, by combining quantum mechanics with the theory of special relativity, Paul Dirac derived an equation in 1928 that describes the motion of electrons while accounting for relativistic and electromagnetic effects. This renowned equation, known as Dirac's equation, is considered a generalization of quantum mechanics. Dirac demonstrated that Schrödinger's wave mechanics is merely an approximation that neglects the relativistic nature of electron dynamics (DIRAC, 1981; GORBAR et al., 2021; ZETTILI, 2009).

However, the history of electrodynamics did not end there. Building upon the previous contributions to understanding the nature and motion of electrons as described by quantum mechanics, various theories and models have been proposed to explain phenomena such as chemical reactions involving electron transfer and electron current through solid-state and molecular systems. In the following section, the main theories regarding electron transport and transfer will be discussed, with a critical examination highlighting their significant contributions and limitations.

2.3 Electron Transfer and Transport Theories

In the previous sections, the historical and theoretical development of electron theory was discussed. This exploration commenced with the discovery of the electron, followed by Thomson's and Millikan's measurements of its mass and charge. The narrative progressed with De Broglie's attribution of wave-particle duality to the electron and culminated in the establishment of quantum mechanics—a predictive framework for electron dynamics developed by Schrödinger and Dirac. These significant contributions led to the formulation of various theories and models aimed at understanding electron behavior in different chemical systems. However, beginning in the 1940s, progress in comprehending electron behavior in materials faced a new intellectual trend: the tendency to study natural phenomena in isolation. Although the subject under investigation remained the same—electron dynamics—physicists and chemists began to approach the issue from two distinct and seemingly irreconcilable perspectives.

Historically, Michael Faraday (1791-1867), a British scientist, is considered the father of electrodynamics due to his significant contributions, such as the laws of electrolysis (FARADAY, 1834) and electromagnetic induction (SERWAY; JEWETT, 2021; SEARS et al., 2014). However, his studies were not interpreted from a unified standpoint of electrodynamic phenomena; instead, they were divided and addressed differently by physicists and chemists. Chemists, based on Faraday's law of electrolysis—which involves generating chemical reactions through electrical perturbation and producing electrical energy from a chemical reaction—developed the field of electrochemistry (OLDHAM et al., 2011; BREITKOPF; SWIDER-LYONS, 2017). Electrochemistry focused on studying chemical reactions caused by electron transfer between reduced and oxidized species in the presence of an electrolytic medium, a solvent that contains ions. In electrochemical reactions, the electron transfer rate constant k constitutes the pivotal kinetic feature. Therefore, most efforts in this field have focused on proposing theoretical and empirical models aiming to accurately calculate this property (BARD et al., 2022). On the other hand, physicists used Faraday's law of electromagnetic induction—the production of an electromotive force (emf) across an electrical conductor in a changing magnetic field—as a key foundation for building the principles of solid-state and molecular electronics. Most studies conducted in these fields involve positioning a molecule or nanoscale semiconducting films between two metallic electrodes and measuring the electron conductance or transport G through these structures (RATNER, 2013; MARQUÉS-GONZÁLEZ; LOW, 2016; CHOI; MODY, 2009; WALLING, 1968). The flow of electrons across these structures is driven by a potential difference applied between the electrodes. It is rather curious that the history of understanding the movement of the protagonist of this narrative, the electron, in the matter has been written since two different perspectives: solid-state electronics and electrochemistry, even though the natural phenomenon at its origin was the same. Nonetheless, the theoretical and empirical models by both physicist and chemists about the electron dynamics constituted significant contributions that led to modern understanding of this phenomena. Accordingly, a brief review about the principal theories of electron electron and transfer, starting by electron transfer theories in electrochemistry.

In this context, the study of electrochemistry can be divided into two distinct subareas: homogeneous and heterogeneous electrochemistry. The former focuses on the study of electron transfer reactions between an electron donor and acceptor chemical species in the solution phase. In contrast, the latter directs its efforts toward the exploration of elec-

tron transfer processes that occur at the interface formed by a solid-state electrode and a donor/acceptor chemical species in solution (BARD et al., 2022; BOCKRIS; REDDY, 1998). Historically, theories of homogeneous electrochemistry were proposed first, with the Marcus Theory being recognized as the most important among them. This theory, developed by Rudolph A. Marcus, a Canadian-born American chemist, explains the rate of electron transfer in homogeneous reactions—the rate at which an electron moves or jumps from the donor species to the acceptor species in the solution phase—providing an expression for the electron transfer constant k associated with this type of electrochemical reaction. It is rather important to mention that the Marcus Theory is entirely based on classical principles and is founded on the Arrhenius empirical model of chemical reaction kinetics and the transition state theory (TST) (MARCUS, 1956b; MARCUS, 1957a; MARCUS, 1957b).

Briefly, Svante Arrhenius, a Swedish scientist, experimentally observed that the rate constant k of most chemical reactions exhibited a common trend with temperature T, specifically $\ln k \propto 1/T$. Based on his observations, Arrhenius proposed an empirical relation for k in activation-controlled reactions, which currently represents the fundamental mechanism of chemical reactions (ARRHENIUS, 1889a; ARRHENIUS, 1889b; LEVINE, 2009). This relation, derived by the brilliant mind of Arrhenius using statistical thermodynamics, is given by:

$$k = A\exp(-E_A/k_BT) \tag{2.6}$$

where R is the gas universal constant, T is the absolute temperature, E_A is the activation energy and A is a frequency factor associated with probability of the chemical reaction taking place. Since Arrhenius relation includes the term e^{-E_A/k_BT}, this describes the mechanism of chemical reactions in terms of the probability of using thermal energy to overcome a energy barrier of high E_A. Hence, a chemical reaction will present a greater probability of occurring according to the fixed pressure and temperature conditions imposed on the system (LAIDLER, 1984; BARD et al., 2022).

Afterward, based on the relation of Eq. 2.6 , many theories were proposed with the objective of determining explicit expressions for the parameters E_A and k for specific

chemical reactions. Among the most renowned theories is the Transition State Theory (TST), developed by Henry Eyring, a Mexico-born American theoretical chemist, in 1935 (EYRING, 1935; EVANS; POLANYI, 1935). The central idea of this theory is that chemical reactions proceed through a well-defined transition state or activated complex, and its foundations can be better understood through an analysis of potential energy surfaces (PES). A PES plot represents the minimum energy reaction path in terms of potential energy along a reaction coordinate, as depicted in Figure 2.10. In a PES plot, the potential energy corresponds to the ordinate axis, and the reaction coordinate matches the abscissa axis. For a certain chemical reaction, the reaction coordinate conforms to a molecular parameter or feature that can be easily identified in the reactions and indicates the progress of the reactions, for instance, a bond angle or the inter-atomic distance (BARD et al., 2022; TRUHLAR et al., 1996). Therefore, for a simple elementary bimolecular reaction as represented in Eq. 2.7:

$$\text{Reactant} \rightleftharpoons \text{Product} \tag{2.7}$$

two domains are identified as energy minima: reactant and product. The chemical reaction proceeds by the change of potential energy from the reactant setup toward the product setup along the reaction coordinate, passing through a energy maximum, named the activated complex. In the TST, there is a strong coupling between both reactant and product setups for forming a defined activated complex, which can be defined as a quasi-equilibrium potential energy state where both chemical structures, reactant and product, are in equilibrium. Hence, according to the Arrhenius postulates, for the chemical reaction to take place in any direction, from reactant to product or vice versa, the system under certain pressure and temperature conditions must present the enough energy to overcome this maximum (or activation energy) (BARD et al., 2022; LEVINE, 2009). Thus, as highlighted in the PES plot, the activation energies $E_{A,f}$, from reactant to product, and $E_{A,b}$, from product to reactant, are defined as the energy differences between the activated complex and the reactant and product minima, respectively. Eyring, by taking into account prior ideas and applying fundamental principles of chemical kinetics to calculate the concentration of the activated complex (EYRING, 1935), derived a formulation of the Arrhenius kinetic relation as follows:

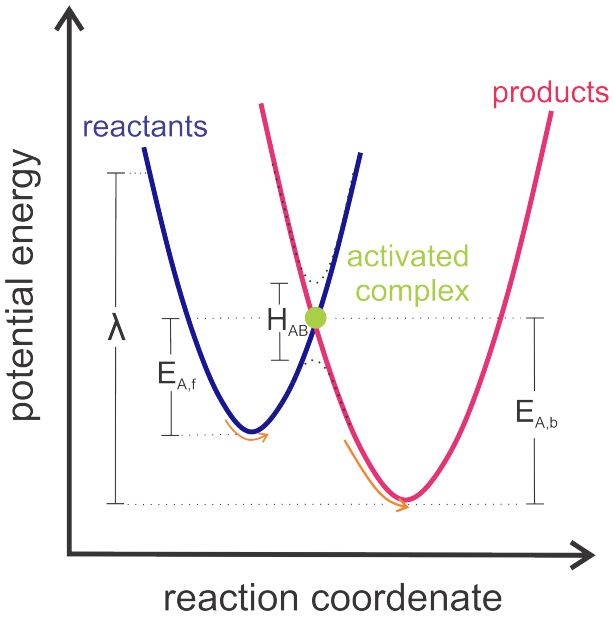

FIGURE 2.10. Schematic representation of the Marcus Theory, in which parabolic potential energies are assumed for both reactants and products. In this model, based on transition state theory, the potential energy is plotted in function of a reaction coordinate. The chemical reaction proceeds by the change of potential energy from the reactant setup toward the product setup along the reaction coordinate, passing through a energy maximum, named the activated complex. Source: Author's own work.

$$k = \kappa \frac{k_B T}{h} \exp(-E_A / K_B T) \tag{2.8}$$

In Equation 2.8, k_B represents the Boltzmann constant and T denotes the absolute temperature. Consequently, Marcus began with the concepts and principles derived from the Arrhenius relation and the transition state theory (STS) to formulate his electron transfer kinetic theory for homogeneous electrochemical reactions (BARD et al., 2022; MARCUS, 1956b). However, Marcus's primary focus was on addressing a longstanding question in chemistry: how can the influence of the solvent on the kinetics and energetic conditions of electrochemical reactions be explained? Numerous experimental data indicated that altering the solvent, pressure and temperature activation conditions and electron transfer reaction's rate constant (k) are affected. These findings suggested that the electrical properties of the solvent significantly impacted the electron transfer process between electron donor and acceptor species. Therefore, it appeared that the movement of the electron was governed by the solvent's dielectric properties. This ultimately constrained the rate of transfer of the electron(MARCUS, 2020; MARCUS, 1956b).

In this context, Marcus developed his theory for homogeneous reactions under the assumption that only changes in the charge of donor and acceptor species occur, while significant modifications in their chemical and solvation shell structures are negligible (BARD et al., 2022; MARCUS, 1956a). Consequently, Marcus modeled the donor and acceptor species, along with their respective solvation shells, as two charged spheres. This model can be applied to outer-sphere electrochemical reactions, such as the electron self-exchange reaction between Fe^{+2} and Fe^{+3}, where modifications in their chemical structures due to electron transfer are minimal. Similarly, for this type of electrochemical reaction, the Franck-Condon principle was taken into account. Therefore, an electron transfer process was described as an isoenergetic event in which the nuclei of the reactants and products, as well as the solvation molecules, experience only small displacements, ensuring that the solvent configuration remains the same before and after the electron transfer (MARCUS, 1956a; MARCUS, 1956b; MARCUS, 1957a). Marcus applied the dipole polarization classical model to interpret the effect of the solvent on electrochemical reactions. However, by considering the processes of electron transfer and solvent polarization, which result from the change of charge, this reaction ultimately infringed upon the Franck-Condon principle. This is because the polarization depends on the charge states of both the reactants and the products, which exhibit distinct charge states (MARCUS, 1964a; MARCUS, 1956a; MARCUS, 2020).

To address this issue, Marcus considered that electron transfer and solvent polarization processes were not in equilibrium, each characterized by time constants, τ_e and τ_p respectively. Hence, the formation of the correct solvent configuration and the electron transfer are decoupled and do not occur simultaneously. The solvent molecules reach the activated complex configuration before the electron transfer takes place. However, this process requires energy, which is provided by the thermal energy of the solvent, leading to the appropriate polarization state. Once this state is achieved, the electron can transfer (MARCUS, 1956a). Therefore, the ability of the solvent to polarize towards the correct configuration determines the activation energy E_A and the rate of the electrochemical reactions (MARCUS, 1956b; MARCUS, 1965).

Based on the previous phenomenological description and an analysis of the PES-plot, Marcus formulated a relationship for the activation energy (E_A) of homogeneous electrochemical reactions. This was achieved by modeling the potential energy of the reac-

tants and products (electron donor and acceptor) using parabolic functions, as illustrated in Figure 2.10. Marcus's relation is expressed in terms of a new theoretical parameter he proposed, the reorganization energy (λ) (MARCUS, 2020; MARCUS, 1964a), which is given by:

$$E_A = \frac{(\lambda + E_0)^2}{4\lambda} \tag{2.9}$$

where E_0 is the standard energy of the electrochemical reaction. The concept of the energy λ can be understood as the energy required to reorganize the solvent molecules' configuration from the reactants to the products without transferring the electron (MATYUSHOV, 2023; GRUHN et al., 2002). For an electron transfer reaction with spherical reactants and products in a polar medium, λ is described in terms of the solvent dielectric constant as follows:

$$\lambda = \frac{e^2}{4\pi\epsilon_0}\left(\frac{1}{d_{AD}} - \frac{1}{r_A} - \frac{1}{r_D}\right)\left(\frac{1}{\epsilon_{op}} - \frac{1}{\epsilon_s}\right) \tag{2.10}$$

In Eq. 2.10, e is the charge of the electron, ϵ_0 is the vacuum dielectric constant, d_{AD} is the distance between the donor and acceptor species, r_A is the radius of the acceptor sphere, r_D is the radius of the donor sphere, ϵ_{op} is the optical dielectric constant at high frequencies, and ϵ_s is the static dielectric constant at low frequencies (BARD et al., 2022; BOCKRIS; REDDY, 1998). Accordingly, λ modulates E_A, and in turn, the electron transfer rate constant k given by Eq.2.8. The relationships described by Eqs. 2.9 and 2.10 constitute Marcus's significant contributions to the kinetics theory, which earned him the Nobel Prize in Chemistry in 1992 for his interpretation of the effect of solvent dielectric properties on the rate of electron transfer reactions. It is important to mention that, as stated at the beginning of this narrative, the aim is to conduct a historical and theoretical review of the principal contributions to electrodynamics, presenting the main ideas of each. Therefore, the mathematical deductions and formalism underlying Marcus's theory were not presented. However, key references are cited, which can be revisited by the readers of this document (MARCUS, 1956b; MARCUS, 1957b; MARCUS, 1965).

Subsequently, Marcus analyzed another important feature aiming to generalize his

formulation for inner-sphere reactions, which involve significant changes in the chemical structures of the reactants and products, as well as in the solvent shell. This feature pertains to the electronic coupling between the electron donor and acceptor states. Marcus suggested that homogeneous electron transfer reactions could be categorized as adiabatic or non-adiabatic depending on the value of this characteristic (MARCUS; SUTIN, 1985a; MARCUS, 1964a). Mathematically, the electron coupling was modeled by the matrix H_{DA}. According to his formulation, in a non-adiabatic reaction, the donor and acceptor states are weakly coupled; H_{DA} (depicted in Fig.2.10) is small compared to the reorganization energy, allowing the donor and acceptor to retain their identity. The system has a certain probability of transitioning from the initial to the final potential energy curves. In contrast, for an adiabatic reaction, the electronic coupling is strong; the gap of H_{DA} is larger, and the system stays on the lower potential energy curve (EBERSON; EBERSON, 1987; ADAM; SCHÖNBERGER, 1992). Therefore, through the mathematical treatment of the previous ideas, Marcus formulated the general equation of this theory, which is given by:

$$k = \frac{2\pi}{h}|H_{DA}|^2 \frac{1}{\sqrt{4\pi\lambda k_B T}} \exp\left(-\frac{(\lambda + E_0)^2}{4\lambda k_B T}\right) \tag{2.11}$$

From the author's perspective, the Marcus theory (Eq. 2.11) stands as the most significant contribution to modern electrodynamics, particularly in the realm of electrochemical reactions. The Marcus theoretical framework was considered foundational for subsequent models. However, it is important to note that this theory was originally formulated to explain the kinetics of homogeneous electrochemical reactions, where both the electron donor and acceptor are in solution. To explore heterogeneous electrochemistry, which involves electron transfer between a solid-state electrode and species in solution, several new theories were proposed. Notably, the Butler-Volmer and Gerisher models (BARD et al., 2022; BOCKRIS; REDDY, 1998) emerged among them. The Butler-Volmer model, rooted in classical concepts of macroscopic thermodynamics, primarily focuses on calculating exchange currents (i) and transfer coefficients (α) that govern the kinetics of heterogeneous electron transfer (NEWMAN; BALSARA, 2021). While this model will be briefly mentioned here, it is not directly relevant to the ongoing PhD thesis under development. Nevertheless, it deserves acknowledgment as a major macroscopic theory in electrochemistry. Relevant references are cited herein to offer readers an overview of the

Butler-Volmer model.

On the other hand, this narrative will shine a spotlight on heterogeneous electrochemistry theories based on the electronic structure of the electrode and the electroactive species in solution. This approach is encapsulated in a microscopic kinetics model proposed by Heinz Gerischer, a German chemist renowned for his significant contributions to electrochemistry (LEWIS et al., 1997). Among his most notable contributions is the model described in the history of electrodynamics, which is based on the distribution of energy states. As illustrated in Figure 2.11, Gerischer's central idea revolves around electron transfer occurring between an occupied state and unoccupied states that are energetically matched by the energy E. Therefore, in a reduction process at the electrode-solution interface, the occupied state resides on the electrode, while the energetically matched unoccupied state is located on the electroactive species in solution. Conversely, in an oxidation process, the occupied state is on the species in solution, and the unoccupied state is on the electrode. However, in a more realistic scenario, the states involved in the electron transfer span a range of energies (see Figure 2.11). Therefore, the total rate of the process is obtained by integrating the rates at each energy level (BARD et al., 2022; BOCKRIS; REDDY, 1998).

The electron density of states of the electrode, as depicted in Figure 2.11, is governed by the Fermi-Dirac electron occupancy function $f(E)$, where the Fermi level E_F —the highest occupied energy level in the electron structure— is identified. Within the electron structure of the electrode, two overlapping bands of electron states exist: occupied and unoccupied states. For energy levels significantly lower than E_F, the electron occupancy probability is unity, indicating complete occupation. Conversely, for energy levels well above E_F, this probability is zero, indicating no occupation. However, for energy levels within approximately $\pm 4k_BT$ of E_F, the value of this probability varies continuously from 0 to 1, reflecting partial occupation. Hence, at the Fermi level E_F the electron occupancy probability is $f = 1/2$.n the solution side, the distribution of donor and acceptor states is governed by the electron structure of two different chemical species. Since the energy levels of the electroactive species in solution are discrete or localized, the distribution of states (DOS) involved in the processes of reduction and oxidation is represented by two Gaussian shapes in Figure 2.11, where D_O and D_R correspond to the DOS of the species that undergo reduction and oxidation, respectively (BARD et al.,

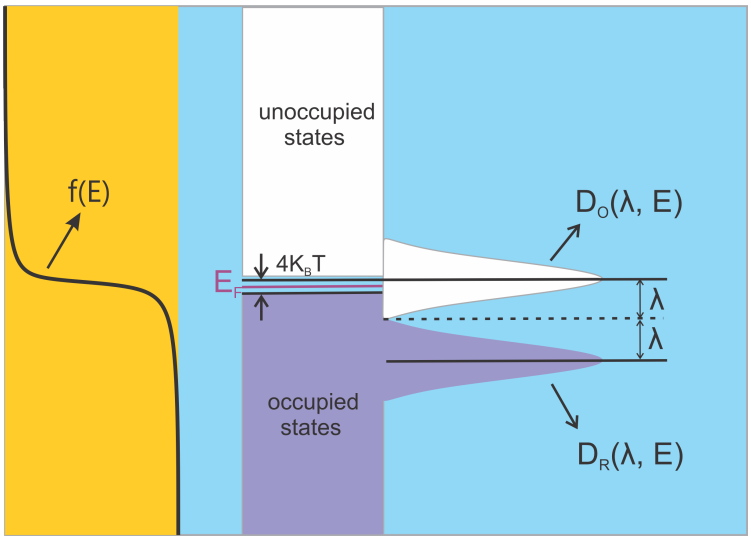

FIGURE 2.11. This scheme describes the relationships between electronic states at the interface between a metal electrode and a solution containing species O and R at equal concentrations. The vertical axis represents electron energy (E) on the absolute scale. On the electrode side, a zone $4k_BT$ wide is centered on the Fermi energy (E_F), where the probability of occupancy, f(E), transitions from nearly 1 below the zone to nearly zero above. On the solution side, the density distributions of states for O and R are represented as Gaussian functions, corresponding to the probability density functions, $W_0(\lambda, E)$ and $W_R(\lambda, E)$. The filled states of the electrode overlap with the empty states of O, allowing reduction to occur. However, since the filled states of R overlap only with filled electrode states, oxidation is blocked. Source: Adapted from Bard et al. 2001, p.124.

2022; GERISCHER, 1978).

When the electrode is polarized, for example, by applying a potential difference relative to a standard reference, the energy levels can shift towards more positive or negative potentials without causing a significant change in the electron occupancy, owing to its high electron density. Thus, E_F varies linearly with the electrode potential. Consequently, these shifts in the electrode energy levels enable the matching of the distribution of occupied states of the electrode with the electron states of D_O, and similarly, the unoccupied states of the electrode with those of D_R, facilitating electron transfer between these states (GERISCHER, 1990; GERISCHER; WILLIG, 2006). Therefore, based on the aforementioned premises, Gerischer derived expressions for the electron transfer rate constants involved in electrochemical oxidation and reduction reactions between a solid electrode and electroactive (redox) species in the solution phase (NEWMAN; BALSARA, 2021; GERISCHER, 1978). Thus, for a heterogeneous reduction reaction, Gerischer's formulation, which consider the electron features, is written as follows:

$$k_R = \nu \int_{-\infty}^{\infty} P_R(E) W_O(\lambda, E) f(E) DOS(E) dE \tag{2.12}$$

where ν is the frequency associated with characteristic time of the reaction, $P_R(E)$ is a proportionality function, $W_O(\lambda, E)$ is the reduction probability density function which include the $D_O(E)$, and $DOS(E)$ is the electron density of states of the electrode. Similarly, for an oxidation reaction the Gerisher's expression is given by:

$$k_O = \nu \int_{-\infty}^{\infty} P_O(E) W_R(\lambda, E)[1 - f(E)] DOS(E) dE \tag{2.13}$$

This equation describes the oxidation rate constant k_O, where $P_O(E)$ is the proportionality function for oxidation, and $W_R(\lambda, E)$ is the oxidation probability density function including $D_O(E)$. In addition, as the reader may have already observed, the probability density term $W(\lambda, E)$, utilized in Eqs. 2.13 and 2.12, depends not only on the energy E but also on the reorganization energy λ introduced by Marcus (BOCKRIS; REDDY, 1998; GERISCHER; WILLIG, 2006). Therefore, Gerisher recognized the significance of the parameter λ in heterogeneous electrochemical reactions and incorporated it into his theory. Specifically, he derived expressions for $W_R(\lambda, E)$ and $W_O(\lambda, E)$ in terms of this parameter, such as:

$$W_R(\lambda, E) = (4\pi\lambda k_B T)^{-1/2} \exp\left[-\frac{(E - E_F + \lambda)^2}{4\lambda k_B T}\right] \tag{2.14}$$

$$W_O(\lambda, E) = (4\pi\lambda k_B T)^{-1/2} \exp\left[-\frac{(E - E_F - \lambda)^2}{4\lambda k_B T}\right] \tag{2.15}$$

The relationships in Eqs.2.14 and 2.14 describe the Gerisher-Marcus theory, a theoretical framework widely employed for studying electron transfer reactions between an electrode and electroactive species in solution. This theory is particularly valuable for semiconducting electrodes, where their electronic structure plays a crucial role in these processes (BARD et al., 2022). Remarkably, to date, the Marcus and Gerisher models have facilitated the description of two scenarios: electron movement within chemical structures in the same phase and between structures in solid and liquid phases. The abil-

ity to develop one's own theories is a privilege reserved for significant figures in history, and the electron possesses this capability. Could there ever be a figure more famous than the electron?

Even more surprising is the fact that theories regarding electron dynamics did not stop there! Both Marcus and Gerisher treated homogeneous and heterogeneous settings, respectively, involving electroactive species in solution (BARD et al., 2022; BOCKRIS; REDDY, 1998; NEWMAN; BALSARA, 2021). Interestingly, both scenarios share a common element: kinetics are controlled by the diffusion of species to the electrode-solution interface. However, the most promising applications in electrochemistry and electronics involve organic or inorganic semiconducting structures confined to the surface of conducting electrodes. Examples include redox molecular monolayers (ECKERMANN et al., 2010), transition metal oxide nanofilms (MADURAIVEERAN et al., 2019), or cyclic organic molecules containing electron donor and acceptor moieties (KABIR; UZZAMAN, 2022). Significant studies have addressed electron transfer phenomena in redox electroactive self-assembled monolayers (SAMs), as represented in Figure 2.12, using the Marcus-Gerisher approaches (ECKERMANN et al., 2010; CHIDSEY, 1991; WEBER; CREAGER, 1994). However, from a physical standpoint, this is not entirely correct. In the case of redox SAMs, electron transfer occurs in a diffusionless regime, suggesting the presence of new physics distinct from the classical framework upon which the Marcus and Gerisher models are based.

In 1979, Georges S. Laviron, a French scientist, presented a method based on linear sweep voltammetry (LSV) measurements to calculate the electron transfer constant (k) for electroactive species absorbed on electrode surfaces (LAVIRON, 1979a; LAVIRON, 1979b). This method elucidated the electron transfer processes occurring between the electrode and these redox electroactive species in a diffusionless physical regime. It is important to note that the term "absorbed" refers to the chemical or physical attachment of electroactive chemical structures to conducting or semiconducting electrodes. In this context, Laviron developed his model based on the classical Butler-Volmer theory, under the condition that in this diffusionless regime, η satisfies $\eta \sim 0$. Here, η represents the overpotential of the junctions, given by $\eta = E_F - \mu$, where E_F is the Fermi level potential of the attached redox species, and μ is the chemical potential of the electrons within the electrode (LAVIRON et al., 1980; LAVIRON, 1980). From his mathematical treatment,

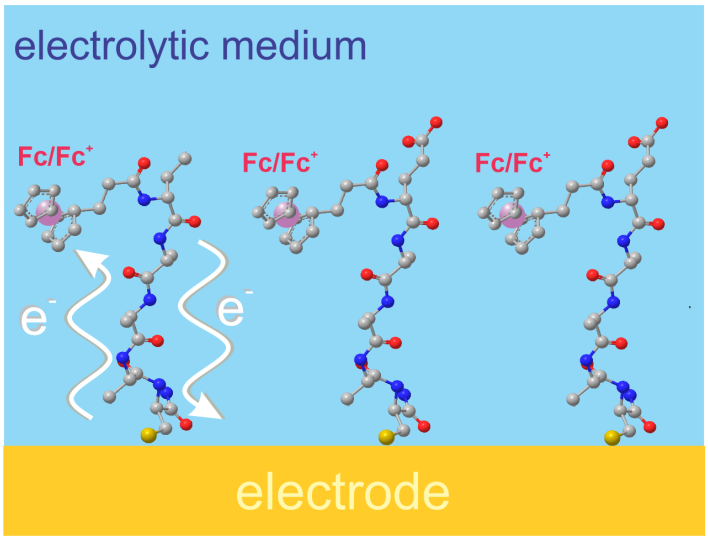

FIGURE 2.12. A schematic representation of a redox-active molecular self-assembled monolayer formed on a gold electrode surface is presented. In this case, the peptide scaffold is modified with a redox-active molecule, such as ferrocene, and is chemically anchored to the electrode. Consequently, the electron transfer between the electrode and the ferrocene probe, and vice versa, can be explored in a diffusionless regime. Source: Author's own work.

Laviron revealed a linear relationship between the peak current density j_p of an LSV experiment, associated with electron transfer, and the scan rate s in cases where electron transfer occurs in a diffusionless regime. This relationship is given by:

$$j_p = \frac{e^2\Gamma}{4Ak_BT}s \tag{2.16}$$

where Γ is the surface coverage. Thus, a proportionality constant exists between j_p and s in this diffusion regime (LAVIRON; ROULLIER, 1980). However, Laviron did not explore the physical-chemical significance of this constant in his formulation, though it will be highly relevant in the final section of this chapter. Furthermore, based on the relationship in Eq.2.16, an experimental approach was established for calculating k for these types of electrochemical reactions. This approach involves conducting LSV measurements at various scan rates and constructing a plot of peak potential V_p versus the logarithm of the scan rate s (> 200 mVs^{-1}) for both oxidation and reduction processes. From the slope of the linear behavior at high scan rates, the parameter α, which is the transfer coefficient describing the symmetry of the energy barrier of the electrochemical reaction, can be calculated. Ideally, $\alpha = 0{,}5$, but it is important to determine this parameter

for each specific reaction of interest (LAVIRON, 1979b; LAVIRON, 1979a). Finally, k is calculated using expressions derived within Laviron's formulation and the values of α calculated for the oxidation (α_O) and reduction (α_R)reactions , such as:

$$k = \frac{\alpha_R e}{k_B T} s = (1 - \alpha_O) \frac{e}{k_B T} s \tag{2.17}$$

The Laviron method is widely used for calculating k for redox chemical structures immobilized on electrodes. However, as evidenced in the detailed derivation of its formulations in references (LAVIRON, 1979a; LAVIRON; ROULLIER, 1980), various constraints are applied in the mathematical treatment, which limit its accuracy in complex systems such as redox proteins and organometallic compounds.

In summarizing the models discussed thus far, all of them are chemical kinetics approaches developed by brilliant chemists to describe electron transfer reactions in the presence of an electrolytic medium—a liquid molecular solvent containing ionic species. Given these significant contributions to electron dynamics by chemists, it is natural to pose the question: what were the contributions of physicists? Did physicists leave this task solely to chemists? Certainly not! It would be incorrect to assume that physicists did not contribute significantly to the understanding of this fundamental issue. While chemists focused on the kinetics of electron transfer reactions in the presence of an electrolytic medium within the field of electrochemistry, physicists concentrated on measuring and predicting the electrical phenomena associated with the movement of electrons or electron transport in chemical structures at the nanoscale in dry mediums, within the realms of nanoelectronics or molecular electronics. In the context of nanoelectronics, physicists commonly employ a two-terminal quantum point contact experimental setup. This setup involves placing the nanoscale chemical structure of interest between two conducting electrodes (CHEN et al., 2007; RATNER, 2002), as illustrated in Figure 2.13. Examples of frequently studied chemical structures in this setup include aliphatic and aromatic organic molecules, organic-metallic complexes, and inorganic quantum dots. Subsequently, a DC voltage is applied between the two electrodes to drive a flux of electrons through the nanoscale bridge. This electron current, denoted as i_e, is measured with the objective of calculating the electrical conductance of the bridge or the chemical structure positioned between the electrodes (HEATH, 2009; VENKATARAMAN et al., 2006).

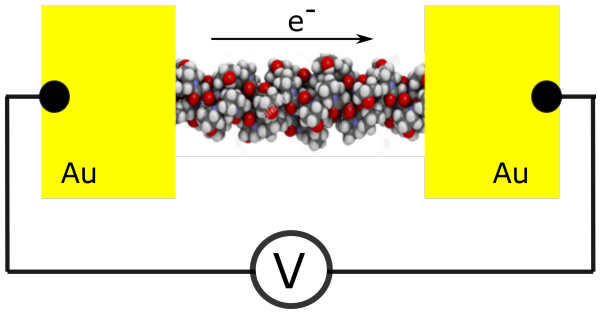

FIGURE 2.13. A two-electrode setup is commonly used in molecular electronics. In this configuration, a single molecule or an ensemble of molecules is extended between two electrodes. A potential difference is applied across the electrodes, and the current or electron flux passing through the molecular structure is measured. Source: Author's own work

The initial inclination might be to apply Ohm's classical law to calculate the conductance, which is the inverse of resistance. However, it's crucial to note that in nanoelectronics, the chemical structures of interest are molecules or inorganic quantum dots, which exhibit quantized physical properties due to discrete energy levels in their electronic structures. Therefore, classical physics struggles to fully explain the electrical characteristics of these structures. For instance, in nanoelectronics, the sum of resistances does not strictly adhere to Kirchhoff's laws (GABELLI et al., 2006). Moreover, at the nanoscale, the movement of electrons—central to this study—follows the wave-particle duality predicted by quantum mechanics (GRIFFITHS; SCHROETER, 2018). Consequently, advancing the study of electron dynamics necessitated theoretical contributions derived from this latter field.

In 1957, concurrently with the proposal of the Marcus theory, Rolf William Landauer (1927-1999), a German-American physicist, introduced the first version of his quantum mechanical model to predict the property of quantum conductance G in two-terminal quantum point contacts (LANDAUER, 1957). The Landauer model defines the conductance G of a quantum conductor—be it a molecule or a quantum dot—in terms of its conductance and the scattering properties of the electron wave, described by the transmission matrix (NAZAROV; BLANTER, 2009; AKKERMANS; MONTAMBAUX, 2007). Therefore, for a two-terminal contact at energy $E = \mu$, where μ represents the Fermi level of the nanoscale junction, Landauer's formulation can be expressed as:

$$G = G_0 \sum_{n=1}^{N} T_n(\mu) = g_s \frac{e^2}{h} \sum_{n=1}^{N} T_n(\mu) \tag{2.18}$$

In Eq. 2.18, the term $G_0 = g_s e^2/h$ denotes the quantum of conductance, which is the quantized unit of electrical conductance. Here, g_s corresponds to the electron spin degeneracy, taking a value of 2 ($g_s = 2$), representing the up and down spin states of the electron. The constant $G_0 = g_s e^2/h \sim 77.5$ μS is a universal constant predicted to be obtained by measuring the conductance of a quantum point contact (FRANK et al., 1998; AKKERMANS; MONTAMBAUX, 2007). Furthermore, G_0 corresponds to twice the inverse of the Von Klitzing constant $R_K = h/e^2$, the quantized unit of resistance, such that $G_0 = 2/R_K$. Theoretically, $R_K = 25.8$ KΩ represents the resistance associated with the ground state in a quantum RC circuit analysis of the electron states (KLITZING, 2005; LAUGHLIN, 1981). Briefly, G_0 can be derived in a straightforward manner by considering a 1D structure, such as a quantum wire, adiabatically connecting two electron reservoirs and analyzing their voltage and current properties. A concise derivation of this can be found in reference (WEES et al., 1988) and is open to review by interested readers.

On the other hand, $\sum_{n=1}^{N} T_n(\mu)$ denotes the electron transmission matrix, which is derived from quantum mechanics calculations. In this matrix expression, $T_n(\mu)$ are the eigenvalues of the matrix, and the sum runs over all transport channels in the conductor (BUENO, 2020; AKKERMANS; MONTAMBAUX, 2007). Therefore, the Landauer formulation given by Eq. 2,18 describes the conductance of a nanoscale conductor as the sum of all the transmission possibilities that an electron has when propagating with an energy equal to the chemical potential, $E = \mu$. According to the electron transport mechanism, the matrix takes a particular form. For instance, in a quantum wire where the mean free path of its electrons (l_{el}) is much larger than its length (L), $l_{el} >> L$, the electron transport occurs through a ballistic mechanism without electron wave scattering (LANDAUER, 1957). Thus, $\sum_{n=1}^{N} T_n(\mu) = 1$, and its conductance is $G = G_0$. In contrast, for electron transport by tunneling, $\sum_{n=1}^{N} T_n(\mu) \propto \exp(-\beta L)$, where the parameters β and L are the height and length of energy barrier tunneled by the electron (WINKLER; GRAY, 2014; NAZIN et al., 2005). Landauer's formula was derived from the assumption of wave-particle duality introduced by De Broglie, thus assuming the electron being transported exhibits wave behavior, including transmission and reflection (LANDAUER, 1957). There are other electron transport formalism's, such as those based on Green's functions

(DEROSA; SEMINARIO, 2001); however, the Landauer formulation constitutes the most widely used formalism in nanoscale electronics and is applied in the ongoing PhD thesis. Accordingly, these other formalism's are not discussed in this narrative.

In summary, electrodynamics, the study of the electron's ability to move through chemical structures, was apparently developed from two distinct perspectives: electrochemistry and molecular electronics. Electrochemistry is based on the understanding of electron transfer phenomena and the determination of its associated rate constant k (Marcus-Gerischer theory) (BARD et al., 2022; BOCKRIS; REDDY, 1998). Molecular electronics, on the other hand, focuses on the exploration of electron transport phenomena through the calculation and measurement of the quantum conductance G property of molecular bridges extended between two electrodes (Landauer formulation) (CHEN et al., 2007; WEES et al., 1988). Nonetheless, when the dynamics or movement of the electron is examined from a fundamental standpoint, the process of leading an electron between two electron states involves transferring the electron from one stationary state to another (electron transfer) and transmitting the electron wave through a chemical structure (electron transport). Hence, it is natural to consider electron transfer and transport as phenomena that occur in a complementary manner in an electron dynamics event, rather than as contrary phenomena as they were historically addressed. This strong postulate states that, although scientifically explored from distinct perspectives, the phenomenon remains just one: Electron Dynamics. It raises two pivotal questions: Is it possible to develop a model that considers both phenomena and enables obtaining a more complete picture of electron dynamics? And, are nanoscale electrochemistry and electronics dictated by the same physical principles? Their answers or possible responses will be discussed in the next section. Although this narrative has been somewhat extensive until this point, its conclusion will arrive shortly.

2.4 The Natural Phenomenon remains Just One: Electron Dynamics.

The construction of the dynamics of the electron has not been easy! It seems that with each advance in understanding this fascinating phenomenon, new questions arise, leading human minds to develop and propose challenging ideas. However, this very fact is the driving force of science. When all questions about a phenomenon have been answered,

science should stop. But as long as there are more questions than answers, science must be based on the proposal of new ideas and critical thinking, challenging what was proposed in the past. In this context as introduced in the last paragraph of the previous section, the current scientific thinking about the electron dynamics is based on the necessity of models derived the quantum mechanics, since the electron is quantum particle (wave-particle duality), that consider a interrelation between the rate constant k associated to the electron transfer, and quantum conductance G describing the electron transport. It was not enough with separate models! The understanding of the dynamic behavior of the electron required a unified model.

In 2001, Abraham Nitzan, an Israeli chemist, published a quite interesting paper where he proposed a theoretical deduction of an expression that related G and k (NITZAN, 2001). Nitzan's formulation is based on applying a mathematical treatment to the expressions obtained for k in non-adiabatic electrochemical reactions and for G of molecular junctions under the condition of near-zero bias. Under the premise of a super-exchange transport mechanism and other approximations such as weak coupling between the different electron structures involved in electron dynamics (donor and acceptor groups, bridge, and electrodes) and high barriers, Nitzan derived his formula. This formula describes a linear relation between G and k and is given by:

$$G = \frac{8e^2}{\pi \Gamma_D^L \Gamma_A^R \mathrm{F}} k \tag{2.19}$$

where Γ_D^L and Γ_A^R represent the widths of the electron donor and acceptor levels due to their couplings to the left and right metal leads, respectively, and F is the Franck-Condon weighted density of nuclear states. Hence, Nitzan's equation was the first attempt at formulating a relationship between G and k (NITZAN, 2001). However, the strong approximations used in its derivation limited its application to experimental systems. Subsequently, Berlin and collaborators extended Nitzan's treatment to derive an expression valid for electron transport by hopping, also finding a linear relationship in this case, although under the condition of high energy barriers compared to $K_B T$. Nevertheless, these works consisted of theoretical derivations, and their predictions did not entirely satisfy the experimental data recorded in electrochemistry and molecular electronics measurements.

In such a scenario, another interesting work was published by Emil Wierzbinski and collaborators in 2013 (WIERZBINSKI et al., 2013). They found an empirical relation between the G and k from the analysis of experimental data obtained in two independent measurement setups. The first setup consisted of cyclic voltammetry (CV) at different scan rates conducted over self-assembled monolayers of stranded double nucleic acid sequences (NA-SAMs), tagged with a cysteine moiety at one end of the sequence and a ferrocene moiety at the other end. The NA-SAMs were formed over a gold surface through the bond between the thiol group of the cysteine and the gold atom (S-Au). From these CV measurements on NA-SAMs of different lengths and structures, and using the Marcus theory, the rate constants k associated with the electron transfers from the gold surface to and from the ferrocene moiety were computed, extracting the mathematical relationships with length and structure parameters. Similarly, they carried out scanning tunneling microscopy (STM) on break junctions built from a gold surface modified with the non-tagged cys-NA-SAMs and an STM gold tip. The single molecule conductance of the stranded double nucleic acid sequence was indirectly determined by measuring the tip-NA sequence-electrode tunneling current at a constant bias voltage as a function of the distance during the retraction of the tip from the substrate electrode. Conductance (G) relations as functions of the length and structure of NA sequences were determined from these measurements.

By combining and mathematically analyzing the empirically obtained expressions for G and k, a non-linear correlation was determined for these properties in the form:

$$G = \alpha k^{\beta} \tag{2.20}$$

where α and β are constants obtained from the mathematical fitting. For instance, for the group of studied NA sequences, the constant β presented a value of 0.68, and α can be computed in terms of experimental parameters. However, they attempted to conduct a correlation between fits obtained for different chemical species, such as double-stranded and single-stranded NA sequences, but observed a lack of correlation when considering an overall set of electrochemical and molecular conductance measurements of both groups. Therefore, the power law described by Eq.2.20 was a relation derived merely from the mathematical fitting, and no generalization can be made about the phenomenological

correlation between G and k (MARQUÉS-GONZÁLEZ; LOW, 2016). The authors themselves suggested that the lack of linearity in their relation could be attributed to significant differences in the measurement settings, which is a key element in assessing the validity of this relation. Subsequently, other works reported in the literature aimed to obtain an expression for the correlation between G and k (BEVAN et al., 2016; HOSSAIN; BEVAN, 2016). However, these efforts resulted in impractical and complex mathematical relations that could not be associated with experimental data. Their applications were limited by the dramatic approximations considered in their derivations.

Nonetheless, the scientific challenges of the 21st century, such as the fabrication of optoelectronic devices demanded the proposal of a consistent model for studying the electron dynamics process in general, addressing as a unified phenomenon of electron transfer and transport. Furthermore, the foundations of this should be based on the postulates of quantum mechanics, and its predictions must be reconciled with experimental methodologies.

2.5 A Quantum Electrodynamics Model: Quantum Rate Theory.

The path traveled in the history of electronic dynamics has been long. It began with the discovery of the electron and the exploration of its arrangement within atomic structure (CHANG; OVERBY, 1986; BROWN, 2009). Subsequently, the debate over its nature as either a particle or a wave emerged, highlighting the inadequacies of classical physics in explaining radiation-matter interactions at the nanoscale. Consequently, the necessity to understand the movement of electrons within chemical structures prompted the birth of quantum mechanics (GRIFFITHS; SCHROETER, 2018; BRANSDEN; JOACHAIN, 2000). Throughout the last century, both physicists, focusing on nanoscale electronics, and chemists, concentrating on electrochemistry, proposed significant models concerning electron transport and transfer, respectively. Nonetheless, the most modern scientific perspective on these phenomena converges on the idea that, although their theories were developed separately, they are governed by common physical principles (BUENO, 2018a): quantum electrodynamics. Therefore, there is a need for a unified model in which nanoscale electronics and electrochemistry are reconciled.

Over a decade ago, researchers began exploring the electron dynamics of electrochemical reactions within redox electroactive self-assembled monolayers (SAMs) on conducting electrode surfaces through a new concept not previously considered by other models. This intriguing concept was electrochemical capacitance (C_μ). As shown in Figure 2.12, the studied redox electroactive SAMs were composed of a dense array of thiolated or cysteine (C)-peptide molecules tagged with a ferrocene (Fc) moiety. This moiety acted as a redox probe, exhibiting electrochemically reversible oxidation and reduction reactions (ECKERMANN et al., 2010). Consequently, the electron transfer process between the Fc moiety and the electrode, within an electrolytic medium, involved a capacitive phenomenon C_μ that cannot be fully explained by classical electrostatics (BUENO; DAVIS, 2014b). The fascinating physical meaning of C_μ will be discussed shortly.

This novel approach, grounded in the concept of C_μ, is predicated on three fundamental premises: the consideration of the wave-particle duality behavior of the electron, revealing its wave-like characteristics in electron transfer; the existence of a characteristic time τ associated with each electron dynamics process; and the ability to model these processes through a quantum resistive-capacitive (RC) circuit (BUENO, 2023c; BUENO; MERCADO, 2022; BUENO; DAVIS, 2020). Hence, it is feasible to obtain the relation $\tau = R_q C_\mu$, where R_q represents the quantum resistance at the nanoscale (BUENO, 2023c). It is crucial to mention that at the atomic and molecular scale, the resistance and capacitance elements cannot be interpreted from the classical circuit standpoint. For instance, the combination of resistances at the molecular scale does not obey Kirchhoff's laws (GABELLI et al., 2006). By considering the expression $\tau = R_q C_\mu$ as a dynamic description of an electrochemical reaction in a diffusionless regime of the redox probe, it is possible to observe that the inverse of the time τ associated with the reaction rate and can be directly linked to the electron transfer rate constant k such that $k = 1/\tau$. Moreover, the inverse of the resistance R_q corresponds to the quantum conductance given by $G = 1/R_q$. Therefore, by substituting these relations into the dynamic expression for τ, a new and intriguing electrodynamic relationship is obtained, expressed as $k = G/C_\mu$ (BUENO; DAVIS, 2020; BUENO, 2024; BUENO, 2023c).

The equation $k = G/C_\mu$ describes a linear correlation between k and G representing a key objective of modern electrodynamics. Furthermore, it reveals an astonishing fact: the proportionality factor between these two properties corresponds to C_μ. This simple

relation already highlights the significance of C_μ in understanding the phenomena of electronic transport and transfer at the molecular scale. To comprehend the generality of this expression, it is essential to consider that G is given by Landauer's quantum formulation of conductance, where the movement of the electron is described in terms of electron transmittance, and its wave-like features are manifested in the electron transfer process (LANDAUER, 1957; BUENO, 2020). Moreover, the definition of C_μ was also derived from quantum mechanical principles using a conceptual density-functional-theory (DFT) approach (BUENO; MIRANDA, 2017; BUENO et al., 2015). This is defined as the series combination of both capacitance contributions, electrostatic C_e and quantum C_q, given by $1/C_\mu = 1/C_e + 1/C_q$. The capacitance C_e is associated with charge separation processes driven by electrostatic interactions between charges, while the capacitance C_q constitutes a pseudocapacitive phenomenon describing charge separation due to electron communication between quantum states. This latter capacitive contribution is directly associated with the electronic structure of the nanoscale structure immobilized over the electrode, such that $C_q \propto$ DOS, where DOS represents the electron density of states (BUENO, 2023c; BUENO; DAVIS, 2020). Accordingly, a general and extended expression $k = G/C_\mu$ can be formulated, incorporating the previous definitions:

$$k(\mu) = \frac{G(\mu)}{C_\mu(\mu)} = G_0 \sum_{n=1}^{N} T_n(\mu) \left(\frac{1}{C_e} + \frac{1}{C_q} \right) \tag{2.21}$$

Accordingly, Eq.2.21 describes the pivotal relationship in this newly established approach, recently named Quantum Rate Theory (QRT) (BUENO; MERCADO, 2022; BUENO, 2023c). The physical predictions and interpretations derived from QRT form the theoretical framework of this ongoing Ph.D. thesis. In the humble opinion of the author, there is no better way to conclude the story of our main character, the electron, than by discussing the foundations of QRT—a theoretical proposal that is both well-established and still evolving. This proposal enables the exploration of electrodynamic processes at a fundamental level, as will be presented in this short introduction and in each research work addressed in the following chapters. This section does not aim to provide a detailed description of the theoretical principles of QRT, as each article used as a chapter in this thesis includes a general and specific discussion of the model necessary for the development of the respective work. Instead, some significant predictions, facts, and applications of this model as a theory of electron dynamics will be briefly addressed,

with the sole purpose of piquing the curiosity of readers about this new proposal. Key points to highlight include:

2.5.1 The QRT Predicts Relativistic Quantum Electrodynamics of the Electron in Matter.

Consider the quantum point contact junction illustrated in Figure 2.14, where a quantum point or nanoscale structure is electronically coupled to a conducting electrode surface through a quantum bridge. Under certain energy conditions, the electron transfer or communication processes between the electrode states and the quantum states of the nanoscale structure occur in the presence of an electrolytic medium. According to the premises of the QRT, this electrodynamics between states is described by Eq. 2.21, which predicts a quantum rate k associated with this process, as the ratio between G and C_μ (BUENO, 2018a; BUENO, 2023c). As previously mentioned, G, the quantum conductance, is given by Landauer's formulation (LANDAUER, 1957), which was discussed in section 2.3. The transmittance term $\sum_{n=1}^{N} T_\mu(\mu)$ in Eqs. 2.18 and 2.21 can be rewritten as $\sum_{n=1}^{N} T_\mu(\mu) = N\kappa$, where N is the total number of quantum channels involved in the electron transfer or communication, and κ corresponds to the electron transfer coefficient. This coefficient is associated with the probability of electron communication among states, taking values from 0 to 1. When considering adiabatic electron transport through a single quantum channel, it holds that $\kappa = 1$ and $N = 1$. Thus, the quantum conductance, G, is now $G_0 = g_s e^2 h$, which corresponds to the ideal transmittance case (BUENO, 2020; SANCHEZ et al., 2022).

Furthermore, when an electron is removed or injected into the quantum point by electron transfer, or when the charge state changes due to the electromagnetic communication between electronic states, the ions present in the electrolyte medium conduct a total screening process of the electric field (PINZON et al., 2022). This aims to maintain the electroneutrality and thermodynamic equilibrium of the interface. Accordingly, under this screening condition, it is stated that $C_e = C_q$. Thus, the definition of C_μ in Eq. 2.21, $1/C_\mu = 1/C_e + 1/C_q$, becomes $1/C_\mu = 2/C_q$, where the factor 2 can be defined as the electron degeneracy g_s due to the overlapping of both capacitive contributions (BUENO, 2023c; BUENO, 2024). This overlapping condition of capacitive states along with the energy degeneracy g_e is more extensively explained in references (BUENO, 2023a; BUENO, 2023b) for the hydrogen atom, and in (BUENO, 2023c; BUENO, 2024) for the case of

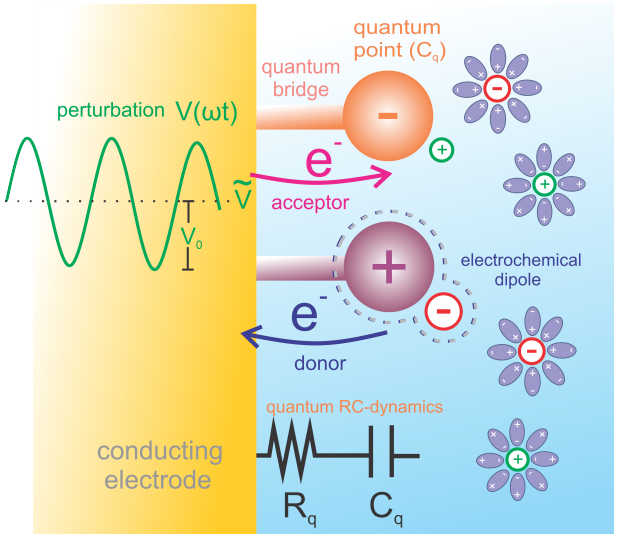

FIGURE 2.14. A quantum point contact, where a quantum point or nanoscale structure is electronically coupled to a conducting electrode in an electrolytic environment. By perturbing this junction with a time-dependent electrical signal, electron transfer or communication between the electrode states and the quantum states of the point is driven. In this context, the transfer or communication can be modeled using a quantum RC circuit. Source: Author's own work.

electrochemical reactions. Nonetheless, before advancing, it is important to mention that from the QRT standpoint, this overlapping of capacitive states constitutes the fundamental electron communication mechanism in an electrolytic medium as observed in nature. Therefore, by extending the concept of the rate constant k to electrodynamic processes in general, not only electrochemical reactions, Eq. 2.21 can be rewritten in terms of an overall concept known as the quantum rate ν (BUENO; MERCADO, 2022; BUENO, 2024), taking into account the previous considerations as follows:

$$\nu = \frac{G}{C_\mu} = g_s g_e \frac{e^2}{hC_q} \tag{2.22}$$

Eq. 2.22 represents a general quantum electrodynamics relation that describes the dynamics or kinetics of an electron process, including electron transfer or communication, as dependent on the C_q-property of the junction—a property that had been overlooked by earlier models. By disregarding both degeneracies, g_s and g_e, and assuming that $E = e^2/C_q$ corresponds to the electron structure energy or the energy required for charging the quantum states in communication, the Planck relation, $E = h\nu$, is naturally obtained (BUENO, 2023c; SÁNCHEZ et al., 2022). But what does this fact signify? As discussed

in section 2.2, Planck's relation (Eq. 7.2) describes the relativistic quantum dynamics of the photon, the particle associated with electromagnetic radiation, in free space (LAND; HORWITZ, 2022; ZETTILI, 2009). Furthermore, by applying the De Broglie relations expressed in Eq. 2.3(BROGLIE, 1930; GRIFFITHS; SCHROETER, 2018), it is possible to derive the following energy relations, which reveal a direct correlation between those derived from the QRT and those from relativistic theory.

$$E = h\nu = \frac{e^2}{C_q} = h\frac{C^*}{\lambda} = \mathbf{p} \cdot \mathbf{C^*} \tag{2.23}$$

Because Eq.2.22, the pivotal equation of QRT, obeys the Planck-De Broglie principles that describe the wave nature of the electron based on relativistic mechanics—QRT predicts a relativistic quantum dynamics of the electron in chemical structures, participating in the communication process of electronic states such that the electron mimics photonic dynamics (BUENO, 2023c; BUENO; MERCADO, 2022; PINZON et al., 2023). Therefore, the charging and discharging of electronic states at the nanoscale adhere to relativistic quantum electrodynamics principles. The study of electron dynamics within the limits of classical and non-relativistic quantum physics restricts the advancement of understanding at a fundamental level in this fascinating domain.

2.5.2 The QRT, an overall model containing the Marcus Theory

The concept of quantum capacitance, C_q, is a key element of quantum rate theory (QRT). Its definition is derived from first-principle quantum mechanical calculations (BUENO et al., 2015), such as $C_q = e^2\partial n/\partial\mu$, where $\partial n/\partial\mu$ corresponds to the electron density of states (DOS) function of the nanoscale structure (PINZON et al., 2021). However, this definition was obtained under the approximation of zero absolute temperature. Therefore, when considering the thermal broadening effect on the energy $E = e^2/C_q$ and invoking the canonical grand statistical ensemble, which assumes electron occupancy governed by the Fermi-Dirac distribution function, $f = [1+\exp(-eV/K_BT)]^{-1}$, an expression for C_q that accounts for thermal effects is derived as follows:

$$C_q = \frac{e^2 N}{K_B T} f(1-f) \tag{2.24}$$

The detailed procedure for deriving Eq.2.24 is outlined in the references (PINZON et al., 2021; ALARCÓN et al., 2021a; SÁNCHEZ et al., 2022). Consider the calculation of the electron transfer rate constant, k, for an electrochemical reaction using Eq.2.21, while disregarding both degeneracies, g_s and g_e. In this context, ν corresponds to k, and Eq.2.21 can be reformulated as $k = e^2\kappa N/hC_q$. By substituting C_q in this expression with Eq.2.24, a general expression for the rate constant k derived from the QRT is obtained as: (BUENO, 2020; SANCHEZ et al., 2022; BUENO et al., 2012)

$$k = \kappa\frac{K_BT}{h}[f(1-f)]^{-1} = \kappa\frac{K_BT}{h}f^{-2}\exp(-E_A/K_BT) \tag{2.25}$$

When the Boltzmann approximation is applied to Eq.2.25, under the conditions $1 \ll \frac{E_A}{k_BT}$ and $f \sim \exp\left(-\frac{E_A}{k_BT}\right)$, it transforms into Eq.2.8: $k = \kappa K_BTh^{-1}\exp(-E_A/K_BT)$. This equation, derived from transition state theory, constitutes the fundamental formulation of Marcus Theory (PINZON et al., 2021; BUENO, 2020), as previously discussed. Therefore, Marcus's theory for homogeneous electrochemical reactions, ones of the most important model of electron transfer, is an approximation of the overall concept of quantum rate theory given by Eq.2.25. This conceptual demonstration confirms the general applicability of the QRT as a physical model for exploring and interpreting electron dynamics in various electronic environments, including diffusion-limited homogeneous and heterogeneous systems, as well as diffusionless scenarios.

2.5.3 The QRT supports a Tool for Measuring the Electronic Structure of Materials

In addition to its predictions concerning relativistic quantum electrodynamics in the communication of quantum states and its overall characteristics as a model for electron dynamics, the foundations of Quantum Rate Theory (QRT) support an experimental approach for in-situ measurement of the electron structure in chemical systems at the nanoscale. This novel approach, recently termed *Quantum Rate Spectroscopy* (PIZÓN et al., 2024; LOPES et al., 2024), is the primary focus of the ongoing PhD thesis and is based on time-dependent electrochemical measurements. Consider the quantum contact point junction depicted in Figure 2.14, where a quantum point or nanoscale structure is electronically coupled to a conducting electrode. Whenever electron communication occurs between the states of the electrode and those of the quantum point, either through elec-

tron transfer or electromagnetic interaction, QRT models this communication via Eq.2.22. This equation states that the electron dynamics event occurs at a characteristic rate ν, which corresponds to a time τ given by the quantum circuit elements as $\tau = R_q C_q$ (see Figure 2.14) (ALARCÓN et al., 2021a; SÁNCHEZ et al., 2022). Consequently, this electrodynamic behavior, $\tau = R_q C_q$, can only be investigated through time-dependent experimental approaches. Among these approaches, electrochemical impedance spectroscopy (EIS) is notable for its ability to operate under mild conditions, such as room temperature, atmospheric pressure, and the presence of an electrolytic medium (BUENO et al., 2012; LOPES et al., 2021).

EIS is commonly used to measure the electron charge transfer resistance, R_{ct}, in electrochemical interfaces involving a conducting or semiconducting electrode and redox-active species dissolved in solution. In this context, the technique is widely applied in corrosion studies and sensing applications, where changes in R_{ct} are primarily assessed in response to oxidation states or biological interactions, respectively (WANG et al., 2021; LAZANAS; PRODROMIDIS, 2023). However, it is often overlooked that EIS, as a time-dependent technique, is a powerful experimental tool for probing the quantum properties of nanoscale systems. This capability has been demonstrated by the works supporting this PhD thesis and others published by the Nanobionics research group in Brazil (BUENO et al., 2012; PINZON et al., 2021; LOPES et al., 2021). In this context, since the electrodynamics at the nanoscale are governed by the dynamic relation $\tau = R_q C_q$, where $R_q = 1/G_0 = h/2e^2$ is a constant, the behavior is dictated by the quantum capacitance property C_q, which has been neglected by previous theories of electron transfer and transport. Specifically, the C_q of the junction, represented in Figure 2.14, is determined by the combination of the left and right densities of states (DOS), $g_L(\mu)$ and $g_R(\mu)$, respectively, such that $1/C_q(\mu) = 1/e^2 g_L(\mu) + 1/e^2 g_R(\mu)$. However, since the left DOS corresponds to the macroscopic electrode DOS, which is effectively infinite, $1/g_L(\mu) \approx 0$. Consequently, the C_q-response of the junction is described by $C_q = e^2 g_R(\mu)$, where $g_R(\mu)$ corresponds to the quantum point DOS, describing the distribution of the quantum states n across different energy levels μ, defined as $\partial n/\partial \mu$ (BUENO; DAVIS, 2014b; BUENO et al., 2012).

Therefore, the relation $C_q = e^2 \frac{\partial n}{\partial \mu}$ offers a significant opportunity for developing a novel electronic spectroscopy approach. This relation indicates a proportionality between the properties C_q and $\frac{\partial n}{\partial \mu}$, suggesting the possibility of accessing the electron density of

states (DOS) in nanoscale materials through the measurement of their C_q. This measurement can, indeed, be conveniently performed using EIS. In this context, by applying the QRS methodology to the nanoscale junction depicted in Figure 2.14, Electrochemical Impedance Spectroscopy (EIS) measurements are carried out using a conventional three-electrode electrochemical cell (BUENO et al., 2015; BUENO et al., 2012). The perturbation involves a time and frequency -dependent sinusoidal potential signal, as shown in Figure 2.14. This sinusoidal signal is applied around a bias potential $\tilde{V}$ that corresponds to the electrostatic or dynamic equilibrium of the nanoscale structure of interest immobilized on the working electrode. For instance, in the case of solid-state or molecular structures exhibiting reversible redox electrochemical reactions, this equilibrium potential is the formal potential of the junction (E_F/e), where oxidation and reduction processes are in kinetic equilibrium (ALARCÓN et al., 2021a; SANCHEZ et al., 2022; SÁNCHEZ et al., 2022). In contrast, for structures that do not undergo electrochemical reactions but possess accessible quantum states, the bias potential is the open circuit potential (OCP), at which charge equilibrium exists at the interface. This is also known as the zero net charge potential (LOPES et al., 2021; LOPES et al., 2024; PIZÓN et al., 2024).

Note that by perturbing the junction under equilibrium conditions, whether electrostatic or dynamic, the net current associated with the flux of electrons is zero throughout it. Nonetheless, due to the time-dependent nature of the perturbation applied over the probe electrode, a time-dependent electrical field is generated, which in turn induces a time-dependent magnetic field, as stated by Faraday's induction principle, generating a displacement current i_d associated with the electron (SEARS et al., 2014; SERWAY; JEWETT, 2021). Hence, the time-dependent perturbation yields an electromagnetic wave associated with the electron traveling through the junction. This wave resonates with stationary electron states of the quantum point, returning a current signal i_d to the probe electrode that contains information regarding the pristine electronic structure of the quantum point. This signal along with perturbation signal are processed by electrochemical equipment to obtain the observable response of electrochemical impedance (BUENO; MERCADO, 2022; PIZÓN et al., 2024; PINZON et al., 2023).

It is essential to note that access to the electronic structure information of the quantum point is facilitated by the electrical field screening performed by the ions in the electrolytic medium (PINZON et al., 2022; BUENO et al., 2020; BUENO, 2023a),

as discussed earlier and extensively explored in the research works comprising this PhD thesis. Remarkably, it is this ion-driven screening process that enables access to quantum insights of nanoscale structures via EIS under mild experimental conditions, such as room temperature and environmental pressure (LOPES et al., 2024; PIZÓN et al., 2024). In this context, when there is electron communication between the electrode states and the quantum point states, the charge state of the quantum point alters due to electron transfer or electromagnetic interaction, generating a net electric field across the interface. In response to this field, the ions in the electrolyte arrange themselves to screen it and maintain the electroneutrality of the interface (PINZON et al., 2022; PINZON et al., 2023). Consequently, if the ions in the medium are capable of screening the charge associated with the charging/discharging process of a quantum state, this state can be accessed by EIS, as illustrated in Figure 2.14.

The QRS-measuring protocol is depicted in Figure 2.15. Initially, as previously mentioned, EIS measurements are conducted at a fixed bias potential, with a frequency scan applied from high to low values. This process produces a semicircle-shaped capacitive response in the Nyquist plot, representing the real and imaginary components of the capacitance, C' and C'' respectively, on the coordinate plane. In the Nyquist plot, the value of C_q corresponds to the real component of capacitance, C', in the low-frequency regime ($\omega \to 0$), or graphically, to the point at which the capacitive semicircle closes. Subsequently, the frequency associated with C_q, termed the equilibrium frequency f_{eq}, is held constant, and electrochemical capacitance measurements are performed over a specific potential range (LOPES et al., 2021; PIZÓN et al., 2024). Within the QRS framework, the ultra-low frequency f_{eq} can be described as corresponding to the equilibrium state at which the nanoscale junction is approximately driven by the time-dependent electrical perturbation, causing the electron-electromagnetic wave to resonate with the electron states of the quantum point (PINZON et al., 2023). Consequently, since $C_q \propto$ DOS, the response of C' at fixed f_{eq} ($\omega \to 0$), as a function of potential or electron energy, reflects the electron density of states (DOS) of the junction (PINZON et al., 2021; ALARCÓN et al., 2021a)

Accordingly, QRS constitutes a powerful tool for revealing, in situ, the electronic structure of chemical systems or assemblies at the nanoscale, offering a novel electron spectroscopy technique that can be operated at room temperature using a conventional

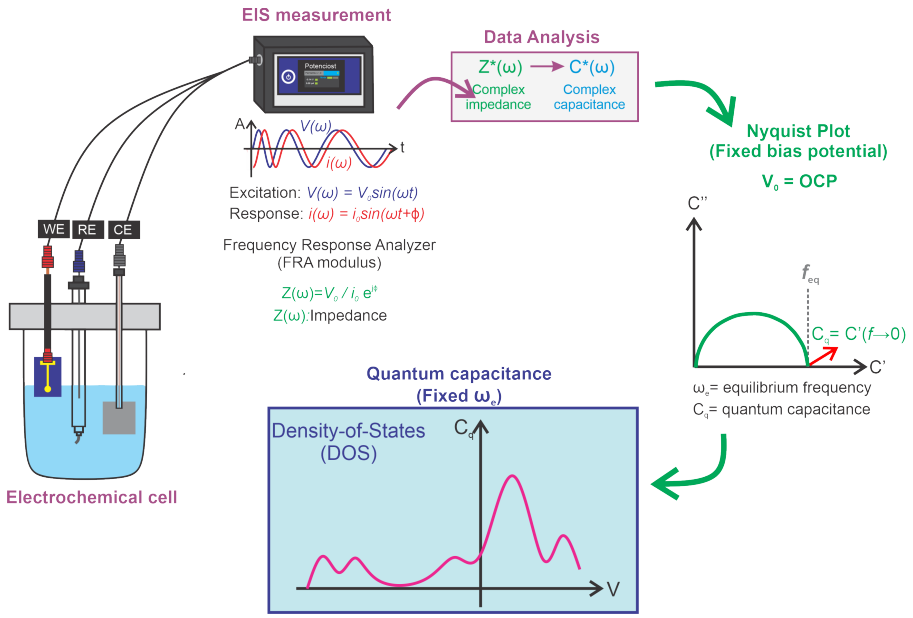

FIGURE 2.15. The measurement protocol for the electron density of states in nanoscale materials is conducted through Quantum Rate Spectroscopy. Measurements are carried out in a conventional three-electrode electrochemical cell using an electrolytic medium. A time-dependent sinusoidal perturbation is applied via a potentiostat equipped with a frequency response analyzer (FRA) module. The recorded impedance data are transformed into capacitance data, thereby resolving the density of states (DOS) function. Source: Author's own work.

electrochemical cell. Currently, multiple electron spectroscopy techniques, such as scanning tunneling microscopy (LILJEROTH et al., 2005; JDIRA et al., 2006; NAZIN et al., 2005) and angle-resolved photoemission spectroscopy (PARK et al., 2009), are widely used to measure the electron density of states (DOS) in nanoscale inorganic and organic assemblies, as well as graphene-derived materials. However, these approaches require complex equipment that operates at ultra-low temperature and high-vaccum conditions, and demands highly specialized personnel, limiting their utility as fast methodologies for measuring electronic structure. In this context, the fast and simple access to the electronic properties by EIS in electrolytic medium represent a great contribution to different scientific fields such as materials science, nanoscience and technology, electrochemistry and electron spectroscopy.

In summary, *Quantum Rate Theory*(QRT) and its associated experimental approach, *Quantum Rate Spectroscopy* (QRS), have made significant strides in recent years in advancing our understanding of electron transfer and transport phenomena in diffusionless electrochemical reactions within redox-active self-assembled molecular monolayers

confined to electrode surfaces (see Figure 2.12). In this context, it was demonstrated that the electron transfer between the electrode states and redox probe states, in presence of electrolytic medium, obeys the relativistic quantum electrodynamics principles with the electron manifesting its wave-particle duality, which according the De Broglie-postulates led to electron process described by the photonic dynamics $E = \vec{p} \cdot \vec{C^*} = h\nu$ with a quantized resistance $R_q = h/e^2$ (SANCHEZ et al., 2022; BUENO, 2023c; BUENO, 2024). Furthermore, the understanding of this electrodynamics, of electrochemical nature, within redox molecular monolayer, led to development of a quantum biosensing approach for disease and virus biomarkers, named *quantum capacitive sensing*. In this methodology, redox molecular monolayer are chemically modified with receptor elements, highly specific to the target biomolecule, and the response of C_q is used as transduction signal for the detection and quantification of different biomarker proteins (GARROTE et al., 2020; GARROTE et al., 2019; GARROTE et al., 2024). .

Nonetheless, if QRT is founded on the principles of relativity, electrodynamics, and the postulates of quantum mechanics, its application should not be limited to electrodynamics based solely on electrochemical reactions. On the contrary, its derivation and foundations suggest broader applicability for studying electrodynamic processes in general. For instance, it can be applied to electron injection and communication between quantum states in nanoscale semiconducting structures. These nanomaterials are widely used for the potential development of quantum devices, whose operation and performance rely on quantum phenomena such as the degeneracy of states, energy state quantization, and quantum entanglement (SHIELDS, 2007; BROADWAY et al., 2018). However, the lack of control over electronic and electrical properties at the nanoscale has hindered the fabrication and commercialization of these types of devices.

Two key requirements, both fundamental and technological, are crucial for advancing the understanding of electron transfer and transport in nanoscale semiconductors. These requirements are: (1) the development of theoretical models based on quantum electrodynamics, and (2) experimental approaches that provide electronic insights under mild conditions in a simple and efficient manner. In this context, in the ongoing PhD project, *Quantum Rate Theory* serves as the theoretical framework, while *Quantum Rate Spectroscopy*, based on the electrochemical impedance measurements, is employed as the experimental methodology. These approaches have been applied to both inorganic

and organic semiconducting structures with varying degrees of quantum confinement and distinct electrodynamics, specifically 0D, 1D, and 2D structures. Consequently, the following four chapters of this thesis present published studies on the electrodynamics and electronic structure governing communication between quantum state within Cu_2O/CuO mixed nanofilms, an ensemble of CdTe quantum dots, single-layer graphene, and an assembly of π-conjugated heterocyclic molecules. Since the electrodynamics within these nanoscale structures do not involve electrochemical reactions, these studies open the door to a new area of research and technological applications: *nanoscale electronics in electrolytic media*, a new approach of nanoscale electronics.

In recent years, there has been a growing trend among writers and filmmakers to conclude stories with inconclusive endings. However, the purpose of this text is not to leave the story of the electron and its dynamics without an ending, but rather to emphasize that this story has no definitive conclusion. On the contrary, the introduction and application of Quantum Rate Theory as a comprehensive model for exploring electrodynamics at the nanoscale has merely opened a new chapter in this ongoing narrative, leading to a reinterpretation of the movement of its central character—the electron—within matter. The author is proud to contribute to this fascinating story through the development of this thesis. He hopes that readers of this text, along with the accompanying articles, will be inspired by the same sense of fascination and curiosity about electron physics and chemistry that fueled the creation of this PhD work.

Chapter 3

Research Objectives

Before discussing the papers used as chapters, a description of the research objectives supporting the current thesis is provided below. Each work published as a result of this PhD research aligns with these objectives.

3.1 General Objective.

The primary objective of this ongoing PhD thesis is to investigate electron transfer and transport phenomena in nanoscale semiconductor structures, including copper oxide nanofilms, an assembly of CdTe quantum dots, single-layer graphene, and an assembly of push-pull heterocyclic molecules. These structures are coupled with conductive electrodes and embedded in an electrolytic environment. The study is conducted within the framework of Quantum Rate Theory, employing electrochemical impedance spectroscopy as a key experimental approach.

3.2 Specific Objectives.

The goals proposed in this research were as follows:

- To obtain nanoscale semiconductor structures of varying chemical compositions and types of quantum confinement, coupled to conductive electrodes.

- To access to the electronic density of states of these semiconductor structures through electrochemical impedance spectroscopy measurement in electrolytic medium.

- To to unveil the relativistic quantum principles governing electron dynamics within these semiconductor structures. A quantum RC circuit analysis was applied to the experimental data obtained from impedance spectroscopy, guided by the relativistic quantum foundations underlying Quantum Rate Theory.

Chapter 4

Density-of-States of Nanoscale Semiconductor Interface as a Transduction Signal for Sensing Molecules

*Edgar F. Pinzón, Adriano Santos and Paulo R. Bueno**

Institute of Chemistry, São Paulo State University (UNESP), 14800-900, Araraquara, São Paulo, Brazil

Keywords: Density-of-states, semiconductor interface, electrochemical capacitance, phenol sensing.

Journal: Applied Electronic Materials 3(8), 3411-3417 (2021).

DOI: https://doi.org/10.1021/acsaelm.1c00387

ABSTRACT

Nanoscale inorganic semiconductors (with interfacial thickness < 10 nm) have superior stability compared to soft organic compounds and are important for the development of enhanced reagentless sensing devices. As a proof-of-concept, this study demonstrated that the density-of-states of a copper oxide mixed-valence semiconducting nanoscale film can be suitably designed as a transducer signal for reagentless sensing of phenol.

4.1 Introduction

Reagentless biological sensors have been designed for point of care platforms with minimal intervention for sample analysis.(BARADOKE et al., 2020; BARADOKE et al., 2021; CECCHETTO et al., 2020; GARROTE et al., 2020; FERNANDES et al., 2013; OLIVEIRA et al., 2019a) These devices are primarily categorized based on the fact that there is no need to add a redox probe or any other reagents to scrutinize the target sample.(BARADOKE et al., 2021; CECCHETTO et al., 2020; MARQUES et al., 2015; BUENO; DAVIS, 2020) To date, the development of reagentless sensing interfaces has been primarily based on thiol(FERNANDES et al., 2013; BRYAN et al., 2013) and peptide self-assembled monolayers(PICCOLI et al., 2018) or alternatively on Prussian Blue(OLIVEIRA et al., 2019b) and redox polymer nanoscale films.(BARADOKE et al., 2020) The disadvantage of this type of soft interface is associated with the low ability to harness oxidative environments; commercialization of these devices requires long-term interfacial durability. Interfaces based on organic compounds are prone to drift problems and signal instability due to conformational changes and oxidation of the soft compounds within the solvent environment.(GARROTE et al., 2019) Thus, the designing of reagentless sensing interfaces for detecting molecules in oxidative environments is important.(ȘERBAN; ENESCA, 2020) Among the wide range of inorganic compounds available for this purpose, metal oxide semiconductors (MOSs) are highly suitable due to their higher chemical stability, morphologica versatility, non-toxicity, and surface functionality.(TRIPATHY; KIM, 2018; CHEN et al., 2017)

The development of MOSs based on TiO_2,(RAJENDRAN et al., 2018; WANG et al., 2019) SnO_2,(ALIM et al., 2019; WANG et al., 2018) and ZnO(FARIA; MAZON, 2019; DONG et al., 2017) for detecting biomarkers and pollutants has been reported. For instance, highly ordered TiO_2 mesoporous films functionalized(WU et al., 2018) with horseradish peroxidase were capable of detecting H_2O_2; meanwhile, SnO_2 nanoparticle modified films were able to sense carbofurans using acetylcholinesterase as a functional agent.(ZHOU et al., 2013) Moreover, ZnO nanorods were employed in detecting glucose.(ZONG; ZHU, 2018) Nevertheless, these examples, albeit based on inorganic MOS structures, require the use of enzymes which can be chemically unstable in certain circumstances and, therefore, a source of problems for commercialization due to the long-lasting and portability requirements(PINO et al., 2016; CHONGSUEBSIRIKUL et al., 2019) of

these types of sensors. Therefore, reagentless non-enzymatic sensing methodologies based on nanoscale MOS structures are desirable for achieving the point-of-care needs. Independent of the material used to modify the interface, the reagentless sensing capability of the interface requires the use of a capacitive signal associated with an electronic confinement, which is crucial in the design of sensitive transducer signals.(BUENO; DAVIS, 2020) To design transducer signals based on the capacitive properties of the interface, the size of the active sensing material of the target interface must be in the order of nanometers in at least one dimension. For instance, the thickness can be controlled to be within 10 nm. Figure 1 shows an illustration of copper oxide modified interfaces.(BUENO; DAVIS, 2020; BUENO, 2018a) The dimension control is required for the quantized effect to be effective and exploitable for producing an effective sensing signal such as an electrochemical capacitive signal,(GARROTE et al., 2019) C_μ, of the interface. It is important to note that for interfaces based on redox switches, C_μ is proportional to the redox density of states (DOS) of the interface,(BUENO et al., 2015; BUENO; DAVIS, 2014b; BUENO; DAVIS, 2014a) which is given by eq.4.1

$$k(\mu) = \frac{G(\mu)}{C_\mu(\mu)} = G_0 \sum_{n=1}^{N} T_n(\mu) \left(\frac{1}{C_e} + \frac{1}{C_q} \right) \tag{4.1}$$

where $G_0 \sum_{n=1}^{N} T_n(\mu)$ and $G_0 = g_s e^2/h$, e is the electron charge, h is Planck's constant, the term e^2/h is the universal conductance constant with a value of approximately 38.7 μS, and g_s is the spin degeneracy of the electron, which takes a value of 2 according to Pauli's rules. G_0 is the conductance quantum, where $\sum_{n=1}^{N} T_n(\mu)$ is appropriately introduced(BUENO; DAVIS, 2020) to generalize G and takes into account the manifolds of the conductance G by incorporating the sum of the transmission probabilities across individual quantum channels n.

In eq.4.1, C_μ is the series combination of two capacitive contributions, where(BUENO, 2018c) $1/C\mu = 1/Ce + 1/Cq$, C_e is the electrostatic capacitance, and C_q is the quantum capacitance. C_e is associated with Coulombic interactions and is geometrically dependent, whereas C_q is proportional to the DOS.(BUENO, 2018a; BUENO et al., 2015; BUENO; DAVIS, 2014b; BUENO; DAVIS, 2014a; BUENO, 2018b; BUENO, 2018c) For interfaces made of electroactive materials with thicknesses < 10 nm, changes in the charge state of the interface are modulated by the DOS because $C_e \gg C_q$, which leads

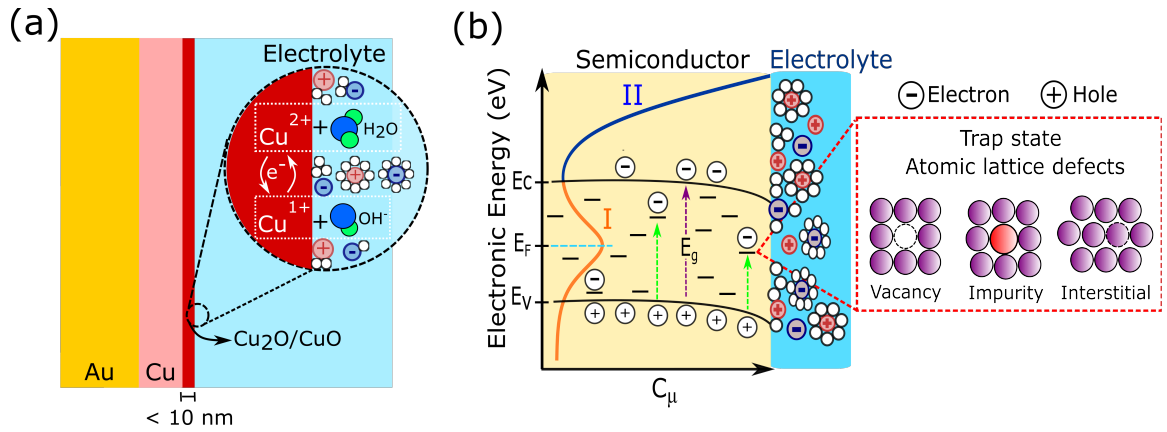

FIGURE 4.1. (a) Schematic representation of the electrochemical interface consisting of a gold electrode modified with a Cu2O/CuO nanoscale film in contact with an electrolytic solution. Electron transfer between Cu^{2+}/Cu^{+} states occurs through the reversible reaction of the copper oxide with species in solution (molecular water and hydroxyl ions). (b) Schematic representation of the electronic structure of a semiconductor nanoparticle interacting and participating in the reactions with the electrolytic medium. The DOS shape of the nanoscale film is resolved by measuring C_μ as a function of electrode potential owing to $C_\mu \propto DOS$. The DOS shape is ascribed as the combination of two distributions of states: (I) a Gaussian DOS associated with states within the band gap (E_g), that is, in between the conduction (E_c) and valence (E_v) band edges and (II) an exponential DOS associated with the continuum of states in the conduction band. Band gap states act as trap states for the charge carriers and are formed due to atomic lattice defects such as vacancies, impurities, and interstitials defects (see inset).

to $C_\mu \sim C_q \propto DOS$, allowing the development of reagentless assays based on the sensing of the DOS in the environment. Hence, the variation of the DOS associated with changes in the C_μ of the interface can be monitored as a function of the analyte concentration, which enables the detection and quantification of the analyte. The aim of this work was to detect phenol by fabricating mixed-valence Cu_2O/CuO nanoscale films by the simple and controllable fabrication process of electrolysis. A schematic of this interface is illustrated in Figure 4.1. Phenol, which was detected by measuring C_μ using the designed DOS of the Cu_2O/CuO film, was selected as the target as this molecule is considered a model environmental pollutant in aqueous samples.(SANTOS et al., 2005; LV et al., 2018)

4.2 Experimental Section

4.2.1 Chemical Reagents and Solutions.

All reagents were of analytical grade and were purchased from Sigma-Aldrich. All electrolyte solutions were prepared using Milli-Q ultrapure water with a resistivity of 18.2

MΩ cm. The phosphate buffer (PB) solution (12 mM PB, pH 7.4) was prepared using 0.2 M KNO_3, 10 mM $Na_2HPO_4 \cdot 12\ H_2O$, and 2 mM KH_2PO_4.

4.2.2 Gold Electrode Pre-treatment.

Gold disk electrodes were cleaned as described elsewhere.(GARROTE et al., 2020) Briefly, the disks (2.0 mm diameter, Metrohm) were mechanically polished with aluminum oxide pads on polishing cloths (Kemet) of progressively decreasing particle size (1.0, 0.3, and 0.05 μm) with intermittent sonication in water. The gold electrodes were then electrochemically cleaned in NaOH solution (0.5 M) between the potentials -1.7 and -0.7 V versus Ag|AgCl (3 M KCl) at a scan rate of 100 mVs^{-1} and then electrochemically cleaned in 0.5 M H_2SO_4 between -0.2 and 1.5 V at 100 mVs^{-1} until the gold reduction peak stabilized ($\sim$50 cycles). Electroactive areas were evaluated by integrating the cathodic peak from gold electropolishing voltammograms and converted to the real surface area using a conversion factor of 410 μCcm^{-2}.(GARROTE et al., 2020)

4.2.3 Fabrication of the Copper Oxide Nanofilms.

Metal copper thin films were electrodeposited on cleaning gold electrodes via potentiostatic deposition in an acidic solution of Cu^{2+} (0.01 M CuSO4 and 0.02 M H_2SO_4) while applying a constant potential of -0.16 V versus Ag|AgCl (3 M KCl) by 180 s. Then, copper surfaces were electrochemically oxidized in 1 M NaOH while applying a potential scan from -0.60 to -0.25 V at a scan rate of 60 mVs^{-1}. The morphology and thickness of the copper oxide nanoscale film were characterized by scanning electron microscopy (SEM) and by electrochemistry (by using Faraday's law, as detailed in the Supporting Information-S2).

4.2.4 Electrochemical measurements.

Electrochemical measurements were performed using an AUTOLAB potentiostat/-galvanostat (PGSTAT30) with the FRA module connected to a three-electrode cell, in which Ag|AgCl (3 M KCl) served as the reference and platinum mesh as the counter electrode. Electrochemical impedance spectroscopy (EIS) measurements were performed on copper oxide nanofilms of different ratios of Cu_2O to CuO (1:0, 3:1, 1:1, 1:3, and 0:1, w/w) in a PB solution (pH 7.4) at 0.0 V and frequencies ranging from 100 kHz to 100 Hz with a peak-to-peak amplitude of 10 mV. The real (C') and imaginary (C'') capac-

itance components were obtained from EIS data using the expressions $C' = \phi Z''$ and $C'' = \phi Z'$, where $\phi = 1/\omega|Z|^2$, $\omega = 2\pi f$, and $|Z|$ is the magnitude of the impedance and f is the linear frequency. Z' and Z'' are the real and imaginary components of the complex impedance function, respectively. DOS mapping measurements were performed by EIS technique in different potentials (from -40 to 140 mV × Ag|AgCl, 3 M KCl).

4.2.5 Phenol Sensing Experiments.

Gold electrodes modified with a nanoscale copper oxide film were used as the working electrode. EIS measurements were performed on the Cu_2O/CuO nanofilms (1:1, w/w) in PB solution (pH 7.4) at different potentials and six different concentrations (from 0.5 to 6 μM) of phenol (C_6H_6O) at frequencies ranging from 100 kHz to 100 Hz with a peak-to-peak amplitude of 10 mV. The measurements take only about 3 min. The impedance data were converted to capacitance data according to the expressions previously described.

4.2.6 Long-Lasting and Specificity.

For specificity assessment, EIS measurements were carried out on Cu_2O/CuO (1:1, w/w) nanofilms in PB solution (pH 7.4) containing 60 μM of aniline and benzyl alcohol at 0.0 V. The durability of the sensing interfaces was assessed by measuring a concentration of 6 μM of phenol in 0, 2, 4, and 6 days after the fabrication of Cu_2O/CuO nanofilms (1:1, w/w). In these experiments, the EIS data were analyzed by converting the EIS data to capacitance representation (C′ and C″), as described previously.

4.3 Results and Discussion.

4.3.1 Theoretical Background.

This section focuses on the energetic term in eq.4.1, that is, $E = \frac{e^2}{C_\mu}$, and discusses the properties of the nanoscale oxide semiconductor film (NOSF) (Figure.4.1a). According to the density functional theory, the term $E = \frac{e^2}{C_\mu}$ is proportional to the energy difference between the highest occupied and lowest unoccupied molecular orbitals. This analysis extended to semiconductive compounds corresponding to the energy difference (band gap) between the conduction (E_C) and valence band edges (E_V) and, in summary, $E = \frac{e^2}{C_\mu} \propto E_C - E_V$ (Figure 1b).

For the realistic evaluation of the energy $E = \frac{e^2}{C_\mu}$ of the film, it is appropriate to consider the thermal broadening of E with respect to the electrical potential using the Fermi-Dirac distribution: $f(eV) = \left[1 + e^{-\beta eV}\right]^{-1}$, where $-eV = \mu - E_F$, $\beta = \frac{1}{k_B T}$, k_B is the Boltzmann constant, T is the absolute temperature, and E_F is the Fermi level (in electrochemistry, this is commonly known as the formal potential of the electrode). Because E_F is a constant referential value, variations in the potential are directly associated with changes in the chemical potential, that is, $-edV = d\mu$. By noting that $dq = -edn$, where dn is the number of electrons allowed to participate in the occupancy of C_μ, the value of C_μ can be calculated by $C_\mu = e\left(\frac{dn}{dV}\right) = e^2\left(\frac{dn}{d\mu}\right)$, where $g(eV) = \left(\frac{dn}{d\mu}\right)$ is the DOS. We note that $n = fN$, where N is the total electron occupancy of the film. Hence, C_μ as a function of f is obtained by observing that $\frac{df}{dV} = \beta f(1-f)$, such that

$$C_\mu = e^2 N \beta f(1-f) \tag{4.2}$$

As noted in the following sections, eq.4.2 is proportional to the DOS, which can be accessible in two different electron occupancies of the NOSF as a function of potential. For example, in the case of analogous soft organic molecular films with $\mu = E_F$, that is, the Fermi level of the electrode, the NOSF can be employed as a sensing interface, as discussed in the following sections.

4.3.2 Resolving the Electronic DOS

As discussed previously, eq.4.2 describes a thermalized C_μ with a maximum value at the electrochemical equilibrium state of the electrode, where eV is null, leading to $\mu = E_F$ and $f = \frac{1}{2}$. The electrochemical equilibrium imposes similar amounts of oxidized and reduced states(BUENO; DAVIS, 2014b; BISQUERT, 2003) and the maximum value of the electrochemical capacitance, C_μ. Accordingly, C_μ is not a constant, but a potential-dependent function from which the total number of states of the NOSF can be obtained by integrating $g(eV)$ over all the available states, such as

$$C_\mu = e^2 \int_{-\infty}^{\infty} g(eV)\, d(eV) = e^2 \int_{-\infty}^{\infty} g(eV) f(1-f)\, d(eV) \tag{4.3}$$

Note that by applying the absolute zero temperature approximation in eq.4.3, we

obtain $C_\mu = e^2 g(eV)$, which confirms the dominance of the quantum contribution (C_q) on C_μ. Additionally, the proportional relationship between C_μ and DOS ($C_\mu \propto DOS$) is explicit. The latter implies the possibility of accessing the DOS of a NOSF by determining C_μ as a function of the potential. The response of C_μ, as described in eq.4.2, theoretically predicts a Gaussian-like shape with a maximum at the Fermi level, which is depicted in region I of Figure 4.1b. The response simulated at a higher oxidative potential is predicted by noting that the state of occupancy is different; that is, the accessible states are those of the conduction band (4.1b) for which $\mu - E_F \gg \frac{1}{\beta}$. Thus, $f \ll 1$ and $f \sim \exp[(\mu - E_F)\beta]$, and eq.4.2 turns into

$$C_\mu \approx e^2 N \beta \exp[(\mu - E_F)\beta] \tag{4.4}$$

The response of C_μ predicted using eq.4.4 is the Boltzmann approximation of eq.4.2, where C_μ is predicted to increase exponentially as a function of the potential (region II of Figure 4.1b). By integrating C_μ of eq.4.4 over all available energy states and applying the absolute zero temperature approximation, we obtain $C_\mu = e^2 g_C(E)$, where $g_C(E)$ corresponds to the distribution of a continuum DOS in the conduction band (CB). Note that the total response of C_μ as a function of potential is a combination of eqs 4.2 and 4.4, as shown in Figure 4.1b. This description of the DOS of a NOSF was tested herein for Cu_2O/CuO mixed oxide electroactive films (1:1, w/w) with thicknesses < 10 nm electrochemically grown on a gold electrode. The results that describe the characterization of the thickness, morphology, and additional capacitive characteristics of Cu_2O/CuO mixed oxide electroactive films are detailed in the Supporting Information-S2-S5. The maximum experimental capacitance of Cu_2O/CuO mixed oxide electroactive films, accessed at the Fermi level at 0.0 V versus Ag|AgCl, was obtained from the Nyquist capacitive diagram, where the equilibrium value of C_μ was obtained at low frequencies, corresponding to the diameter of the semicircle(BUENO et al., 2012) in the diagram (Figure 4.2a).

The experimental DOS of the Cu_2O/CuO nanoscale mixed valence film was resolved by plotting the equilibrium C_μ as a function of the potential. As depicted in Figure 4.2b, the experimental C_μ follows the shape predicted by the model, which is adequately adjusted (yellow line) to eqs 4.3 and 4.4. The Gaussian-like shape predicted by eq 4.3 is observable in potentials ranging from -0.05 to 0.05 V, with a capacitance maximum

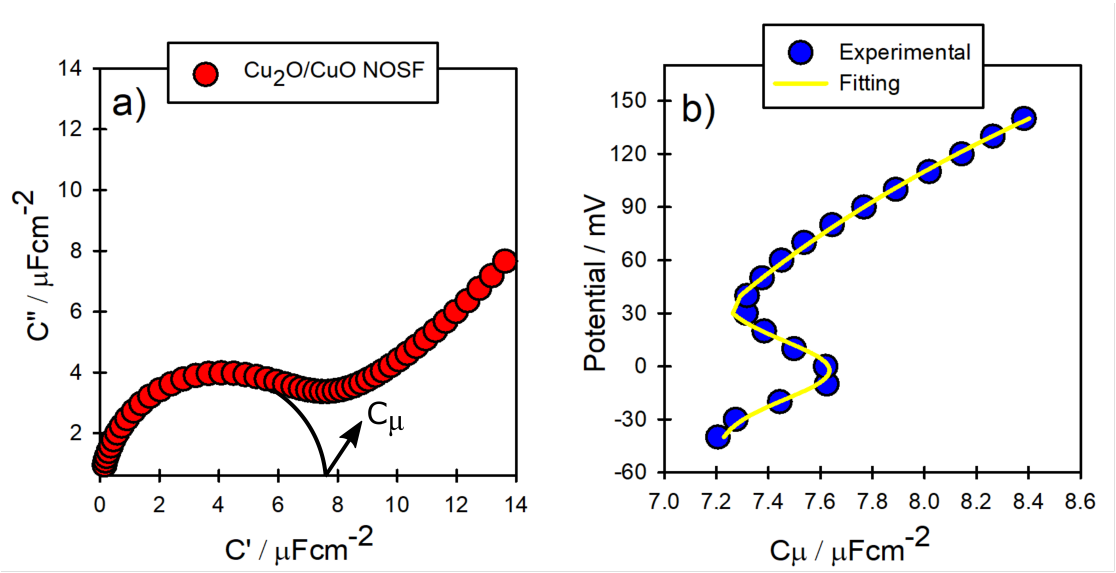

FIGURE 4.2. (a) Nyquist capacitive diagram obtained for a Cu_2O/CuO mixed electroactive nanofilm (1:1, w/w) by EIS-derived capacitive methods at the Fermi level of the junction (0.0 V vs Ag|AgCl) in PB solution (pH 7.4). The value of C_μ is equal to the diameter of the semicircle in the Nyquist capacitive diagram. (b) The DOS is resolved for a Cu_2O/CuO mixed thin film (1:1, w/w) through the determination of C_μ as a function of potential in the same electrolytic medium of (a). The red line corresponds to the theoretical fitting performed on the experimental data from the response of C_μ predicted by eqs 4.2 and 4.4.

of 7.6 μF cm^{-2} at the Fermi level. In this case, the oxidation states are Cu^{2+} and Cu^{+} (Figure 4.1a), and the electronic transition between these states follows the reversible electrochemical reaction described in eq.4.5, where Cu_2O reacts with hydroxyl ions in solution forming CuO and water, and vice-versa,(SCHERZER et al., 2019; WAN et al., 2013) as shown below

$$Cu_2O + 2OH^- \rightarrow 2CuO + H_2O + 2e^- \quad (5) \tag{4.5}$$

Note that at the Fermi level, half of the accessible redox states are oxidized (Cu^{2+}) and half are reduced (Cu^{+}); the origin of these redox states is related to the trap states due to induced defects in the copper oxide crystalline lattice, such as atomic vacancies, impurities, and interstitial defects (Figure 4.1b).(MCCLUSKEY; JANOTTI, 2020; MAHAJAN, 2000) Thus, the density of defects in the crystalline lattice modifies the potential energy of the semiconductor film, which generates a Gaussian-like distribution of energy states ($\propto C_\mu$) between the conduction and valence bands(ROCKETT, 2008; SHLUGER,

2020) (Figure 4.2b) due to their occupancy being determined by the thermal broadening term $f(1-f)$ in eq.4.3. In addition to the Gaussian-like distribution, the response of C_μ associated with the occupancy of CB states (higher energy) is observed in the potential window between 50 and 150 mV (Figure 4.2b). This agrees with the theoretical exponential pattern depicted in Figure 1b and eq.4.4, that is, the Boltzmann distribution.

Although the probing and tuning of the electrical properties of these nanostructured semiconductors, particularly the generation of energy states within the band gap, are considered to be of utmost importance in solar cell and supercapacitor applications,(DEY, 2018; ZHU et al., 2016) the use of the DOS of nanoscale semiconductors as transducer signals in molecular sensing assays has not yet been explored. Accordingly, we demonstrated a simple procedure to use the C_μ of Cu_2O/CuO nanofilms, which is associated with their DOS, as a transducing signal for sensing phenol. Herein, we introduce a new approach for molecular sensing, which is based on the monitoring of the C_μ of semiconductors at a nanoscale interface and which can be easily measured using impedance-derived methods.

4.3.3 Demonstrating the Sensing Functionality.

In this section, we demonstrate how the C_μ signal of the NOSF measured at the electrochemical equilibrium, which corresponds to the peak of the Gaussian distribution in Figure 2b, can be used to sense phenol (C_6H_6O), which was used herein as a model phenolic compound. The phenolic compounds are considered as key pollutants across many industries. For instance, pharmaceutical, petrochemical, and food companies use complicated analytical methods to detect these substances as a standard for controlling the quality of the wastewater. The detection of these compounds is necessary due to their high environmental toxicity.(LV et al., 2018) The use of low-cost and real-time sensing platforms that allow in situ detection of harmful concentrations of phenolic compounds in water effluents (>70 μM) is highly desirable(PINO et al., 2016). Among non-enzymatic approaches for phenol-derived compound sensing, electrocatalytic methods are preferred due to their ability to leverage the efficient catalytic properties of metal oxides.(FENG; LI, 2003) Copper oxide nanostructures have demonstrated a larger catalytic activity for the oxidation of phenolic compounds in comparison with other structures such as nickel, cobalt, and manganese oxide.(SANTOS et al., 2005)

Aiming at evaluating the durability of Cu_2O/CuO sensing interfaces, it was selected

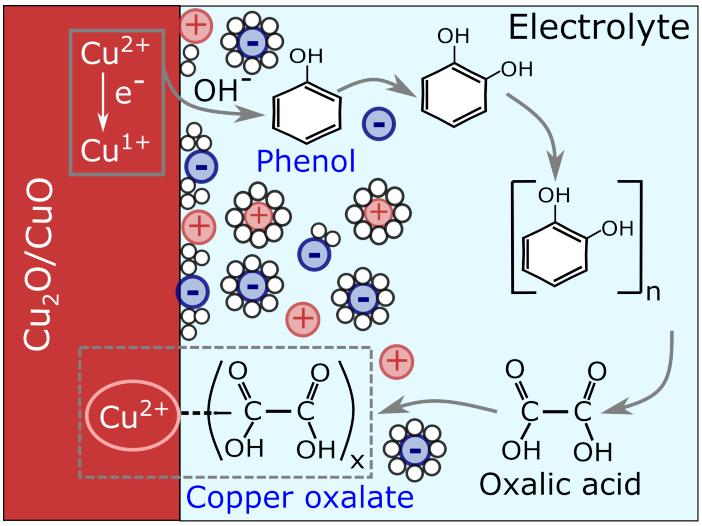

FIGURE 4.3. Schematic representation of electrocatalytic oxidation of phenol in solution over a copper oxide electrode. Different intermediate compounds are generated in this process; among them, oxalic acid reacts with surface species Cu^{2+}, forming metal complexes on the copper oxide surface.

a particular Cu_2O/CuO composition in between five studied compositions, that is, 1:0, 3:1, 1:1, 1:3, and 0:1 (w/w). Because the transducer signal is based on the DOS of these films, as mapped by impedance and discussed in the previously section, and owing to the DOS being proportional to C_μ,(SANTOS et al., 2014) an optimal condition is considered for interfaces with the highest value of the C_μ signal as possible. As demonstrated in Supporting Information-S5, the highest C_μ signal was attained for 1:1 (w/w), and thus, this was the composition investigated for sensing phenol.

In the electrocatalytic oxidation of phenol over copper oxide electrodes, the highly reactive hydroxyl ions (OH^-) generated during the redox reaction Cu^+/Cu^{2+} can be used to catalyze the oxidation of the organic molecules, as schematically shown in Figure 4.3. The OH^- ions attack the phenol molecules in solution, triggering a chain reaction in which different acid intermediaries are formed. Figure 4.3 depicts the reaction of oxalic acid, an intermediary widely identified in phenol oxidation, which can react with Cu^{2+} located on the copper oxide surface to form metal complexes known as copper oxalates.(SANTOS et al., 2005; SANTOS et al., 2002)

Figure 4.4a shows the resolved C_μ (or DOS) around the electrochemical equilibrium potential of the Cu_2O/CuO nanofilms in a PB solution (pH 7.4) for different concentra-

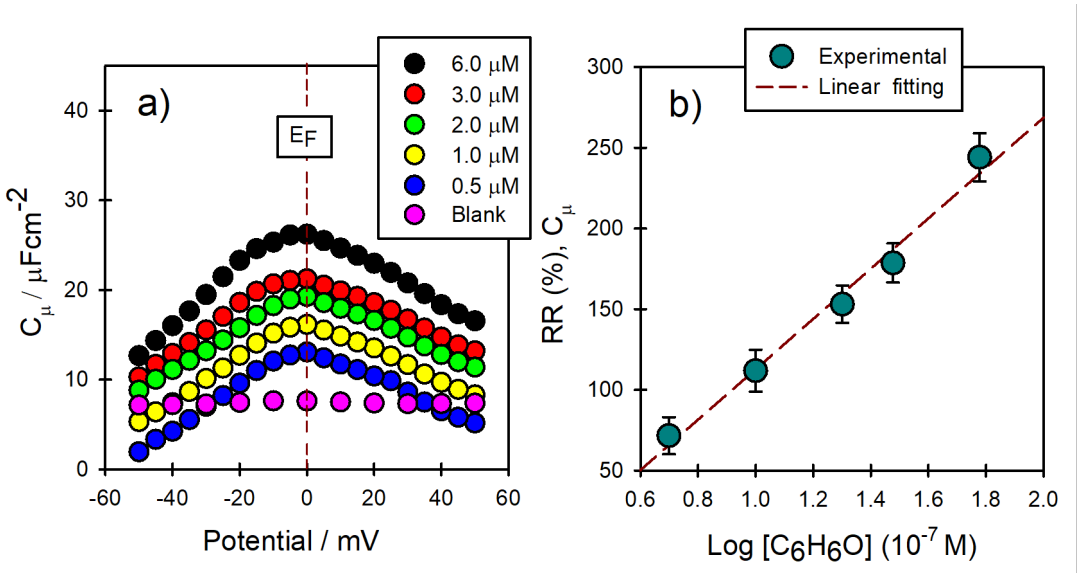

FIGURE 4.4. (a) Gaussian shape DOS resolved for the Cu_2O/CuO nanofilm in a buffer solution at six different concentrations of phenol (C_6H_6O). The red line represents the Fermi level (E_F) of the nanoscale semiconductor junction. (b) Analytic curve reporting the variation of C_μ at the Fermi level of Cu_2O/CuO nanofilm for the sensing of phenol. Plotted data points represent means and standard deviations across two independent interfaces. The coefficient of determination (R^2) is 0.985. (c) Relative responses of C_μ obtained for phenol (6 μM) and two interfering compounds, aniline and benzyl alcohol, both at 60 μM.

tions of phenol. The value of C_μ at the Fermi level increases with the target concentration, demonstrating that C_μ can be effectively used as a transducer signal to sense phenol, as predicted by eq 1. A chemical binding event associated with the formation of copper complexes on the surface of the Cu_2O/CuO nanofilm generates a variation in the chemical potential μ of the electrons, which is detectable as a change in the electron occupancy and modulates the response of $C_\mu \propto (dn/d\mu)$.

Notably, a linear response is obtained for the relative response of C_μ as a function of the logarithm of the concentration of phenol (Figure 4b), that is, $\mathrm{RR}(\%) = \left[\frac{(C_{\mu,[\mathrm{phenol}]} - C_{\mu,\mathrm{blank}})}{C_{\mu,\mathrm{blank}}}\right] \times 100$, where $C_{\mu,[\mathrm{phenol}]}$ and $C_{\mu,\mathrm{blank}}$ are the C_μ signals for a particular phenol concentration and for the blank, respectively. It is noteworthy that the concentrations used in this assay were lower than the acceptable threshold of phenolic compounds in water effluents (70 μM) established by governmental environmental agencies.(PINO et al., 2016) Using the capacitive approach, it is possible to detect phenol in a linear range of 0.5-6 μM with a sensitivity of 156% per decade of phenol concentration. The obtained limit of detection (LOD) was 0.2 μM, determined as 3S/b, where S is the standard

deviation of the y-intercept and b the sensitivity.(SHRIVASTAVA; GUPTA, 2011) The reported LOD is comparable to that obtained by other electroanalytical methods.(PINO et al., 2016; ALIABADI et al., 2020)

The reproducibility was evaluated by calculating the relative standard deviation from measurements carried out in different days for all phenol concentrations over replicates, which was of 9.6%, similar to deviations reported by others.(PINO et al., 2016; ALIABADI et al., 2020) To further evaluate the applicability of this reagentless capacitive approach for sensing phenolic compounds, the performance on selectivity was assessed using aniline ($C_6H_5NH_2$) and benzyl alcohol (C_7H_8O) as interferents because these two compounds are prevalent in contaminated samples. As depicted in Figure 4.4c, the relative response of C_μ for the aniline and benzyl alcohol was 4.30 and 8.90%, respectively, for a concentration 10 times higher (60 μM) than the highest phenol concentration (6 μM) evaluated in this work within a RR (%) value of 244.13%. Hence, the selectivity of the Cu_2O/CuO interface for phenol is evident.

Finally, the long-term stability was evaluated by performing capacitance measurements at a 6 μM concentration of phenol for 2, 4, and 6 days after the fabrication of the Cu_2O/CuO nanofilms as stored in ambient air at 25 °C. These results are introduced in detail in S6 of the Supporting Information. Figure S8 (see the Supporting Information) indicates a small decrease of the RR (%) within days, resulting in a loss of signal of about 11% for the sixth day. This decrease on the RR (%) signal is attributed to a potential interaction between copper oxide and air oxygen. However, the Cu_2O/CuO sensing interface continues to be highly specific (from 244.13 to 216.63%) compared to the response of the interferents (i.e., 4.30 and 8.90%) and, more important, measurements take only 3 min. Therefore, the capacitive sensing of oxide interfaces is demonstrated as a potential analytical methodology for the fast detection and quantification of phenolic compounds in wastewater.

4.4 Conclusions.

In this study, we demonstrated the fabrication of Cu_2O/CuO mixed valence nanofilms. The appropriate design of the films enabled the corresponding C_μ, and its associated DOS to be used for fast sensing of phenol with high sensitivity and via a

reagentless and point-of-care approach. This concept can be extended to the detection of other types of molecules by the appropriate functionalization of the oxide surface of the Cu_2O/CuO mixed valence nanofilm.

Associated Contents.

The Supporting Information is available free of charge at <https://pubs.acs.org/doi/10.1021/acsaelm.1c00387>. Electrochemical fabrication of the nanoscale films of copper oxide; electrochemical estimation of the Cu_2O/ CuO (1:1, w/w) nanofilm thickness; estimation of the ratio of Cu_2O and CuO in the copper oxide mixed nanofilms; surface morphological analysis of Cu_2O/CuO (1:1, w/w) nanofilm by SEM; capacitive analysis of copper oxide nanofilms containing different Cu_2O/CuO proportions; and sensing surface stability for phenol over time (PDF).

Corresponding Authors

Adriano dos Santos - Institute of Chemistry, São Paulo State University (UNESP), Araraquara 14800-900 São Paulo, Brazil; <https://orcid.org/0000-0001-6812-5609>; Email: adriano.santos1@unesp.br

Paulo R. Bueno - Institute of Chemistry, São Paulo State University (UNESP), Araraquara 14800-900 São Paulo, Brazil; <https://orcid.org/0000-0003-2827-0208>; Email: pauloroberto.bueno@unesp.br

Author

Edgar F. Pinzón - Institute of Chemistry, São Paulo State University (UNESP), Araraquara 14800-900 São Paulo, Brazil.Complete contact information is available at: <https://pubs.acs.org/10.1021/acsaelm.1c00387>

Notes The authors declare no competing financial interest.

Acknowledgments

This work was supported by the Sao Paulo State Research Funding Agency (FAPESP) process number 2018/24545-9 and 2017/24839-0.

Chapter 5

Quantum Rate as a Spectroscopic Methodology for Measuring the Electronic Structure of Quantum Dots

Edgar Fabian Pinzón,[a] Laís Cristine Lopes,[a] André Fonseca,[b] Marco Antonio Schiavon,[b] & Paulo Roberto Bueno,*[a]

[a] *Sao Paulo State University, Rua Francisco Degni, 55 - Araraquara, Sao Paulo, Brazil*, [b] *The Federal University of São João del-Rei, Praça Frei Orlando, 170 - São João del-Rey, Minas Gerais, Brazil*

Keywords: quantum rate theory, heterocyclic molecule, quantum electrodynamics, quantum capacitance, density-of-state, quantum conductance

Journal: Journal of Materials Chemistry C, 12(13), 4606-4617,(2024)

DOI: https://doi.org/10.1039/D4TC00347K

Abstract

The electronic structure of nanoscale moieties (such as molecules and quantum dots) governs the properties and performance of the bottom-up fabricated devices based on their assemblies. Accordingly, simple and faster experimental methods to resolve the electronic density of states of these nanoscale materials (of which quantum dots are a

particular example) are of great importance for the development of man-made nanoscale interfaces and nanoelectronics. In the present work, we propose the quantum rate spectroscopy methodology (and introduce the fundamental physical basis of this technique that was previously demonstrated for measuring the electronic structure of two-dimensional compounds such as graphene (LOPES et al., 2024)) as a tool for resolving the electronic structure of zero-dimensional (quantum dot) structures at room temperature and environmental pressure conditions. This method is simpler than the traditional methods based on scanning tunneling microscopy. This spectroscopic approach based on the quantum rate theory was demonstrated for CdTe quantum dots and was used to measure a spectrum that provides discrete energy levels that are consistent with those obtained by tunneling microscopy measurements.

5.1 Introduction

Charge carriers dynamics in semiconducting quantum dot (QD) structures are restricted in all of the three possible Cartesian geometric directions at the nanoscale in a range of 2-10 nm. Accordingly, QDs are referred to as zero-dimensional structures due to their spatial point characteristics governed by the above-mentioned nanoscale size features. This unique feature of QDs makes them the closest man-made semiconducting inorganic constructions with electronic structure comparable to that of organic molecules, as noted in Fig 5.1. Hence, QDs provide discrete quantized energy levels accessible at room temperature. Accordingly, QDs are special materials that offer excellent optical and electronic properties(AKBARI et al., 2020) that are unique compared to those of microscopic structures or bulk materials(EDVINSSON, 2018).

The electronic structure of molecules or nanoscale spatially-restricted atomic assemblies is often analyzed in terms of their electron density of states (DOS) that is a function that accounts for the amount of quantum-mechanical states of electrons (or electron energy levels) per interval of energy normalized by the volume of the atomic structure. Therefore, the DOS is a fingerprint of the electronic structure of atomic and molecular assemblies that is an important tool for predicting the properties of man-made nanoscale materials, particularly when the DOS can be experimentally measured(HOUTEPEN; VANMAEKELBERGH, 2005).

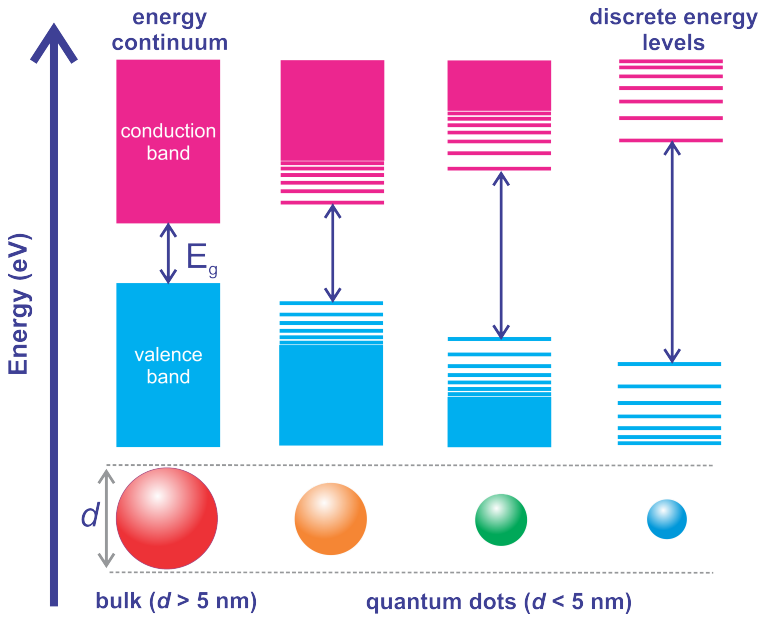

FIGURE 5.1. Schematic representation of the energy levels for low-dimensional QD semiconducting materials. Note the evolution of the quantum confinement of the energy levels as a function of the dimension of the QD. For instance, the QD with dimensions greater than 5 nm (on the left) has a pattern that is more similar to a bulk semiconducting material in which the electronic structure is formed by two separated bands (termed conduction and valence bands and the separation between these bands is termed the band gap because it constitutes an energy interval in which electron occupation is prohibited) within the internal energy levels that are quite close to each other, forming a continuum of characteristic energy levels referred as the band structure. As the size of the QDs decreases below 5 nm, the separation between the energy levels in these bands increases, forming a set of discrete (rather than a continuum) energy states that at a certain size resembles the energy levels observed in molecules (scheme at right). Note also that the band gap of semiconducting materials increases with decreasing particle size due to the above-described quantum confinement effect. In this figure 5 nm size of QD was used as a reference. The precise cut-off depends on the definition of the Bohr radius of a QD. For instance, for CdTe QDs this value is calculated as $\sim$ 6.8 nm (PARK HYUNG J. ANDN SHIN; YU, 2021).

Techniques commonly applied for experimental study of the electronic properties of QDs are based on optical excitations and energy level transitions that can be easily applied to the investigations of the electronic transition properties of nanocrystals. Useful information about the influence of the size and shape on the properties of these nanoscale crystals can be deduced by optical absorbance, luminescence, and excitation spectroscopic methods(JDIRA et al., 2006). However, the inherent limitations of these techniques do not allow a full investigation of the DOS; rather only some energy levels can be investigated in an indirect manner.

For the scanning tunneling microscopy (STM) and spectroscopy (STS) methods, it is challenging to separately investigate the electron and hole energy levels, and additionally the electron beam used to obtain the information can damage the nanostructures and cause undesirable atomic strain and extrinsic defects(ERNI et al., 2008). Although investigations of the local density of states (LDOS) of single nanoparticles have been performed using these methods, it is experimentally challenging to discern the variation of LDOS within and between QDs(BAKKERS et al., 2001).

The use of STS to characterize CdSe QDs of different sizes is a direct approach to determine the relationship between the energy levels and the size of QDs(JDIRA et al., 2006). A combination of STS with optical spectroscopy demonstrated that the relative rates of the tip-to-dot and dot-to-substrate tunneling currents influence the electron occupancy in the QDs. Therefore, the tunneling current has been measured as a function of the tip-substrate potential bias difference controlled via the STS feedback settings. A large number of experiments for each set-point of electric current were carried out to successfully improve the reproducibility of the results. The transitions in the tunneling spectra were explained by a master equation accounting for the electron-hole occupancy of the discrete energy levels ascribed to the conduction and valence band states (or orbitals) of CdSe QDs.

Even though STM- and STS-based methodologies have made significant contributions to the on-going understanding of the electron energy levels of QDs, the wide use of these methodologies is either not practical or requires unique and expensive equipment that is not easy to operate because of the required high-vacuum and/or low-temperature conditions. Therefore, experimental approaches that are both simpler and have benchtop capability are desired to advance the characterization of the electronic density of low-dimensional structures.

Therefore, the goal of the present work is to demonstrate a proof-of-principle of a methodological approach, named quantum rate spectroscopy (QRS), as a simpler method of probing the electronic structure of nanoscale chemical assemblies of interest of material scientists, chemists, and physicists. The use of QRS was successfully applied to reveal the electronic structure of two-dimensional compounds such as graphene (LOPES et al., 2024). This electrochemical QRS method of measuring the electronic structure

of graphene was demonstrated to be in good agreement with the electronic structure measured angle-resolved photo-emission spectroscopy and that theoretically computed by density-functional theory (LOPES et al., 2024). QRS is an electric spectroscopy method that is fundamentally based on the quantum rate theoretical principles(BUENO; DAVIS, 2020; BUENO, 2018d; BUENO, 2023c). For instance, besides the application of the principles to characterize single-layer graphene(LOPES et al., 2021; LOPES et al., 2024), it has also been possible to access the DOS of mixed metal-oxide films(PINZON et al., 2021) and organic assemblies(FELICIANO; BUENO, 2020a), such as molecular redox-active films(BUENO, 2023c). Furthermore, quantum rate theory has been useful for the study of quantum electrochemical principles (ALARCÓN et al., 2021b; BUENO, 2023c), for example demonstrating that charge transfer resistance is essentially a specific setting of the quantum conductance principle (SANCHEZ et al., 2022). This has provided the basis for the design of improved electrochemical interfaces for electron transport (SÁNCHEZ et al., 2022) with multiple applications.

In this work, the QRS methodology is demonstrated as a useful electric spectroscopic tool for evaluating the electronic structure of CdTe QD assemblies. Two different nanocrystal sizes (2.25 and 3.27 nm) are studied and the obtained experimental spectra are mathematically fit to a quantum mechanical statistical equation following the quantum rate principles, hence demonstrating that the measured electronic spectra are in agreement with the quantum rate theory predictions. Furthermore, it is demonstrated that the energy levels obtained in these CdTe QD spectra are in agreement with those obtained by other studies, for example by using the STM method.

5.2 Experimental Section

5.2.1 Chemical Reagents and Solutions

$CdCl_2 \cdot H_2O$ (99%) was purchased from Vetec. 3-mercapropropionic acid (MPA; 98%), NaOH (99%), Na_2TeO_3 (99%), $NaBH_4$ (99%), and Rhodamine 6G (99%) were obtained from Sigma Aldrich. Acetone (98%) was obtained from Synth. All chemicals were used as received, without further purification. Milli-Q water was used for all experiments. Phosphate buffer (PB) solution (12 mM PB, pH 7.4) was prepared using 0.2 M KNO_3, 10 mM $Na_2HPO_4 \cdot 12\ H_2O$, and 2 mM KH_2PO_4.

5.2.2 Synthesis of CdTe Quantum Dots

Cadmium telluride (CdTe) QDs were synthesized via the One-Pot colloidal method. Initially, $CdCl_2.H_2O$ (0.40 mmol) and surface ligand (3 mercaptopropionic acid MPA, 0.80 mmol) were solubilized in Milli-Q ultrapure water (80 mL) in a three-neck flask and the pH of this solution was adjusted to 10.00 with 1.0 mol.L^{-1} sodium hydroxide. Then, Na_2TeO_3 (0.04 mmol) and $NaBH_4$ (0.1 mmol) were added and the system was heated to 100 °C under reflux to keep the precursors at constant concentrations. When the temperature reached 100 °C, aliquots were taken out at different time intervals to measure the sizes of the quantum dots. After the synthesis, the QD dispersion was purified by the precipitation method, using acetone as a non-solvent to destabilize the colloidal suspension. Then, the precipitate was collected by centrifugation at 9000 rpm for 5 min and resuspended in Milli-Q ultra-pure water.

5.2.3 Characterization of CdTe Quantum Dots

Absorption spectra were acquired in the 200–700 nm region using a spectrophotometer (Shimadzu, UV-2450/2550, Japan) with a spectral resolution of 1.0 nm and a slit width of 1.0 nm. UV-Vis absorption spectra were acquired using a spectrophotometer (Shimadzu, UV-2450/2550, Japan), with a spectral resolution of 1.0 nm, and a slit width of 1.0 nm. Photoluminescence (PL) spectra were obtained using a spectrofluorometer (Shimadzu, RF-5301 PC, Japan) equipped with a 150 W Xenon lamp. The spectral resolution utilized was 1.0 nm, the excitation and emission slits were both set to 3.0 nm and the excitation wavelength to 355 nm. All spectroscopy studies were performed using 10.00 mm quartz cuvettes (Shimadzu) at room temperature. Powder X-ray diffraction (XRD) was performed with a diffractometer (XRD-600, Shimadzu, Japan) using CuKα radiation with a 0.3 mm divergence slit. The diffraction angle (2θ) was varied from 10 to 60 degrees at a rate of 1° min^{-1} and a step of 0.02°. The results obtained from the characterization of the CdTe QDs are presented in detail in the SI.

5.2.4 Preparation of the Assemblies of Quantum Dots

Gold electrodes (Au electrodes) were fabricated by radio-frequency sputtering. Briefly, titanium and gold were sequentially deposited over silicon oxide wafers (0.8 x 0.5 cm^2) obtaining gold electrodes with an average geometric area of approximately 0.04 cm^2. These Au electrodes were initially cleaned via sonication periods of 12 min following

the use of a sequence of solvents, namely isopropyl alcohol, acetone, isopropyl alcohol, and ultrapure water. Then, these surfaces were cleaned by 30 min under ultraviolet/ozone. The pre-treated Au electrodes were incubated in a solution containing 50 mmol L^{-1} of L-cysteine during 16 h at room temperature to form a L-cysteine monolayer over the surface of the Au. After this chemical modification of the surface, the electrode was rinsed with ultrapure water. The L-cysteine monolayer-modified Au electrodes were incubated in an aqueous solution containing 0.2 mmol L^{-1} of CdTe QDs, 100 mg mL^{-1} EDC and 100 mg mL^{-1} NHS during 3 h in the dark. The EDC and NHS are added in the solution to activate the carboxyl groups (COOH) of the QDs surface, allowing their conjugation with the amine groups (NH_2) of the L-cysteine (contained in the surface of the Au electrode) through amide bonding. Finally, the CdTe-QD-modified Au electrodes were rinsed with ultrapure water.

5.2.5 Electrochemical Measurements

Electrochemical impedance spectroscopy (EIS) was performed using a portable potentiostat (PalmSens4) equipped with a frequency response analyzer (FRA) in a three-electrode setup. The CdTe QDs assembled over Au electrodes served as the working electrode, Ag|AgCl (3M KCl) as the reference electrode and a platinum mesh as the counter electrode. All electrochemical measurements were carried out in a phosphate buffer solution (pH 7.4). EIS spectra were obtained at a fixed bias potential (which in the case of this study was 0.14 V *versus* Ag|AgCl (3M KCl)), corresponding to the value of the open-circuit potential, OCP) using an amplitude potential perturbation of 10 mV and frequencies ranging from 1 MHz to 0.05 Hz. The obtained raw EIS data were used to calculate real C' and imaginary C'' capacitive components by applying the following relationship $Z^*(\omega) = 1/j\omega C^*(\omega)$, where $Z^*(\omega)$ and $C^*(\omega)$ are the impedance and capacitance complex functions, respectively. ω is the perturbing angular frequency used in the measurements. The complex capacitance $C^*(\omega)$ function has a particular meaning within the quantum rate theory (LOPES et al., 2021)

$$C_q^*(\omega) = \frac{C_q}{1 + j\omega\tau} \sim C_q\,(1 - j\omega\tau) + O(\omega^2), \tag{5.1}$$

corresponding to a relaxation function that can be described in terms of the equivalent quantum circuit elements. For instance, this relaxation function is expressed in terms of

a series combination of R_q and C_q, providing a characteristic frequency ω_c with a time $\tau = 2\pi R_q C_q$ (or $\omega_c = 1/R_q C_q$) that directly provides information regarding the quantum rate $\nu = 1/\tau$ as defined further in Eq. 7.1.

Therefore, noting that the complex quantum capacitive relaxation function $C_q^*(\omega)$ can be expressed as $C_q^*(\omega) = C' + jC''$ and that $C' = \varphi Z''$ and $C'' = \varphi Z'$, where $\varphi = 1/\omega|Z|^2$, it can be observed that C' and C'' can be obtained from EIS measurements. From the EIS spectra, real Z' and imaginary Z'' impedance components can be readily measured. $|Z|$ is the impedance modulus that can be calculated from Z' and Z'' components. The frequency associated with the maximum value of the real capacitive term, i.e., corresponding to the diameter of the Nyquist capacitive semicircle (see Fig. 5.2*b*), which is theoretically obtained for $\omega \to 0$ in Eq. 6.15, is experimentally obtained as a finite value and is fixed as a constant charge-occupancy equilibrium state. By fixing this ω_0 limit frequency value and performing a potential scan (which in the present study ranged from -1.8 to 1.8 V *versus* Ag|AgCl (3M KCl), the $C_q(\omega_0)$ function is obtained. This $C_q(\omega_0)$ plotted as function of potential energy at the fixed ω_0 of the electrode is used to obtain the shape of the DOS by noting that $C_q \propto$ DOS (see theory discussed below). The QRS method is illustrated in Fig. 5.2. Note that all potentials used in the present work are reported *versus* Ag|AgCl (3M KCl) reference.

5.3 Results and Discussion

Before describing how the electronic DOS of an ensemble of semiconducting QDs is measured using QRS, it is useful to introduce the key concepts of the QRS method, which is based on the quantum rate theory, as mentioned above.

5.3.1 Fundamentals of Quantum Rate Theory

We start by assuming that an ensemble of QDs with an average size lower than 5 nm (with an electronic structure such as shown in Figure 5.5) can be assembled over a conducting electrode (see Fig. 5.3). Therefore, the electronic states (including valence and conduction band states) are accessible by perturbing electrons and holes by a sinusoidal wave potential or energy E perturbation imposed from the electrode in which $E = h\nu$ is the quantum mechanical principle that specifies the relationship between energy E and frequency ν (in hertz) that can be applied to investigate the DOS of a QD ensemble

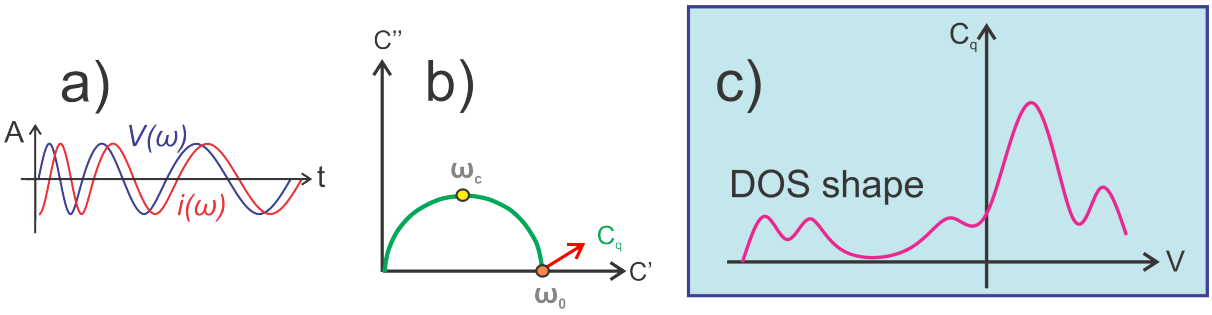

FIGURE 5.2. Schematic representation of the measurements of the DOS of QDs based on the quantum rate principles as can be obtained from EIS measurements. (a) EIS measurement consists of a sinusoidal potential or energy perturbation of the QDs that provide an electric current response to this perturbation from which a complex impedance function $[Z^*(\omega)]$ is obtained. From $Z^*(\omega)$, a complex capacitive function $[C^*(\omega)]$ is obtained and plotted as shown in a capacitive (b) Nyquist diagram, enabling the measurement of the equilibrium charge occupancy. This equilibrium charge occupancy is obtained from the capacitive Nyquist diagram as a particular low-frequency value from which C_q is taken, corresponding to the value of the diameter of the semi-circle in the diagram. Once the equilibrium angular frequency ω_0 is obtained as the frequency at which C_q is obtained, a potential scan of C_q at ω_0 provides the (c) DOS pattern of a QD ensemble assembled at the interface. Note that in (b) $\omega_c = 1/R_qC_q$ refers to the characteristic angular frequency, which is directly related to the quantum rate as described in Eq. 7.1.

assembled on the electrode. Note that following the usual notation, h is the Planck's constant.

One of the key assumptions of the quantum rate theory (BUENO, 2023a; BUENO, 2023b; BUENO, 2023c) is that it allows us to model electron particles and information exchanged between two different quantum mechanical states and hence to better understand the $E = h\nu$ dynamics phenomenon at super or extremely low energies perturbation, i.e. down to 30 Hz, corresponding to energies lower than 124 feV, as it is the case of redox reactions (BUENO; DAVIS, 2020; BUENO, 2023c) and of the long-range electron transport in respiration chains (BUENO, 2024). For inorganic quantum dots, similarly to the case of graphene (BUENO; MERCADO, 2022; LOPES et al., 2024), as will be demonstrated in the present work, this lower energy perturbation phenomenon obeys quantum mechanical rules that cannot be correctly modeled using Schrördinger's non-relativistic quantum-wave methods but can be using relativistic quantum electrodynamics within Planck-Einstein $E = h\nu$ relationship.

Note that the quantum electrodynamics related to the quantum rate theory is dif-

ferent of the common sense for relativistic electrodynamics in which it is guessed that a particle must to be close to the velocity of a photon. It must be clarified that this note the case. Quantum rate theory implies quantum electrodynamics and Planck-Einstein relationship because the principles of the theory complies with the Dirac equation (DIRAC, 1928), which was an equation formulated exactly with the purpose to comply with Planck-Einstein relationship wherein the Schrödinger equation fails, though it is a particular setting of the Dirac equation whenever spin dynamics is disregarded. In general, the Dirac equation implies a wave description of the electron in which the massless character is implicit. The meaning of this is that electrons can, in certain circumstances, behave like waves by presenting a null rest mass m_0. This massless Fermionic characteristic implies relativistic behaviour simply because it follows a particular setting of the relativistic relationship $E^2 = p^2c_*^2 + m_0^2c_*^4$, where for $m_0 = 0$ it leads to $E = pc_*$, not only obeying the Planck-Einstein relationship but also complying with the Dirac quantum mechanical equation.

In other words, the quantum rate theory defines a fundamental rate ν principle based on the ratio between the reciprocal of the von Klitzing constant $R_k = h/e^2$ and the quantum (or chemical) capacitance, such as (BUENO, 2023c)

$$\nu = \frac{e^2}{hC_q} = \frac{E}{h}, \tag{5.2}$$

where by noting that $E = e^2/C_q$ is an energy intrinsically associated with the electronic structure, it straightforwardly leads to the Planck-Einstein relationship, i.e.

$$E = h\nu = \hbar\mathbf{c}_* \cdot \mathbf{k}, \tag{5.3}$$

which follows a linear relationship dispersion between the energy E and wave-vector[1] $\mathbf{k}$, where $\mathbf{c}_*$ is the Fermi velocity and $\hbar$ is the Planck constant h divided by 2π. Hence, the quantum rate principle within Eq. 7.1 predicts relativistic dynamics that comply with Dirac (DIRAC, 1928) instead of with the non-relativistic Schrördinger equation. Note that

[1]Note that $\mathbf{k}$ in bold refers to the wave-vector and its magnitude will be referred to as $|\mathbf{k}|$ to avoid notation issues with the meaning of k that, in previous works (BUENO, 2023c; SANCHEZ et al., 2022), was referred to as the electron transfer rate constant.

the linear relationship between $\mathbf{k}$ and E is intrinsically relativistic which is demonstrable by invoking De Broglie relationship, which states that the momentum $\mathbf{p} = \hbar\mathbf{k}$ is directly related to the $\mathbf{k}$; hence Eq. 7.2 turns into $E = \mathbf{p}\cdot\mathbf{c}_*$, demonstrating its intrinsic relativistic character.

It has been experimentally demonstrated (ALARCÓN et al., 2021b; BUENO, 2023c; SANCHEZ et al., 2022) that $E = e^2/C_q$ is a degenerated state of energy for experiments conducted in an electrolyte environmental medium, such as that effectively E is $E = g_s g_e(e^2/hC_q)$, where g_s is the electron spin degeneracy and g_e is the energy degeneracy state associated with the electric-field screening effect of the electrolyte over the quantum states contained in molecules(BUENO, 2023c), graphene(BUENO; MERCADO, 2022; LOPES et al., 2024), as well as quantum dots (as will be demonstrated here).

There are two equivalent interpretations of g_e degeneracy. The first is based on the existence of resonant electric currents, i.e., there are time-dependent (displacement) electric currents within the junction. This type of resonant electric current is owing to the existence of two charge carriers (electrons and holes) that promote a net current denoted here as i_0. The origin of this displacement electric current is owing to the role played by the electrolyte that allows the superimposition of the electrostatic C_e and quantum capacitive C_q modes of charging the molecular junction states. In this situation, the elementary charge e is subjected to an equivalent electric potential, i.e., $e/C_e \sim e/C_q$, conducting locally to $C_e \sim C_q$.

Hence, the equivalent C_μ capacitance of the junction is $1/C_\mu = 2/C_q$, with an energy degeneracy of $e^2/C_\mu = 2e^2/C_q$, where 2 is accounted as g_e in the formulation of $\nu = g_e G_0/C_q$ concept, as stated in Eq. 5.5 (BUENO, 2023c). This energy degeneracy is equivalent to the previous electrical current degeneracy consideration of the origin of g_e because $1/C_\mu = 2/C_q$ implies $C_q = 2C_\mu$. Noting that the capacitance of the interface is a result of the equivalent contribution of C_e and C_q, there is an electric current degeneracy for charging the quantum capacitive states of the interface that is proportional to C_μ with an electric current of $i_0 = C_\mu s = (1/2)(C_q)s$, which is equivalent to $2i_0 = C_q s$, where $s = dV/dt$ is the time-dependent potential perturbation (scan rate) imposed to the interface to investigate the energy $E = e^2/C_q$ level, electronically coupled to the electrode states. Note that it is owing to the equivalence of e^2/C_e and e^2/C_q energy states that

there is an energy degeneracy that inherently permits two electric currents contributing to the net (electrons and holes) current i_0 of the interface, which is thus said to be a ambipolar electric current.

The next section will introduce how the above concepts permit us to establish a low-energy electrodynamics that allows us to spectroscopically measure (in an electrolyte and room temperature environment) the electronic structure of ensembles attached to an electrode.

5.3.2 Quantum Rate Spectroscopic: Method and Principles

Spectroscopic methods based on $\nu = E/h$ phenomenon within Eq. 7.1 are well-known. The 'novelty' brought by the quantum rate theory is noting that a spectroscopic method can be applied if the quantum capacitance C_q is experimentally accessible at super or extremely low-frequencies, where the electronic communication with the quantum states of the QDs can be established using a perturbation imposed by the electrode that serves as a probe or a frequency source for a spectroscopic method based on this principle. This can be achieved in a range of super or extremely low frequencies ν, and communication with the quantum energy states of the QDs is possible owing to the electronic coupling of the QD states with those of the electrode within an electrolyte environment. The electronic coupling κ can be of different natures and intensities, according to the chemical way of coupling the moieties – molecules or QDs, for instance – to the electrodes, but it will allows a rate frequency such as $\nu = \kappa E/h$ to measurable and hence the QRS method will apply, as will be demonstrated further here.

Note that $E = h\nu$ has a particular setting in this spectroscopic methodology, where the energy E of the accessible states is related to the quantum capacitive C_q (BUENO; MIRANDA, 2016) states of the QDs such as $E \propto e^2/C_q$ and ν is the quantum rate, i.e., the rate (the inverse of the characteristic time constant) at which the E states of the QDs are communicating with those of the electrode.

Equivalently to the case of graphene (LOPES et al., 2024), the information about the QD electronic density of states is accessible through the measurement of the quantum capacitance C_q (BUENO; DAVIS, 2020; BUENO; MIRANDA, 2016) in an electrochemical experimental setting without requiring high-vacuum or low-temperature conditions such

as those required in the case of STM/STS method, for instance. Note that C_q directly reports on the density of states DOS $= C_q/e^2 = (dn/dE)$ of the molecular compounds assemblies over the electrode. Nonetheless, the presence of an electrolyte is vital because it allows the suppression of the Coulomb effect (PINZON et al., 2022) and permits the direct measurement of C_q of the QDs, as will be demonstrated below. This QRS methodology allows us to define the rate at which the states of the QDs communicate with the electrode owing to an electric-field perturbation of the QD states through the electrode. Theoretically, this quantum rate can be equivalently defined as the ratio between the quantum of conductance G and the electrochemical capacitance C_μ as, given by (FELICIANO; BUENO, 2020a; BUENO, 2023c; BUENO, 2018d)

$$\nu = \frac{G}{C_\mu} = g_s \frac{e^2}{h} \sum_{n=1}^{N} T_n(\mu) \left(\frac{1}{C_e} + \frac{1}{C_q} \right), \tag{5.4}$$

where $G = g_s(e^2/h) \sum_{n=1}^{N} T_n(\mu)$, with g_s as the spin degeneracy of the electron (thus taking a value of 2) and e as the elementary charge of the electron. The term $\sum_{n=1}^{N} T_n(\mu)$ of G represents the electron transmission probability through n individual quantum channels communicating with the QDs by an energy perturbation imposed by the electrode owing to the modulation of the electric field, stating for a function that models the nature and strength of the electron coupling of the QD states with the electrode.

Whenever the transmittance of the information from the electrode to the QD states and *vice-and-versa* occurs in the ideal (adiabatic) mode, i.e., particularly when $\sum_{n=1}^{N} T_n(\mu)$ is unitary (meaning that the communication between the electrode and the QDs occurs adiabatically), the conductance G is maximum and so it allows quantum mechanics to operates with particular settings such as G equal to the conductance quantum $G_0 = g_s(e^2/h) \sim 77{,}5$ μS(BUENO, 2020), meaning that the transport or the transmittance operates adiabatically.

Particularly, C_μ, in Eq. 5.4, is defined as the series combination of two capacitive contribution as given by $1/C_\mu = 1/C_e + 1/C_q$ (see Eq. 5.4), where C_e is the electrostatic contribution associated with the spatial separation of charge due to Coulomb's interactions and thus depends on the geometric features, and C_q is the quantum-mechanical contribution related to the energy related to the work required for

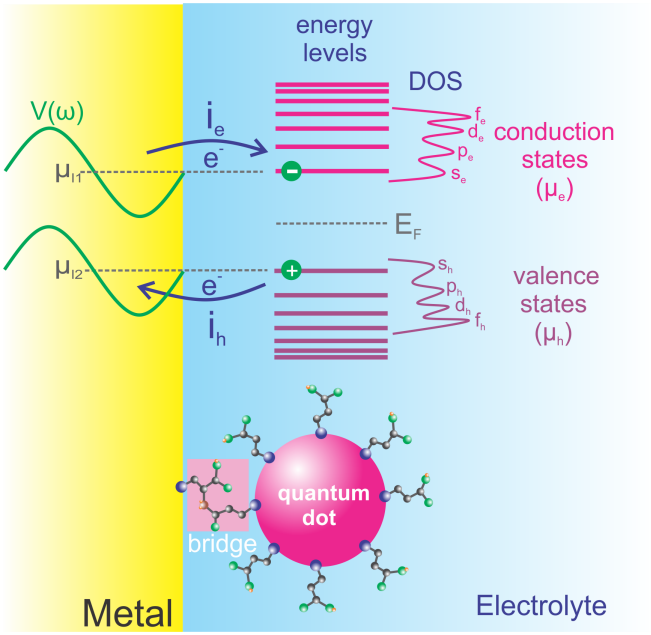

FIGURE 5.3. Schematic representation of a semiconducting dot structure contacted to a gold electrode through an L-cysteine self-assembled monolayer. This interface is embedded into an electrolytic medium where the electron communication with a rate ν occurs from the electrode to the QD (upper picture) and *vice-versa* (bottom picture) under a sinusoidal electric field perturbation from the electrode. This perturbation allows the measurement of the resonance electric current between the electrode states and the discrete energy states of the QDs. The resonant electric current is due to electron (i_e) and hole (i_h) charge carriers.

the occupancy of the quantum states (see Fig. 5.3)(BUENO; DAVIS, 2020) defined as $1/C_q = 1/e^2(1/(dN/d\mu)_l + 1/(dN/d\mu)_r)$. Note that in the definition of C_q, $(dN/d\mu)_l$ corresponds to the DOS of the metal electrode and $(dN/d\mu)_r$ to the DOS of the low-dimensional QD structures. Furthermore, the DOS of the metallic side of the junction is hundreds of times higher in magnitude than that of the QDs, i.e. $1/(dN/d\mu)_l$ and, therefore, C_q measured in this interface is directly proportional to $e^2(dN/d\mu)_r$(BUENO; DAVIS, 2014b), i.e. to the DOS of the QD structures assembled at the interface of the electrode is serving as the spectroscopic probe.

Finally, the presence of an electrolyte (Fig. 5.3) containing counter-ions contributing to electric-field screening is required for experimental measurements and permits the crucial approximation ($C_e \sim C_q$) (PINZON et al., 2021) to be stated in Eq. 5.4, enabling QRS to be a suitable methodology for measuring the DOS of QDs. Therefore, the approximation $C_e \sim C_q$ in Eq. 5.4 implies an energy degeneracy, as discussed in section 5.3.1. Therefore, analyzing Eq. 5.4 under the situation of modeling an adiabatic single electron

transport within the degeneracy of the states consideration, it can be experimentally evidenced that the electrolyte environment (PINZON et al., 2022) plays a key role for the degeneracy condition, where it is noted a superposition of C_e and C_q capacitive states owing to an appropriate electric-field screening mechanism of the electrolyte (BUENO, 2023c). These two superimposed capacitive states implying that the electron charge is shared between two capacitive states (classical and quantum) within the same electric potential, i.e. $e/C_e \sim e/C_q$, conducting locally (which can be either redox sites undergoing electron transfer reaction (BUENO, 2023c) or electronic states in organic semiconductor compounds) to $C_e \sim C_q$ in Eq. 5.4. Hence, the equivalent C_μ capacitance, in this situation, is set as $1/C_\mu = 2/C_q$ in Eq. 5.4, a state that is interpreted as an additional degeneracy of energy (besides that of the spin of the electron) owing to $e^2/C_\mu = 2e^2/C_q$, where 2 is accounted as the g_e contribution in the formulation of rate $k = G_0/C_\mu$ that reduces to (ALARCÓN et al., 2021b)

$$\nu = g_s g_e \left(\frac{e^2}{hC_q}\right) = g_e \left(\frac{G_0}{C_q}\right) = g_s g_e \left(\frac{E}{h}\right), \tag{5.5}$$

Eq. 5.5 was successfully verified by experiments and theoretically demonstrated to comply with diffusionless ET dynamics of redox reactions (ALARCÓN et al., 2021b), also with the electrodynamics and molecular electronics of organic semiconductor compounds (PINZON et al., 2023) and with the relativistic electrodynamics of graphene (BUENO; MERCADO, 2022). Note that origin of g_e was introduced in the previous section and does not requires further additional analysis.

These energy and electric current degeneracies imply that the electric current is ambivalent, as is the case of redox reaction dynamics (BUENO, 2023c) and the quantum electrodynamics of organic semiconducting compounds and graphene (BUENO; MERCADO, 2022). The implication that the ambivalent electric current phenomenon is equivalently observed in organic semiconductor compounds (as will be demonstrated further) and graphene (BUENO; MERCADO, 2022) is owing to the quantum rate theory being applicable despite the existence of redox reaction, but with the presence of ambivalent electric current. For instance, in graphene, there are negative and positive charge carrier concentrations within a two-dimensional structure that conforms with electron and holes representation (LOPES et al., 2021) that are, in ET reaction processes, associated with

oxidation and reduction currents, which is well-known and referred to as faradaic current.

In other words, Eq. 5.5 implies only the consideration of additional g_e degeneracy besides g_s in the heterogeneous electron transport rate mechanism stated by Eq. 5.4. Note that for the specific case of molecular electronics, there is an adiabatic transport of a single electron (that conforms with ballistic electrodynamics) with the meaning that G, in Eq. 5.4, is equivalent to $G_0 = g_s e^2/h$. This boundary condition implies simply considering a single adiabatic electron transport ideal situation in which $\sum_{n=1}^{N} T_n(\mu) = N\exp(-\beta L) = N\kappa \sim 1$, or a non-adiabatic situation in which $\nu = \kappa g_e G_0/C_q$, with κ explicitly considered in the expression of ν. Note that κ in $\nu = \kappa g_e G_0/C_q$ implies the consideration of a non-adiabatic electron transport which is modeled as taking κ lower than unity, but higher than null for electron transmittance to occur. Therefore, the only differences between the dynamics existing in electrochemistry reactions and that of electron resonant transport within push-pull semiconducting compounds are regarding the adiabatic (for push-pull dynamics) or non-adiabatic (for redox reactions dynamics) settings, but both electrodynamics, follows a relativistic character as is predicted by the quantum rate model depicted in Eq. 5.5.

In adiabatic or non-adiabatic situations, it has been demonstrated experimentally that the charge transfer resistance is equivalent to the resistance quantum $R_q = 1/G_0 = h/g_s e^2 \sim 12.9\ \mathrm{k\Omega}$, which experimentally validates the quantum rate theory (SANCHEZ et al., 2022) in both situations of ET or ballistic transport of electrons. The demonstration of a quantum limit value of R_q for the transport of electrons is achievable because κ (for non-adiabatic processes) can be experimentally measured as well as the number of channel N that is obtained from the measurement of C_q (SANCHEZ et al., 2022). Therefore, besides quantum rate theory (BUENO, 2020; BUENO, 2023c; BUENO, 2018d) encompasses other electron transport models and approaches such as that developed by Marcus (MARCUS, 1964b; MARCUS; SUTIN, 1985b; MARCUS, 1993), the advantage of the quantum rate theory consists in its easy experimental test and applications owing to all the fundamental parameters of the theory are measurable.

Particularly, the fulfilment of the $C_e \sim C_q$ condition permits a direct correlation between G and C_q through ν, where ν is related to the characteristic time-scale τ, such as $\nu = 1/\tau$(BUENO; DAVIS, 2020) (see Eq. 6.15). This energy degeneracy state (imposed by

the presence of an electrolyte) corresponds to a particular setting of Eq. 7.1 (see Eq. 5.5) and permits the study of the electronic structure of low-dimensional materials at room temperature without the need for ultra-high vacuum, hence not only constituting the requirement for the QRS methodology but also making this method advantageous. This fundamental basis of QRS can be established by noting that $\nu = E/h = e^2/hC_q$, where the only variable to be measured is C_q. Since C_q can be obtained by electronic spectroscopy means, as described in detail in the experimental section through Eq. 6.15, QRS is quite simple experimentally, although it does require a careful assembly and contact of the QDs to the probe electrode.

To resolve any questions related to the principles of a spectroscopic method based on the quantum-rate concept, defined in Eq. 5.5, let us demonstrate the correspondence between the duality particle $E = e^2/C_q$ (or $\mathbf{p}$) and $\mathbf{k}$ (ω) wave of the electron whenever there is a time-dependent perturbation on C_q that corresponds to a coherent response of $\mathbf{k}$ and *vice-versa*. Hence, $C_q = e^2(dn/dE)$ can be rewritten as

$$\left(\frac{dE}{dn}\right) = \frac{e^2}{C_q}, \tag{5.6}$$

where $e^2/C_q = \hbar\mathbf{c}_* \cdot \mathbf{k} = E$ is the energy associated with C_q, according to Eq. 7.2 and premises of the quantum-rate theory. Evidently, $dE = \hbar\mathbf{c}_* \cdot \mathbf{k}dn$ and a time perturbation in E corresponds to a time perturbation of $n = q/e = L/\lambda$ (where L is the length of the quantum channel and λ the wave length associated to this length within n as an integer quantum number) such that

$$\left(\frac{dE}{dt}\right) = \hbar\mathbf{c}_* \cdot \mathbf{k}\left(\frac{dn}{dt}\right), \tag{5.7}$$

where E and n are the only time-dependent variables; $dE/dt = E(t)$ and $dn/dt = n(t)$. Therefore, an energy perturbation $E(t)$ of a quantum RC system as a function of time corresponds to a coherent response of quantum RC states $n(t)$ as a function of time. These time-dependent and related functions can be stated as $E(t) = \bar{E} + \tilde{E}$ and $n(t) = \bar{n} + \tilde{n}$, respectively, where $\tilde{E} = E_0 \exp(j\omega t)$ and $\tilde{n} = n_0 \exp(j\omega t - \phi)$ are the oscillatory perturbation of E and the corresponding oscillatory response of n to a defined E perturbation.

E_0 and n_0 are the amplitudes of the energy perturbation of the quantum RC state response, respectively, and ϕ is the coherent phase difference between energy perturbation and quantum RC state response. $\bar{E}$ and $\bar{n}$ denote steady-state levels of the system where the oscillatory perturbation is performed.

The aforedescribed analysis shows that $E(t) = E_0 \exp(j\omega t)$ and $n(t) = n_0 \exp(j\omega t - \phi)$ allows defining a complex $E^*(\omega)$ energy state function such as

$$E^*(\omega) = \left[\frac{dE(t)}{dn(t)}\right] = \left(\frac{E_0}{n_0}\right) \exp(j\phi), \tag{5.8}$$

wherein the real component of $E^*(\omega)$ is identified as

$$\Re\left[E^*(\omega)\right] = \left(\frac{E_0}{n_0}\right) \Re\left[\exp(j\phi)\right] = \hbar \mathbf{c}_* \cdot \mathbf{k}, \tag{5.9}$$

As discussed previously, if ω, in Eq. 6.19, is considered ω_0, there is a limit for the energy $E_0 = e^2/C_q^0$ that corresponds to a limit of Eq. 6.15 in which $e^2/n_0 C_q^0 = \hbar \mathbf{c}_* \cdot \mathbf{k}$. This previous analysis implies a correspondence between e^2/C_q^0 and $\hbar \mathbf{c}_* \cdot \mathbf{k}$ that allows for the measurement of the electronic structure of QDs *in-situ* by using an electric time-dependent method.

The mechanical statistics consideration of the QRS method will be considered in the next section.

5.3.3 The Thermal Broadening Analysis of the QRS Method

Since $C_q = e^2/E$ is a quantum variable obtained at room temperature (BUENO; MIRANDA, 2016; BUENO; MIRANDA, 2019), as is the case with optical spectroscopic methods, it requires additional statistical mechanical inputs to appropriately treat the experimental signal of C_q. Hence, we note that in Eq. 7.1, C_q was defined at the zero absolute temperature limit (BUENO et al., 2015) ($T \to 0$ K) and, therefore, a more realistic setting requires a finite-temperature treatment of the C_q measured at room temperature. This can be attained by considering the thermal broadening of the energy associated with C_q, i.e. $E = e^2/C_q$.

The appropriate statistical mechanics treatment for this is achieved by considering the grand-canonical ensemble (BUENO; MIRANDA, 2019; BUENO; MIRANDA, 2016) or more directly by using the Fermi-Dirac distribution function $f(eV) = [1 + \exp(-\beta eV)]^{-1}$ to compute the dynamical occupancy of C_q states coupled to the electrode at different potential energy levels of the electrode $-eV = \mu - E_F$, where $\beta = \alpha/k_B T$ and k_B is the Boltzmann constant. α is the only *ad-hoc* term that was introduced in this equation for modeling intrinsic inhomogeneities during the fitting of the experimental DOS peaks to this model (see Fig. 5.5). E_F is the Fermi level of the QDs electronically coupled to the electrode and μ is the chemical potential of the electrons perturbed in the probe electrode.

Considering that E_F is pinned, the changes in the potential level of the electrode are directly associated with the variations in μ owing to a V applied with respect to E_F (which is constant) such as that $d\mu = -edV$ is obeyed. Hence, the capacitance can be written as $C_q = dq/dV = e^2(dn/d\mu)$, where $dq = -edn$ is the charge variation due to $d\mu$ variations, where n is the number of electrons (or states) communicating between the electronically-coupled QDs ensemble and the electrode. By noting that $n = Nf$, where N is the total electron occupancy availability and $df/d\mu = f(1-f)$, a thermally broadened expression for C_q is obtained as (PINZON et al., 2021)

$$C_q = e^2 N \beta f(1-f), \tag{5.10}$$

where C_q, in Eq. 7.4, is a function that predicts the thermal broadening of energy $E = e^2/C_q$ and consequently of the DOS(BUENO; DAVIS, 2014b). This C_q function can be experimentally measured by the EIS method as described in the experimental section, particularly within the analysis of Eq. 6.15. Thus, it enables a methodology for interpreting the QR spectra peaks, as will be demonstrated in the next section for the measured spectra of the CdTe QDs structures.

Nonetheless, before continuing our analysis on the using of QRS for resolving the DOS of QDs structures, some practical concerns must be observed to ensure the accuracy and reliability of the results. The first is regarding the chemical or physical immobilization of the QDs over the probe electrode, which must be performed in a way that assures an appropriate electronic coupling and contact between electrode and QD states, allowing

electrical contact and the formation of an appropriate junction that enables electronic communication between the electrode and attached QDs.

Additionally, as QRS methodology is essentially based on electrochemistry, the chemical stability of the electrolyte must be a concern within the applied range of potential. Still regarding the properties of the electrolyte and the physical principles of QRS operation, as discussed in section 5.3.1, the ability to access the DOS of QD nanoscale assemblies through QRS is primarily attributed to the electrical field screening performed by the electrolyte over the charge of the quantum states. Hence, the concentration of the electrolyte used in the analysis is important for a suitable electric field screening. According to the previous works about the application of QRS methodology in graphene(LOPES et al., 2021), organic molecules(PINZON et al., 2023) and inorganic semiconducting nanofilms(PINZON et al., 2021), electrolyte concentrations typically ranges from 1 to 10 mM.

5.3.4 Resolving the DOS of Quantum Dot Assemblies

In this section, the usefulness of the QRS as a tool for revealing the electronic structure of low-dimensional assemblies (besides graphene (BUENO; MERCADO, 2022; LOPES et al., 2023)) is demonstrated by resolving the DOS function of a particular type of semiconducting QDs. Accordingly, CdTe QDs were assembled on a gold surface through a molecular bridge electronic coupling in order to follow the methodology described in the experimental section to study the electronic structure of a CdTe QDs ensemble using the QRS method (summarized in Fig. 5.2). C_q was obtained at the equilibrium potential(SUN et al., 2002; WANG et al., 2021), corresponding to the open circuit potential (OCP) of the interfaces (0.14 V *versus* Ag|AgCl). Hence, from QRS measurements, C_q was directly extracted using the capacitive Nyquist plot for which the diameter of the semi-circle corresponded to the value of C_q at equilibrium communication dynamics. In other words, the low-frequency limit of the capacitive spectra, corresponding to ($\omega \to 0$), as given by Fig. 5.2*b*, allowed to obtain the C_q values of 3.28 and 1.55 μF cm^{-2} for two different QDs assemblies with the average nano-particle sizes of 2.23 and 3.27 nm, respectively (see more details in SI.3)

To measure the DOS, the equilibrium frequency ω_0, as indicated in Fig. 5.4*b*, was kept constant and a potential scan (from negative to positive) was applied to record C_q

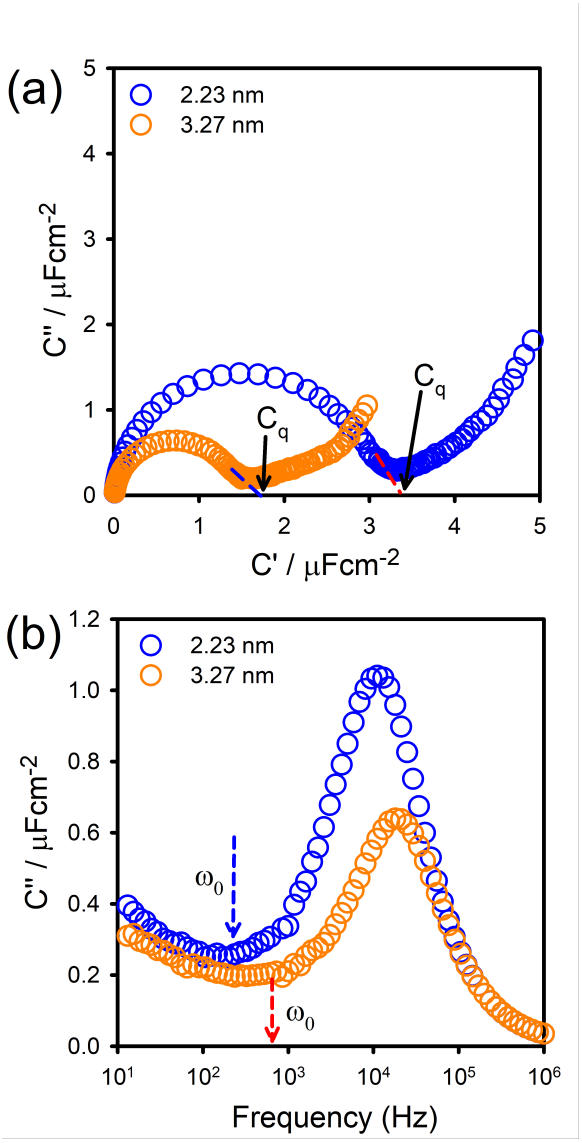

FIGURE 5.4. (a) Capacitive Nyquist diagrams recorded for different QDs assemblies with two mean-average particle sizes (in a phosphate buffer solution with a pH of 7.4 at the equilibrium potential). The C_q values for each of these assemblies were graphically obtained as the values of the semi-circle diameter, corresponding to two different equilibrium ω_0 frequencies as indicated in the (b) Bode plots using the imaginary capacitance component of the spectra for these two QD assemblies.

as a function of the electrode potential. It is important to emphasize that the DOS measurements[2] are independent of scan perturbation direction, as depicted in Figure S2 of the SI document. This independence of scan direction and history of potential perturbation is owing to QRS consisting of an ultra-low energy perturbation methodology and consequently, this small potential perturbation allows electronic communication between the

[2]Observe that there are some differences in the intensity of the peaks, but not in their potential positions.

electrode and QDs assemblies without affecting the stability of the electronic structure.

The DOS function ($C_q \propto$ DOS) is obtained based on the $C_e \sim C_q$ approximation of the capacitive contribution, according to discussions conducted in a particular experimental setting of Eq. 5.5, as discussed in the section 5.3.1. The C_q responses attained for the gold electrode and the L-cysteine monolayer in the absence of QDs are noteworthy. In the presence of QDs, as expected, the response is significantly distinct with regard to magnitude and shape, as can be noted in Figure S1 of the SI, demonstrating the successful immobilization of the QDs. The measurements, gold and L-cysteine, attained in the absence of the QDs serves as a baseline reference of the signal.

Two sets of Gaussian-like functions separated by a roughly linear response were identified for both QD assemblies, as shown in Fig. 5.5a and 5.5b. These responses were suitably fitted using the Eq. 7.4 (red and dark blue line in Fig. 5.5), indicating good agreement between the experiments and the quantum rate theory (the fit R-squared coefficient of determination was ~ 0.999). For an in-depth interpretation of the obtained DOS shape, it is important to recall the typical semiconducting QD electronic structures discussed in Fig. 5.1. This permits, in terms of quantum mechanical wave-function and atomic orbital representation, to note that the responses are correlated to symmetries that are referred to as s, p, d and so on (VANMAEKELBERGH; LILJEROTH, 2005).

Therefore, valence and conduction band states of QDs are identified, respectively, as s_h, p_h and s_e, p_e, where the subscript h denotes hole states whereas e refers to electron states. It is also important to highlight that for typical QD assemblies such as that depicted in Fig 5.3, individual QDs are weakly coupled to each other by van der Waals interactions owing to the capping molecules that separate the dots. Hence, the experimentally obtained Gaussian-like shape corresponds to the average response of the individual CdTe QDs in the ensemble(JDIRA et al., 2006) (see Fig. 5.5).

Accordingly, the Gaussian-like response corresponding to the most negative peak potential in Fig. 5.5 and assigned at a peak potential of $\sim$ -1.4 V, is ascribed to the s_h (HOMO) and p_h valence states. These states were identified by using a deconvolution process as described in detail in the SI. Moreover, for both QD assemblies, it is observed that trapping states denoted as E_t that are located in the band gap of the electronic structure are present near the conduction band edge. These trapping states on average

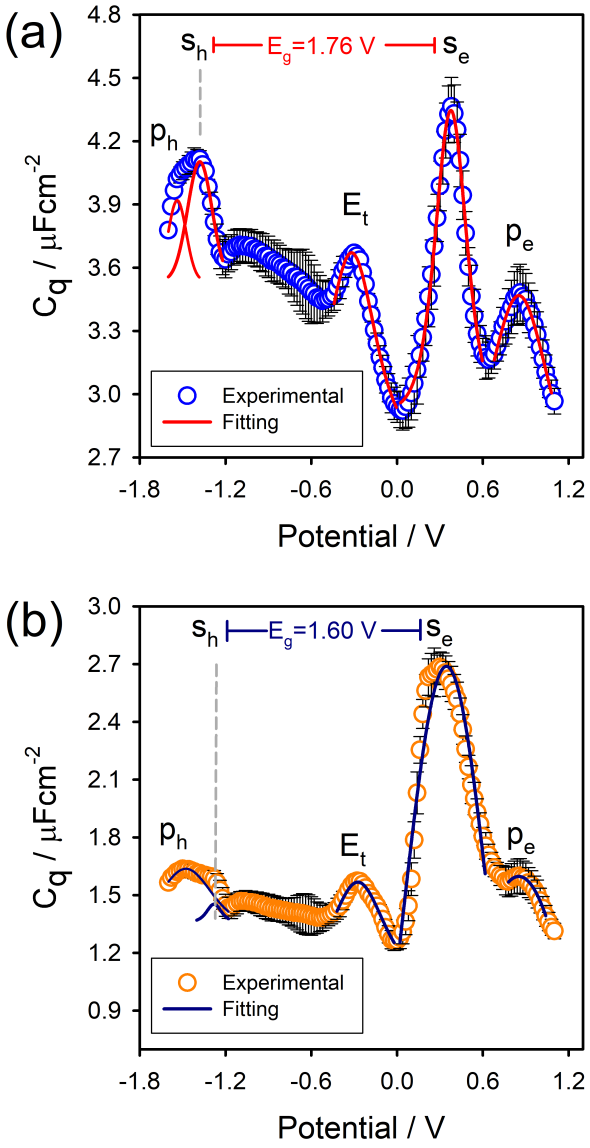

FIGURE 5.5. Electronic DOS resolved from the measurements of the quantum capacitance C_q for two different CdTe QDs assemblies with different nano-particle sizes, i.e. (a) 2.23 nm and (b) 3.27 nm. Each DOS plot is the average obtained for three independent QDs-interfaces and the error bar indicated the respective deviation. Potentials are reported *versus* Ag|AgCl (3M KCl) reference electrode.

have maximum population at -0.30 V and -0.28 V, respectively, for the 2.23 nm (a) and 3.27 nm (b) nano-particle sizes, as depicted in Fig. 5.5.

The presence of these trapping states was confirmed by independent photo-luminescence spectrum measurements that showed the presence of an additional emission besides the main peak expected in the photo-luminescence spectrum (as shown in

SI.5). Finally, the peaks observed at more positive potentials in Fig. 5.5 were ascribed to the conduction states s_e (LUMO) and p_e. The electronic structure measured here using the QRS approach is in agreement with the DOS obtained for the CdSe and PbSe QDs assemblies via STS(LILJEROTH et al., 2005; JDIRA et al., 2006).

For instance, in STS measurements, a potential difference is applied between a QDs-modified substrate and the microscope tip with the differences ascribed to the QDs electronic energy state levels within the electronic resonant (tunneling) currents established between the electrode-tip and QDs states with the transfer of electrons from the substrate (containing the assembly of QDs) to the tip or *vice-versa*. The conductance response, as function of the potential energy, is obtained through these electric currents, where two sets of Gaussian-like shapes are identified in the STS measurements that are ascribed to the valence and conduction states of the QDs. The conductance response profile obtained by STS is comparable to the response of C_q resolved by QRS (Fig. 5.5), demonstrating that both methodologies can access the electronic structure (DOS) of semiconducting QDs assemblies through a resonance electric response[3] established between the electronic states and the probe (respectively tip and electrode in these two comparable methods of resolving the electronic structure of QDs). However, the DOS resolved by STS requires the use of expensive equipment as well as low temperature (5 K) and ultra-high vacuum conditions, whereas the DOS resolved by QRS is obtained at mild experimental conditions (room temperature and atmospheric pressure) due to the charge screening performed by the ions in the solvent-electrolyte environment, as introduced previously, in association with the meaning of g_e.

Additionally, based on the QR spectra shown in Fig. 5.5, the band gap (E_g) energy can be estimated for these QD assemblies by calculating the differences between the s_h (HOMO) and s_e (LUMO) energy states. Hence, the band gap values of 1.76 and 1.60 eV were obtained for the QD assemblies with the mean particle sizes of 2.23 nm and 3.27 nm, respectively. The higher band gap obtained for the smaller QD indicates a greater quantum confinement effect, in agreement with the expected correlation between the semiconducting nanocrystals band gap and the nanoparticle size(JDIRA et al., 2006). Nevertheless, the band gap values estimated via the electrochemical QRS method are

[3]Note that in the case of QRS, the resonance electric response obtained from a conductance plot (see also Fig. 5.6) is associated to a resonance electric current denoted previously here as $i_0 \propto C_q$ electric current, which is ambipolar in nature.

significantly lower than those obtained by optical approaches based on the absorption spectra of the same QDs in a solution environment (2.50 and 2.24 eV), as noted in Table SI.1 of the SI document.

The discrepancy between these methods can be explained by considering that for a QDs solution, there are less interactions between the QDs and the surrounding environment such as the electrode and capping molecules. Therefore, in the QRS method, the requirement for the attachment of QDs to the probe surface can be a source of errors in the quantitative estimation of the band gap energy. The electronic interaction between adjacent QDs in the assembly is noted when there exists a coupling of the electronic states between the adjacent QDs which is known as the quantum resonance phenomena between the dots (LEE et al., 2020; KIM, 2015). This phenomenon has been commonly observed in assemblies of QDs with short-chain capping molecules and short separation (less than 2 nm) between the neighboring QDs, such as the assembly of CdTe QDs capped by MPA-molecules (chain-length of 0.7 nm) studied here. Accordingly, the electronic coupling and communication between nearby QDs directly impacts the electronic properties of the assemblies, so that the values of the band gaps are smaller than for the condition of non-interacting QDs. These are the sources of errors or differences between the methodologies. It is clear that in the QR spectroscopic method, the preparation of the sample (assembly on the substrate) is important; however, this problem can be overcome by designing an experimental set-up in which the assembly will be molecularly coupled to the probe (electrode) in a suitably 'diluted' way (with a reasonable distance established between adjacent QD moieties).

As shown in Figure 5.5, each data point in the C_q response represents the average value obtained from measurements performed on three independent QD interfaces. The error bars indicate deviations, which are quite small. Specifically, for the nanoparticle size of 2.23 nm, the magnitude for each QD size assembly varies from $1{,}92 \times 10^{-8}$ to $1{,}34 \times 10^{-7}$ μF cm^{-2}, and for the nanoparticle size of 3.27 nm, it varies from $0{,}81 \times 10^{-8}$ to $1{,}26 \times 10^{-7}$ μF cm^{-2}. These deviations are one or two orders of magnitude lower than the average value of the C_q response. Therefore, this methodology allows for reproducible measurements between electrodes, demonstrating its potential as a faster and simpler tool for accessing the electronic structure of nanoscale assemblies in general.

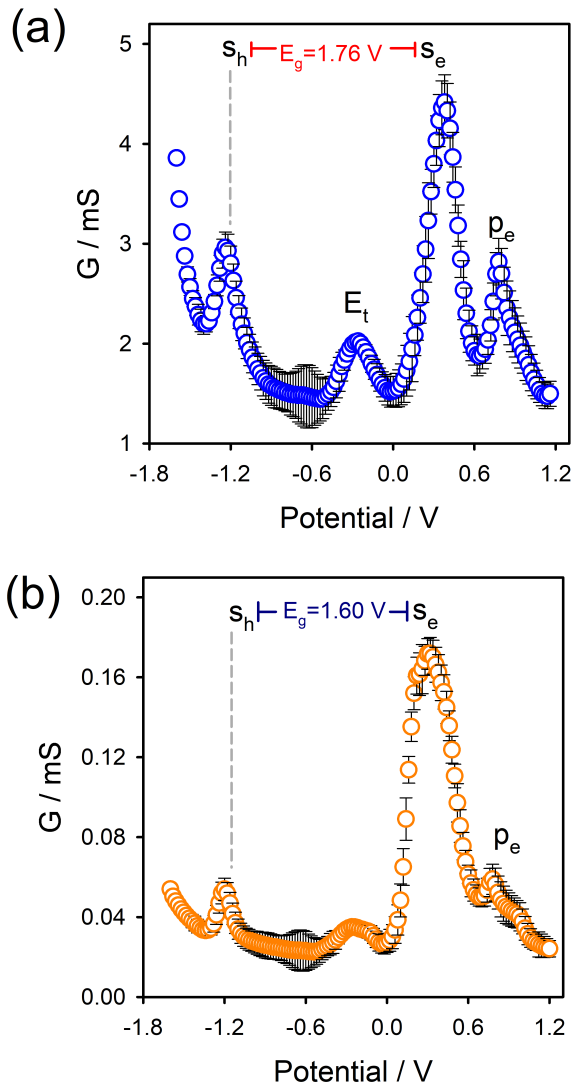

FIGURE 5.6. Electronic DOS resolved from quantum conductance for two assemblies of CdTe QDs with different nanoparticle sizes of (a) 2.23 nm and (b) 3.27 nm. Each plot represents the average obtained from of the measurements over three independent electrodes and the error bar indicate their respective deviation. Potentials are reported *versus* Ag|AgCl (3M KCl) reference electrode.

Finally, it is important to note that according to Eq. 5.5, there exists a relationship between G and C_q through the rate ν. This permits the construction of alternative methods for analyzing QRS spectra and validating the method. Therefore, due to this $\nu = G/C_q$ relationship, G can be alternatively utilized to obtain information regarding the electronic structure of QDs. For instance, G can be obtained as $G = \omega C''$ and a potential scan of G at a fixed ω_0 allows us to deduce the electronic structure and DOS pattern of the QDs similarly to using the C_q signal of the response. Accordingly, following

this reasoning, G was obtained as a function of the potential, as depicted in Fig. 5.6. As expected, the $G - V$ pattern has a similar profile to that obtained for $C_q - V$ (Fig. 5.5). In summary, the obtained G spectra confirmed the theory underlying the proposed QRS methodology and validated the method.

5.4 Conclusions

Electronic structures of assemblies of CdTe quantum dots were experimentally resolved from the measurements of the responses of the quantum capacitance C_q and conductance G using the quantum rate spectroscopic methodology in mild experimental conditions of ambient temperature and pressure in the presence of an electrolyte ambient. The methodology is based on the principles of quantum rate theory, as introduced in Eq. 7.1, and is a novel tool that permits easier access to the information about the electronic structure of nanoscale materials, making it useful to the fields of physics, chemistry, nanoscience and nanotechnology. The results obtained for the specific case of CdTe quantum dots constitute an additional proof-of-concept of this spectroscopic methodology besides its use for measuring the electronic structure of graphene, as demonstrated previously (LOPES et al., 2024); hence, this method is not restricted to zero- or two-dimensional structures and can be also applied for the characterization different nanoscale structures of interest in different material science and chemistry fields.

Author Contributions

Edgar Fabian Pinzón Nieto: Methodology, Investigation, Visualization. **Laís Cristine Lopes**: Methodology, Investigation, Visualization. **André Fonseca**: Methodology, Investigation, Visualization. **Marco Antonio Schiavon**: Methodology, Investigation, Visualization. **Paulo Roberto Bueno**: Conceptualization, Supervision, Resources, Methodology, Writing - Original draft.

Conflicts of interest

There are no conflicts to declare.

Acknowledgements

This work was supported by the Sao Paulo State Research Funding Agency (FAPESP) grants 2018/24545-9 and 2017/24839-0. The authors also acknowledge the support of the National Council for Scientific and Technological Development (CNPq) and Minas Gerais Research Funding Agency (FAPEMIG) for the grant PPM-00690-18.

Chapter 6

Electrochemical Measurement of the Electronic Structure of Graphene by Quantum Mechanical Rate Spectroscopy

Laís Cristine Lopes,[a] Edgar Fabian Pinzón,[a] Gabriela Dias-da-Silva,[a] Gustavo Troiano Feliciano,[a] & Paulo Roberto Bueno,*[a]

[a] *Departmnet of Engineering, Physics and Mathematics, Institute of Chemistry, São Paulo State University, Rua Francisco Degni, 55 - Araraquara, Sao Paulo, Brazil*

Keywords: quantum rate spectroscopy, graphene electronic structure, quantum capacitance, density-of-state, conductance quantum, density-functional theory

Journal: Electrochimica Acta, 480, 143837 (2024)

DOI: https://doi.org/10.1016/j.electacta.2024.143837

Abstract

The quantum-rate theory defines a quantum mechanical rate ν concept that complies with the Planck-Einstein relationship $E = h\nu$, where $\nu = e^2/hC_q$ is a frequency associated with the quantum capacitance C_q and $E = e^2/C_q$ is the energy associated to ν. This ν concept was successfully employed to define a quantum mechanical meaning for the electron-transfer (ET) rate constant of redox reactions, where faradaic electric currents

involved with ET reactions were demonstrated to be governed by relativistic quantum electrodynamics at room temperature. In the present work, it will be demonstrated that the definition of ν implies relativistic quantum electrodynamics intrinsically related to the way with which the density-of-states $(dn/dE) = C_q/e^2$ is perturbed by an external harmonic oscillatory potential energy variation, permitting to calculate the electronic structure of graphene embedded in an electrolyte environment. The electronic structure measured by quantum-rate spectroscopy (QRS) is in good agreement with that measured by angle-resolved photo-emission spectroscopy (ARPES) or calculated by computational density-functional theory (DFT) methods. The experimental advantage of the electrochemical QRS over ARPES is obvious. QRS permits to obtain the electronic structure of graphene at room temperature and electrolyte environment, whereas ARPES requires low temperature and ultra-high vacuum conditions. Furthermore, QRS can be operated *in-situ* using a held-hand inexpensive piece of equipment, whereas ARPES cannot besides requires costly apparatus.

6.1 Introduction

The quantum-rate concept (BUENO, 2018d; BUENO, 2020) is straightforwardly introduced here. For a more extensively analysis of this concept, it is recommended to study its applications to the field of electrochemical reactions, as it was detailed in reference (BUENO, 2023c), where more in-depth details can be obtained about how this rate concept reports on the electrodynamics of electron-transfer reactions. Furthermore, for the particular case of the application of the quantum-rate theory and a ν quantum-rate concept to graphene, there is also a dedicated reference to this topic (BUENO; MERCADO, 2022). The present work is focused on the uses of this concept as a tool for the *in-situ* measurement of the electronic structure of graphene.

6.1.1 Quantum Mechanical Rate

Quantum-rate theory (BUENO, 2023a; BUENO, 2023b) is based on a first-principle quantum mechanical rate concept that is defined as the ratio between the reciprocal of the von Klitzing constant $h/e^2 \sim 25.8$ kΩ and the quantum capacitance such as

$$\nu = \frac{e^2}{hC_q} = \frac{E}{h}, \tag{6.1}$$

where e is the elementary charge of the electron, h is Planck constant and C_q is the quantum capacitance, where $E = e^2/C_q$ is the energy state of a single electron in a single quantum channel with Fermi velocity c_*. Therefore, this ν concept permits to establishment a direct correlation with the relativistic electron transport occurring in between quantum states within and between molecules.

Note that this type of electrodynamics is totally different of the classical transport of electrons because it predicts that the transport of electrons is in between quantum states connected by quantum channels. Furthermore, the velocity with which charge carriers are transported besides of be coherent with a time-dependent potential source perturbation is associated with the Fermi velocity. Hence this type of transport of charge is not related to the traditional drift velocity of electrons, for instance, obtained for describing the electric current in metallic structures. The latter transport of carriers within molecular structures implies relativistic eletrodynamics where an external electric potential perturbation is the origin of a coherent transport in such a way that the charge transport between quantum states is in phase coherence with electronic structure, which can be measured by measuring C_q at a particular low-frequency equilibrium perturbation ω_0, as will be further discussed.

6.1.2 Relativistic Electrodynamics

The relativistic electrodynamics within Eq. 7.1, that is $E = h\nu = e^2/C_q$, as the relationship between energy e^2/C_q of the electronic structure and a frequency ν with which it can be perturbed, combined with the De Broglie relationship $\mathbf{p} = \hbar\mathbf{k}$ of particle-wave duality, implies a relativistic quantum electrodynamics of charged particles within the electronic structure (that can be quantified through its quantum capacitance C_q) owing to the linear proportionality between the energy and wave-vector $\mathbf{k}$ such as

$$E = \hbar\mathbf{c}_* \cdot \mathbf{k} = \mathbf{p} \cdot \mathbf{c}_*, \tag{6.2}$$

where $\hbar$, in Eq. 7.2, is h divided by 2π. The intrinsic relativistic nature of Eq. 7.2 implies that electron spin degeneracy is important to be considered in the electrodynamics.

In the next section, it will be demonstrated that with the consideration of the spin degeneracy g_s combined with C_q, it permits us to definite a ν concept for describing

the relativistic quantum electrodynamics. It is owing to a phase coherence between the relativistic quantum transport of charge and C_q that it is permitted to obtain information on the electronic structure.

6.1.3 Spin Energy State Degeneracy and Conductance Quantum

To consider electron spin degeneracy g_s in the definition of ν, the energy of the electronic structure is written as $E = g_s e^2/C_q$ and hence Eq. 7.1 turns into

$$\nu = \frac{g_s e^2}{hC_q} = \frac{G_0}{C_q}, \tag{6.3}$$

where $G_0 = g_s e^2/h$ is identified as the conductance quantum, which is a constant of magnitude of ~ 77.5 μS. Note that $R_q = 1/G_0$ is a resistive quantum limit of ~ 12.9 kΩ.

In summary, the introduction of the spin degeneracy implies a characteristic quantum resistive-capacitive (RC) time constant $\tau = R_q C_q = 1/\nu$ that depends only on the meaning of C_q to be settled with a phase coherence that can be experimentally resolved by electric time-dependent perturbation methods. As will be shown further, the analysis of the quantum RC circuit for graphene permits to reveal its the electronic structure and hence the energy of the wave and the associated particle dynamics, permitting to measure the electronic structure by measuring the quantum characteristic τ of the system.

6.1.4 A Three-dimensional Analysis of Graphene Momentum

In a previous work it was demonstrated the meaning of the quantum rate specifically for 2D graphene structures where $\mathbf{k}$ was considered to be three-dimensional. This was required to decouple the space and time dependence of the bispinors for resolving the Dirac equation considering considering $\varphi_e = e^{-j\omega_e t}\psi_e$ and $\varphi_h = e^{j\omega_h t}\psi_h$, where $\hbar\omega_e = E_e - eV_{ch} + m_c c_*^2$ were considered for electrons and $\hbar\omega_h = -E_h + eV_{ch} + m_c c_*^2$ for hole carries. It was supposed that the time perturbation of the external potential V_t is much lower than E_e/e and E_h/e, which is a good approximation for interpreting the impedance-derived capacitance spectra for graphene. Note that this was the constraint imposed to solve the Dirac equation. The solution of the equation conducted to the Helmholtz equation as the solution, such as

$$\nabla^2\psi + |\mathbf{k}|^2\psi = 0, \tag{6.4}$$

where the wavevector $|\mathbf{k}|$ is resolved as a space variable separate from the time such as

$$|\mathbf{k}| = \left(\frac{E_e E_h}{c_*^2\hbar^2}\right)^{1/2}, \tag{6.5}$$

which encompasses both the relativistic and non-relativistic energy-wave vector dispersion relationship. For instance, note that if we consider the symmetry of electrons and holes in graphene with respect to the Dirac point, it can be stated that $E_e = E_h = E$ and the dispersion relationship in Eq. 6.5 conforms to $E = \hbar c_*|\mathbf{k}|$, in agreement with that predicted using the quantum rate theory, as discussed in the introduction section, where $E = \hbar c_*|\mathbf{k}| = h\nu$, with $k = 1/\tau$ as the quantum rate.

The most important result that arises from a 3D interpretation of the graphene structure is that we can consider the effect of an external potential V perturbation in the spinor ψ, such as that the effect of a V stimulus in the plane $x - y$ can be measured by a perturbation in the z direction. This is owing to the fact that mathematically the plane $x - y$ can be modelled separately from the perpendicular z direction. The latter can be observed by invoking symmetry properties of the spinor ψ and the quantum rate can be spatially interpreted within the spatial quantum electrodynamics setting of Eq. 6.4.

For instance, consider $\psi(x, y, z) = \phi(x, y)\zeta(z)$ in such a way that we set $\zeta(z) = \zeta_0 \sin(k_z z)$ and $\phi(x, y) = \phi_0 \sin(|\mathbf{k}|_x x + |\mathbf{k}|_y y)$, where $|\mathbf{k}|_x^2 + |\mathbf{k}|_y^2 + |\mathbf{k}|_z^2 = |\mathbf{k}|^2 = E_e E_h/(c_*\hbar)^2$. This interpretation allows us to impose boundary conditions for a 2D SLG, permitting us to use the quantisation mode that obeys $|\mathbf{k}|_z = 2\pi n_\nu/L_z$, where L_z is the thickness of the SLG and n_ν is a non-zero natural number associated with the quantum number (or quantum channel) modes for charge motion in the z direction perpendicular to the $x - y$ plane of graphene and with a time t_z corresponding to the characteristic relaxation time for the transport of charge carriers within the thickness L_z such that $L_z = c_* t_z$ with $\tau_z = t_z/2\pi$ and $|\mathbf{k}|_z = n/c_*\tau_z$.

Observe that a charge perturbation transversal to the $x - y$ plane of conductance in graphene, according to $\zeta(z)$, describes a stationary harmonic motion perturbation that

propagates as a wave in the $x-y$ plane of graphene at a velocity c_*, promoting a charge flowing as a displacement current in the z-direction, which is coupled to the $x-y$ plane. The induced displacement electric current is established by externally perturbing the system using an oscillatory electric potential perturbation, allowing us to measure the $x-y$ DOS property of graphene by imposing an oscillatory perturbation in the thickness.

6.1.5 Quantum Capacitance in a Relativistic Situation

A quantum capacitance C_q can be associated with relativistic dynamics by noting that frequency $\nu = (E/h) = (c_*/L_z)$ can be directly correlated with the L_z length of graphene and $E = e^2/C_q$. The quantum channels of the electronic structure of graphene permit the relativistic transport of charge carriers, such as electrons and holes, owing to $\nu = (c_*/L_z)$, which directly provides the energy of the channel through the Planck constant and hence it is dependent of C_q. The above analysis implies that $L_z = n\lambda$, where n is the number of quantum states within L_z and λ is the wavelength directly related to $|\mathbf{k}| = 2\pi/\lambda$, where $|\mathbf{k}|$ is the modulus of the wave-vector $\mathbf{k}$.

Accordingly, the energy can be written as a function of the number of states (or quantum channels) $n = L_z/\lambda$ such as $E = nh\,(c_*/\lambda) = n\,(h\nu)$, where $E = h\,(c_*/\lambda) = h\nu$ is the energy e^2/C_q of a single state. Hence, the density-of-states (DOS) can be obtained simply as $(dn/dE) = C_q/e^2$, and the quantum capacitance is thus defined as

$$C_q = e^2 \left(\frac{dn}{dE} \right), \tag{6.6}$$

from where it can be noted that C_q is directly proportional to the DOS.

In the next section, it will be defined the DOS and the quantum capacitance of graphene, as well as the characteristic time constant associated with a coherent transport of carriers with the electronic structure defined by C_q.

6.1.6 The 2D Density-of-States of Graphene

The relativistic quantum dynamics of Eq. 7.2 permits to define $E/\mathbf{k}_{x-y} = dE/d\mathbf{k}_{x-y} = \hbar c_*$ in the $x-y$ plane of graphene, as depicted in Figure 6.1, where $|\mathbf{k}|_{x-y} = (|\mathbf{k}_x| + |\mathbf{k}_y|)^{1/2}$ is the modulus of the resultant wave-vector. The number of

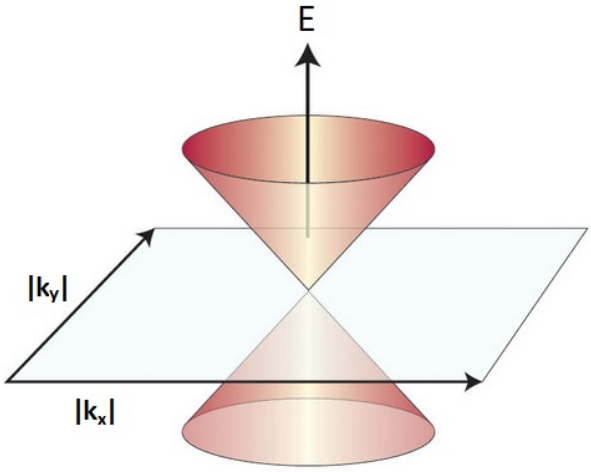

FIGURE 6.1. Representation of the the relativistic quantum electrodynamics $E(\mathbf{k}) = \hbar \mathbf{c}_* \cdot \mathbf{k}$ of graphene, where for the $x-y$ plane of graphene, the modulus of $|\mathbf{k}|_{x-y}$ is given by $(|\mathbf{k}_x| + |\mathbf{k}_y|)^{1/2}$. In the quantum-rate theory of graphene, the conductance in the x and y directions are quantized by the integer number of the conductance quantum G_0 as well as the rate ν.

states $\mathrm{n}(\mathbf{k}_{x-y})\mathrm{d}\mathbf{k}_{x-y}$, accounted in the $k-$space, per differential interval of $\mathrm{d}\mathbf{k}_{x-y}$ in the $x-y$ plane of graphene, can be expressed as (NETO et al., 2009)

$$n\left(\mathbf{k}_{x-y}\right) d\mathbf{k}_{x-y} = g_s g_v \frac{A}{2\pi}\left[\frac{EdE}{\left(\hbar c_*\right)^2}\right], \tag{6.7}$$

where $A = L_x L_y$ is the area of the $x-y$ plane, in which L_x and L_y are quantum channel lengths in the x and y directions of the plane, respectively. g_v is the degeneracy of the valley and is related to the conical symmetry above and below the $x-y$ plane. There are different interpretations for the consideration of g_v. The most accepted is that g_v implies an ambipolar electric current owing to electron and hole charge carriers that are directly associated with the conical symmetry of K point space, as depicted in Figure 6.2.

This conical symmetry (BOSTWICK et al., 2007; GEIM; NOVOSELOV, 2010), related to electrons and holes in graphene, implies the well-known semimetal characteristics of conduction and valence bands with a singularity at the Dirac point. The spatial geometric interpretation implies six locations in momentum space, corresponding to the vertices of the hexagonal Brillouin zone (BOSTWICK et al., 2007; GEIM; NOVOSELOV, 2010). These six locations can be divided into two non-equivalent sets of three points, resulting in two sets that are labeled K and K', i.e., a valley g_v degeneracy.

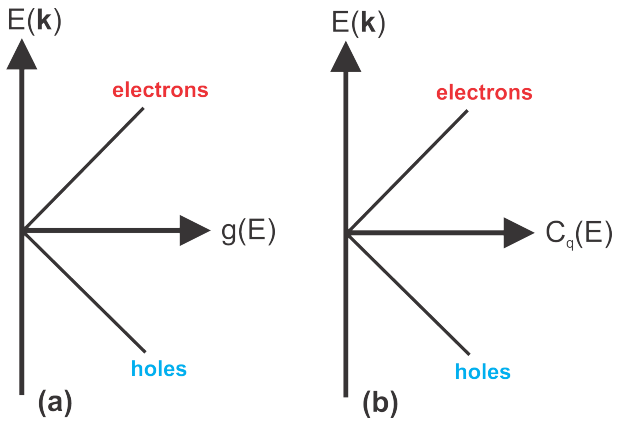

FIGURE 6.2. The representation of the well-known V-shape of graphene in which an experimental measurement of electron or hole injections into the electronic structure permits access to the density-of-states function $g(E)$. (a) Shows the traditional analysis of $E(\mathbf{k})$ *versus* $g(E)$, in which $\delta E(\mathbf{k}) = e\delta V$ corresponds to different charge state and energy $\Delta E(\mathbf{k})$ occupancies of the electronic structure of graphene as a function of the bias potential ΔV concerning the Dirac point used as zero of energy reference. (b) Depicts the analysis proposed by the quantum-rate theory where quantum capacitance C_q is measured in different energy levels of occupancy of the electronic structure by electron or holes in an equilibrium charge occupancy situation driven by different bias energy $e\delta V$ established in respect to the Dirac point as the reference of energy for the vacuum level. As $C_q(E)$ directly correlates with a coherent $\nu = 1/R_q C_q$ perturbation of the electronic structure, the measurement of C_q permits obtaining information of the momentum through Eq. 6.11 and so spatial information can be obtained.

Note now, from Eq. 6.7, that $\left[n\left(\mathbf{k}_{x-y}\right) d\mathbf{k}_{x-y}\right]/dE$ is only function of energy, such as

$$g(E) = g_s g_v \left(\frac{A}{2\pi}\right)\left[\frac{E}{(\hbar c_*)^2}\right], \tag{6.8}$$

is known as the density-of-states DOS. Particularly, $g(E)$, in Eq. 6.8, is the DOS of graphene.

6.2 The Quantum Rate and Density-of-States of Graphene

Note now that $g(E)$ of Eq. 6.8 corresponds to the DOS (dn/dE) and can be combined with the result of Eq. 6.6 such as that

$$C_q(E) = e^2 g(E) = g_s g_v e^2 \frac{A}{2\pi} \left[\frac{E}{(\hbar c_*)^2} \right], \tag{6.9}$$

permitting defining C_q as a function of E. Consequently, Eq. 6.9 permits to define a $\tau(E) = 1/\nu(E) = R_q C_q = G_0/C_q(E)$ that, according to Eq. 6.3, can be stated as

$$\tau(E) = g_v \frac{A}{\hbar} \left(\frac{E}{c_*^2} \right), \tag{6.10}$$

By noting that $|\mathbf{k}|/E = d|\mathbf{k}|/dE = 1/\hbar c_*$, the function $\tau(E)$ represented in Eq. 6.10 can be also expressed as a linear function of $\mathbf{k}$ such as

$$\tau(\mathbf{k}) = \left(\frac{g_v A}{c_*} \right) \mathbf{k}, \tag{6.11}$$

where $\tau(\mathbf{k}) = 1/\nu(\mathbf{k})$ has a direct proportionality with the particle's momentum $\mathbf{p} = \hbar\mathbf{k}$.

To summarize thus far, the quantum-rate concept $\nu = G_0/C_q = 1/\tau$ defines a characteristic $\tau = R_q C_q$ time constant for the transport of electrons within an electronic structure with a DOS defined as C_q/e^2 that, owing to its intrinsic relativistic characteristics, can be stated as a function of both the energy and momentum of the particle's dynamics. In the particular case of the electronic structure of graphene, the characteristic ν or τ as a function of E or $\mathbf{p}$ are defined in Eq. 6.10 and Eq. 6.11, respectively.

6.3 Remarks on the Experimental Analysis of the Electronic Structure

It is important to note that in a photo-emission spectroscopic experiment such as that of ARPES (PARK et al., 2009), the structure of graphene is revealed by imposing a photonic energetic $h\nu$ perturbation with a threshold frequency ν that corresponds to the energy level that permits photo-electron emission from $x-y$ plane of graphene. The emitted photo-electron with particular energy and momentum is detected at different angles by a photodetector, and it allows to reveal the electronic structure of graphene (PARK et al., 2009).

In a quantum-rate spectroscopic experiment a $\tau(E)$ (in agreement with Eq. 6.10) is measured as a result of a time-dependent perturbation of the momentum $\mathbf{p} = \hbar\mathbf{k}$ (in agreement with Eq. 6.11) of the electron particle in the $x - y$ plane of graphene, permitting to reveal the electronic structure thanks to the phase coherence between the time perturbation of energy $\tau(E)$ and momentum $\tau(\mathbf{k})$ with relativistic electrodynamics that implies that the ratio between the perturbation E and $\mathbf{k}$ is coherent such as

$$\frac{\tau(\mathbf{E})}{\tau(\mathbf{k})} = \frac{E}{\mathbf{p}\cdot\mathbf{c}_*} = \frac{\omega}{\mathbf{c}_*\cdot\mathbf{k}}, \tag{6.12}$$

where $\omega = e^2/\hbar C_q$ can be identified as the angular version of ν defined in Eq. 7.1. Note that the null resting mass m_0 of Fermions in graphene implies, from a relativistic perspective $E = \sqrt{(\mathbf{p}\cdot\mathbf{c}_*)^2 + (m_0c_*^2)^2}$, that $E = \mathbf{p}\cdot\mathbf{c}_*$.

Accordingly, the goal of the present manuscript is to demonstrate that a time perturbation of E implies a response of $\mathbf{k}$ and $vice - versa$. Therefore, by measuring C_q, a plot of $E = g_s g_v e^2/C_q$ can be constructed directly as a function of $\mathbf{k}$[1]. The plot of E *versus* $\mathbf{k}$ corresponds, in good quantitative agreement, to the electronic structure that is computationally calculated by DFT or measured by ARPES.

6.4 Experimental and Computational Methods

6.4.1 Experimental Methods

Single-layer graphene (SLG) on 90 nm SiO_2/Si substrate, as provided by Graphenea company, was obtained via chemical vapor deposition. Electric contacts for an electrochemical frequency-response analysis were made on SLG surfaces with sizes of 10 *versus* 10 mm. The contacts consisted of an area of 8 *versus* 2 mm and were fabricated via radio frequency sputtering consisting of a deposition of a first layer of titanium of $\sim$ 10 nm thickness over which it was deposed a layer of gold of $\sim$ 100 nm thickness.

[1]Note that the relationship between E and $\mathbf{k}$ was only possible to be established here because in graphene the Dirac point energy state is determined experimentally and it corresponds to K spatial point. By invoking spatial symmetry rules and taking the tight-binding structural model as the reference of the spatial information in the $x - y$ plane of graphene, it was possible to estimate the M and Γ positions with respect to the referential K spatial Dirac point. This was useful to plot energy *versus* spatial position for the QRS method, as shown in Figure 6.5.

The frequency-response analysis was conducted using a portable potentiostat (PalmSens4) equipped with a frequency-response analyzer. The analysis consisted of performing a small potential sinusoidal perturbation $\tilde{V} = |V_0| \exp(j\omega t)$ with a root mean square potential amplitude of $|V_0|$ of 10 mV over a potential bias $\bar{V}$ measured concerning the Fermi-level potential of electrode E_F/e (here corresponding to the Dirac point of graphene), where ω is the angular perturbation frequency and $j = \sqrt{-1}$. The supporting electrolyte of the electrochemical cell was constituted of 1-Butyl-3-methylimidazolium tetrafluoroborate [BMIM]BF_4 ionic liquid (IL) with purity $\sim 98\%$ (Sigma Aldrich) that has the role of acting as a dielectric layer over the plane of graphene. The measurements were conducted at steady-state potential $\bar{V}$ with perturbing frequencies ranging from 1 MHz to 3 Hz or in a fixed frequency with potential scanned positively or negatively to the Fermi level potential E_F/e.

Observe that for the frequency-response analysis, an electric current response $I(t) = \bar{I} + \tilde{I}$ is measured as a response to $V(t) = \bar{V} + \tilde{V}$ time potential perturbation. The ratio between the potential perturbation and current response permit to perform a transfer-function spectroscopic analysis. For instance, an admittance of $G^*(\omega) = \tilde{I}/\tilde{V} = j\omega C^*(\omega)$ or impedance $Z^*(\omega) = \tilde{V}/\tilde{I} = 1/[j\omega C^*(\omega)]$ complex function can be taken as a particular electric transfer-function. From the above-mentioned functions, the complex $C^*(\omega)$ capacitive spectra are of particular interest for studying graphene, as will be discussed further during the analysis of Eq. 6.15 and its related spectra.

For the measurement of $C^*(\omega)$ spectra of SLGs, graphene layers were embedded in an electrochemical cell using a two-electrode configuration, where SLG served as the working and a platinum mesh as the counter/reference electrode, for SLGs perturbed in a time-dependent voltage or current mode of measurement a particular electrochemical cell configuration was employed. This cell configuration is permitted to employ graphene layer serving as working electrodes in a particular quantum transistors configuration, in which the electric current flowing in the channel of the graphene transistor is 'purely' capacitive with the series equivalent capacitance dominated by the quantum capacitance. Hence, this electrochemical cell configuration corresponded to the use of graphene layers as quantum AC transistors (specifically a diode mode of an AC transistor configuration).

Therefore, unlike DC-transport where particle-wave currents cannot be investi-

gated, here the time-dependent transport of the total current $\mathbf{j}(\mathbf{r})$ is the sum of the displacement current $\epsilon\,(\delta\mathbf{E}/\delta t)$ and particle $\mathbf{j}_p(\mathbf{r})$ which leads to

$$\mathbf{j}\,(\mathbf{r}) = \epsilon\left(\frac{\delta\mathbf{E}}{\delta t}\right) + \mathbf{j}_p\,(\mathbf{r})\,, \tag{6.13}$$

where $\mathbf{r}$ correspond to the position vector of the particle, ϵ (for simplicity taken to be space and time-invariant) is the dielectric constant, and E is the dielectric field. The total current of Eq. 6.13 must be conserved, such as

$$\nabla \cdot \mathbf{j}\,(\mathbf{r}) = 0, \tag{6.14}$$

Eq. 6.14 states that along a line that is tangential to the current vector $\mathbf{j}$, the length of this vector is invariant. Therefore, as the conservation law of energy permits the transformation of kinetic into potential energy, so similarly here, it is permitted to transform particle current into displacement current and *vice-versa*. Very important for the analysis to be conducted in this work, it should be noted that while the particle current exists only inside the electric conductors that are required to be scrutinized, the displacement current is not limited to the conductor and can be detected by an external probe.

In other words, wherever there is a time-dependent electric field perturbation, a displacement current can be measured by a contact probe. If this measured displacement current is a result of a particle perturbation response inside the conductor (here graphene), hence the particles are detected as a result of the displacement current response to the perturbation. This analysis is a straightforward consequence of particle-wave duality associated with relativistic characteristics within Eq. 7.1 and Eq. 7.2 and of phase coherence between the perturbation and the response.

Accordingly, note that the use of an electrochemical AC transistor configuration permits us to measure the properties of the channel of the transistor by short-circuiting the drain and source contact; the capacitive property of the channel is resultant of a field effect obtained by the AC response of the channel to the external field-perturbation. This configuration of measurement was successfully tested and previously reported as a suitable way

of obtaining, for instance, the conductive and capacitive V-shapes of graphene (LOPES et al., 2021).

Here, it will be shown that the analysis of $C^*(\omega)$, which theoretically correlates with Eq. 6.10 and Eq. 6.11, permits us to analyze the electronic structure of graphene. Complex capacitance spectra can be constructed either from the raw admittance or impedance data. For instance, using impedance data as an example, capacitive spectra can be obtained by converting the complex impedance $Z^*(\omega)$ function into a complex capacitance $C^*(\omega)$ using the relationship $C^*(\omega) = 1/[j\omega Z^*(\omega)]$. The real and imaginary components of $C^*(\omega)$ are $C^{'} = Z''/\omega|Z|^2$ and $C'' = Z'/\omega|Z|^2$, respectively, where $|Z| = \sqrt{Z'^2 + Z''^2}$ is the modulus of $Z^*(\omega)$.

6.4.2 Computational Methods

The electronic structure of SLG containing 180 atoms was calculated in a vacuum using first-principles calculations within a DFT framework (HOHENBERG; KOHN, 1964), as implemented in the SIESTA code by employing a generalized gradient approximation (GGA) in its PBE formulation for the exchange and correlation potential. It used a finite real-space grid corresponding to a 200 Ry plane-wave cut-off for the integrals in real space.

The Kohm-Sham wave functions (KOHN; SHAM, 1965) for the valence electrons were expanded in a double-zeta-polarized (DZP) basis set of soft-confined finite-support numerical atomic orbitals (JUNQUERA et al., 2001). The band-structure calculations were performed using SIESTA code (SANZ-NAVARRO et al., 2011), sampling the Brillouin zone with k-points along the $\Gamma \rightarrow M \rightarrow K \rightarrow \Gamma$ path, as detailed in the SI document.

6.5 Results and Discussions

As predicted by Eq. 6.9, the electronic structure of graphene is directly proportional to $C_q(E)$. Therefore, in agreement with the quantum-rate theory, as stated in Eq. 7.1, the measurement of a complex capacitive spectra $C^*(\omega)$ of graphene must correspond to the response of a quantum resistive-capacitive (RC) such as that (BUENO, 2018d)

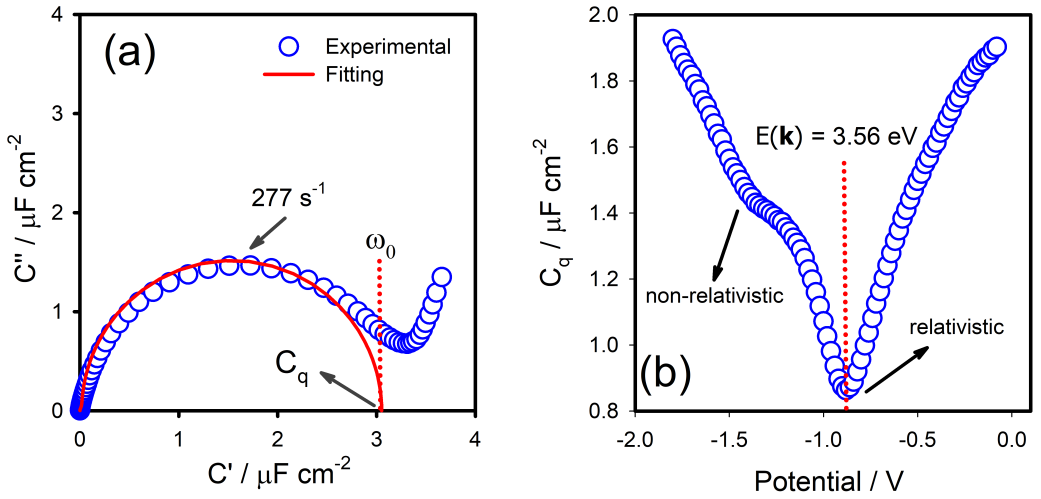

FIGURE 6.3. (a) Nyquist capacitive diagram of a SLG graphene. A resonance frequency of 277 s^{-1} whereas a $\omega_0/2\pi \sim 13$ s^{-1} as the low-frequency limit where C_q^0 can be obtained according to Eq. 6.15. A fitting to Eq. 6.15 considering an additional series resistance contributions in such a way that R_q is obtained as the total series resistance $R_{s,t}$ and this corresponds in good agreement to the theoretical limiting value of $R_q \sim 12.9$ kΩ as discussed in the text. (b) Depicts the capacitive V-shape obtained at Ω_0 limiting frequency.

$$C_q^*(\omega) = \frac{C_q^0}{1 + j\omega\tau} \sim C_q^0 \left(1 - j\omega\tau\right) + O(\omega^2), \tag{6.15}$$

as demonstrated in previous works (LOPES et al., 2021; LOPES; BUENO, 2021). Noteworthy that a $C_q^*(\omega)$ spectrum of graphene can be measured by a direct frequency-response analysis.

The $C_q^*(\omega)$ spectrum corresponds to the capacitive frequency response of a quantum RC equivalent circuit that can be expressed, according to the quantum-rate theory, solely as a response of series R_q and C_q quantum circuit elements, thus providing a characteristic frequency $\omega_c = 1/(R_q C_q)$ with a characteristic time of $\tau = 2\pi R_q C_q$.

In other words, in agreement with the relativistic quantum mechanics predicted by the quantum-rate theory, Eq. 7.1, the quantum electrodynamics of graphene can be studied in-depth using a simple electrochemical experimental set-up. As an example, it will be demonstrated here that such type of experiments permit the development of an *in-*

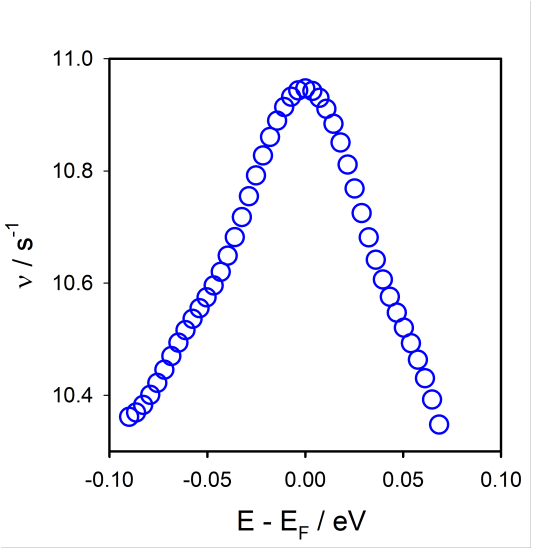

FIGURE 6.4. This figure depicts the $\nu = G_0/C_q$ measured for a SLG around the Dirac-point. As theoretically expected, this ν is maximum at the Dirac point owing to C_q, and the conductance is maximum. This is the theoretically expected result as, in contraction to the common classical sense for an RC circuit, for a quantum RC circuit, the resistance is minimum (corresponding to a maximum conductance) for a maximum capacitance relaxed capacitance.

situ spectroscopic method of measuring the electronic structure of graphene, although the method is note limited to revealing the electronic structure of graphene. The electronic structure molecular organic (BUENO, 2023c) and inorganic (PINZON et al., 2021) films as well as quantum dots (PINZON et al., 2023) can also be revealed using quantum-rate spectroscopic method.

6.5.1 Quantum RC Circuit and Quantum Capacitance of Graphene

Note that Eq. 6.15 permits to evaluate the quantum-rate characteristic response of graphene in a quite important quantum electrodynamics setting. This corresponds to a particular frequency ω_0 (see Figure 6.3) where the electronic structure is measured (or responds to a perturbation) in a quasi-equilibrium condition. Mathematically, this corresponds to ω_0 tending to null, where a C_q^0 value can be evaluated.

From a theoretical physical analysis, C_q^0 measured at ω_0 corresponds to a frequency in which there is minimal influence of the imaginary component of $C^*(\omega)$ spectra. In this case, there is a dominant response of the real component of $C^*(\omega)$ that corresponds to $C^*(\omega)$ responding to a limiting perturbation frequency ω_0, as indicated in Figure 6.3*a*.

Nonetheless, from a quantum mechanical RC point-of-view, at this limiting frequency ω_0, the imaginary component of $C_q^* = jC'' + C'$, that is correlated to $G(\omega_0) = \omega_0 C''$ is not zero, as it should be expected in a classical analysis of a series RC circuit, corresponding to null electric current circulating in the resistor. According to the quantum-rate theory, at the limit of ω_0, the quantum RC circuit analysis corresponds to the minimum quantum resistance of the circuit with a non-zeroed current in the conductor. In other words, a quantized displacement current exists in the resistor, and this quantum resistive current is measured at $\omega C''$ and is associated with the value of C_q^0.

This electric current that is different from null and is expected to be associated with multiples of conductance e^2/h permits us to find out a quantum limit of perturbation to the energy of the system $E_0 = e^2/C_q^0$. Owing to the resistance being quantized and different of zero (with multiples of n states), it permits coherent dynamics between the perturbation of potential (or energy) and the current (or quantum states) response for an equilibrium charge condition $C_q^0 = ne/V_0$. This equilibrium charge relaxation between the perturbation of the probe and the response of the quantum RC system is an important physical characteristic that allows quantum-rate spectroscopy to be useful. As is expected for classical RC circuit analysis, at low frequencies, the current in the resistor is expected to be null or dissipative and not coherent with the potential perturbation. This is not the case in a quantum RC circuit analysis.

Therefore, at the Dirac point level of energy, the resistance scrutinized at the limit of ω_0 must correspond to the resistance quantum $R_q = 1/G_0 \sim 12.9$ kΩ. This is owing to $L = \lambda$, i.e., a situation that corresponds to perturbing the single n quantum state mode of the quantum channels of graphene (with lengths L_x and L_y as noted in Figure 6.1 in the plane) at the Dirac point.

The mean average of G value measured over three different samples (see SI document for more information) was obtained as $G(\omega) = \omega_0 C'' \sim 19 \pm 0.9$ mS that multiplied by g_s and g_v, as required for the consideration of energy degeneracies, led to $\sim 76.1 \pm 1.8$ mS. This mean experimental value corresponds to 2% of deviation of the theoretical expected value of $G_0 = g_s e^2/h \sim 77.5$ mS.

Additionally, the experimental value obtained by us from the analysis of the whole $C^*(\omega)$ spectra obtained at the Fermi level (for three different SLG samples), as shown

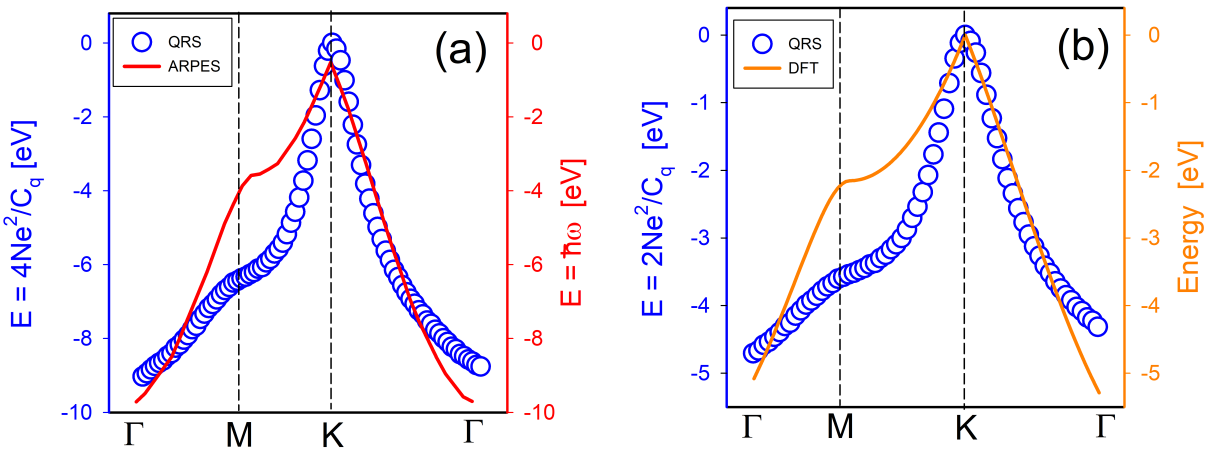

FIGURE 6.5. (a) In blue dots is the electronic structure of an SLG graphene as measured by QRS, which is compared with the red curve as it was obtained by ARPES. (b) The same as in (a), but now the electronic structure obtained by QRS is compared with that calculated by DFT, which is depicted in orange color. In both (a) and (b), there is an excellent agreement between the QRS method and ARPES or DFT. The differences observed mainly around the M position are attributed to the presence of [BMIM]BF_4 electrolyte, as discussed in the text.

in Figure 6.3, corresponded to $R_q = 1/G_0 \sim 12.9 \pm 1.6$ kΩ, in excellent agreement with the theory that predicts a value of ~ 12.9 kΩ. This limit resistance quantum value was obtained from the fitting of the spectra to Eq. 6.15, and it should be observed that R_q in Eq. 6.15 was considered as the total series resistance of the circuit encompassing the resistance of the contacts; see SI document for more details.

The above-mentioned method of calculating R_q is similar to that used with success in the analysis of faradaic quantum conductance of redox-active monolayers (SANCHEZ et al., 2022; BUENO, 2023c). As observed in electrochemical experiments of redox-active monolayers (SANCHEZ et al., 2022), in the analysis of graphene, it is the total current (indicated in Eq. 6.13) that accounts experimentally, not the particle's current $\mathbf{j}_p$. This is in agreement with Eq. 6.14, and the quantum circuit cannot be treated separately from the external circuit.

Note that in the case of graphene, it was considered g_s and g_v degeneracies, such as the experimental $\omega_{c,e} = 1/(R_{s,t}C_q)$ equates to the theoretical characteristic frequency of $\omega_c = g_s g_v e^2/\hbar C_q$, where $R_{s,t}$ is the total series resistance and it is this $R_{s,t}$ that equates to the resistance quantum, that includes the contact resistance. By equation $\omega_{c,e} = \omega_c$ a

value of $R_q = [2\pi(g_s g_v)R_{s,t}] \sim 12.9 \pm 1.6$ kΩ is obtained. It should be noted that g_s and g_v comes from theoretical analysis, whereas the measured resistance quantum effectively measured for graphene at the Dirac point was h/e^2, which is in agreement with a previous work (LOPES et al., 2021).

As demonstrated in previous work, conductive and capacitive V-shapes for graphene can be obtained by using time-dependent analysis (LOPES et al., 2021). These V-shapes were obtained at a minimal perturbation of the electronic structure, that is, by measuring C_q^0 at ω_0 as a function of the energy $E = -eV$ of the electrode from where electrons and holes can be injected/ejected in an equilibrium charge condition of quantum RC relaxation. The smallest value of $C_q^0(E)$ is obtained at the Dirac point, but it cannot be zero in agreement with Eq. 7.1, as it would correspond to a zero Fermi-energy, which would be not physically correct, as better argued in previous work (BUENO; MERCADO, 2022).

The minimal of energy corresponds to $\Delta E(\mathbf{k}) = E - E_F = 0$, hence $E(\mathbf{k}) = E_F(\mathbf{k}) = -3{,}56$ eV to the vacuum energy reference level, in good agreement with the theoretical value of -3.45 eV calculated in the present work by using DFT computational method. Note that ten mV differences between -3.45 eV and -3.56 eV can be attributed owing to the experimental -3.56 eV value was obtained for an SLG measured in ionic-liquid ([BMIM]BF_4) electrolyte environment where -3.45 eV was calculated by DFT for an SLG placed in vacuum.

In other words, as better discussed in a previous work (BUENO; MERCADO, 2022), C_q^0 cannot be zero as this would conduct to an infinite value of E_F. Although the energy at the Fermi level or Dirac point must be minimal with a minimal C_q^0, as shown in the capacitive V-shape of Figure 6.3*b*, it cannot be zero as suggested by some authors (XIA et al., 2009). This inference for a zeroed capacitance at the Dirac point was based on an analysis of the absence of a net charge carrier density at the Dirac point where there would be not a polarization of the graphene and so no net charge carriers to charge a capacitance (XIA et al., 2009). The net number of charge carriers is null at the Dirac point, but this implies an ambivalent displacement electric current according to the analysis of Eq. 6.13 that permits scrutinize for a particle dynamics even in the absence of a net DC current. Furthermore, the time-dependent quantum analysis of this problem

permits us to note that the quantum mode n can correspond to that of the ground state where there is no charge net current. This analysis is corroborated by the value of e^2/h found by the quantum of conductance at the Dirac point, corresponding to the ground state fermionic energy e^2/C_q^0 that has its minimum value, but which is different from a null capacitance as suggested from an analysis (XIA et al., 2009) of the charge density perspective to interpret the quantum capacitance of graphene at the Dirac point.

According to the meaning of C_q^0 introduced above, although there is no net charge carriers at the Dirac point, the value of C_q^0 cannot be zero not only owing to statistical mechanics, but to quantum mechanical reasons. Accordingly, the non-zeroed minimal value for C_q^0 obtained experimentally that implies null net charge carriers cannot be null from a quantum mechanical perspective, where it would be related to a limiting value of resistance governed by the quantum limit of R_q around $E_F = e^2/C_q^0$ with a minimum C_q^0 that is different of null owing to a quantum resistance limit. The minimum R_q and C_q predicted values at the Dirac point conduct to a maximum rate $\nu \propto e^2 e/hC_q^0 = E_F/h$, as shown in Figure 6.4. Noteworthy is that albeit the minimum of the capacitance ~ 0.83 μF cm^{-2} obtained from a V-shape capacitive measurement at ω_0, as observed in Figure 6.3b, is in good agreement with the expected statistical mechanical theoretical value of C_q^0 of 0.8 μF cm^{-2}; this value can vary according to the electrolyte imposed external potential and can be lower than 0.8 μF cm^{-2} in certain circumstances but not zero.

In the next section, it will be demonstrated how the electronic structure of graphene is obtained using the quantum-rate spectroscopic concept.

6.6 Quantum Rate Spectroscopy of Graphene

Note that Eq. 6.12 is equivalent to $E\,\mathbf{k} = \omega\,\mathbf{p}$, corresponding to a different way of expressing De Broglie or Einstein-Planck relationships. This equation is also equivalent to $E\tau = |\mathbf{p}|\lambda$, and the meaning of this is that there is a phase coherence between the perturbation and the response to the perturbation, as it is expected from the quantum coherent RC circuit analysis, as discussed in previous sections.

To resolve any doubts related to the principles of a spectroscopic method based on the quantum-rate concept, defined in Eq. 7.1, let us demonstrate the correspondence between the duality particle $E = e^2/C_q$ (or p) and $\mathbf{k}$ (ω) wave of the electron whenever

there is a time-dependent perturbation on C_q that corresponds to a coherent response of $\mathbf{k}$ and *vice-versa*.

Hence, let us start invoking Eq. 6.6 that can be rewritten as

$$\left(\frac{dE}{dn}\right) = \frac{e^2}{C_q}, \tag{6.16}$$

where $e^2/C_q = \hbar\mathbf{c}_* \cdot \mathbf{k} = E$ is the energy associated with C_q, according to Eq. 7.2 and premises of the quantum-rate theory. It is straightforward to observe now that $dE = \hbar\mathbf{c}_* \cdot \mathbf{k}dn$ and a time perturbation in E corresponds to a time perturbation of $n = q/e = L/\lambda$ such as that

$$\left(\frac{dE}{dt}\right) = \hbar\mathbf{c}_* \cdot \mathbf{k}\left(\frac{dn}{dt}\right), \tag{6.17}$$

from where E and n are the only time-dependent variable such as $dE/dt = E(t)$ and $dn/dt = n(t)$. Therefore, an energy perturbation $E(t)$ of a quantum RC system as a function of time corresponds to a coherent response of quantum RC states $n(t)$ as a function of time. These time-dependent and related functions can be, respectively, stated as $E(t) = \bar{E} + \tilde{E}$ and $n(t) = \bar{n} + \tilde{n}$, where $\tilde{E} = E_0 \exp(j\omega t)$ and $\tilde{n} = n_0 \exp(j\omega t - \phi)$ are the oscillatory perturbation of E and the corresponding oscillatory response of n to a defined E perturbation.

E_0 and n_0 are the amplitudes of the energy perturbation of the quantum RC state response, respectively, and ϕ is the coherent phase difference between energy perturbation and quantum RC states response. $\bar{E}$ and $\bar{n}$ denote steady-state levels of the system where the oscillatory perturbation is performed. In the present situation of measurement conducted here in graphene, steady-state energy levels $\bar{E} = -eV + E_F$ correspond to positive or negative bias voltage V applied to the Dirac point E_F.

Note from the above analysis that $E(t) = E_0 \exp(j\omega t)$ and $n(t) = n_0 \exp(j\omega t - \phi)$ permit us to define a complex $E^*(\omega)$ energy state function such as

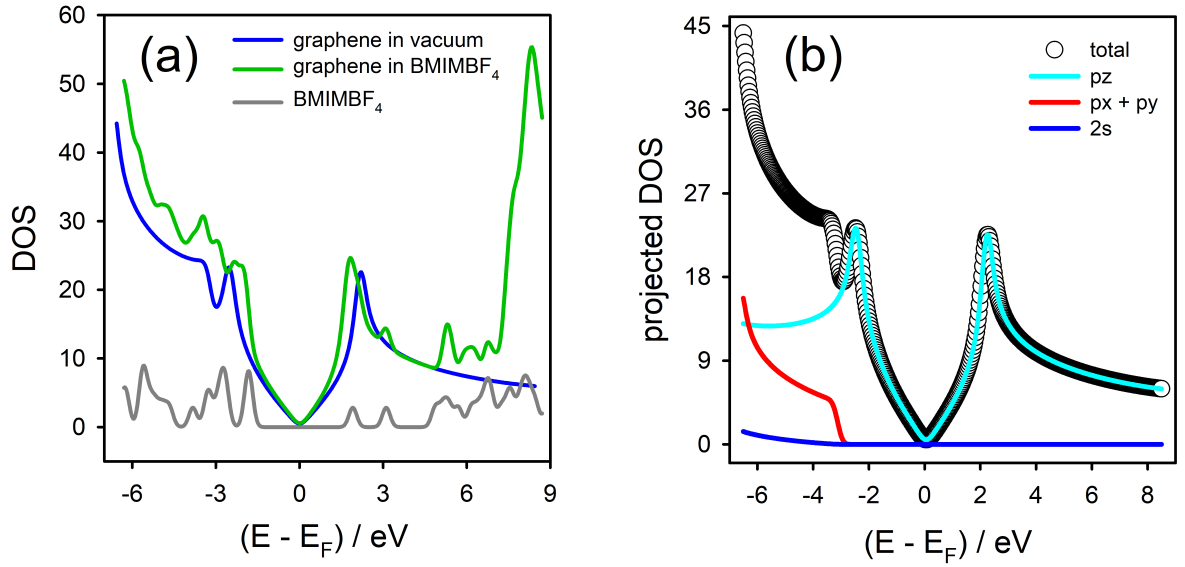

FIGURE 6.6. (a) The analysis of the individual contribution of $[BMIM]BF_4$ to the DOS of graphene in contact with this electrolyte. As can be seen, the presence of $[BMIM]BF_4$ affects the electronic structure of graphene measured in the presence of $[BMIM]BF_4$, and this was identified as the main difference between the electronic structure of graphene measured in vacuum by ARPES and that measured by QRS in the presence of $[BMIM]BF_4$. (b) Shows the projected DOS of graphene in a vacuum calculated by DFT with the different individual contributions of the orbitals to the total response that is indicated in black dots.

$$E^*(\omega) = \left[\frac{dE(t)}{dn(t)}\right] = \left(\frac{E_0}{n_0}\right) \exp\left(j\phi\right), \tag{6.18}$$

from where the real component of $E^*(\omega)$ is identified as

$$\Re\left[E^*(\omega)\right] = \left(\frac{E_0}{n_0}\right) \Re\left[\exp\left(j\phi\right)\right] = \hbar \mathbf{c}_* \cdot \mathbf{k}, \tag{6.19}$$

As discussed previously, if ω, in Eq. 6.19, is taken as ω_0, there is a limit for the energy $E_0 = e^2/C_q^0$ that corresponds to a limit of Eq. 6.15 in which $e^2/n_0 C_q^0 = \hbar \mathbf{c}_* \cdot \mathbf{k}$, *quod erat demonstrandum*. This previous demonstration implies that there is a correspondence between e^2/C_q^0 and $\hbar \mathbf{c}_* \cdot \mathbf{k}$ that permits us to measure the electronic structure of graphene *in-situ* using an electric time-dependent method.

The capacitive V-shape depicted in Figure 6.3*b*, which was obtained at ω_0, is the

basement to calculate the electronic structure of graphene following physical concepts discussed in Eqs. 6.10 to Eq. 6.12. Accordingly, using the capacitive V-shape of Figure 6.3*b* and the relationship $e^2/n_0 C_q^0 = \hbar \mathbf{c}_* \cdot \mathbf{k}$, the electronic structure of graphene is revealed in Figure 6.5. Note that whereas the ordinate axis was obtained experimentally in Figure 6.5, the abscissa axis was estimated using tight-binding model considering the symmetry of graphene spatial structure with respect to the Dirac point (which is determined experimentally for QRS method). Observe that albeit the calculation of abscissa axis is an approximation, it provides, for graphene particularly, a very good approximation as noted by comparing the results of QRS to DFT and ARPES methods.

In Figure 6.5*a*, the electronic structure of SLG measured by quantum-rate spectroscopic (QRS) method in electrolyte and room-temperature environment is compared with that obtained by ARPES (PARK et al., 2009) in vacuum and low-temperature. In Figure 6.5*b*, the electronic structure measured by the QRS method is compared with that calculated by DFT computational method. As noted, the measured electronic structure by QRS is in good agreement with those obtained theoretically by DFT and experimentally measured by ARPES. It must be also noted that the absolute agreement between the scale of energy $E_0 = e^2/C_q^0$ obtained by DFT and QRS methods depends on the consideration of g_v. As the DFT method does not take into account g_v in the calculation of the electronic structure, a comparison of the QRS method with that obtained by DFT requires QRS to not consider g_v as well, and so there is a very good agreement between both methods.

The differences between QRS and ARPES/DFT spectra observed in the M position were confirmed by DFT calculations to be owing to the presence of an electrolyte ([BMIM]BF_4) environment over SLG, as noted in Figure 6.6*a*. In this Figure, it can noted the comparison between the DOS of graphene placed in the vacuum environment, a graphene in [BMIM]BF_4 environment, and the DOS of [BMIM]BF_4 isolated from graphene. It can be observed that at energies around $(E - E_F) \sim -3{,}56$ eV $+1{,}5 \sim -2$ eV, there is a strong contribution of the DOS of the [BMIM]BF_4 to that of graphene that affect the total DOS of graphene measured in [BMIM]BF_4, as indicated in the figure.

Finally, Figure 6.6*b* depicts the project DOS within the individual contributions of the graphene's orbitals separately. It can be noted in this figure that the pz component,

which corresponds to an orbital direction that is perpendicular to that of $x-y$ plane of graphene, is the most affected by the adsorption of [BMIM]BF_4 over the $x-y$ plane, as indicated in red, which explains the difference in the electronic structure around M position, as depicted Figure 6.5.

In summary, QRS permits with great accuracy to measure the electronic structure of graphene in a *in-situ* manner at room-temperature electrolyte environment conditions. This constitutes the great advantage of this spectroscopic method over others, which requires expensive equipment and time-consuming procedures to operate.

6.7 Final Remarks and Conclusions

It is demonstrated the principles of the electrochemical quantum-rate spectroscopy, which is based on a quantum-rate principle that permits to study relativistic electrodynamics of graphene with great precision. Although the focus of the present study was on describing a spectroscopic method of measuring the electronic structure of graphene compared with theoretical calculations (DFT) and other experimental (ARPES) methods, it was additionally possible to demonstrate that graphene has a quantum conductance e^2/h at the Dirac point that is in phase coherence with its equilibrium DOS state, that is $(dn/dE) = C_q^0/e^2$, permitting a relationship such as $(\hbar\omega_c)(dn/dE) = n_0$.

The phase coherence analysis of the quantum RC characteristics of graphene, measured at an equilibrium charge dynamics, permitted to measure the characteristic energy $E_c = \omega_c\hbar$ of the graphene through a time-dependent perturbation of n_0 or E_0 as a function of the energy state $E = -eV + E_F = \hbar c_* \cdot \mathbf{k}$ of the probe (electrode).

The plot of E_c as a function of E or $\mathbf{k}_{x-y}$ is the essence of the introduced quantum-rate spectroscopic methodology for graphene and allows us to measure, in an *in-situ* manner, the electronic structure of Wey semi-metal structures generally. In other words, albeit the QRS method is not restricted to graphene, in the present work, the meaning of C_q was defined specifically for graphene in Eq. 6.9

Nonetheless, observe that to study the quantum electrodynamics of other 2D structures at different conditions, the theoretical DOS $\sim C_q/e^2$ of the structure is not required as the purpose of QRS to be a simple experimental way of measuring the DOS $\sim C_q/e^2$

of different Weyl semi-metal structures. From an experimental point-of-view, the presence of an electrolyte is primordial, because it permits the equivalent capacitance of the interface C_μ to be written as a function of C_q, i.e., for graphene, it would be written as $1/C_\mu = g_v/C_q$, as it is better discussed in reference (BUENO, 2023c).

6.8 Credit author statement

Laís Cristine Lopes: Data curation, data acquisition and editing, review final draft.

Edgar Pinzón: Data curation and editing, picture-writing, review final draft.

Gabriela Dias-da-Silva: Computational calculation, picture-writing, review final draft.

Gustavo Troinano Feliciano: Computational calculation,

Paulo R. Bueno: Conceptualization, theory and method development, data curation, writing original and final draft, picture-writing and editing, funding acquisition.

6.9 Acknowledgments

The authors are grateful to Sao Paulo State Research Foundation (FAPESP) for grants 2017/24839-0 and 2018/24525-9 and National Council for Scientific and Technological Development (CNPq).

Chapter 7

Quantum Rate Electrodynamics and Resonant Junction Electronics of Heterocyclic Molecules

Edgar Fabian Pinzón,[a] Laís Cristine Lopes,[a] Adriano dos Santos,[a] Maria Manuela Marques Raposo,[b] & Paulo Roberto Bueno,*[a]

[a] *Departmnet of Engineering, Physics and Mathematics, Institute of Chemistry, São Paulo State University, Araraquara, Sao Paulo, Brazil*, [b] *Centre of Chemistry, University of Minho, Campus de Gualtar, Braga, 4710-057, Braga, Portugal*

Keywords: density-of-states, quantum dots, quantum capacitance, electrochemical impedance.

Journal: Electrochimica Acta, 501, 144749 (2024).

DOI: https://doi.org/10.1016/j.electacta.2024.144749

Abstract

The quantum rate theory provides a framework to understand electron-transfer reactions by correlating the electron-transfer rate constant (ν) with the quantum capacitance (C_q) and the molecular conductance (G). This theory, which is rooted in relativistic quantum electrodynamics, predicts a fundamental frequency $\nu = E/h$ for electron-transfer reactions, where E is the energy associated with the density of states C_q/e^2. This work demonstrates the applicability of the quantum rate theory to the inter-

molecular charge transfer of push-pull heterocyclic compounds assembled over conducting electrodes. Remarkably, the observed differences between molecular junction electronics formed by push-pull molecules and the electrodynamics of electrochemical reactions on redox-active modified electrodes can be attributed solely to the adiabatic setting of the quantum conductance in push-pull molecular junctions. The electrolyte field-effect screening environment plays a crucial role in modulating the resonant quantum conductance dynamics of the molecule-bridge-electrode structure. In this context, the intermolecular electrodynamics within the frontier molecular orbital of push-pull heterocyclic molecules adhere to relativistic quantum mechanics, consistent with the predictions of the quantum rate theory.

7.1 Introduction

Organic and molecular electronics represent modern fields of electronics in which the semiconducting properties of organic molecules are utilized. One notable application is the design of modern computer and mobile phone displays, exemplified by organic light-emitting diodes (OLEDs) (MA et al., 2010). The advantage of organic electronics over traditional ones, based on inorganic semiconducting materials, lies in their lower fabrication cost and formability (MA et al., 2010). Organic molecules containing delocalized π-electron systems have garnered widespread interest due to their applications as active materials in OLEDs, organic field-effect transistors, and photovoltaic devices (BUREŠ, 2014). Within deslocalized π-electron compounds, the π-conjugated push-pull heterocyclic subclass of molecules is particularly important. These molecules contain electron donor (D) and acceptor (A) electronic groups bridged by a π-system, establishing a proper $D - A$ electron coupling and forming $D - \pi - A$ type resonant electronic structures (FERNANDES et al., 2018) (see Figure7.1).

Synthetic chemistry and computational simulation studies have shown that replacing the benzene ring of a chromophore bridge with easily delocalized five-membered heteroaromatic rings, such as thiophene, pyrrole, and (benzo) thiazole, enhances the optoelectronic properties of push-pull molecules. Thiophene and pyrrole derivatives, as donors, substituted with appropriate acceptor groups, are promising candidates among such push-pull systems (MEYER et al., 2012; BUREŠ, 2014; RAPOSO et al., 2006). In recent years, researchers have investigated several push-pull heterocyclic molecules,

including oligothiophene and thienylpyrrole derivatives. These compounds exhibit advantageous properties used in the manufacturing of semiconductor materials, sensitizers, compounds for optical data storage, photoswitches, chemosensory probes, and bioimaging probes (MEYER et al., 2012; BUREŠ, 2014; RAPOSO et al., 2006; OLIVA et al., 2006; MARIN-HERNANDEZ et al., 2014; CASTRO et al., 2016; GARCIA-AMORÓS et al., 2016; FERNANDES et al., 2017; GONÇALVES et al., 2022; GARCIA-AMORÓS et al., 2023).

The utilization of $D-\pi-A$ heterocyclic structures is a viable strategy for designing high-performance organic semiconductors, exploiting the benefits of $D-A$ resonant intermolecular electron coupling provided by π-conjugated molecular bridges (CAI et al., 2013). This electronic coupling phenomenon, referred to in the literature as intramolecular charge-transfer (ICT), involves a relatively lower HOMO-LUMO energy gap (ΔE_{H-L}), excited by photons in the visible region of the electromagnetic spectrum. Hence, the photo-absorption of push-pull heterocyclic compounds is tunable by the judicious choice of D and A groups and π-system constituent moieties of these compounds (FERNANDES et al., 2018; FERNANDES et al., 2021). The design of $D-\pi-A$ push-pull molecules facilitates the development of optoelectronic devices. Electrochemical and optical methods are commonly employed to investigate the ΔE_{H-L} gap and electronic transitions between HOMO and LUMO states. Cyclic voltammetry is frequently used to estimate the energy accessibility of an electrode to the HOMO and LUMO of $D-\pi-A$ molecules in an electrolyte environment. Complementary absorption spectroscopy provides information about the ICT dynamics of $D-\pi-A$ compounds (CARDONA et al., 2011; FERNANDES et al., 2017).

Electrochemical techniques have been indirectly used to access the electronic properties of organic heterocyclic compounds in contact with electrodes employed as a probe to observe the electronic communication. For example, a series of push-pull molecules consisting of bithiophene and thienothiophene moieties as π-bridges structures were characterized using cyclic voltammetry (FERNANDES et al., 2017; FERNANDES et al., 2018).

In these types of experiments, the molecules are not chemically attached to the electrode but are free in a solvent environment, where electronic communication with the

electrode is governed by the diffusion of the molecules to the electrode. In this type of experimental setting, the purpose is to estimate the HOMO and LUMO energy levels of the structures through the determination of the oxidation and reduction potentials of the compounds. The estimation of HOMO and LUMO energy levels is relevant for applications in nonlinear optics and dye-sensitized solar cells (DSSCs) owing to the achievement of the alignment between HOMO and LUMO levels of these organic molecules to semiconductor band gap levels is important for achieving better DSSC devices.

Furthermore, organic structures comprising the self-assembling of thiol-terminated dendritic oligothiophenes of varying lengths on gold surfaces (JIANG et al., 2010) can effectively be used for blocking electron-transfer reactions occurring between the gold electrode and redox species added to the electrolyte. The employment of this type of molecular junction conducts to what is named blocking layers whose goal is to switch off the redox processes.

An additional example of the use of molecular junctions is related to the study of electron transport in organic electronic junctions, for instance, those comprising azobenzene molecules bridging carbon/gold electrodes. This type of junctions were investigated in a solid-state environment using impedance measurements (SANTOS et al., 2020) of the junctions. Recorded impedance spectra of the junctions permitted to study of the conductance and the electron injection rate responses also in adherence to quantum mechanical principles described by Eq. 7.1, demonstrating that electronic and electrochemical principles are common at the molecular scale (BUENO, 2018a) and follows similar quantum mechanical dynamics based on resistive-capacitive components of the junctions within in a molecular energy and length scale.

Although the above-discussed experimental methods and junction fabrication approaches provide insights into the electronic structure of organic compounds, the electronic properties of molecular junctions constructed using physical or chemical covalent attachment of push-pull molecules to metallic or semiconducting electrodes are rarely studied. In this work, the electronic properties of molecular junctions fabricated using push-pull heterocyclic compounds are characterized using time-dependent methods within a quantum rate theoretical viewpoint (BUENO, 2018d; BUENO, 2023c; BUENO, 2020; BUENO, 2023a; BUENO, 2023b). As a molecular junction model, we studied the

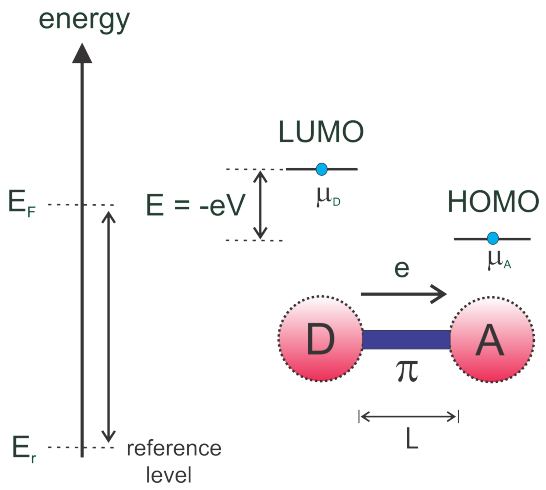

FIGURE 7.1. The schematic representation (for the sake of simplicity without the consideration of the thermal broadening effect) of a $D-\pi-A$ intra-molecular charge resonant structure within the quantum rate theory, where μ_D and μ_A states for the chemical potential of D (LUMO) and A (HOMO) energy levels, respectively. Note that there is no energy barrier activation for the electron dynamics with a quantum channel of length L within this molecular electronic structure, corresponding to an adiabatic setting for quantum electrodynamics within the quantum rate theory. The energy difference between $\mu_D - \mu_A$ is equivalent to the HOMO-LUMO energy gap and numerically it equates to $E = -eV = \mu - E_F$ that, within the quantum rate theory, corresponds to $h\nu = g_e e^2/C_q$, where $\nu = g_e G_0/C_q$ with $G_0 = g_s e^2/h$, where V corresponds to the bias potential of the electrode regarding to E_F/e. E_F states for the Fermi level of the resonant and adiabatically coupled D and A states for a E_r reference level of energy, whereas μ is the chemical potential of the electrons in the electrode side of the junction. Note that the scheme of this figure considers $E = -eV = h\nu$ as an external excitation of electrons from HOMO to LUMO states that hence further relax to the HOMO level in a $D-\pi-A$ molecular structure.

4*H*-thieno[3,2-*b*]pyrrole-5-carboxylic acid (**1,TPC**) molecule attached to a gold metallic electrode surface. The characterization of this **TPC**-Au junction was based on a spectroscopic low-energy perturbation of this molecular junction (quantum rate spectroscopy) in an electrolyte medium, providing an accurate characterization of this junction and revealing its low-energy quantum relativistic electrodynamics.

In the next section, we employ concepts of the quantum rate theory and a spectroscopic method based on the theory to characterize the **TPC**-Au junctions.

7.1.1 Quantum Rate Theory

The quantum rate theory, as elucidated by previous works (BUENO, 2018d; BUENO, 2020), correlates the electron transfer rate concept (ν) with the molecular con-

ductance (G), also known as quantum conductance, through the quantum capacitance (C_q). This theory provides a comprehensive framework for understanding the rate of electron transfer in various contexts, including electrochemical reactions (SÁNCHEZ et al., 2022; ALARCÓN et al., 2021c), the electrodynamics of graphene in electrolyte environments (BUENO; MERCADO, 2022), the respiration in Geobacter (BUENO et al., 2015; BUENO, 2024) and the intramolecular electrodynamics in π-conjugated heterocyclic molecules, as will be demonstrated here.

The quantum rate theory allows for modeling electron exchange between D and A states, elucidating the dynamics of intramolecular electrodynamics in push-pull molecules, akin to redox reactions (BUENO, 2020; BUENO, 2023c). In both scenarios, as verified in this study, the phenomenon adheres to quantum mechanical principles that cannot be accurately described using Schrödinger's non-relativistic quantum-wave methods but can be adequately addressed using quantum electrodynamics. The theory establishes a fundamental quantum rate (ν) principle, expressed by the ratio between the reciprocal of the von Klitzing constant ($R_k = h/e^2$) and the quantum capacitance (C_q), as follows

$$\nu = \frac{e^2}{hC_q}, \tag{7.1}$$

which leads directly to the Planck-Einstein relationship

$$E = h\nu = \hbar \mathbf{c}_* \cdot \mathbf{k}, \tag{7.2}$$

where $\mathbf{c}_*$ represents the Fermi velocity and $\hbar$ is the reduced Planck constant ($h/2\pi$). The relativistic dynamics predicted by this relationship conform to Dirac's relativistic wave mechanics, rather than the non-relativistic Schrödinger equation. This is evidenced by employing the de Broglie wave-particle duality relationship, in which the momentum is defined as $\mathbf{p} = \hbar\mathbf{k}$, being directly proportional to the wave-vector $\mathbf{k}$ and leading to $E = \mathbf{p} \cdot \mathbf{c}_*$ in Eq. 7.2. This constitutes an energy-momentum relationship that is described by relativistic quantum electrodynamics, which is the first success theory where quantum mechanics agree with relativistic principles (GLUCK; AGMON, 2009; GREINER et al., 2000; LAND; HORWITZ, 2022).

The quantum rate theory operates within the framework of quantum electrodynamics, reflecting the intrinsic relativistic character of electrons, but it does not mean that electrons are traveling with the speed of light as naively interpreted by those not familiar with these types of electrodynamics. The meaning is owing that electrons follow Eq. 7.2, exhibiting a massless character (in which electrons are referred to as Fermionic particles) and thus behaving as waves within a constant Fermionic velocity $\mathbf{c}_*$. This is evidenced whenever the electron's rest mass m_0 is null in the relativistic equation $E^2 = (\mathbf{p} \cdot \mathbf{c}_*)^2 + (m_0 c_*^2)^2$, thus predicting the particular $E = \mathbf{p} \cdot \mathbf{c}_*$ quantum electrodynamics situation that conforms with Dirac's equation of the electrodynamics (DIRAC, 1928). It is not novel that the electrodynamics of bidimensional single-layer graphene obeys this relativistic quantum electrodynamics (NOVOSELOV et al., 2005b), but there is experimental evidence (ALARCÓN et al., 2021a; BUENO, 2023c; SANCHEZ et al., 2022; LOPES et al., 2024) supporting that the electrodynamics of diffusionless electrochemical reactions follows this massless Fermionic dynamics within a degenerate energy state $E = \mathbf{p} \cdot \mathbf{c}_* \propto e^2/C_q$. Specifically, in electrolyte environment, E is proportional to e^2/C_q by the g_s and g_e degeneracies, such as $E = g_s g_e (e^2/hC_q)$, where $g_s = 2$ represents electron spin degeneracy and $g_e = 2$ signifies the degeneracy associated with the electric-field screening effect of the electrolyte on molecular states.

Two equivalent interpretations of g_e degeneracy are proposed. Firstly, resonant electric currents, resulting from the combination of electrostatic and quantum capacitances, give rise to an ambipolar electric current, as depicted in Figure 7.2. This current, denoted as i_0, arises due to the electrolyte's role in the superposed electrostatic and quantum capacitive charging modes of molecular junctions. The equivalence of energy states e^2/C_e and e^2/C_q leads to an energy degeneracy that permits two electric currents contributing to the net current i_0 of the interface, referred to as a bipolar electric current.

In the subsequent section, the concept of ν, defined by Eq. 7.1 and stated in terms of the conductance quantum ($G_0 = g_s e^2/h$), which has a constant value of approximately 77.5 μS, will be further elucidated.

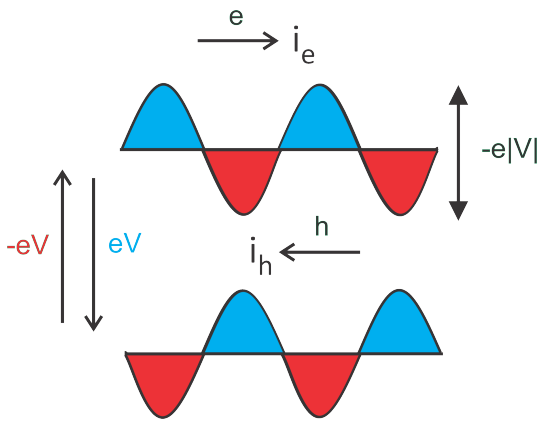

FIGURE 7.2. Schematic representation of the electric current degeneracy predicted by the quantum rate theory owing to the energy degeneracy of the equivalent electrochemical capacitance of the interface C_μ, which is a result of the series combination of electrostatic C_e and quantum C_q capacitances, where $C_e \sim C_q$. The resultant electric current $2i_0 = C_q(dV/dt)$ is an ambipolar electric current where the electron wave flows in the opposite direction to the hole wave. An oscillatory harmonic potential perturbation of the particles in the perpendicular direction of the propagation of the wave permits to assume that $dV(t)/dt = j\omega\tilde{V}$, where ω is the frequency of perturbation over $\tilde{V} = |V|\exp(j\omega t)$ with an amplitude $|V|$ (with an energy $-e|V|$ for the electron and $e|V|$ for the hole) of the potential perturbation. Note that i_0 physically corresponds to a displacement electric current where there is no net transport of charge or particle mass transversal to the perturbation of the particle, which conforms with the quantum electrodynamics viewpoint of the transport of a massless Fermionic-Dirac particle, as stated in Eq. 7.2.

7.1.2 Conductance, Capacitance, and Quantum Mechanical Rate at Atomic and Molecular Scales

It is demonstrable that ν can be expressed in terms of G_0 (BUENO, 2023c), a molecular-scale conductance, by accounting for the degeneracies g_s and g_e in the electrodynamics predicted by Eq.7.1. This relationship is given by

$$\nu = g_e g_s \left(\frac{e^2}{hC_q}\right) = g_e g_s \left(\frac{E}{h}\right) = g_e \frac{G_0}{C_q}, \tag{7.3}$$

where the atomic and molecular-scale definition of capacitance, $C = dq/dV$, is considered, in which $dq = -edn$ and $dV = -d\mu/e$, with $d\mu$ representing the chemical potential energy associated with the perturbation of potential dV. The chemical potential energy per unit charge can be defined as $d\mu/dn = e^2/C_q$. For a single state $dn = 1$, this provides the capacitance of a single resonance mode, leading to $\Delta\mu = e^2/C_q = \mu_D - \mu_A$ for this single quantum channel mode of electron transport. By noting that $dE = -edV = d\mu$, it is

possible to demonstrate that $C_q = e^2\,(dn/dE)$, where $(dn/d\mu)$ corresponds to the density-of-states (DOS). The analysis demonstrates that C_q is directly proportional to the DOS. A more detailed analysis of the significance of C_q is given in the SI (Support Information) document.

The interpretation of ν at room temperature, as described by Eq. 7.3, necessitates the incorporation of statistical mechanics considerations, accounting for the thermal broadening of energy states E associated with the electrodynamics. In the subsequent section, an analysis of C_q and ν incorporating statistical mechanics will be explored.

7.1.3 The Statistical Mechanics of the Quantum Rate

The thermodynamic effects contributing to the thermal broadening of $E = e^2/C_q$ are quantifiable through statistical mechanics, employing the presumption of the grand canonical ensemble (BUENO, 2018d; BUENO, 2023c; BISQUERT et al., 2008). This leads to the expression

$$C_q = \left(\frac{e^2 N}{k_B T}\right)[f(1-f)]\,, \tag{7.4}$$

where $f = (1+\exp{(E/k_B T)})^{-1}$ represents the Fermi-Dirac distribution function, where k_B is the Boltzmann constant and T is the absolute temperature. Under this statistical mechanics analysis, C_q, an experimental observable, transforms into

$$\nu = g_e G_0 \left(\frac{k_B T}{e^2 N}\right)[f(1-f)]^{-1}\,, \tag{7.5}$$

where N denotes the total number of states. Eq. 7.5 describes the overall concept of quantum rate ν for the electronic communication between quantum states at finite-temperature. The definition of ν in Eq. 7.5 corresponds to the electron-transfer rate constant k for diffusionless electrochemical reactions (ALARCÓN et al., 2021c). Eq. 7.5 also incorporates Marcus electron-transfer theory (MARCUS, 1964b) as a particular setting of quantum rate ν, as demonstrated in details in references (BUENO, 2020; BUENO, 2023c). Shortly, by considering the charge-transfer of a single electron in which N equations to the unit and by applying the Boltzmann approximation to f, in which

$\exp(E/k_BT) >> 1$ condition is used for $f = (1 + \exp(E/k_BT))^{-1}$, and finally noting the definition of $G_0 = g_s e^2/h$, Eq. 7.5 provides a $\nu \propto (k_BT/h)\exp(-E/k_BT)$ from which Marcus defined $E = (eV + \lambda/)^2/4\lambda$, with λ as the reorganization energy of the solvent.

Additionally, at the Fermi level of a junction, where $f = 1/2$, and with a single electron transmittance in an ideal adiabatic mode, ν of Eq. 7.5 simplifies to $\nu = k_BT/h$, as anticipated, demonstrating the adherence to quantum mechanical principles at room temperature and the dynamics predicted by the Planck-Einstein relationship for $E = k_BT$. This analysis implies that the electron dynamics between push-pull molecular states and electrodes adhere to Dirac (relativistic) rather than Schrödinger (non-relativistic) equations, as will be elucidated in this manuscript, showcasing that the communication rate is quantized at room temperature, with a value of $G_0/C_q = g_sE/h$ for a perfectly adiabatic quantum channel transmittance setting.

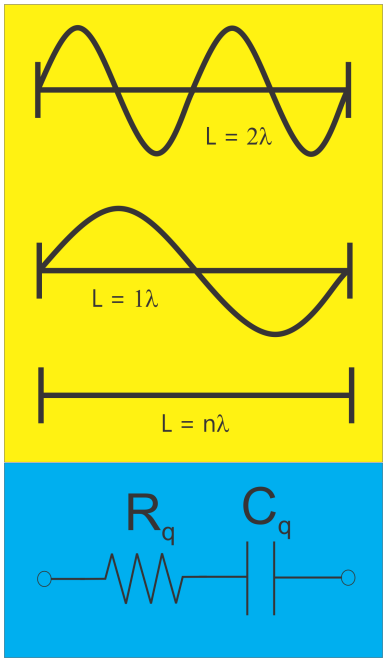

FIGURE 7.3. According to the quantum rate theory within a π molecular bridge of length L separating D and A of push-pull molecular structure, there can be different n wavelength quantum modes λ for an adiabatic intra-molecular electron transfer dynamics to occurs. Independently of the quantum modes of electron transport, the quantum electrodynamics can be studied, according to dynamics predicted by Eq. 7.6, by measuring $\nu = 1/\tau = G_0/C_q$, where $\tau = R_qC_q$ with $R_q = 1/G_0$. In practical experimental terms, $R_q \sim 12.9$ kΩ corresponds to the total series resistance of the molecular junction, encompassing R_e and R_c state for the resistances of electrolyte and contact, respectively.

Owing to $\nu \propto G_0/C_q = 1/R_qC_q = 1/\tau$, where $R_q = 1/G_0 \sim 12.9$ kΩ represents the resistance quantum and $\tau = R_qC_q$ signifies the quantum RC characteristic time of the molecular junction's electrodynamics, we can model the electrodynamics using quantum RC-circuit dynamics. This also permits us to utilize the electric impedance of the interface as a valuable quantum mechanical spectroscopic method, as will be demonstrated in the subsequent section.

7.1.4 Equivalent Circuit and Spectroscopic Analysis of the Quantum Rate Dynamics

Within the framework of the quantum rate theory (BUENO, 2023a; BUENO, 2023b; BUENO, 2023c), the quantum RC dynamics of push-pull molecular junctions can be examined using impedance-derived capacitance spectroscopy, wherein a complex capacitance (BUENO, 2023c; BÜTTIKER et al., 1993) can be measured and analyzed. This complex capacitance is represented by

$$C^*(\omega) = \frac{C_q^0}{1 + j\omega\tau} \approx C_q^0 \left(1 - j\omega\tau\right), \tag{7.6}$$

where C_q^0 in Eq. 7.6 denotes the equilibrium capacitance, attained at $\omega \to 0$, where the imaginary component of the complex capacitance becomes negligible.

A spectroscopic examination based on Eq.7.6 allows for the construction of useful DOS *versus* energy spectra, a technique referred to as quantum rate (QR) spectroscopy (PIZÓN et al., 2024; LOPES et al., 2023). For instance, the analysis of QR spectra, utilizing Eq. 7.6, has been successfully employed to ascertain the electronic structure of graphene (LOPES et al., 2023) and quantum dots (PIZÓN et al., 2024). In the present study, we scrutinize complex capacitive spectra based on Eq. 7.6 for push-pull molecular junctions, enabling us to investigate the applicability of the QR theory in probing the relativistic quantum electrodynamics of organic semiconducting junctions.

7.2 Experimental

7.2.1 Chemical Reagents and Solutions

Commercially available ethyl 2-azidoacetate ($N_3CH_2CO_2C_2H_5$), sodium ethoxide, ($NaOC_2H_5$), sodium hydroxide (NaOH), ethanol, xylene, tetrabutylammonium perchlorate ($TBAClO_4$), dimethylformamide (DMF) and cysteamine were purchased from Sigma–Aldrich. *N,N'*-Diisopropylcarbodiimide (DIC), and 1-hydroxybenzotriazole hydrate (HOBT) were purchased from Chess GmbH. All chemicals were used as received, without further purification. Milli-Q water was used for all the experiments.

7.2.2 Instrumentation

Melting points were determined using a Stuart SMP3 melting point apparatus. TLC analyses were conducted on silica plates pre-coated with a 0.25 mm layer (Merck Fertigplatten Kieselgel $60F_{254}$), and spots were visualized under UV light. NMR spectra were acquired on a 250 MHz Bruker AC 250, 300 MHz Varian Unity Plus Spectrometer, and Bruker Avance III 400, operating at frequencies of 62.9 MHz for ^{1}H and 100.6 MHz for ^{13}C. Chemical shift values (δ relative to TMS) are provided in parts per million (ppm), with the solvent peak serving as an internal reference at 25 °C.

7.2.3 Synthesis and characterization of 4*H*-thieno[3,2-*b*]pyrrole-5-carboxylic acid (1, TPC)

The thienylpyrrole derivative (**1, TPC**) was synthesized via condensation of thiophene-2-carbaldehyde (**I**) and ethyl azidoacetate in the presence of sodium ethoxide and ethanol at -30°C, followed by warming to room temperature, yielding ethyl 2-azido-3-(thiophen-2-yl)acrylate (**II**). Subsequent reflux of azide (**II**) in toluene afforded the condensed system ethyl 4*H*-thieno[3,2-*b*]pyrrole-5-carboxylate (**III**)(KEENER et al., 1968). Hydrolysis of compound **III** using NaOH aqueous solution yielded the corresponding 4*H*-thieno[3,2-*b*]pyrrole-5-carboxylic acid (**1, TPC**), as depicted in Figure 7.4. All compounds underwent thorough characterization, and their structures were confirmed using standard spectroscopic techniques. Compound **1** was obtained for the first time with an 85% yield using a different synthetic approach (WELCH; PHILLIPS, 1999).

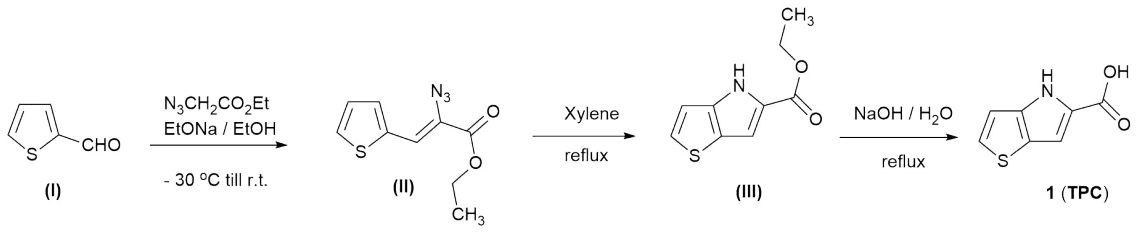

FIGURE 7.4. Schematic depiction of the sequence of synthesis of thienylpyrrole derivative (1, TPC) applied for constructing the molecular junctions studied in the present work.

7.2.4 Preparation of TPC Assembly

Gold electrodes (Au electrodes) were fabricated by radio frequency sputtering, depositing titanium and gold sequentially onto silicon oxide wafers measuring 0.8 x 0.5 cm, resulting in electrodes with an average geometric area of approximately 0.04 cm^{-2}. These Au electrodes underwent a cleaning process involving sequential immersion in solvents: isopropyl alcohol, acetone, isopropyl alcohol, and ultrapure water, each followed by sonication for 12 minutes. Subsequently, the surfaces were dried with N_2 and cleaned under ultraviolet/ozone for 30 minutes. The pretreated Au electrodes were then immersed in an aqueous solution containing 50 mmol L^{-1} of cysteamine for 16 hours at room temperature, facilitating the formation of a cysteamine monolayer over the Au surface. Following this step, the electrodes were rinsed thoroughly with ultrapure water. Next, the cysteamine monolayer-modified Au electrodes were immersed in a solution containing 1.0 mmol L^{-1} of 4*H*-thieno[3,2-*b*]pyrrole-5-carboxylic acid (**1, TPC**) in dimethylformamide (DMF), supplemented with 50 mmol L^{-1} of diisopropylcarbodiimide (DIC) and 50 mmol L^{-1} of 1-hydroxybenzotriazole (HOBT). This incubation step occurred in the dark for 4 hours. Finally, the **TPC** molecule-modified Au electrodes were rinsed again with ultrapure water prior to any measurements being conducted.

7.2.5 Electrochemical Measurements

Electrochemical impedance spectroscopy (EIS) measurements were conducted using a portable potentiostat (PalmSens4) equipped with a frequency response analyzer (FRA) in a three-electrode setup. The working electrode was the **TPC** molecule-modified gold electrode, while a platinum mesh served as the counter electrode. All electrochemical measurements were performed in a 20 mmol L^{-1} solution of tetrabutylammonium perchlorate ($TBAClO_4$) in dimethylformamide (DMF).

EIS spectra were recorded at a fixed bias potential corresponding to the open circuit potential (OCP), which in this study was -0.62 V. A root mean square (RMS) amplitude potential perturbation of 10 mV was applied, with a frequency ranging from 1 MHz to 0.05 Hz. From the raw EIS data, the real (C') and imaginary (C'') capacitive components were obtained using the relationship $Z^*(\omega) = 1/j\omega C^*(\omega)$, where $Z^*(\omega)$ and $C^*(\omega)$ are the impedance and capacitance complex functions, respectively. Here, ω represents the perturbing angular frequency and j refers to the imaginary unit $\sqrt{-1}$. The complex $C_q^{(}\omega)$, consistent with Eq. 7.6, was expressed as $C_q^{(}\omega) = C' + jC''$, where C' and C'' were derived from the real (Z') and imaginary (Z'') components of the measured complex impedance function $Z^*(\omega) = Z' + jZ''$. Note that $|Z| = \sqrt{(Z')^2 + (Z'')^2}$ represents the modulus of impedance. The diameter of the semicircle observed in the Nyquist capacitive diagram, where the C'' component is minimal, corresponds to a frequency denoted as the equilibrium frequency (ω_0). This frequency ω_0 characterizes the charge equilibrium state and is determined for $\omega \to 0$ in Eq. 7.6. It allows access to the DOS function as a function of the junction potential (or electrode potential), which in this study ranged from -2.4 to -0.5 V *versus* a platinum pseudo-reference electrode.

7.3 Results and Discussions

As noted in section 6.1, electrochemistry is frequently used to characterize the electronic properties of push-pull heterocyclic compounds. However, the use of a current-voltage pattern provided by cyclic voltammetric methods is applied to access the electronic properties of push-pull molecules free in an electrolyte medium, as depicted in Figure 7.5*a*. As is the case for redox reactions, this experimental setting, in which the investigated D and A moieties are freely in the electrolyte environment, implies that there is a classical diffusional control of the electron transport from D species to the electrode or the electrode to A species, with the electron transport dynamics controlled by mass diffusion of D and A species from/to the surface of the electrode. In other words, in this setting of electrochemical investigation, the electron transport has a charge transfer kinetics controlled by mass diffusion. Hence, a diffusional control of the electron transport implies that there is no associated quantum capacitance or quantum RC dynamics, as discussed in the context of Eq. 7.6 and, consequently, for this type of electrochemical experimental settings, there is no quantum electrodynamics within a quantum rate approach to be studied.

The above analysis can be confirmed by investigating the current-voltage (CV) pattern, as depicted in Figure S1 of the SI document, obtained by placing a gold working electrode, used as a probe, in direct contact with **TPC** moieties diluted in an electrolyte in a concentration of 1 mmol L^{-1}. From the CV pattern, a potential energy separation, $E_g \sim 2.08$ eV between the first oxidation and reduction current peaks is measured with the potential difference of these peaks not owing be to a resonant dynamics between D and A energy states of **TPC** communicating with the electrode, which is confirmed by conducting an impedance measurement at first reduction peak of the CV pattern. Impedance and capacitance spectra at this peak, corresponding to a potential of -0.65 V in the CV, are shown in Figure 7.6. The impedance spectrum (Figure 7.6a) is typical of a kinetically diffusion-limited process, and the measured electrochemical current in the CV peak is confirmed to be owing to an irreversible reduction of the **TPC** compounds, rather than a resonant electric current.

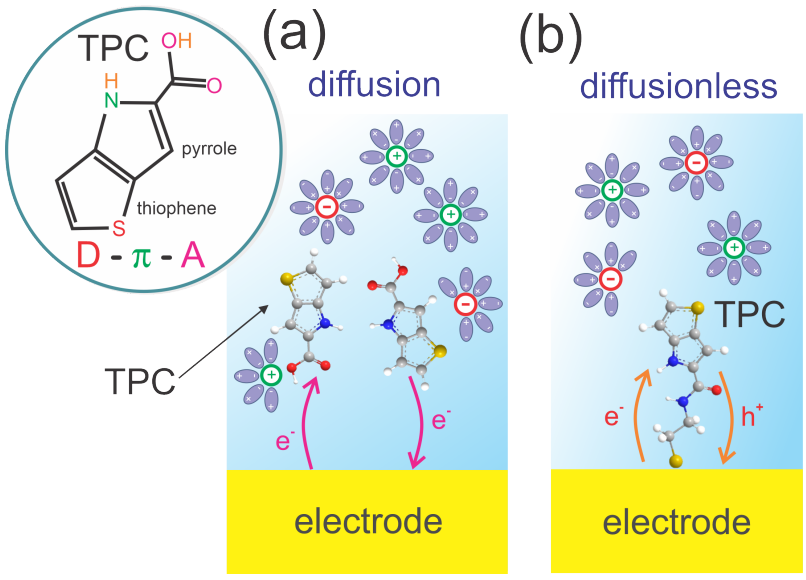

FIGURE 7.5. Schematic representation of two electrochemical setups for studying the electronic structure of push-pull heterocyclic molecules, focusing on the structure of 4H-thieno[3,2-b]pyrrole-5-carboxylic acid (**1, TPC**) molecule in two distinct electrode configurations. (a) This depicts the conventional electrochemical setup, where electron transfer (ET) between the electrode and **TPC** molecules, freely existing in an electrolytic bulk environment, occurs under diffusion-limited conditions. (b) Illustrates the electrochemical configuration investigated in this study, where **TPC** molecules are covalently bonded to electrodes, forming a single-contact molecular junction structure. The supporting electrolyte provides an appropriate electric-field screening condition to explore the electronic properties of the **TPC** molecular ensemble by quantum rate theory. The analysis's alignment with quantum rate theory confirms the quantum electrodynamics governing the interaction of the electrode with the quantum states of the **TPC** molecules.

Also, the Nyquist capacitance spectra measured at the reduction potential of −0.65 V *versus* platinum (as pseudo-reference potential), shown in Figure 7.6*b*, confirmed the above interpretation of the CV pattern. The analysis of this capacitive spectrum is consistent with the irreversible transfer of the electrons from the electrode to the A state (carboxylic acid group, see inset of Figure 7.5*a*) of the **TPC** molecule, as expected for the measurement conducted at the −0.65 V.

Accordingly, both impedance and capacitive Nyquist diagrams of Figure 7.6 confirmed a diffusion-controlled electron transfer process kinetically limited by the transport of **TPC** molecules from the electrolyte bulk medium to the surface of the electrode, and this diffusion-limited ET electric current is well-modeled using a Randle circuit, as shown (see Figure 7.7*a*). Hence, the ET between the electrode and **TPC** molecules free in solution is governed by a series combination of charge transfer resistance R_{ct} and Warburg (W) impedance circuit elements, as indicated in the green box of Figure 7.7*a*. The Warburg impedance element accounts for a diffusion-controlled mass process within a diffusion length region in the surface of the electrode.

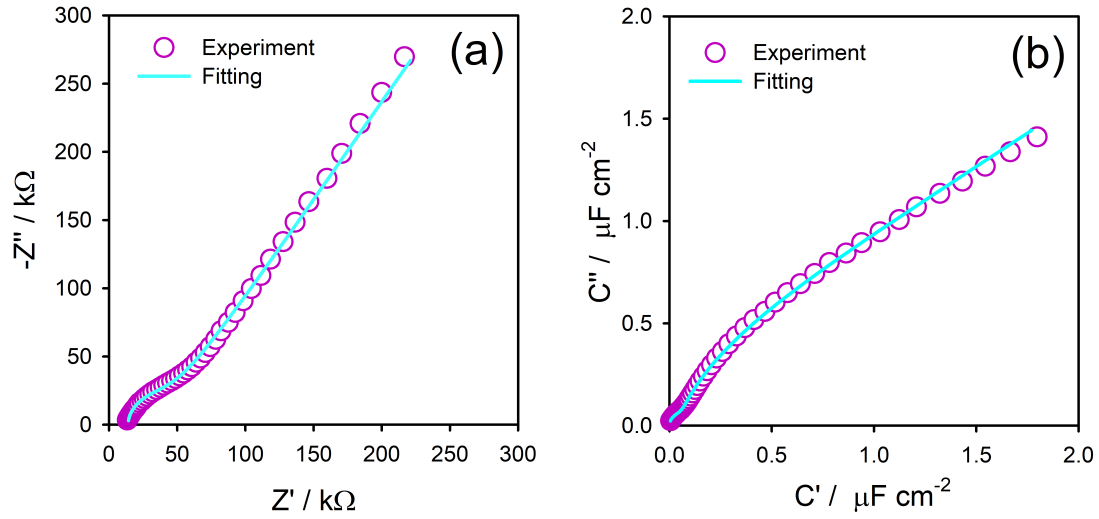

FIGURE 7.6. (a) Impedance and (b) capacitance Nyquist diagrams obtained from the impedance spectroscopic measurements of **TPC** free in an electrolyte environment and in contact with a conducting electrode. The electrolyte, in which 1 mmol L^{-1} **TPC**, was added to DMF with 20 mmol L^{-1} of $TBAClO_4$. These spectra were collected at a potential bias of −0.65 V, corresponding to the first reduction peak in the cyclic voltammogram shown in Figure S1. These spectra were well-fitted to the Randle equivalent circuit model illustrated in Figure 7.7*a*, confirming the governance of ET kinetics of the reactants to the electrode by diffusion.

The fitting of the impedance and capacitance spectra, shown (blue line) in Figure 7.6, to the Randle circuit of Figure 7.7*a* is quite good (with a confidence of 99%) and confirms the diffusion-controlled characteristics of this form of electrochemically evaluating the **TPC** push-pull electronic structure. For the above analysis, an almost three times larger value than the quantum resistance theoretical limit ~ 12.9 kΩ was obtained, i.e. $R_{ct} \sim 42.46$ kΩ.

An additional electrochemical way of characterizing push-pull molecular electronic junctions that complies with quantum rate theory and opens a new possible interpretation of the electrodynamics of molecular junctions in an electrochemical medium, will be evaluated in the next section.

7.3.1 Resonant Molecular Junctions at Electrochemical Environments

In contrast to the electrochemical setting of measuring the electronic properties of push-pull molecular junctions, discussed in the previous section, another way of characterizing the electronic properties of **TPC** heterocyclic molecules that correlates with the quantum rate theory will be discussed here. As depicted in Figure 7.5*b*, **TPC** molecules covalently anchored to a probe conductive electrode, from which the molecular ensemble, is investigated, corresponding to a molecular junction with similar quantum electrodynamics to that measured in redox-active molecular junctions, in which explicitly there are electrochemical reactions and hence electron transfer (ET) undergoing in the junction. However, there are two main differences between push-pull and redox-active junctions: (i) in push-pull junctions, there is no ET process between the molecule and the electrode, and (ii) the quantum conductance in the junctions follows adiabatic electrodynamics.

Accordingly, if an experimental setting, as that illustrated in Figure 7.5*b*, is used for obtaining information on the **TPC** organic/molecular electronic junction, the communication of quantum resonant states of the **TPC** junction with the electrode occurs (i) without ET and (ii) adiabatically, as confirmed by studying the lower frequency region of the impedance/capacitance spectrum measured in this electrochemical setting. The analysis is different from that depicted in Figure 7.5*a* and in the experimental setting of Figure 7.5*b* push-pull molecules are covalently attached to the electrode, with the presence of C_q in place of W circuit element. It implies that, from a physics viewpoint, there is a

diffusionless electron communication of the resonant quantum states of **TPC** molecules with the electrode.

Furthermore, the presence of a C_q term in the **TPC**-electrode junction implies that the DOS of **TPC** resonant states is accessible from a potential perturbation in the electrode and the communication of these states with those of the electrode follows quantum electrodynamics, as predicted by the quantum rate theory and discussed in section 6.1. That the resonant electron communication of the molecules with the electrode involves an electric (resonant) current will now be demonstrated. The physical nature of this current implies an ambipolar electric current even though there is no associated redox reaction nor an effective ET reaction occurring in this type of molecular junction. Although there is no redox reaction, the frequency (or the comunication dynamics) obeys relativistic quantum mechanical rate characteristics, as predicted by Eq. 7.5, in agreement with the quantum rate theory premises. Accordingly, in kinetic terminology, the electron transmittance of wave communication occurs in diffusionless controlled dynamics (Figure 7.5*b*), equivalent to that discussed in references (BUENO, 2023c; ALARCÓN et al., 2021c; SÁNCHEZ et al., 2022) for electrochemical reactions, albeit no ET is effectively occurring.

The resonant electric current (referred to in physics as a displacement electric current) allows us to investigate the quantum electrodynamics of push-pull molecular junctions, measured by imposing a time-dependent perturbation. As the **TPC** junction is formed by the covalent attachment of **TPC** molecules over a conducting electrode, as illustrated in Figure 7.5*b*, there is π-type bridge group that connects D or A to the electrode. Therefore, there is a $D/A-\pi$ resonance communication with the electrode, in which the A group of the pristine $D-\pi-A$ electronic structure of the **TPC** compound, covalent attachment to the electrode, as detailed in section 7.2, permits to the remaining D state to perform either as D or A states for the energy level of the electrode (for more details, refers to Figures 7.1 and 7.10). The attachment of **TPC** molecules to the electrode was attained by chemically modifying the carboxylic acid A group of the **TPC** molecules, allowing the chemical attachment of this A group to the electrode through amine groups present in a previously assembled cysteamine molecular film over the gold electrode.

Figure 7.8 shows the Nyquist capacitive spectrum of the **TPC** molecular junction

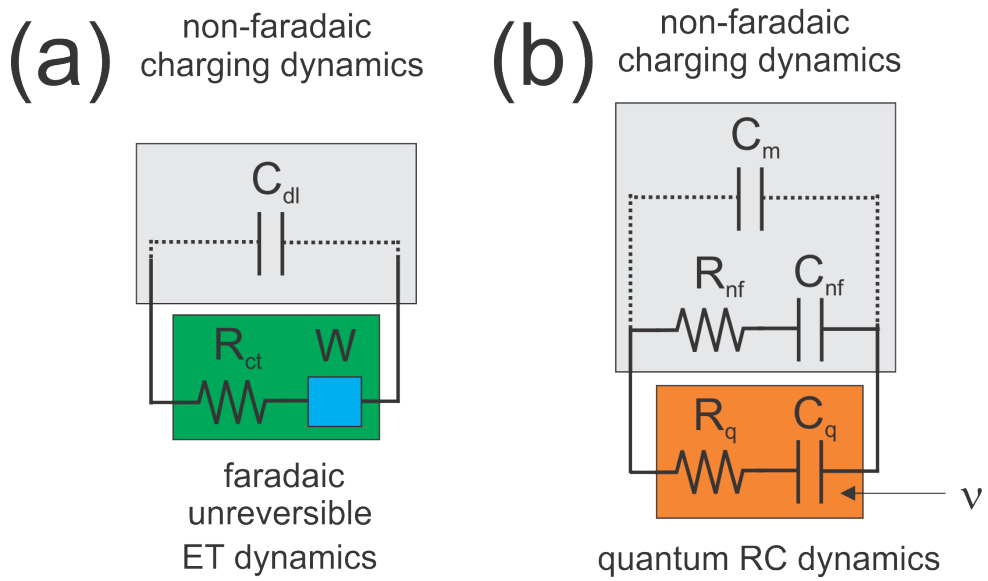

FIGURE 7.7. (a) The traditional Randle equivalent circuit models the direct electric contact of electro-active molecules or compounds, whether undergoing electrochemical reactions or not, within an electrolyte medium, with a conducting electron reservoir (a probe electrode). The series combination of charge transfer resistance R_{ct} and Warburg W circuit elements in the equivalent circuit branch (depicted in green) signifies electron transfer kinetics governed by diffusion. The presence of the W element accounts for electrodynamics controlled by the transport of mass of reacting species toward the electrode. The parallel capacitance C_{dl} corresponds to double-layer capacitance. (b) This equivalent circuit models the electrodynamics of molecularly modified electrodes within an electrolyte environment. The non-faradaic charging dynamics (illustrated in gray) refers to dynamics that do not follow quantum RC dynamics (depicted in red), which involve a series combination of quantum resistive R_q and capacitive C_q elements. The quantum RC dynamics obey the quantum rate dynamics predicted by the quantum rate model, where $\tau = R_q C_q$ corresponds directly to $\nu = 1/\tau \propto e^2/hC_q$ rate.

(blue circles) recorded at the open circuit potential (OCP) and compared with the Nyquist capacitive diagram recorded only with the cysteamine film (red circles), before the chemical attachment of the **TPC** organic structure to the interface containing the cysteamine film. The differences concerning the nature of the electric current $i = C_q s$ are evident in both molecular films, despite an equivalent magnitude of the electric currents, as shown in Figure 7.9*b*, for each of these interfaces. The quantum RC relaxation characteristics are evident in the semi-circle shape of the junction containing **TPC** anchored moieties with the characteristic resonance of the electric current associated with C_q confirmed in Figure 7.9*b*, where now the prevailing resonant electric current $i_0 = C_q s$ measured at the Fermi level of the molecular junction is at least two orders of magnitude higher than that observed in the OCP.

Note that the data shown in Figure 7.9 were measured by firstly constructing the electronic DOS curve of the interface, in agreement to the theory introduced within Eq. 7.4, corresponding to measuring $C_q \propto$ DOS at the room temperature and ambient electrolyte conditions. This room and electrolyte ambient implies that C_q is related to a thermal broadened energy $E = e^2/C_q$ state of the interface, as theoretically introduced in section 7.1.3. The DOS curve, shown in Figure 7.9*b*, was measured by considering a frequency of $\omega_0 \sim 60$ rad/s, as indicated in Figure 7.8, in agreement to the quantum RC dynamics predicted by Eq. 7.6. In other words, the measurement of C_q at different potentials of the electrode for a fixed $\omega_0 \sim 60$ rad/s frequency allowed us to construct the DOS curves for both interfaces, as shown in blue and red dots in Figure 7.9*b*.

Note that the $\omega_0 \sim 60$ rad/s corresponds to the lower possible frequency for Eq. 7.6, which theoretically corresponds to a DC electric measurement. However, for this lower-energy quantum RC dynamics, there is no physical correspondence to DC measurements or ω_0 equating to zero. The latter is owing to the quantum meaning of the conductance, which does not leave a DC-zeroed resistive possibility of interpreting the experiment. The minimum value of ω_0 is equivalent to $\omega_0 = 1/\tau$ that corresponds to a maximum rate owing to the minimum value of $R_q = g_s e^2/h \sim 12.9$ kΩ allowed for the quantum communication between two electronic states in the interface, as better discussed in the context of the quantum rate theory applied to the case of the electrodynamics within graphene (BUENO; MERCADO, 2022).

From the DOS pattern obtained for cysteamine (red circles) and **TPC** (blue circles) junctions, as indicated in Figure 7.9*b*, it is evident that only the **TPC** molecular junction contains aromatic states resonating with the electrode, thus presenting a significant resonant DOS contribution within a i_0 ambipolar type of displacement electric current. Astonishing is the fact that albeit there is no redox reaction or electrochemical faradaic states in the interface, there is a significant pseudo-capacitive contribution at the Fermi level (-1.43 V *versus* platinum pseudo-potential reference), corresponding to a capacitance value ~ 225 μF cm^{-2}. This maximum capacitance value is measurable at the peak of the $C_q = i_0/s$ *versus* potential curve of Figure 7.9*b*. This value of capacitance is confirmed by measuring the Nyquist capacitive diagram at the Fermi level of the junction, obtained as the diameter value of the semi-circle of the Nyquist capacitive diagram, as shown in Figure 7.9*a*.

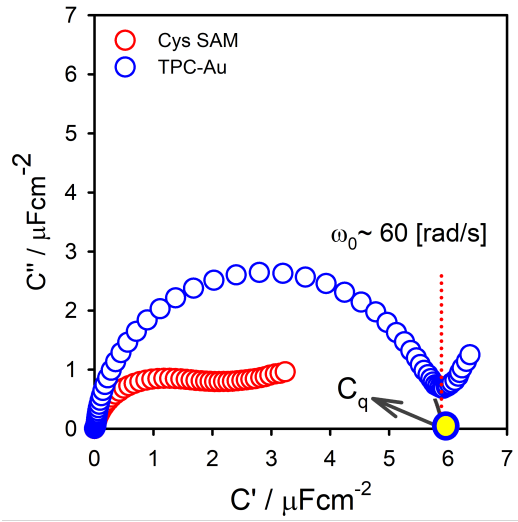

FIGURE 7.8. Nyquist capacitive diagrams measured at the OCP for the cysteamine (denoted in red as Cys SAM) and **TPC** (indicated in blue as **TPC**)-Au junctions in 20 mmol L^{-1} of $TBAClO_4$. The **TPC** junction comprises **TPC** molecules chemically attached to the surface of the electrode employing the cysteamine film. The C_q of the interfaces is accessible as the measurement of the real component of the complex capacitance obtained as the diameter of the Nyquist capacitive diagram. The corresponding frequency for this value of C_q corresponds to the charge equilibrium frequency indicated as ω_0.

The relativistic room-temperature quantum electrodynamics of **TPC**-electrode junctions, is demonstrated in the next section.

7.3.2 Quantum Electrodynamics of Molecular Junction at Room temperature

Note also that the equilibrium charge relaxation frequencies of the cysteamine and the **TPC** molecular junction are very different. The DOS of the cysteamine was resolved as at $\omega_0 \sim 565$ rad/s, whereas for the **TPC** junction, it was at $\omega_0 \sim 60$ rad/s. The Gaussian-shaped response of the **TPC** molecular junction confirms the theory not only because it indicates the existence of the displacement electric current associated with interfacial quantum states but because these are electronic quantum mechanical states measured at room temperature. There is a good agreement ($R^2 \sim 0.998$) with the quantum rate theory, as verified in Figure 7.9*b*, where the fitting (yellow line) of Eq. 7.4 to the experimental thermal broadened DOS curve (blue circles) is demonstrated. It is worth noting that at the Fermi-level (E_F = -1.43 V) of the junction, corresponding to an occupancy of $f = 1/2$ in Eq. 7.4, C_q is resolved as $C_q = e^2N/4k_BT$. Owing to C_q, at

Fermi-level, is experimentally measured as the maximum of the Gaussian-like response of Figure 7.9*b*, as predicted by Eq. 7.4, the total number of quantum states N is thus calculated as $N = 4k_BTC_q/e^2 \sim 6{,}3 \times 10^{12}$.

This value of $N \sim 6{,}3 \times 10^{12}$, calculated at the Fermi level, corresponds to a quarter of the total number of states owing to that the expression $N = 4k_BTC_q/e^2$ does not take into account the energy $E = e^2/C_q$ degeneracy which, in agreement to the quantum rate theory, must be taken into account for an appropriate interpretation and quantification of the quantum electrodynamics of communication with the electrode existing via the ambipolar nature of the electric displacement current. Hence, by calculating the total amount of states as $N = 1/e \int C_q(V)dV$, which is a pure mathematical analysis without a physical interpretation where the integral $\int_0^V C_q(V)$ corresponds to the area under the curve of the Gaussian-shaped response of C_q (Figure 7.9*b*), a value of $\sim 25{,}4 \times 10^{12}$ is obtained, which is, as expected, approximately four times higher than the value calculated by $N = 4k_BTC_q/e^2$. The above-stated analysis confirms the physical interpretation of the energy degeneracy and electric current displacement required to interpret the physical chemistry of the electronic communication of the **TPC** molecular states with the electrode. Finally, note that a consideration of the energy degeneracy would theoretically lead to $N = k_BTC_q/e^2$ at the Fermi level, which fits quite well to the mathematical analysis of the DOS curve of Figure 7.9*b*.

To understand that the electrode can act as both D or A states for the thiophene group of the **TPC** organic compounds communicating with the electrode, as illustrated in Figure 7.10, note the bias potential applied above or below the Fermi level of the junction. Assuming a negative elementary charge for the electron and the Fermi level as the reference, as depicted in Figure 7.10, a positive potential bias of the electrode acts as D states for the **TPC** molecular states and a negative bias as A. Note also that the displacement electric current can only be measured, as the case of redox junctions, by using a time-dependent perturbation.

The above analysis demonstrates that the electron transport (or wave communication phenomenon) is intrinsically associated to a quantum electrodynamic event investigated only under an appropriate time-dependent electric potential perturbation. The Gaussian-shaped DOS resolved for an ensemble of **TPC** organic molecules assembled to

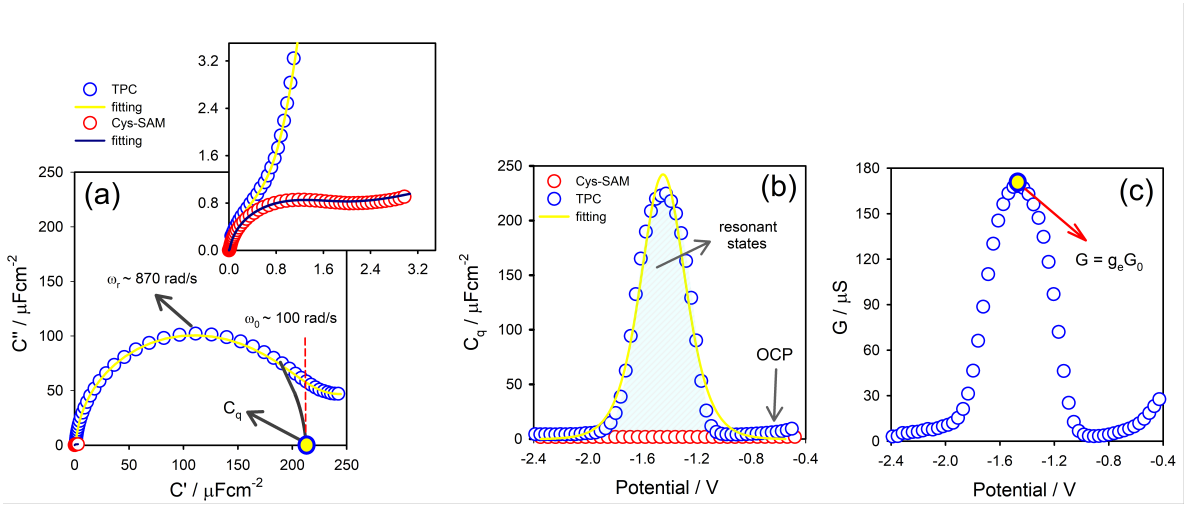

FIGURE 7.9. (a) Nyquist capacitive diagrams were recorded at the Fermi level of the electrode, denoted as E_F/e, corresponding to a potential bias of -1.43 V *versus* a platinum pseudo-reference. The electrode was composed of either cysteamine (Cys SAM) alone or containing **TPC**-Au on top. Electrochemical measurements were conducted in a 20 mmol L^{-1} concentration of $TBAClO_4$ in DMF. The C_q value of junctions containing **TPC** (measured at $\omega_0 \sim 100$ rad/s) is two orders of magnitude higher than the capacitance of the junction solely comprising cysteamine. (b) By measuring the capacitance of junctions containing only cysteamine or with **TPC** on top, it is evident that the quantum relaxation dynamics and the relativistic communication of states between the electrode and the thiophene group contained in the junction containing **TPC** give rise to a C_q state associated with a conductance quantum of $g_s e^2/h$. (c) The response of quantum conductance $G \sim \omega_0 C''$ of the junction containing **TPC** is depicted as a function of the energy of the electrode, where C'' represents the imaginary component of the capacitance of the interface (Eq.7.6). As anticipated from the analysis of Eq.7.4 and Eq. 7.5, G exhibits a Gaussian-shaped behavior. Furthermore, at the Fermi level, both C_q and G reach their maximum values. The maximum value of G attained at the Fermi level was calculated as $g_e G_0$, confirming not only the degeneracy of energy g_e as predicted by the quantum rate model but also demonstrating the adiabatic establishment of relativistic quantum electrodynamics for the dynamics of the **TPC** junction studied in this work.

the electrode represents a particular quantum mechanical event not yet well-understood. In other words, albeit this electrodynamic phenomenon follows the well-known Einstein-Planck $E = h\nu$ phenomenology, which is quite specific for the physics of high energy particles that precisely quantifies and explains the photon-electric phenomenon, the electronic communication established and measured here between **TPC** molecular states and electrode is a low energy electrodynamics in which the intrinsic frequency of the quantum RC process corresponds to an ultra-low frequency of the electromagnetic spectrum.

For instance, in the present experimental study, the ν characteristic frequency for

thiophene electronic states to communicate with the electrode corresponds to frequencies ~ 140 s^{-1} or 870 rad s^{-1}, as indicated in Figure 7.9*a*, meaning an electromagnetic phenomenon with energies $E = h\nu$ in between peV to feV. Note that this characteristic low-energy quantum RC dynamics is here investigated using a small amplitude perturbation of 10 mV RMS, meaning an amplitude perturbation of about seven mV peak-to-peak, corresponding to an electric-field amplitude perturbation that is about three times lower than that of the thermal voltage, i.e. $k_BT/e \sim 25.7$ mV. In other words, despite a thermal energy (k_BT) three times higher than that used for taking information from the experiment, there is a phase resolution of the electric signal. The latter is explained based on the existence of an experimental quantum coherence despite the thermodynamics and of the entropy.

As previously noticed, the communication between **TPC** molecule moieties and electrode states does not involve the transfer of electrons nor electrochemical reactions limited by diffusion. The latter conjunction of facts effectively demonstrates that the low-frequency electromagnetic perturbation of the electrode permits a resonant communication with thiophene molecular states through an electric displacement current that is essentially dynamic. This electromagnetic communication between electrons perturbed in the electrode and the electric current resonance in the thiophene moiety of the **TPC** compound is additionally an adiabatic type of electric communication, as was previously observed in measurements conducted in single-layer graphene (BUENO; DAVIS, 2020).

This section demonstrated that by applying a time-dependent potential perturbation (with an amplitude that is at least three times lower than the thermal energy), with a specific frequency of ω_0, in the electrode, there is an induced electric and magnetic field that implies a low-energy electromagnetic wave propagation from the electrode toward **TPC** molecules. This electromagnetic wave can perturb the quantum resonant states of the thiophene in the **TPC** molecular film, implying a low-energy electrodynamic way of studying electronics. The response to the sinusoidal potential perturbation of the electrode measured as a time-dependent induced electric current (referred as to displacement current) associated with the meaning of C_q obeys the quantum RC dynamics of Eq. 7.6.

The physical interpretation for this observed low-energy electrodynamic phenomenon is that there is a quantum coherence phase dynamics between the potential

perturbation and electric signal responses, not affected by the thermodynamics. Using the $E = h\nu$ electrodynamics interpretation of this electric perturbation or spectroscopic analysis, it implies a viewpoint of the phenomenon governed by the propagation of a $E = h\omega_0$ electromagnetic wave energy (a massless transport of energy that resembles an antenna electromagnetic communication) toward the **TPC** molecular film that, contrary to the sole cysteamine chemistry of the interface, has intra-molecular resonant dynamics owing to the present thiophene-pyrrole aromatic rings within the film. Quite interesting is that the quantum coherence at room temperature allows for perturbing the quantum states (with extremely low-energy) spectroscopic energy that permits studying of the quantum mechanics of push-pull compounds in its almost pristine electrodynamics (there is no perturbation or interaction of a high energy particle with the electrons of the system, as is the case of traditional electron or photon spectroscopic measurements). The nature of this electromagnetic perturbation allows us to idealize a new electric spectroscopic way of characterizing the electronic structure and to measure the DOS through direct measurement of C_q, as was predicted in reference (MIRANDA; BUENO, 2016).

This spectroscopic methodology was referred to as quantum-rate spectroscopy (QRS) and allowed us to measure the electronic structure of graphene (LOPES et al., 2023) and inorganic quantum dots (PIZÓN et al., 2024) at room temperature and electrolyte medium with an accuracy that is comparable to those obtained by angle-resolved photoemission (ARPES) and scanning tunneling (STS) spectroscopic methods that require low-temperature and ultra-high vacuum environment besides of expensive piece of equipment whereas QRS use hand-held inexpensive potentiostats. Furthermore, calculated by density-functional computational methods (DFT) agreed with QRS spectra. DFT computational methods were employed to model the electronic structure of molecular junctions, where the equilibrium charging dynamics of redox molecular junctions were studied (FELICIANO; BUENO, 2020b; BUENO et al., 2021; BUENO et al., 2015). Conceptual DFT can be easily correlated with the meaning of C_q as the energy e^2/C_q corresponds to the variation of the chemical potential upon the exchange of electronic particles (MIRANDA; BUENO, 2019). Furthermore, C_q can serve as an experimental functional of the electron density (BUENO; MIRANDA, 2017) and a detailed theoretical approach for the meaning of electrochemical capacitance[1] based on conceptual DFT was also recently demonstrated

[1]The meaning of the electrochemical capacitance incorporates other contributions besides the energy of the quantum states, such as electrostatics. In the case of Tobias's work (TOBIAS, 2023), it also

by others (TOBIAS, 2023). The correlation between C_q and electron transport properties was previously established within a DFT approach (BUENO; MIRANDA, 2017). However, to better understand the electrodynamics within the quantum-rate viewpoint, time-dependent DFT is probably the right approach for future works.

In the next section, it will be discussed, in more detail, the adiabatic nature of the above-discussed quantum electromagnetic phenomenon.

7.3.3 Adiabatic Quantum Electrodynamics of Push-Pull Molecular Junctions

An analysis of the adiabatic nature of the quantum electromagnetic phenomenon discussed in section 7.3.2 enables investigating the efficiency of the electrodynamics of communication of measured DOS of thiophene-pyrrole aromatic rings with the electrode. The confirmation that there is an adiabatic electron coupling signifies that there is a maximum efficiency of electron 'transport' or better said, transmittance. Effectively, as demonstrated in preceding sections, there is no mass diffusional transport of species and the phenomenon follows a relativistic Dirac-like electrodynamics (DIRAC, 1928), in agreement to Eq. 7.2 and experiments conducted in graphene (BUENO; MERCADO, 2022), implying that for push-pull molecular junctions there is a relativistic quantum electrodynamics equivalent to dynamics followed by massless Fermionic particle within a quantum rate theoretical interpretation of the quantum electrodynamics of graphene.

In other words, within the quantum rate analysis of Eq. 7.2, there is the meaning of $\nu = e^2/hC_q = E/h$, as stated in Eq. 7.1, that, with the consideration of g_e electric-field or potential degeneracy owing to an electron-ion pair dynamics within the electrolyte, leads to define a quantum electrodynamics frequency that follows Eq. 7.3. This electrodynamics frequency, according to Eq. 7.3, is proportional to the resistance quantum $R_q = 1/G_0 = h/2e^2 \sim 12.9$ kΩ of the molecular junction.

This resistance was here shown to be adiabatic, implying a perfect transmittance of electrons through a resistance quantum R_q of 12.9 kΩ within the junction without any potential decaying term, meaning that $\kappa = \exp(-\beta L) \sim 1$ and demonstrating a perfect electronic coupling κ between molecular D/A quantum and electrode A/D energy states.

incorporates exchange-correlation contributions as a term within DFT's Hamiltonian.

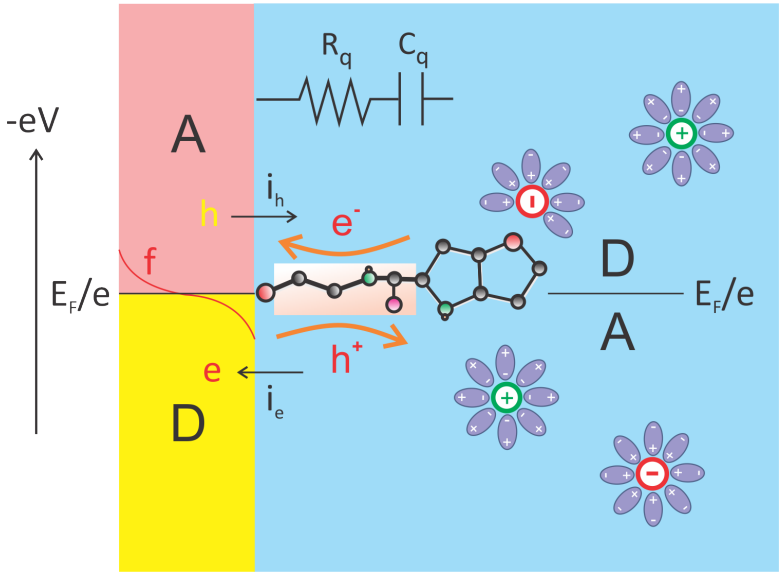

FIGURE 7.10. The electron/hole communication dynamics of the electrode with the thiophene group of **TPC** molecular film depends not only on the existence of a potential perturbation in the electrode but also on the bias for the Fermi potential E_F/e of the junction. Depending on the Fermi energy E_F level of the electrode, there is an electron or hole current, and the thiophene group of the (**TPC** can act as a D or A level, for instance. For positive bias of potential (providing the elementary charge of the electron is assumed as negative value) concerning E_F/e, the thiophene groups of **TPC** molecular film act as D and the electrode as A state and *vice-versa*. In this schematic depicting of the quantum electrodynamics, there is an electric hole current from the electrode to thiophene, and 'effectively' an electronic communication of the electrode with the molecular film, as illustrated in this figure.

For redox reactions (BUENO, 2023c), as studied within the quantum rate theory, there is a charge transfer resistance (SÁNCHEZ et al., 2022) that is equivalent to the quantum resistance of $R_q = N\exp(-\beta L)/G \sim 12.9$ kΩ of the electrochemical junction undergoing redox reactions within an electron tunneling dynamics that contains a potential decaying term of $\exp(-\beta L)$, where G is the total (measurable) conductance of the junction and N the total (measurable) number of quantum states participating in the redox reaction, L is the length of the barrier and β (both experimentally estimated) is a parameter associated with the potential barrier height.

The present study of the molecular electronics and electrodynamics of push-pull heterocyclic resonant junctions demonstrates that the R_q measured at the Fermi level ($E_F/e = -1.43$ V) is astonishingly close to the theoretical value of 12.9 kΩ, and contrary to redox-active junctions, is not associated to a tunneling mechanism and hence there is no $\exp(-\beta L)$ decaying term. For the case of push-pull heterocyclic resonant junctions, the

quantum conductance G corresponds to $g_e G_0$ (see SI document, section S4 for additional information) and the communication of the quantum (resonant) states of the molecules with the electrode is adiabatic and do not depend on the properties of the linker, which is, in the present junction, a chemical π-type bridge.

The above statement confirms the findings from the equivalent circuit analysis of **TPC** molecular junctions. The equivalent circuit was constructed using a circuital mathematical fitting approach for junction modeling. This circuit predicts a dominant quantum RC dynamics over the classical polarization dynamics of the interface, consistent with Eq.7.6. Accordingly, the capacitive complex function depicted in Figure7.9*a* was fitted to the equivalent circuit shown in Figure 7.7*b*. In this model, the polarization dynamics of the interface, including those associated with the cysteamine underlying film (Cys-SAM), were considered to increase the accuracy of the analysis. Mathematically, at the Fermi level of the junction, the RC response is predominantly governed by the quantum RC term.

The fitting (yellow line) of the complex capacitance function (blue dots) of the interface to the circuit in Figure 7.7*b* is illustrated in Figure 7.9*a*, demonstrating a suitable numerical mathematical fitting. A value of ~ 225 μF cm^{-2} was obtained for C_q, while a value of ~ 2.3 μF cm^{-2} was assigned to the capacitive C_{nf} contribution of the cysteamine film, consistent with the equivalent circuit in Figure 7.7*b*. The minimal C_{nf} contribution was confirmed by separately fitting (black line) the complex capacitive spectrum of the cysteamine film (red dot), as shown in the inset of Figure 7.9*a*, to the equivalent circuit highlighted in the gray box of Figure 7.7*b*. The average values obtained for each circuital element of the equivalent circuit analysis are presented in Table 7.1. Therefore, this equivalent circuit analysis demonstrates that the quantum RC dynamics govern over the non-faradaic polarization charging dynamics at the Fermi level.

It is noteworthy that the resistance quantum of molecular junctions embedded in an electrolyte environment, as observed in the case of redox-active molecular junctions (SÁNCHEZ et al., 2022; BUENO, 2023c) undergoing electrochemical reaction, comprises the total series resistance of the interface and not only the resistance of the **TPC**-cysteamine film. Specifically, $R_q = R_s + R_{qt}$, where R_s includes the contact and solution resistance, and R_{qt} is an internal resistance within the molecular film, sometimes

referred to as uncompensated resistance (BUENO et al., 2013). In other words, the resistance quantum of the interface encompasses the total series resistance of the junction and not just the resistance of the **TPC**-cysteamine film assembled over the electrode.

TABLE 7.1. Values of circuit parameters were derived from the fitting of the impedance spectra to the equivalent circuit illustrated in Figure 7.3*b*. Here, $\overline{x}$ denotes the mean average value, and $\sigma_{\overline{x}}$ represents the standard error of the mean of three independently constructed junctions incorporating **TPC** molecules anchored to a cysteamine film.

Parameter	$\overline{x}$	$\sigma_{\overline{x}}$
R_s(kΩ)	1.13	0.02
C_m (μF cm^{-2})	0.056	0.008
R_{nf} (kΩ)	3.0 x 10^{-4}	0.5 x 10^{-4}
C_{nf} (μF cm^{-2})	2.3	0.3
R_{qt} (kΩ)	0.93	0.05
C_q (μF cm^{-2})	224	16

Note also that the characteristic angular frequency associated to ν is ascribed to as $\omega = e^2/\hbar C_q$ which, in agreement to $\omega\tau$ nomenclature stated in Eq. 7.6, leads to $\tau = 2\pi R_q C_q$, where $R_q = R_s + R_{qt}$, such as that $R_q = 2\pi(R_s + R_{qt})$ (SANCHEZ et al., 2022). The values of R_s and R_{qt} computed from the fitting to the equivalent circuit, as shown in Table 7.1, conduct to $R_q \sim 12.92 \pm 0.44$ kΩ. This experimental value of R_q, within the experimental error, is indubitably very close to the theoretical value of 12.99 kΩ and demonstrates the certainty of the quantum rate theory and the adiabatic character of the quantum electrodynamics of push-pull molecular junctions.

In other words, the above analysis demonstrates that the measured resistance at the Fermi level of the **TPC**-electrode junction, embedded in an electrolyte medium, obeys the quantum limit of $R_q = h/2e^2 \sim 12.99$ kΩ and confirms that there is a maximum quantum mechanical efficiency of the electron transport in this type of organic molecular junctions with an adiabatic electron coupling regime that follows relativistic dynamics, fulfilling Eq. 7.2. The analysis do not only validates the quantum rate analysis of these types of junctions but also predicts a Fermionic massless particle dynamics that conforms to the electrodynamics of graphene, as previously studied using a quantum rate theoretical approach.

Besides the calculation of $R_q \sim 12.92$ kΩ via the resistive elements that comprise the **TPC** molecular junction using an equivalent circuit analysis, as conducted above, the

value of $R_q = 1/G_0$ is alternatively quantified through an analysis of $\nu = g_e g_s e^2/hC_q = g_e(G_0/C_q)$ measured at the Fermi level of the junction, from where the measurements of ν and C_q permits to evaluate G_0, self-consistently demonstrating that R_q is $R_q = g_e/\nu C_q$. Average values of $\nu = \omega/2\pi$ and C_q, at the Fermi level, were measured in three independently fabricated junctions, as detailed in section S3 of the SI document. C_q, obtained at the maximum of the Gaussian-shaped response, corresponded to the value of C_q at the peak of the DOS function (measured at a frequency of ω_0), as shown in Figure 7.9*b*. The average value of G_0 estimated from the above analysis was 76 ± 3 μS that, within experimental error, is close to the theoretical value of $G_0 = 77.5$ μS and confirms the certain of the analysis.

Still, another analysis reveals the certainty of the quantum rate theory, consisting in calculating the quantum of the conductance G of the junction directly from the complex capacitance associated with Eq. 7.6, from where $G = \omega_0 C''$ is obtainable. The measurement of G at ω_0, as a function of electrode potential level, is shown in Figure 7.9*c*. Such as in the case of the C_q, shown in Figure 7.9*b*, G has a maximum value at the Fermi level of the junction. The peak of G at the Fermi level has a value of $\sim 154.7 \pm 2.0$ μS, corresponding to a mean value (among three independently fabricated junctions) that is quite close to the theoretical value of $g_e G_0 \sim 154.9$ μS, i.e. twice $G_0 \sim 77.5$ μS. Precisely, as shown in more detail in the S4 section of the SI document, the mean value of G obtained from three different junctions corresponds to 154.7 ± 2.0 μS, corresponding to about 1% of difference with the theoretical $g_e G_0 \sim 154.9$ μS value.

The analysis conducted in the last paragraph for the calculation of G as $G = \omega_0 C''$ not only demonstrated the confidence of a quantum rate theoretical analysis of electrodynamics of push-pull organic molecular junctions but also confirmed that the g_e is critical for the analysis of molecular junctions embedded in an electrolyte environment.

Finally, the consistency is confirmed of a comparative analysis of irreversible and reversible electric modes of push-pull moiety electronic states to communicate with the electrode, which can be conducted using different electrochemical settings, as discussed in section 7.3.3. Particularly in the schemes illustrated in Figure 7.5, there is an irreversible (scheme depicted in Figure 7.5*a*) or reversible (in Figure 7.5*b*) way of electronic communication of the push-pull molecular states with the electrode.

In the irreversible (kinetically controlled by diffusion) scheme, in which the molecules are freely in an electrolyte environment, there is an electric potential separation of ~ 2.08 V between the first oxidation (electrons flowing from the HOMO state of the molecules to the electrode) and first reduction (electrons flowing from the electrode to the LUMO state of the molecules) current peaks, which have not an ambipolar character but can be associated with ΔE_{H-L} gap, as introduced in section 6.1. On the other hand, in the case of a reversible resonant communication of the molecular states with the electrode, which occurs thankfully due to a chemical attachment of the molecules to the electrode (with diffusionless kinetics), the electric current is intrinsically ambipolar, as illustrated in Figure 7.10. In this case, there is a resonant adiabatic quantum electrodynamics, as concluded in the present section, implying, as was demonstrated in a previous work (BUENO, 2018d), that the energy $E = e^2/C_q$ is related to the HOMO and LUMO gap of molecular ensemble attached to the electrode. This ΔE_{H-L} gap is estimated as the width of the DOS depicted in Figure 7.9*b*, hence computed as ~ 1 eV, corresponding approximately to the half of ΔE_{H-L} gap of ~ 2.08 eV estimated from the CV pattern measured in an irreversible electrochemical setting.

The above analysis strengthens the interpretation of the degeneracy g_e as being due to the presence of an ambipolar electric current associated with the overlap of quantum (C_q) and classical (C_e) capacitive states of the junction. Equivalently, this can be interpreted as an energy degeneracy linked to the electric potential ($e/C_e \sim e/C_q$) arising from the electric-field screening conducted by the electrolyte medium over the quantum resonant states of the push-pull moieties communicating with the electrode.

7.4 Final Remarks and Conclusions

The present study demonstrates the feasibility of establishing an adiabatic electron coupling between a push-pull molecular ensemble and a probe electrode. This adiabatic electron coupling enables the investigation of the quantum resonant states of the molecules with the electrode. The exploration of quantum states resonating with the electrode occurs through an electromagnetic communication, adhering to the premises of quantum electrodynamics, which follow the Einstein-Planck relationship $E = h\nu$. This implies a quantum relativistic dynamics between quantum states in push-pull heterocyclic sites and the electrode, wherein, according to the quantum rate theory, the $\nu = e^2/hC_q$ rate is

directly linked to the quantum capacitance $C_q \propto e^2$DOS of the junction. This capacitance is proportional to the accessible density of junction quantum resonant states, where DOS $= (dn/dE)$.

As C_q is experimentally accessible through conventional impedance spectroscopic measurements such as impedance or impedance-derived capacitance spectra (within the interpretation of Eq. 7.6), it provides a way of studying the quantum electrodynamics of molecular junctions embedded in an electrolyte environment. The presence of an electrolyte environment implies an additional electric-field degeneracy g_e that summed to the electron spin degeneracy, conducts to an electromagnetic communication way, demonstrated to follow $E = g_s g_e h\nu$ quantum relativistic electrodynamics, permitting demonstration that $\nu = g_e G/C_q$, which is not only in agreement to the quantum rate theory but also establish an alternative way of designing molecular electronics junctions and nanoscale electronic circuits.

The observed quantum relativistic phenomenology of **TPC** push-pull molecular junctions is equivalent to that observed for electro-active interfaces undergoing redox reactions; however, for the case of **TPC** junctions there is a particular adiabatic electron coupling in which effectively $\nu = g_e G_0/C_q$ is obeyed, instead of $\nu = g_e G/C_q$, as observed for redox-active molecular junctions, where a $G \propto \exp(-\beta L)$ exists. The existence of $G \propto \exp(-\beta L)$ for redox-active junctions, thus with a tunneling mechanism governing the electronic coupling, is different from that observed in push-pull that implies that $G = G_0$, possibly associated with the π-type molecular bridge electronic coupling. In one (electrochemical) or another (electronic) situation, the coupling of states to the electrode obeys a relationship consistent with the quantum rate $\nu = g_e G/C_q$ concept.

Author Contributions

Edgar Fabian Pinzón Nieto: Methodology, Investigation, Visualization, Writing - Original Draft. **Laís Cristine Lopes**: Methodology, Investigation, Visualization. **Adriano dos Santos**: Methodology and Investigation. **Maria Manuela Raposo**: Methodology, Investigation, Visualization, Synthesis of **TPC** Compound, Writting original-draft of the manuscript. **Paulo Roberto Bueno**: Conceptualization, Theoretical Analysis, Supervision, Resources, Methodology, Writing - Original Draft and Final

Versions of this text.

Conflicts of interest

There are no conflicts to declare

Acknowledgements

Paulo R. Bueno: Grateful to the Sao Paulo State Research Foundation (FAPESP) for grants 2017/24839-0 and the National Council for Scientific and Technological (CNPq).

Edgar F. Pinzón: Acknowledges FAPESP for his PhD scholarship (grant 2018/24525-9).

Fundação para a Ciência e Tecnologia (FCT) and FEDER-COMPETE: For financial support through the research center CQUM (UID/QUI/0686/2016) and (UID/QUI/0686/2020).

National NMR Network (PTNMR): Partially supported by Infrastructure Project Nº 022161, co-financed by FEDER through COMPETE 2020, POCI and PORL, and FCT through PIDDAC.

Microfabrication procedures: Were performed with the assistance of Dr. R. C. Teixeira and the Electronic Packaging Staff at CTI Renato Archer Brazil under proposal PAP : 2019-06568-5.

Chapter 8

Discussion: Nanoscale Electronics in an an Electrolytic Medium

As discussed in Section 2 , QRS, based on the quantum electrodynamics principle $E = h\nu = e^2/C_q$, is a powerful tool for experimentally obtaining quantum insights into nanoscale structures (LOPES et al., 2021; BUENO; DAVIS, 2014b; SANCHEZ et al., 2022). This novel approach involves performing impedance-derived capacitance measurements in an electrolytic medium at room temperature, using a three-electrode electrochemical cell, and a potentiostat with a frequency analyzer as the measuring equipment. In this context, building upon the foundations of QRT discussed in previous studies, QRS not only facilitates probing the intrinsic electrodynamics of these structures but also offers direct access to their electronic properties, such as the electron density of states (DOS), through the measurement of the response of C_q.

Given the current challenges in fabricating nanoscale optoelectronic devices with semiconductor structures smaller than 10 nm—where electrical properties deviate from classical physics, complicating their control (BUENO, 2018a; DHILLON; KANT, 2017)—this PhD research explored the electrodynamics and electronic DOS in four nanoscale structures with different types of quantum confinement and chemical nature. This research was based on the premise that the electronic properties of the core material govern device performance, making access to its electronic structure essential. In this context, the study examined these structures from the perspective of QRT and utilized time-dependent electrochemical impedance measurements. The exploration of each of these structures progressively contributed to establishing the foundations QRS as an electronic spectroscopic methodology. The following paragraphs present a synthesis of

the principal results and conclusions from the studies conducted on these semiconductor structures. The author, admittedly influenced by romanticist tendencies, invites readers to view this synthesis as a narrative of a journey in pursuit of an objective that transcends academic boundaries, for that is what this work represented to him.

In this context, the journey began with the study of a redox-active transition metal oxide structure: Cu_2O/CuO mixed nanofilms. These semiconductor structures were fabricated on a gold electrode surface using electrochemical techniques, including cyclic voltammetry, linear sweep voltammetry, and chronoamperometry (Figure 4.1a). Electrochemical and morphological characterization indicated that the copper oxide nanofilms contained a 1:1 mixture of Cu_2O and CuO, had a thickness of approximately 3.0 nm, and exhibited a morphology characterized by larger, heterogeneous particle distributions. As reported elsewhere, metal oxide semiconducting structures composed of equivalent domains with different oxidation states exhibit pseudocapacitive properties due to the electrodynamics associated with electron transitions between oxidation states (LOW et al., 2019; ISLAM et al., 2021). Consequently, these Cu_2O/CuO mixed nanofilms represent an intriguing inorganic structure with potential quantum confinement in one dimension. Electrochemical impedance measurements conducted on this nanofilm revealed its quantum capacitance (C_q) response as a function of potential (in the low-frequency regime). This response exhibited two distinct domains: a Gaussian-shaped peak centered around 0 V versus the Ag/AgCl reference electrode and an exponential-like response at higher potentials, with capacitance increasing as a function of potential (Figure 4.2b).

Although C_q is defined from the QRT perspective, based on quantum mechanical first principles, as being proportional to the electron density of states (DOS), $\partial n/\partial \mu$, such that $C_q = e^2 \partial n/\partial \mu$, challenges remained regarding the interpretation of this response of C_q or DOS. Considering that the previous definition of C_q was derived at absolute zero temperature, a statistical mechanical treatment can be applied when the thermal broadening effect on the energy levels of the semiconductor structure is included in the analysis. Therefore, by assuming that the system represents a grand canonical ensemble and that electron occupancy follows Fermi-Dirac distribution function, a thermalized expression for C_q is obtained as $C_q = (e^2 N/k_B T) f(1-f)$, which describes a Gaussian-shaped distribution of discrete energy states. Further, by examining higher electron energies where $eV \gg k_B T$, and thus $f \ll 1$ and $f \sim \exp(-eV/k_B T)$, a new expression for C_q was

derived: $C_q = (e^2 N/k_B T)\exp(-eV/k_B T)$, which follows an exponential behavior that increases with the potential.

Accordingly, both C_q equations describe two distinct electron occupancy functions. The response of C_q, as experimentally recorded by electrochemical impedance spectroscopy (EIS), was analyzed using these equations, revealing excellent fits with fitting parameters $R^2 \sim 0{,}999$. This demonstrates that the experimental results align closely with the behaviors predicted by the QRT. In this context, the first equation, $C_q = (e^2 N/k_B T) f(1-f)$ describes a Gaussian-shaped distribution of discrete states located within the band gap of the semiconductor nanofilm. These band gap states correspond to redox states associated with the electrochemical reaction between the copper oxidation states, specifically the electronic transition from Cu^{1+} ions to Cu^{2+} and vice versa. Additionally, the presence of defects in the copper oxide atomic lattice—such as vacancies, impurities, and interstitial defects—introduces these gap states into the electronic structure. In contrast, the second equation, $C_q = (e^2 N/k_B T)\exp(-eV/k_B T)$ represents an exponential response corresponding to a distribution of continuous states in the conduction band of the copper oxide nanofilm (Figure 4.1b).

Therefore, the DOS of Cu_2/CuO semiconducting mixed nanofilms, as measured by EIS at room temperature and utilizing a phosphate buffer solution as the electrolytic medium, was resolved from the QRT foundations. This characterization revealed a Gaussian-like distribution of discrete states located in the band gap of the semiconductor, as well as an exponential-like distribution of electronic states corresponding to the continuum of states in the conduction band. The resolution of the DOS for this semiconducting nanofilm, as determined by measuring its C_q response in an electrolytic medium, suggested two key directions for the next stage of the PhD research. These were: first, the development of a new in-situ methodology for accessing the electronic structure, which, while underway, requires a deeper understanding of its underlying physical principles; and second, the observation that the exponential-like distribution of states in the conduction band, which does not involve electrochemical reactions, indicates that access to the DOS of nanomaterials through EIS measurements is not restricted to structures with reversible redox behavior, such as ferrocene-tagged peptide monolayers, previously studied, and transition metal oxides.

In this context, an assembly of zero-dimensional (0D) semiconducting structures was electronically coupled to a gold electrode surface through a molecular monolayer. Specifically, cadmium telluride (CdTe) quantum dots (QDs) of two distinct nanoparticle sizes, and consequently different electronic structures, were chemically immobilized on a gold electrode modified with L-cystein. A chemical bond formed via an amide linkage between the carboxylic acid moieties on the QD surfaces and the terminal amine groups in the L-cysteine molecules 5.3). It is important to note that QDs are semiconducting nanoparticles exhibiting quantum confinement effects in all three dimensions and, thus, their electronic structures display distributions of discrete energy states. Consequently, these nanomaterials are often referred to as "artificial atoms" because the confinement of their charge carriers results in discrete energy levels within the structures, analogous to atomic states (identified as s, p, d, etc.)(Figure 5.1. The electron DOS of a QD assembly is commonly measured experimentally by scanning tunneling spectroscopy (STS), which enables a comprehensive characterization of the electronic structure by capturing Gaussian-like distributions of the valence, conduction, and band gap states of the assembly. This technique involves applying a potential difference (V) between the substrate supporting the QD assembly and a microscope tip positioned above it, measuring the resonance current (I) related to electron injection or removal between the tip and the electronic states of the QDs. From this resonance current, the electron conductance, dI/dV, is calculated as a function of the applied potential, which is proportional to the DOS.

Although STS measurements enable the experimental resolution of the DOS for QD assemblies, their operation requires ultra-low temperatures, vacuum conditions, and highly trained personnel to operate the equipment. These requirements make this approach impractical for routine electronic characterization of nanomaterials. Consequently, the need for a fast and straightforward method to access electronic structures at the nanoscale remains a challenge in nanoscience and nanotechnology. Accordingly, by recording the response of C_q for the CdTe QD assembly as a function of the potential of the gold electrode, which acts as a probe, using a phosphate buffer solution (pH 7.4) at room temperature, a Gaussian-like distribution profile of the QD states, comparable to that obtained by STS, was achieved (5.5). In this case, the set of Gaussian-like responses observed at negative potentials corresponds to the valence states s_h and p_h, where the subscripts indicate hole states. Meanwhile, the Gaussian-like behaviors identified at pos-

itive potentials correspond to the conduction states s_e and p_e, with e denoting electron states. Each of these Gaussian-like responses was fitted using the thermalized expression for C_q applied to the gap states within copper oxide nanofilms, yielding an excellent fit parameter ($R^2 = 0{,}999$), which confirmed that these responses correspond to the electronic states of the QDs.

Accordingly, the measurement of the DOS of CdTe quantum dot assemblies through electrochemical EIS at room temperature using an electrolytic medium was demonstrated, which represents a great contribution for the field of nanomaterials characterization and led the development of a novel electronic spectroscopic approach for in situ examination of the electronic structure in nanomaterials, termed *Quantum Rate Spectroscopy*. However, further clarification of the spectroscopic mechanism underlying this methodology is required. In the absence of electrochemical reactions, QRT predicts an electromagnetic antenna-type communication between the states of the electrode probe and the discrete energy states of the QD assembly. This electronic mechanism can be understood as follows: when a time-dependent, low-frequency sinusoidal perturbation is applied to the probe electrode, the oscillating electrons generate an electromagnetic wave associated with the electron, which propagates through the junction. This electromagnetic wave resonates with the electronic structure of the QDs, generating a current signal as a response. This response does not involve a net flow of electrons, as there is no electron transport; rather, it corresponds to a displacement current. Nonetheless, this current response provides information about the electronic structure of the assembly. The potentiostat, equipped with a frequency analyzer, captures both the perturbation and response signals and converts them into an impedance function.

Therefore, the spectroscopic mechanism of QRS is based on energy resonance between the perturbation electromagnetic wave and the electronic states of the quantum dots QDs. Building on this proposed mechanism and considering the results obtained for both inorganic structures—copper oxide nanofilms and CdTe QDs—the research focus was directed towards organic structures to demonstrate the generality of quantum rate as both a theoretical framework and an experimental methodology. In this regard, the electrodynamics in single-layer graphene (SLG), a monolayer of carbon atoms arranged in a highly symmetric hexagonal lattice, was explored using EIS measurements. As result, the V-shaped DOS characterizing this organic structure, was measured by EIS at room

temperature, using an ionic liquid as the electrolytic medium (Figure 6.3b). Furthermore, by applying quantum RC circuit analysis to the capacitance spectrum, semicircle-shaped response, which was recorded at Fermi level, or Dirac point of SLG . This analysis demonstrated that the electrodynamics of graphene adhere to quantum electrodynamics principles, revealing a resistance value equivalent, within experimental error, to the quantum limit of resistance, R_q=12.99 KΩ. Hence, the electrodynamics of SLG without electron transfer, as explored by EIS, follow the electron mechanism described below under adiabatic coupling conditions of states.

With each studied structure, significant advances in understanding and utilizing the extensions of the QRT were achieved. In this context, by calculating the energy $E = g_e g_s N e^2/C_q$, associated with the electronic structure from the response of quantum capacitance C_q as a function of electrode potential, and employing tight-binding calculations as a spatial resolution model, the band structure of SLG within the energy-wave vector framework was experimentally resolved. The band structure determined from EIS measurements in an electrolytic medium showed excellent agreement with the electronic structure measured by other spectroscopic techniques, such as angle-resolved photoemission spectroscopy (ARPES), which requires low temperatures and ultrahigh vacuum conditions for operation. In addition, this result also aligned well with band structure computed for SLG through density functional theory (DFT) calculations (Figure 6.5). Therefore, the QRS, based on EIS measurements constitutes a powerful in-situ experimental tool for characterizing the electronic structure of the SLG.

The previous results obtained for SLG revealed the potential to explore alternative types of electrodynamics within organic structures. Accordingly, attention was directed toward examining the physical principles governing electrodynamics within a special class of molecular systems: Push-Pull π-conjugated heterocyclic molecules. These molecules possess a chemical structure in which electron donor and acceptor moieties are electronically coupled through π-conjugated bridges, enabling electron communication between the donor and acceptor groups (RAPOSO et al., 2006). Typically, this communication is facilitated by photo-induced electron transfer when visible light irradiates the molecule, resulting in an electron transition from the HOMO (highest occupied molecular orbital) to the LUMO (lowest unoccupied molecular orbital), a process known as intramolecular charge transfer (PIGOT et al., 2020). Consequently, the electronic characteristics of these

structures offered the possibility of probing intermolecular communication among donor and acceptors states from the standpoint QRT through EIS measurements.

In this context, an assembly of 4*H*-thieno[3,2-*b*]pyrrole-5-carboxylic acid (TPC) molecules was chemically attached to a gold surface through a cysteamine monolayer (Figure 7.5), which acts as quantum or molecular channel. The TPC molecule contains thiophene and carboxylic acid moieties, which act as electron donor and acceptor groups, respectively, connected by a pyrrole moiety. It is important to note that the acceptor group was chemically modified to facilitate attachment to the cysteamine monolayer, establishing resonance between the electrode states and the donor group states. Electrochemically, this molecule does not exhibit reversible redox behavior, and thus, intermolecular communication between the donor and acceptor groups is not associated with oxidation and reduction reactions. By exploring the TPC molecular junction using EIS measurements in dimethylformamide (DMF) and tetrabutylammonium perchlorate ($TBAClO_4$), a Gaussian-like response of C_q was observed, corresponding to an electron DOS accessed via time-dependent perturbations (Figure 7.9b). This Gaussian-like response is therefore associated with electron communication between the electrode states and the states of the thiophene moiety. However, as in the case of CdTe QDs and SLG, this communication does not correspond to an electron transfer process, but rather to electromagnetic resonance between electron states, following the mechanism discussed above.Under time-dependent perturbation at equilibrium conditions, an electromagnetic wave associated with the electron propagates through the molecular junctions, resonating with the electronic structure of the molecule. In response, a displacement current is generated, providing insights into electronic behavior.

Additionally, analysis of the capacitance spectrum and Nyquist plots recorded at the potential corresponding to the peak of the Gaussian-like response, using a quantum RC circuit model derived from QRT, revealed that the resistance associated with this electron dynamics between states is approximately 12.92 KΩ. This value, within experimental error, corresponded to $R_q = 12.99$ KΩ, the quantum limit of resistance. Consequently, electron communication between the electrode states and the donor moiety of the molecule occurs with maximal quantum efficiency, consistent with the principles of quantum electrodynamics. This result also revealed that this type of electrodynamics, which does not involve electrochemical reactions, occurs under an adiabatic coupling condition of electron

states, as observed in SLG. Therefore, this pioneering work with π-conjugated heterocyclic molecules from the perspective of QRT demonstrated the potential to characterize and fine-tune the electronic structures of molecular junctions formed from these molecules under mild conditions, which is crucial for the design and development of molecular electronic devices.

In summary, each advancement in understanding electron dynamics brings new perspectives and introduces challenging, disruptive ideas. Based on the results obtained in this PhD research across the four studied structures, it is possible to state that the (QRT) framework—rooted in quantum electrodynamics principle $E = h\nu$, and its experimental methodology, (QRS)—represents a versatile tool for exploring electrodynamics in nanoscale chemical structures. This research demonstrated the general applicability of this approach for studying electrodynamics in structures of various chemical natures and types of quantum confinement. However, these findings are only the beginning of a new field in nanoscience, *Nanoscale Electronics in Electrolytic Media*, based on a low-energy electrodynamics and with potential applications ranging from studying intriguing phenomena, such as quantum entanglement and mechanical-electromagnetic coupling of electrons, to developing devices whose operational principles are governed by non-classical phenomena. Thus, this PhD work serves as a preface to astonishing possibilities.

Chapter 9

Conclusions

Modern technological advances and film industry may lead one to assume that significant scientific contributions require the use of cutting-edge equipment and highly controlled experimental conditions. Even today, there is a tendency to believe that groundbreaking scientific work comes from scientists of specific nationalities. However, meaningful contributions can also emerge from the simple observation of nature's efficient operating principles. Controlling these principles often requires theoretical models, laboratory experiments, and practical applications. Furthermore, an open mind is essential to recognizing that current concepts, theories, and models—though foundational in the construction of knowledge—may be incomplete and can pave the way for new, disruptive contributions. The understanding of physical, chemical, and biological principles is not a closed book. The exploration and study of electron dynamics within chemical and biological systems, remains an open field of inquiry.

In this context, QRT is a theoretical model based on relativistic quantum electrodynamics, addressing the dynamics of electrons within chemical structures (BUENO, 2023b; BUENO; MERCADO, 2022; BUENO, 2024). This theory predicts the existence of a temporal property—time or frequency—associated with the transmittance of the electron between energy states. From these foundations, a characteristic frequency ν associated with the electrodynamic event is defined as the inverse of the Von Klitzing constant, $R_K = h/e^2$ (KLITZING et al., 1980), and the quantum capacitance C_q, a property tied to the electronic structure of the chemical system (where $C_q \propto DOS$) and previously overlooked by other models. Accordingly, this frequency is given by $\nu = g_s g_e e^2/hC_q$, where g_s represents spin degeneracy, and g_e arises from a superposition of electrostatic and quantum energies ($E_e = E_q$) at interfaces involving a nanoscale structure and an

electrolytic medium. This energetic superposition, resulting from electric field screening by solution ions, is a fundamental aspect of the theory (BUENO, 2023a; BUENO, 2023c).

As an electrodynamic model predicting that every quantum event has a characteristic time, QRT supports its predictions and implications through time-dependent electrical approaches, such as EIS. This technique applies a time-dependent electrical perturbation to the structure of interest in the presence of an electrolytic medium at room temperature. Traditionally, EIS has been primarily used as an electrochemical technique to characterize interfacial charge transfer resistance between a surface and redox species in solution (DHILLON; KANT, 2017). However, its potential as a time-dependent method for revealing insights into the electronic structure and quantum properties of nanomaterials has been overlooked, as demonstrated in the ongoing thesis. Under this premise, interpreting EIS measurements from the QRT perspective led to the development of a new electronic spectroscopy approach, *Quantum Rate Spectroscopy* (QRS), which enables experimental access to the electron DOS of organic and inorganic structures. This method employs a standard electrochemical cell with an electrolytic medium, solvent, and ions, as well as a potentiostat equipped with a frequency analyzer module. Thus, QRS exemplifies how significant scientific contributions do not always require complex equipment. Have you ever considered measuring the electronic structure of materials using nothing more than an electrochemical cell and a potentiostat?

Initially, QRT and its experimental approach, QRS, were applied to reveal the physical principles governing diffusionless electrochemical reactions in redox-active self-assembled molecular monolayers confined to an electrode surface (BUENO, 2023c; ALARCÓN et al., 2021b). This application demonstrated that electron transfer between the electrode states and the redox probe state adheres to quantum electrodynamic principles, with a constant quantum resistance of $R_q = h/2e^2 \approx 12{,}99\ \mathrm{k}\Omega$ and a nonadiabatic coupling of the electron states, highlighting the quantum nature of electrochemistry(SANCHEZ et al., 2022). However, in line with the rigor of scientific inquiry, a significant proposal must be dynamic, evolving and advancing over time. This raised an intriguing question: Was it possible to apply these theoretical and experimental frameworks to explore electrodynamics outside the realm of electrochemical reactions? To address this question, the ongoing PhD project was formulated.

In summary, QRT was applied to reveal the electrodynamics of four nanoscale structures of differing chemical compositions and levels of quantum confinement: a mixed Cu_2O/CuO nanofilm, an assembly of CdTe quantum dots, a single layer of graphene, and an ensemble of π-conjugated heterocyclic molecules. Through this study, DOS was experimentally accessed in an electrolytic medium via EIS measurements. The DOS measurements obtained through time-dependent electrochemistry were consistent with those obtained through other techniques, demonstrating the potential of QRS as a spectroscopic approach. For these semiconducting structures, where electron transfer processes do not occur, access to the DOS using time-dependent electrochemical measurements relies, from the QRT perspective, on electromagnetic communication between energy states. When the probe (or electrode) is subjected to a time-dependent sinusoidal signal at ultra-low frequency, its electrons oscillate, generating an electron-electromagnetic wave that propagates through the nanoscale material and resonates with its electronic structure. As a result of this resonance, a displacement current is generated and received, which does not correspond to a net electron flow but carries electronic information about the nanomaterials. The frequency response analyzer (FRA) impedance equipment processes the two signals—perturbation and response—and converts them into an impedance signal that reveals the electronic properties.

Therefore, QRT constitutes a quantum electrodynamics model which, due to its generality and derivation from first principles, can be applied to explore both electrodynamic processes involving electron transfer reactions and electronic phenomena associated with the electromagnetic communication of energy states . In addition, QRS, an experimental approach derived from the foundations of QRT and supported by previous measurement mechanisms, provides an in situ methodology for accessing the electronic structure of nanomaterials under mild conditions in a rapid and straightforward manner. Consequently, the findings and conclusions drawn from the four research works described in the ongoing PhD thesis represent a significant contribution to the field of quantum electrodynamics, paving the way for a new fundamental and applied research area: *"Nanoelectronics in Electrolytic Media."*. Through this scientific field, it is possible to envision the development of nano-devices operating with maximum quantum efficiency under low-energy quantum electrodynamics principles in electrolytic media, including applications such as biosensors, chemical sensors, transistors, and quantum computing. Hence, the narrative does not end here. On the contrary, this PhD thesis marks the beginning of a

new chapter in the study of electron dynamics. The author feels honored and proud to have contributed to this small but meaningful part of scientific progress.

Bibliography

ADAM, W.; SCHÖNBERGER, A. Application of the marcus theory on the reaction of substituted dibenzoyl peroxides with hydroquinones: Evidence for an inner-sphere electron transfer (et) mechanism. *Chemische Berichte*, Wiley Online Library, v. 125, n. 9, p. 2149–2153, 1992.

AKBARI, M.; RAHIMI-NASRABADI, M.; EGHBALI-ARANI, M.; BANAFSHE, H. R.; AHMADI, F.; GANJALI, M. R. et al. Cdte quantum dots prepared using herbal species and microorganisms and their anti-cancer, drug delivery and antibacterial applications; a review. *Ceramics International*, Elsevier, v. 46, n. 8, p. 9979–9989, 2020.

AKKERMANS, E.; MONTAMBAUX, G. *Mesoscopic physics of electrons and photons*. [S.l.]: Cambridge university press, 2007.

ALARCÓN, E. V. G.; SANTOS, A.; BUENO, P. R. Perspective on quantum electrochemistry. a simple method for measuring the electron transfer rate constant. *Electrochimica Acta*, Elsevier, v. 398, p. 139219, 2021.

ALARCÓN, E. V. G.; SANTOS, A.; BUENO, P. R. Perspective on quantum electrochemistry. a simple method for measuring the electron transfer rate constant. *Electrochimica Acta*, Elsevier, v. 398, p. 139219, 2021.

ALARCÓN, E. V. G.; SANTOS, A.; BUENO, P. R. Perspective on quantum electrochemistry. a simple method for measuring the electron transfer rate constant. *Electrochimica Acta*, Elsevier, v. 398, p. 139219, 2021.

ALIABADI, M. H.; ESMAEILI, N.; JAHROMI, H. S. An electrochemical composite sensor for phenol detection in waste water. *Applied Nanoscience*, v. 10, p. 597–609, 2020.

ALIM, S.; KAFI, A. K. M.; RAJAN, J.; YUSOFF, M. M. Application of polymerized multiporous nanofiber of sno2 for designing a bienzyme glucose biosensor based on hrp/gox. *International Journal of Biological Macromolecules*, v. 123, p. 1028–1034, 2019.

ARRHENIUS, S. Über die dissociationswärme und den einfluss der temperatur auf den dissociationsgrad der elektrolyte. *Zeitschrift für physikalische Chemie*, De Gruyter Oldenbourg, v. 4, n. 1, p. 96–116, 1889.

ARRHENIUS, S. Über die reaktionsgeschwindigkeit bei der inversion von rohrzucker durch säuren. *Zeitschrift für physikalische Chemie*, De Gruyter Oldenbourg, v. 4, n. 1, p. 226–248, 1889.

ATKINS, P.; JONES, L. *Chemical principles: The quest for insight*. [S.l.]: Macmillan, 2007.

ATKINS, P. W.; FRIEDMAN, R. S. *Molecular quantum mechanics*. [S.l.]: Oxford University Press, USA, 2011.

BAKKERS, E.; HENS, Z.; ZUNGER, A.; FRANCESCHETTI, A.; KOUWENHOVEN, L.; GUREVICH, L.; VANMAEKELBERGH, D. Shell-tunneling spectroscopy of the single-particle energy levels of insulating quantum dots. *Nano Letters*, ACS Publications, v. 1, n. 10, p. 551–556, 2001.

BARADOKE, A.; HEIN, R.; LI, X.; DAVIS, J. J. Reagentless redox capacitive assaying of c-reactive protein at a polyaniline interface. *Analytical Chemistry*, v. 92, p. 3508–3511, 2020.

BARADOKE, A.; SANTOS, A.; BUENO, P. R.; DAVIS, J. J. Introducing polymer conductance in diagnostically relevant transduction. *Biosensors and Bioelectronics*, v. 172, p. 112705, 2021.

BARD, A. J.; FAULKNER, L. R.; WHITE, H. S. *Electrochemical methods: fundamentals and applications*. [S.l.]: John Wiley & Sons, 2022.

BERGMAN, D. L. Conflict of atomism and creationism in history. In: *Proceedings of the International Conference on Creationism*. [S.l.: s.n.], 1998. v. 4, n. 1, p. 6.

BEVAN, K. H.; HOSSAIN, M. S.; IQBAL, A.; WANG, Z. Exploring bridges between quantum transport and electrochemistry. i. *The Journal of Physical Chemistry C*, ACS Publications, v. 120, n. 1, p. 179–187, 2016.

BISQUERT, J. Chemical capacitance of nanostructured semiconductors: its origin and significance for nanocomposite solar cells. *Physical Chemistry Chemical Physics*, v. 5, p. 5360–5364, 2003.

BISQUERT, J.; FABREGAT-SANTIAGO, F.; MORA-SERÓ, I.; GARCIA-BELMONTE, G.; BAREA, E. M.; PALOMARES, E. A review of recent results on electrochemical determination of the density of electronic states of nanostructured metal-oxide semiconductors and organic hole conductors. *Inorganica Chimica Acta*, Elsevier, v. 361, n. 3, p. 684–698, 2008.

BOCKRIS, J. O.; REDDY, A. K. *Modern electrochemistry 2B: electrodics in chemistry, engineering, biology and environmental science*. [S.l.]: Springer Science & Business Media, 1998.

BOHR, N. Lxxiii. on the constitution of atoms and molecules. *The London, Edinburgh, and Dublin Philosophical Magazine and Journal of Science*, Taylor & Francis, v. 26, n. 155, p. 857–875, 1913.

BORN, M. Die theorie des starren elektrons in der kinematik des relativitätsprinzips. *Annalen der Physik*, Wiley Online Library, v. 335, n. 11, p. 1–56, 1909.

BOSTWICK, A.; OHTA, T.; SEYLLER, T.; HORN, K.; ROTENBERG, E. Quasiparticle dynamics in graphene. *Nature Physics*, v. 3, n. 1, p. 36–40, 2007. ISSN 17452481.

BRANSDEN, B.; JOACHAIN, C. *Quantum Mechanics, pages 293,299,308,311,684,714*. [S.l.]: Pearson Education International, 2000.

BREITKOPF, C.; SWIDER-LYONS, K. Electrochemical science—historical review. *Springer Handbook of Electrochemical Energy*, Springer, p. 1–9, 2017.

BROADWAY, D. A.; DONTSCHUK, N.; TSAI, A.; LILLIE, S. E.; LEW, C.-K.; MCCALLUM, J. C.; JOHNSON, B.; DOHERTY, M.; STACEY, A.; HOLLENBERG, L. et al. Spatial mapping of band bending in semiconductor devices using in situ quantum sensors. *Nature Electronics*, Nature Publishing Group UK London, v. 1, n. 9, p. 502–507, 2018.

BROGLIE, L. D. *Recherches sur la théorie des quanta*. Tese (Doutorado) — Migration-université en cours d'affectation, 1924.

BROGLIE, L. d. Recueil d'exposés sur les ondes et corpuscules. *(No Title)*, 1930.

BROWN, T. L. *Chemistry: the central science*. [S.l.]: Pearson Education, 2009.

BRYAN, T.; LUO, X.; BUENO, P. R.; DAVIS, J. J. An optimised electrochemical biosensor for the label-free detection of c-reactive protein in blood. *Biosensors and Bioelectronics*, v. 39, p. 94–98, 2013.

BUENO, P. R. *Common principles of molecular electronics and nanoscale electrochemistry*. [S.l.]: ACS Publications, 2018.

BUENO, P. R. Electrochemistry and first principles of quantum mechanics. In: _____. *Nanoscale Electrochemistry of Molecular Contacts*. Cham: Springer International Publishing, 2018. p. 27–49.

BUENO, P. R. Introduction to fundamental concepts. In: _____. *Nanoscale Electrochemistry of Molecular Contacts*. Cham: Springer International Publishing, 2018. p. 1–26.

BUENO, P. R. Book. *The Nanoscale Electrochemistry of Molecular Contacts*. [S.l.]: Springer, 2018. (SpringerBriefs in Applied Sciences and Technology). ISBN 978-3-319-90486-3.

BUENO, P. R. Electron transfer and conductance quantum. *Physical Chemistry Chemical Physics*, v. 22, n. 45, p. 26109–26112, DEC 7 2020.

BUENO, P. R. On the electromagnetic nature of planck constant. *Preprint arXiv:2302.10797*, p. 1–5, 2023.

BUENO, P. R. Quantum electromagnetic rate theory of the electron and the meaning of the fine-structure constant. *Preprint arXiv:2302.12886*, p. 1–9, 2023.

BUENO, P. R. Quantum rate theory and electron-transfer dynamics: A theoretical and experimental approach for quantum electrochemistry. *Electrochimica Acta*, v. 466, p. 142950, 2023.

BUENO, P. R. On the fundamentals of quantum rate theory and the long-range electron transport in respiratory chains. *Chemical Society Reviews*, Royal Society of Chemistry, 2024.

BUENO, P. R.; CRUZEIRO, V. W. D.; ROITBERG, A. E.; FELICIANO, G. T. The density-of-states and equilibrium charge dynamics of redox-active switches. *Electrochimica Acta*, Elsevier, v. 387, p. 138410, 2021.

BUENO, P. R.; DAVIS, J. J. Elucidating redox level dispersion and local dielectric effects within electroactive molecular films. *Analytical Chemistry*, v. 86, p. 1977–2004, 2014.

BUENO, P. R.; DAVIS, J. J. Measuring quantum capacitance in energetically addressable molecular layers. *Analytical Chemistry*, v. 86, n. 3, p. 1337–1341, FEB 4 2014.

BUENO, P. R.; DAVIS, J. J. Charge transport and energy storage at the molecular scale: from nanoelectronics to electrochemical sensing. *Chemical Society Reviews*, v. 49, p. 7505–7515, 2020.

BUENO, P. R.; FABREGAT-SANTIAGO, F.; DAVIS, J. J. Elucidating capacitance and resistance terms in confined electroactive molecular layers. *Analytical Chemistry*, v. 85, n. 1, p. 411–417, JAN 1 2013.

BUENO, P. R.; FELICIANO, G. T.; DAVIS, J. J. Capacitance spectroscopy and density functional theory. *Physical Chemistry Chemical Physics*, Royal Society of Chemistry, v. 17, n. 14, p. 9375–9382, 2015.

BUENO, P. R.; HEIN, R.; SANTOS, A.; DAVIS, J. J. The nanoscopic principles of capacitive ion sensing interfaces. *Physical Chemistry Chemical Physics*, v. 22, p. 3770–3774, 2020.

BUENO, P. R.; MERCADO, D. A. M. Quantum rate theory for graphene. *Journal of Physical Chemistry C*, v. 126, n. 36, p. 15374–15385, SEP 15 2022.

BUENO, P. R.; MIRANDA, D. A. Density functional theory and an experimentally-designed energy functional of electron density. *Physical Chemistry Chemistry Physics*, v. 18, n. 37, p. 25984–25992, 2016.

BUENO, P. R.; MIRANDA, D. A. Conceptual density functional theory for electron transfer and transport in mesoscopic systems. *Physical Chemistry and Chemical Physics*, v. 19, p. 6184–6195, 2017.

BUENO, P. R.; MIRANDA, D. A. Chemical hardness of mesoscopic electrochemical systems directly analyzed from experimental data. *The Journal of Physical Chemistry C*, v. 123, n. 34, p. 21213–21223, 2019.

BUENO, P. R.; MIZZON, G.; DAVIS, J. J. Capacitance spectroscopy: A versatile approach to resolving the redox density of states and kinetics in redox-active self-assembled monolayers. *The Journal of Physical Chemistry B*, ACS Publications, v. 116, n. 30, p. 8822–8829, 2012.

BUENO, P. R.; SCHROTT, G. D.; BONANNI, P. S.; SIMISON, S. N.; BUSALMEN, J. P. Biochemical capacitance of geobacter sulfurreducens biofilms. *ChemSusChem*, v. 8, n. 15, p. 2492–2495, 2015.

BUREŠ, F. Fundamental aspects of property tuning in push–pull molecules. *RSC Advances*, Royal society of chemistry, v. 4, n. 102, p. 58826–58851, 2014.

BÜTTIKER, M.; THOMAS, H.; PRÊTRE, A. Mesoscopic capacitors. *Physics Letters A*, Elsevier, v. 180, n. 4-5, p. 364–369, 1993.

CAI, Z.; GUO, Y.; YANG, S.; PENG, Q.; LUO, H.; LIU, Z.; ZHANG, G.; LIU, Y.; ZHANG, D. New donor–acceptor–donor molecules with pechmann dye as the core moiety for solution-processed good-performance organic field-effect transistors. *Chemistry of Materials*, ACS Publications, v. 25, n. 3, p. 471–478, 2013.

CAMPBELL, J. Rutherford-a brief biography. *Rutherford. org. nz*, 2013.

CANIOU, J. *Passive infrared detection: theory and applications*. [S.l.]: Springer Science & Business Media, 2013.

CARDONA, C. M.; LI, W.; KAIFER, A. E.; STOCKDALE, D.; BAZAN, G. C. *Electrochemical considerations for determining absolute frontier orbital energy levels of conjugated polymers for solar cell applications*. [S.l.]: Wiley Online Library, 2011.

CASTRO, M. C. R.; BELSLEY, M.; RAPOSO, M. M. M. Synthesis and characterization of push–pull bithienylpyrrole nlophores with enhanced hyperpolarizabilities. *Dyes and Pigments*, Elsevier, v. 131, p. 333–339, 2016.

CECCHETTO, J.; SANTOS, A.; MONDINI, A.; CILLI, E. M.; BUENO, P. R. Serological point-of-care and label-free capacitive diagnosis of dengue virus infection. *Biosensors and Bioelectronics*, v. 151, p. 111972, 2020.

CHADWICK, J. The existence of a neutron. *Proceedings of the Royal Society of London. Series A, Containing Papers of a Mathematical and Physical Character*, The Royal Society London, v. 136, n. 830, p. 692–708, 1932.

CHADWICK, J.; CONSTABLE, J.; POLLARD, E. Artificial disintegration by α-particles. *Proceedings of the Royal Society of London. Series A, Containing Papers of a Mathematical and Physical Character*, The Royal Society London, v. 130, n. 814, p. 463–489, 1931.

CHANG, R.; OVERBY, J. *General chemistry*. [S.l.]: Random House New York, 1986.

CHEN, F.; HIHATH, J.; HUANG, Z.; LI, X.; TAO, N. Measurement of single-molecule conductance. *Annu. Rev. Phys. Chem.*, Annual Reviews, v. 58, n. 1, p. 535–564, 2007.

CHEN, H.; RIM, Y. S.; WANG, I. C.; LI, C.; ZHU, B.; SUN, M.; GOORSKY, M. S.; HE, X.; YANG, Y. Quasi-two-dimensional metal oxide semiconductors based ultrasensitive potentiometric biosensors. *ACS Nano*, v. 11, p. 4710–4718, 2017.

CHIDSEY, C. E. Free energy and temperature dependence of electron transfer at the metal-electrolyte interface. *Science*, American Association for the Advancement of Science, v. 251, n. 4996, p. 919–922, 1991.

CHOI, H.; MODY, C. C. The long history of molecular electronics: Microelectronics origins of nanotechnology. *Social Studies of Science*, Sage Publications Sage UK: London, England, v. 39, n. 1, p. 11–50, 2009.

CHONGSUEBSIRIKUL, J.; SAKDARAT, P.; PHONGPHUT, A.; KLINTHINGCHAI, Y.; PRICHANONT, S.; THANACHAYANONT, C.; PUNGETMONGKOL, P. Copper oxide nanorods electrodes for organophosphate pesticide sensor. In: *2019 IEEE 14th International Conference on Nano/Micro Engineered and Molecular Systems (NEMS)*. [S.l.: s.n.], 2019. p. 520–523.

DAVISSON, C.; GERMER, L. H. Diffraction of electrons by a crystal of nickel. *Physical review*, APS, v. 30, n. 6, p. 705, 1927.

DAVISSON, C.; GERMER, L. H. The scattering of electrons by a single crystal of nickel. *Nature*, Nature Publishing Group UK London, v. 119, n. 2998, p. 558–560, 1927.

DEROSA, P. A.; SEMINARIO, J. M. Electron transport through single molecules: Scattering treatment using density functional and green function theories. *The Journal of Physical Chemistry B*, ACS Publications, v. 105, n. 2, p. 471–481, 2001.

DEVONS, S. Rutherford and the science of his day. *Notes and Records of the Royal Society of London*, The Royal Society London, v. 45, n. 2, p. 221–242, 1991.

DEY, A. Semiconductor metal oxide gas sensors: A review. *Journal of Materials Science: Materials in Electronics*, v. 29, p. 206–217, 2018.

DHILLON, S.; KANT, R. Theory for electrochemical impedance spectroscopy of heterogeneous electrode with distributed capacitance and charge transfer resistance. *Journal of Chemical Sciences*, Springer, v. 129, p. 1277–1292, 2017.

DIRAC, P. A. M. The quantum theory of the electron. *Proceedings of the Royal Society A: Mathematical, Physical and Eng. Sci.*, v. 117, n. 778, p. 610–624, 1928.

DIRAC, P. A. M. *The principles of quantum mechanics*. [S.l.]: Oxford university press, 1981.

DONG, S.; TONG, M.; ZHANG, D.; HUANG, T. The strategy of nitrite and immunoassay human igg biosensors based on zno@zif-8 and ionic liquid composite film. *Sensors and Actuators B: Chemical*, v. 251, p. 650–657, 2017.

EBERSON, L.; EBERSON, L. How to use the marcus theory. *Electron Transfer Reactions in Organic Chemistry*, Springer, p. 39–66, 1987.

ECKERMANN, A. L.; FELD, D. J.; SHAW, J. A.; MEADE, T. J. Electrochemistry of redox-active self-assembled monolayers. *Coordination chemistry reviews*, Elsevier, v. 254, n. 15-16, p. 1769–1802, 2010.

EDVINSSON, T. Optical quantum confinement and photocatalytic properties in two-, one-and zero-dimensional nanostructures. *Royal society open science*, The Royal Society, v. 5, n. 9, p. 180387, 2018.

EINSTEIN, A. On a heuristic viewpoint concerning the emission and transformation of light. *Annalen der Physik*, v. 17, p. 132, 1905.

ERNI, R.; LAZAR, S.; BROWNING, N. D. Prospects for analyzing the electronic properties in nanoscale systems by veels. *Ultramicroscopy*, Elsevier, v. 108, n. 3, p. 270–276, 2008.

EVANS, J.; THORNDIKE, A. S. *Quantum mechanics at the crossroads: New perspectives from history, philosophy and physics*. [S.l.]: Springer Science & Business Media, 2006.

EVANS, M. G.; POLANYI, M. Some applications of the transition state method to the calculation of reaction velocities, especially in solution. *Transactions of the Faraday Society*, Royal Society of Chemistry, v. 31, p. 875–894, 1935.

EYRING, H. The activated complex in chemical reactions. *The Journal of Chemical Physics*, AIP Publishing, v. 3, n. 2, p. 107–115, 1935.

FALCONER, I. Corpuscles, electrons and cathode rays: Jj thomson and the 'discovery of the electron'. *The British journal for the history of science*, Cambridge University Press, v. 20, n. 3, p. 241–276, 1987.

FARADAY, M. Vi. experimental researches in electricity.-seventh series. *Philosophical Transactions of the Royal Society of London*, The Royal Society London, n. 124, p. 77–122, 1834.

FARIA, A. M.; MAZON, T. Early diagnosis of zika infection using a zno nanostructures-based rapid electrochemical biosensor. *Talanta*, v. 203, p. 153–160, 2019.

FELICIANO, G. T.; BUENO, P. R. Two-dimensional nature and the meaning of the density of states in redox monolayers. *The Journal of Physical Chemistry C*, ACS Publications, v. 124, n. 27, p. 14918–14927, 2020.

FELICIANO, G. T.; BUENO, P. R. Two-dimensional nature and the meaning of the density of states in redox monolayers. *Journal of Physical Chemistry C*, v. 124, n. 27, p. 14918–14927, JUL 9 2020.

FENG, Y. J.; LI, X. Y. Electro-catalytic oxidation of phenol on several metal-oxide electrodes in aqueous solution. *Water Research*, v. 37, p. 2399–2407, 2003.

FERGUSSON, J. E. *The history of the discovery of nuclear fission*. [S.l.]: Springer, 2011.

FERNANDES, F. C. B.; GóES, M. S.; DAVIS, J. J.; BUENO, P. R. Label free redox capacitive biosensing. *Biosensors and Bioelectronics*, v. 50, p. 437–440, 2013.

FERNANDES, S. S.; CASTRO, M. C. R.; IVANOU, D.; MENDES, A.; RAPOSO, M. M. M. Push-pull heterocyclic dyes based on pyrrole and thiophene: synthesis and evaluation of their optical, redox and photovoltaic properties. *Coatings*, MDPI, v. 12, n. 1, p. 34, 2021.

FERNANDES, S. S.; CASTRO, M. C. R.; PEREIRA, A. I.; MENDES, A.; SERPA, C.; PINA, J.; JUSTINO, L. L.; BURROWS, H. D.; RAPOSO, M. M. M. Optical and photovoltaic properties of thieno [3, 2-b] thiophene-based push–pull organic dyes with different anchoring groups for dye-sensitized solar cells. *ACS Omega*, ACS Publications, v. 2, n. 12, p. 9268–9279, 2017.

FERNANDES, S. S. M.; BELSLEY, M.; PEREIRA, A. I.; IVANOU, D.; MENDES, A.; JUSTINO, L. L.; BURROWS, H. D.; RAPOSO, M. M. M. Push–pull n, n-diphenylhydrazones bearing bithiophene or thienothiophene spacers as nonlinear optical second harmonic generators and as photosensitizers for nanocrystalline tio2 dye-sensitized solar cells. *ACS Omega*, ACS Publications, v. 3, n. 10, p. 12893–12904, 2018.

FLETCHER, H. My work with millikan on the oil-drop experiment. *Physics Today*, American Institute of Physics, v. 35, n. 6, p. 43–47, 1982.

FRANK, S.; PONCHARAL, P.; WANG, Z.; HEER, W. A. d. Carbon nanotube quantum resistors. *science*, American Association for the Advancement of Science, v. 280, n. 5370, p. 1744–1746, 1998.

GABELLI, J.; FÈVE, G.; BERROIR, J.-M.; PLAÇAIS, B.; CAVANNA, A.; ETIENNE, B.; JIN, Y.; GLATTLI, D. Violation of kirchhoff's laws for a coherent rc circuit. *Science*, American Association for the Advancement of Science, v. 313, n. 5786, p. 499–502, 2006.

GARCIA-AMORÓS, J.; CASTRO, M. C. R.; COELHO, P.; RAPOSO, M. M. M.; VELASCO, D. Fastest non-ionic azo dyes and transfer of their thermal isomerisation kinetics into liquid-crystalline materials. *Chemical Communications*, Royal Society of Chemistry, v. 52, n. 29, p. 5132–5135, 2016.

GARCIA-AMORÓS, J.; CASTRO, M. C. R.; RAPOSO, M. M. M.; VELASCO, D. Photochromic heteroarylethenes with fast thermal isomerization kinetics. *Dyes and Pigments*, Elsevier, v. 210, p. 111000, 2023.

GARROTE, B. L.; SÁNCHEZ, Y. P.; LOPES, L. C.; SANTOS, A.; BUENO, P. R. Electron transmittance by means of quantum capacitive states as a signal amplification mechanism for biosensing applications. *Sensors and Actuators B: Chemical*, Elsevier, v. 399, p. 134786, 2024.

GARROTE, B. L.; SANTOS, A.; BUENO, P. R. Perspectives on and precautions for the uses of electric spectroscopic methods in label-free biosensing applications. *ACS Sensors*, v. 4, p. 2216–2227, 2019.

GARROTE, B. L.; SANTOS, A.; BUENO, P. R. Label-free capacitive assaying of biomarkers for molecular diagnostics. *Nature Protocols*, v. 15, p. 3879–3893, 2020.

GEIM, A. K.; NOVOSELOV, K. S. The rise of graphene. In: *Nanoscience and technology: a collection of reviews from nature journals*. [S.l.]: World Scientific, 2010. p. 11–19.

GERISCHER, H. Electrochemistry of the excited electronic state. *Journal of The Electrochemical Society*, Citeseer, v. 125, n. 5, p. 218C, 1978.

GERISCHER, H. The impact of semiconductors on the concepts of electrochemistry. *Electrochimica Acta*, Elsevier, v. 35, n. 11-12, p. 1677–1699, 1990.

GERISCHER, H.; WILLIG, F. Reaction of excited dye molecules at electrodes. *Physical and Chemical Applications of Dyestuffs*, Springer, p. 31–84, 2006.

GLUCK, P.; AGMON, D. *Classical And Relativistic Mechanics*. [S.l.]: World Scientific Publishing Company, 2009.

GOLDSTEIN, E. Vorläufige mittheilungen über elektrische entladungen in verdünnten gasen. *Berlin Akd. Monatsber*, v. 279, 1876.

GONÇALVES, R. C.; BELMONTE-RECHE, E.; PINA, J.; SILVA, M. Costa da; PINTO, S. C.; GALLO, J.; COSTA, S. P.; RAPOSO, M. M. M. Bioimaging of lysosomes with a bodipy ph-dependent fluorescent probe. *Molecules*, MDPI, v. 27, n. 22, p. 8065, 2022.

GOODSTEIN, D. L. In defense of robert andrews millikan. *Engineering and Science*, California Institute of Technology, v. 63, n. 4, p. 30–38, 2000.

GORBAR, E. V.; MIRANSKY, V. A.; SHOVKOVY, I. A.; SUKHACHOV, P. O. *Electronic properties of Dirac and Weyl semimetals*. [S.l.]: World Scientific, 2021.

GREINER, W. et al. *Relativistic quantum mechanics*. [S.l.]: Springer, 2000. v. 2.

GRIFFITHS, D. J.; SCHROETER, D. F. *Introduction to quantum mechanics*. [S.l.]: Cambridge university press, 2018.

GRUHN, N. E.; FILHO, D. A. da S.; BILL, T. G.; MALAGOLI, M.; COROPCEANU, V.; KAHN, A.; BRÉDAS, J.-L. The vibrational reorganization energy in pentacene: molecular influences on charge transport. *Journal of the American Chemical Society*, ACS Publications, v. 124, n. 27, p. 7918–7919, 2002.

HEATH, J. R. Molecular electronics. *Annual Review of Materials Research*, Annual Reviews, v. 39, n. 1, p. 1–23, 2009.

HEILBRON, J. L. Jj thomson and the bohr atom. *Physics today*, American Institute of Physics, v. 30, n. 4, p. 23–30, 1977.

HEISENBERG, W. Über den anschaulichen inhalt der quantentheoretischen kinematik und mechanik. *Zeitschrift für Physik*, Springer, v. 43, n. 3, p. 172–198, 1927.

HEISENBERG, W. *Encounters with Einstein: And other essays on people, places, and particles*. [S.l.]: Princeton University Press, 1989. v. 4.

HERTZ, H. Ueber einen einfluss des ultravioletten lichtes auf die electrische entladung. *Annalen der Physik*, WILEY-VCH Verlag Leipzig, v. 267, n. 8, p. 983–1000, 1887.

HERTZ, H. Ueber sehr schnelle electrische schwingungen. *Annalen der Physik*, Wiley Online Library, v. 267, n. 7, p. 421–448, 1887.

HOFFMANN, D. *Max Planck: Die Entstehung der modernen Physik*. [S.l.]: CH Beck, 2008. v. 2442.

HOHENBERG, P.; KOHN, W. Inhomogeneous electron gas. *Phys. Rev.*, American Physical Society, v. 136, p. B864–B871, Nov 1964.

HON, G.; GOLDSTEIN, B. R. Jj thomson's plum-pudding atomic model: The making of a scientific myth. *Annalen der physik*, v. 525, n. 8-9, p. A129–A133, 2013.

HOSSAIN, M. S.; BEVAN, K. H. Exploring bridges between quantum transport and electrochemistry. ii. a theoretical study of redox-active monolayers. *The Journal of Physical Chemistry C*, ACS Publications, v. 120, n. 1, p. 188–194, 2016.

HOUTEPEN, A. J.; VANMAEKELBERGH, D. Orbital occupation in electron-charged cdse quantum-dot solids. *The Journal of Physical Chemistry B*, ACS Publications, v. 109, n. 42, p. 19634–19642, 2005.

ISLAM, M.; JAVED, S.; AKRAM, M. A.; USMAN, M. Metal/metal oxide thin film electrodes for supercapatteries. In: *Advances in Supercapacitor and Supercapattery*. [S.l.]: Elsevier, 2021. p. 175–198.

JDIRA, L.; LILJEROTH, P.; STOFFELS, E.; VANMAEKELBERGH, D.; SPELLER, S. Size-dependent single-particle energy levels and interparticle coulomb interactions in cdse quantum dots measured by scanning tunneling spectroscopy. *Physical Review B*, APS, v. 73, n. 11, p. 115305, 2006.

JIANG, G.; DENG, S.; BABA, A.; HUANG, C.; ADVINCULA, R. C. On the monolayer adsorption of thiol-terminated dendritic oligothiophenes onto gold surfaces. *Macromolecular Chemistry and Physics*, Wiley Online Library, v. 211, n. 24, p. 2562–2572, 2010.

JUNQUERA, J.; PAZ, O.; SÁNCHEZ-PORTAL, D.; ARTACHO, E. Numerical atomic orbitals for linear-scaling calculations. *Phys. Rev. B*, American Physical Society, v. 64, p. 235111, Nov 2001. Disponível em: <https://link.aps.org/doi/10.1103/PhysRevB.64.235111>.

KABIR, E.; UZZAMAN, M. A review on biological and medicinal impact of heterocyclic compounds. *Results in Chemistry*, Elsevier, v. 4, p. 100606, 2022.

KEENER, R. L.; SKELTON, F. S.; SNYDER, H. R. Synthesis of 6-substituted thieno [3, 2-b] pyrroles. *The Journal of Organic Chemistry*, ACS Publications, v. 33, n. 4, p. 1355–1359, 1968.

KEITHLEY, J. F. *The story of electrical and magnetic measurements: from 500 BC to the 1940s*. [S.l.]: John Wiley & Sons, 1999.

KIM, S. Advancements in materials science. *Materials Today*, v. 18, n. 2, p. 87–101, 2015.

KLITZING, K. V. Developments in the quantum hall effect. *Philosophical Transactions of the Royal Society A: Mathematical, Physical and Engineering Sciences*, The Royal Society London, v. 363, n. 1834, p. 2203–2219, 2005.

KLITZING, K. v.; DORDA, G.; PEPPER, M. New method for high-accuracy determination of the fine-structure constant based on quantized hall resistance. *Physical review letters*, APS, v. 45, n. 6, p. 494, 1980.

KOHN, W.; SHAM, L. J. Self-consistent equations including exchange and correlation effects. *Phys. Rev.*, American Physical Society, v. 140, p. A1133–A1138, Nov 1965.

KRAGH, H. Niels bohr's second atomic theory. *Historical Studies in the Physical Sciences*, JSTOR, v. 10, p. 123–186, 1979.

LAIDLER, K. J. The development of the arrhenius equation. *Journal of chemical Education*, ACS Publications, v. 61, n. 6, p. 494, 1984.

LAND, M.; HORWITZ, L. P. *Relativistic classical mechanics and electrodynamics*. [S.l.]: Springer Nature, 2022.

LANDAUER, R. Spatial variation of currents and fields due to localized scatterers in metallic conduction. *IBM J. Res. Dev.*, v. 1, p. 223–231, 1957.

LAUGHLIN, R. B. Quantized hall conductivity in two dimensions. *Physical Review B*, APS, v. 23, n. 10, p. 5632, 1981.

LAVIRON, E. General expression of the linear potential sweep voltammogram in the case of diffusionless electrochemical systems. *Journal of Electroanalytical Chemistry and Interfacial Electrochemistry*, Elsevier, v. 101, n. 1, p. 19–28, 1979.

LAVIRON, E. The use of linear potential sweep voltammetry and of ac voltammetry for the study of the surface electrochemical reaction of strongly adsorbed systems and of redox modified electrodes. *Journal of Electroanalytical Chemistry and Interfacial Electrochemistry*, Elsevier, v. 100, n. 1-2, p. 263–270, 1979.

LAVIRON, E. A multilayer model for the study of space distributed redox modified electrodes: Part i. description and discussion of the model. *Journal of Electroanalytical Chemistry and Interfacial Electrochemistry*, Elsevier, v. 112, n. 1, p. 1–9, 1980.

LAVIRON, E.; ROULLIER, L. General expression of the linear potential sweep voltammogram for a surface redox reaction with interactions between the adsorbed molecules: applications to modified electrodes. *Journal of Electroanalytical Chemistry and Interfacial Electrochemistry*, Elsevier, v. 115, n. 1, p. 65–74, 1980.

LAVIRON, E.; ROULLIER, L.; DEGRAND, C. A multilayer model for the study of space distributed redox modified electrodes: Part ii. theory and application of linear potential sweep voltammetry for a simple reaction. *Journal of Electroanalytical Chemistry and Interfacial Electrochemistry*, Elsevier, v. 112, n. 1, p. 11–23, 1980.

LAZANAS, A. C.; PRODROMIDIS, M. I. Electrochemical impedance spectroscopy a tutorial. *ACS Measurement Science Au*, ACS Publications, v. 3, n. 3, p. 162–193, 2023.

LEE, T.; ENOMOTO, K.; OHSHIRO, K.; INOUE, D.; KIKITSU, T.; HYEON-DEUK, K.; PU, Y.-J.; KIM, D. Controlling the dimension of the quantum resonance in cdte quantum dot superlattices fabricated via layer-by-layer assembly. *Nature communications*, Nature Publishing Group, v. 11, n. 1, p. 1–10, 2020.

LEVINE, R. D. *Molecular reaction dynamics*. [S.l.]: Cambridge University Press, 2009.

LEWIS, N. S.; TRIBUTSCH, H.; NOZIK, A. J. Biography: Heinz gerischer. *The Journal of Physical Chemistry B*, ACS Publications, v. 101, n. 14, p. 2391–2391, 1997.

LILJEROTH, P.; EMMICHOVEN, P. A. Z. van; HICKEY, S. G.; WELLER, H.; GRANDIDIER, B.; ALLAN, G.; VANMAEKELBERGH, D. Density of states measured by scanning-tunneling spectroscopy sheds new light on the optical transitions in pbse nanocrystals. *Physical review letters*, APS, v. 95, n. 8, p. 086801, 2005.

LOPES, L. C.; BUENO, P. R. Sensing the quantized reactivity of graphene. *Analytica Chimica Acta*, v. 1177, SEP 8 2021.

LOPES, L. C.; PINZÓN, E. F.; SILVA, G. Dias-da; FELICIANO, G. T.; BUENO, P. R. Electrochemical measurement of the electronic structure of graphene via quantum mechanical rate spectroscopy. *Electrochimica Acta*, Elsevier, v. 480, p. 143837, 2024.

LOPES, L. C.; PINZóN, E. F.; SILVA, G. Dias-da; FELICIANO, G. T.; BUENO, P. R. Electrochemical measurement of the electronic structure of graphene via quantum mechanical rate spectroscopy. *Preprint arXiv:2308.13525*, n. 1, p. 10, 2023.

LOPES, L. C.; SANTOS, A.; BUENO, P. R. Measuring quantum conductance and capacitance of graphene using impedance-derived capacitance spectroscopy. *Carbon*, Elsevier, v. 184, p. 821–827, 2021.

LOW, W. H.; KHIEW, P. S.; LIM, S. S.; SIONG, C. W.; EZEIGWE, E. R. Recent development of mixed transition metal oxide and graphene/mixed transition metal oxide based hybrid nanostructures for advanced supercapacitors. *Journal of Alloys and Compounds*, Elsevier, v. 775, p. 1324–1356, 2019.

LV, G.-F.; CHEN, Y.-H.; YANG, T.; LI, J.-G. Electrocatalytic oxidation removal of phenol from aqueous solution with metal oxides doped carbon aerogel. *Journal of the Brazilian Chemical Society*, v. 29, p. 689–694, 2018.

MA, H.; YIP, H.-L.; HUANG, F.; JEN, A. K. Y. Interface engineering for organic electronics. *Advanced Functional Materials*, v. 20, n. 9, p. 1371–1388, MAY 10 2010. ISSN 1616-301X.

MADURAIVEERAN, G.; SASIDHARAN, M.; JIN, W. Earth-abundant transition metal and metal oxide nanomaterials: Synthesis and electrochemical applications. *Progress in Materials Science*, Elsevier, v. 106, p. 100574, 2019.

MAHAJAN, S. Defects in semiconductors and their effects on devices. *Acta Materialia*, v. 48, p. 137–149, 2000.

MARCUS, R. On the theory of oxidation-reduction reactions involving electron transfer. ii. applications to data on the rates of isotopic exchange reactions. *The Journal of Chemical Physics*, American Institute of Physics, v. 26, n. 4, p. 867–871, 1957.

MARCUS, R. On the theory of oxidation-reduction reactions involving electron transfer. iii. applications to data on the rates of organic redox reactions. *The Journal of Chemical Physics*, American Institute of Physics, v. 26, n. 4, p. 872–877, 1957.

MARCUS, R. A. Electrostatic free energy and other properties of states having nonequilibrium polarization. i. *The Journal of Chemical Physics*, AIP Publishing, v. 24, n. 5, p. 979–989, 1956.

MARCUS, R. A. On the theory of oxidation-reduction reactions involving electron transfer. i. *The Journal of chemical physics*, AIP Publishing, v. 24, n. 5, p. 966–978, 1956.

MARCUS, R. A. Chemical and electrochemical electron-transfer theory. *Annual review of physical chemistry*, v. 15, n. 1, p. 155–196, 1964.

MARCUS, R. A. Chemical and electrochemical electron-transfer theory. *Annu. Rev. Phys. Chem.*, v. 15, p. 155, 1964. ISSN 0066-426X.

MARCUS, R. A. On the theory of electron-transfer reactions. vi. unified treatment for homogeneous and electrode reactions. *The Journal of Chemical Physics*, American Institute of Physics, v. 43, n. 2, p. 679–701, 1965.

MARCUS, R. A. Electron-transfer reactions in chemistry - theory and experiment. *Rev. Mod. Phys.*, v. 65, n. 3, p. 599–610, 1993. ISSN 0034-6861.

MARCUS, R. A. Electron transfer reactions in chemistry. theory and experiment. In: *Protein electron transfer*. [S.l.]: Garland Science, 2020. p. 249–272.

MARCUS, R. A.; SUTIN, N. Electron transfers in chemistry and biology. *Biochimica et Biophysica Acta (BBA)-Reviews on Bioenergetics*, Elsevier, v. 811, n. 3, p. 265–322, 1985.

MARCUS, R. A.; SUTIN, N. Electron transfers in chemistry and biology. *Biochimica et Biophysica Acta*, v. 811, n. 3, p. 265–322, 1985.

MARIN-HERNANDEZ, C.; SANTOS-FIGUEROA, L. E.; MORAGUES, M. E.; RAPOSO, M. M. M.; BATISTA, R. M.; COSTA, S. P.; PARDO, T.; MARTINEZ-MANEZ, R.; SANCENON, F. Imidazoanthraquinone derivatives for the chromofluorogenic sensing of basic anions and trivalent metal cations. *The Journal of Organic Chemistry*, ACS Publications, v. 79, n. 22, p. 10752–10761, 2014.

MARQUÉS-GONZÁLEZ, S.; LOW, P. J. Molecular electronics: history and fundamentals. *Australian Journal of Chemistry*, CSIRO Publishing, v. 69, n. 3, p. 244–253, 2016.

MARQUES, S. M.; SANTOS, A.; GONçALVES, L. M.; SOUSA, J. C.; BUENO, P. R. Sensitive label-free electron chemical capacitive signal transduction for d-dimer electroanalysis. *Electrochimica Acta*, v. 182, p. 946–952, 2015.

MARTIN, A. Cathode ray tubes for industrial and military applications. *Advances in electronics and electron physics*, Elsevier, v. 67, p. 183–328, 1986.

MATYUSHOV, D. V. Reorganization energy of electron transfer. *Physical Chemistry Chemical Physics*, Royal Society of Chemistry, v. 25, n. 11, p. 7589–7610, 2023.

MCCLUSKEY, M. D.; JANOTTI, A. Defects in semiconductors. *Journal of Applied Physics*, v. 127, p. 190401, 2020.

MCQUARRIE, D. Physical chemistry: A molecular approach. *University Science Book*, 1997.

MEYER, J.; HAMWI, S.; KROEGER, M.; KOWALSKY, W.; RIEDL, T.; KAHN, A. Transition metal oxides for organic electronics: Energetics, device physics and applications. *Advanced Materials*, v. 24, n. 40, p. 5408–5427, OCT 23 2012. ISSN 0935-9648.

MILLIKAN, R. A. The isolation of an ion, a precision measurement of its charge, and the correction of stokes's law. *Physical Review (Series I)*, APS, v. 32, n. 4, p. 349, 1911.

MILLIKAN, R. A. On the elementary electrical charge and the avogadro constant. *Physical Review*, APS, v. 2, n. 2, p. 109, 1913.

MIRANDA, D. A.; BUENO, P. R. Density functional theory and an experimentally-designed energy functional of electron density. *Physical Chemistry Chemical Physics*, v. 18, n. 37, p. 25984–25992, OCT 7 2016.

MIRANDA, D. A.; BUENO, P. R. Chemical hardness of mesoscopic electrochemical systems directly analyzed from experimental data. *Journal of Physical Chemistry C*, v. 123, n. 34, SI, p. 21213–21223, AUG 29 2019.

NAZAROV, Y. V.; BLANTER, Y. M. *Quantum transport: introduction to nanoscience*. [S.l.]: Cambridge university press, 2009.

NAZIN, G.; WU, S.; HO, W. Tunneling rates in electron transport through double-barrier molecular junctions in a scanning tunneling microscope. *Proceedings of the National Academy of Sciences*, National Acad Sciences, v. 102, n. 25, p. 8832–8837, 2005.

NETO, A. H. C.; GUINEA, F.; PERES, N. M. R.; NOVOSELOV, K. S.; GEIM, A. K. The electronic properties of graphene. *Reviews of modern physics*, APS, v. 81, n. 1, p. 109, 2009.

NEWMAN, J.; BALSARA, N. P. *Electrochemical systems*. [S.l.]: John Wiley & Sons, 2021.

NITZAN, A. A relationship between electron-transfer rates and molecular conduction. *The Journal of Physical Chemistry A*, ACS Publications, v. 105, n. 12, p. 2677–2679, 2001.

NOVOSELOV, K. S.; GEIM, A. K.; MOROZOV, S. V.; JIANG, D.; KATSNELSON, M. I.; GRIGORIEVA, I.; DUBONOS, S.; FIRSOV, a. Two-dimensional gas of massless dirac fermions in graphene. *nature*, Nature Publishing Group, v. 438, n. 7065, p. 197–200, 2005.

NOVOSELOV, K. S.; GEIM, A. K.; MOROZOV, S. V.; JIANG, D.; KATSNELSON, M. I.; GRIGORIEVA, I. V.; DUBONOS, S. V.; FIRSOV, A. A. Two-dimensional gas of massless dirac fermions in graphene. *Nature*, v. 438, n. 7065, p. 197–200, Nov 2005. ISSN 1476-4687. Disponível em: <https://doi.org/10.1038/nature04233>.

OLDHAM, K.; MYLAND, J.; BOND, A. *Electrochemical science and technology: fundamentals and applications*. [S.l.]: John Wiley & Sons, 2011.

OLIVA, M. M.; CASADO, J.; RAPOSO, M. M. M.; FONSECA, A. M. C.; HARTMANN, H.; HERNÁNDEZ, V.; NAVARRETE, J. T. L. Structure- property relationships in push- pull amino/cyanovinyl end-capped oligothiophenes: Quantum chemical and experimental studies. *The Journal of Organic Chemistry*, ACS Publications, v. 71, n. 20, p. 7509–7520, 2006.

OLIVEIRA, R. M. B.; FERNANDES, F. C. B.; BUENO, P. R. Pseudocapacitance phenomena and applications in biosensing devices. *Electrochimica Acta*, v. 306, p. 175–184, 2019.

OLIVEIRA, R. M. B.; FERNANDES, F. C. B.; BUENO, P. R. Pseudocapacitance phenomena and applications in biosensing devices. *Electrochimica Acta*, v. 306, p. 175–184, 2019. ISSN 0013-4686.

PARK, C.-H.; GIUSTINO, F.; SPATARU, C. D.; COHEN, M. L.; LOUIE, S. G. Angle-resolved photoemission spectra of graphene from first-principles calculations. *Nano Letter*, v. 9, n. 12, p. 4234–4239, 2009.

PARK HYUNG J. ANDN SHIN, D. J.; YU, J. Categorization of quantum dots, cluster, nanoclusters, and nanodots. *Journal of Chemical Education*, v. 98, p. 703–709, 2021.

PAULING, L. *General chemistry*. [S.l.]: Courier Corporation, 1988.

PETRUCCI, R.; HARWOOD, W.; HERRING, F. *General Chemistry: Principles and Modern Applications. USA 2002*. [S.l.]: Prentice-Hall, Inc, 2022.

PICCOLI, J.; HEIN, R.; EL-SAGHEER, A. H.; BROWN, T.; CILLI, E. M.; BUENO, P. R.; DAVIS, J. J. Redox capacitive assaying of c-reactive protein at a peptide supported aptamer interface. *Analytical Chemistry*, v. 90, p. 3005–3008, 2018.

PIGOT, C.; NOIRBENT, G.; BRUNEL, D.; DUMUR, F. Recent advances on push-pull organic dyes as visible light photoinitiators of polymerization. *European Polymer Journal*, v. 133, p. 109797, JUN 15 2020. ISSN 0014-3057.

PINO, F.; MAYORGA-MARTINEZ, C. C.; MERKOçI, A. High-performance sensor based on copper oxide nanoparticles for dual detection of phenolic compounds and a pesticide. *Electrochemistry Communications*, v. 71, p. 33–37, 2016.

PINZON, E. F.; SANTOS, A. d.; BUENO, P. R. Density of states of a nanoscale semiconductor interface as a transduction signal for sensing molecules. *ACS Applied Electronic Materials*, ACS Publications, v. 3, n. 8, p. 3411–3417, 2021.

PINZON, E. F. N.; ALARCON, E. V. G.; SANCHEZ, Y. P.; BUENO, P. R. Quantum rate dynamics and charge screening at the nanoscale level. *Physical Chemistry Chemical Physics*, v. 24, n. 26, p. 16200–16206, 2022.

PINZON, E. F. N.; LOPES, L. C.; SANTOS, A.; RAPOSO, M. M. M.; BUENO, P. R. Quantum rate electrodynamics and resonant junction electronics of heterocyclic molecules. *Preprint arXiv:2309.05754v1*, p. 1–14, 2023.

PIZÓN, E. F.; LOPES, L. C.; FONSECA, A. F. V.; SCHIAVON, M. A.; BUENO, P. R. Quantum rate as a spectroscopic methodology for measuring the electronic structure of quantum dots. *Journal of Materials Chemistry C*, Royal Society of Chemistry, 2024.

PLANCK, M. The theory of heat radiation. *Entropie*, v. 144, n. 190, p. 164, 1900.

PLANCK, M. *Über das gesetz der energieverteilung im normalspektrum*. [S.l.]: Springer, 1978.

PULLMAN, B. *The atom in the history of human thought*. [S.l.]: Oxford University Press, USA, 2001.

RAJENDRAN, S.; MANOJ, D.; RAJU, K.; DIONYSIOU, D. D.; NAUSHAD, M.; GRACIA, F.; CORNEJO, L.; GRACIA-PINILLA, M. A.; AHAMAD, T. Influence of mesoporous defect induced mixed-valent nio (ni2+/ni3+)-tio2 nanocomposite for non-enzymatic glucose biosensors. *Sensors and Actuators B: Chemical*, v. 264, p. 27–37, 2018.

RAPOSO, M. M. M.; SOUSA, A. M.; KIRSCH, G.; CARDOSO, P.; BELSLEY, M.; GOMES, E. de M.; FONSECA, A. M. C. Synthesis and characterization of dicyanovinyl-substituted thienylpyrroles as new nonlinear optical chromophores. *Organic Letters*, ACS Publications, v. 8, n. 17, p. 3681–3684, 2006.

RATNER, M. A brief history of molecular electronics. *Nature nanotechnology*, Nature Publishing Group UK London, v. 8, n. 6, p. 378–381, 2013.

RATNER, M. A. Introducing molecular electronics. *Materials today*, Elsevier, v. 5, n. 2, p. 20–27, 2002.

ROBINSON, J. M. *Early Greek Philosophy*. [S.l.]: New York: Houghton Mifflin, 1958.

ROCKETT, A. Defects in semiconductors. In: _____. *The Materials Science of Semiconductors*. Boston, MA: Springer US, 2008. p. 289–356.

RUTHERFORD, E. Collision of α particles with light atoms; 4, an anomalous effect in nitrogen. *Philos. Mag.*, v. 37, p. 581, 1919.

RUTHERFORD, E. The scattering of α and β particles by matter and the structure of the atom. *Philosophical Magazine*, Taylor & Francis, v. 92, n. 4, p. 379–398, 2012.

SANCHEZ, Y. P.; SANTOS, A.; BUENO, P. R. Quantum mechanical meaning of the charge transfer resistance. *Journal of Physical Chemistry C*, v. 126, n. 6, p. 3151–3162, FEB 17 2022. ISSN 1932-7447.

SÁNCHEZ, Y. P.; SANTOS, A.; BUENO, P. R. Quantum rate efficiency of the charge transfer mediated by quantum capacitive states. *Electrochimica Acta*, Elsevier, v. 434, p. 141194, 2022.

SANTOS, A.; DAVIS, J. J.; BUENO, P. R. Fundamentals and applications of impedimetric and redox capacitive biosensors. *Journal of Analytical & Bioanalytical Techniques*, S7, p. 016, 2014.

SANTOS, A.; TEFASHE, U. M.; MCCREERY, R. L.; BUENO, P. R. Introducing mesoscopic charge transfer rates into molecular electronics. *Physical Chemistry Chemical Physics*, Royal Society of Chemistry, v. 22, n. 19, p. 10828–10832, 2020.

SANTOS, A.; YUSTOS, P.; QUINTANILLA, A.; RODRíGUEZ, S.; GARCíA-OCHOA, F. Route of the catalytic oxidation of phenol in aqueous phase. *Applied Catalysis B: Environmental*, v. 39, p. 97–113, 2002.

SANTOS, A.; YUSTOS, P.; QUINTANILLA, A.; RUIZ, G.; GARCIA-OCHOA, F. Study of the copper leaching in the wet oxidation of phenol with cuo-based catalysts: Causes and effects. *Applied Catalysis B: Environmental*, v. 61, p. 323–333, 2005.

SANZ-NAVARRO, C. F.; GRIMA, R.; GARCÍA, A.; BEA, E. A.; SOBA, A.; CELA, J. M.; ORDEJÓN, P. An efficient implementation of a qm–mm method in siesta. *Theoretical Chemistry Accounts*, v. 128, n. 4-6, p. 825–833, mar 2011. ISSN 1432-881X.

SCHERZER, M.; GIRGSDIES, F.; STOTZ, E.; WILLINGER, M.-G.; FREI, E.; SCHLöGL, R.; PIETSCH, U.; LUNKENBEIN, T. Electrochemical surface oxidation of copper studied by in situ grazing incidence x-ray diffraction. *Journal of Physical Chemistry C*, v. 123, p. 13253–13262, 2019.

SCHWABL, F. *Quantum mechanics*. [S.l.]: Springer Science & Business Media, 2007.

SEARS, F. W.; ZEMANSKY, M. W.; YOUNG, H. D.; FREEDMAN, R. A. *Sears and Zemansky's University Physics: With Modern Physics: Technology Update*. [S.l.]: Pearson, 2014.

SERWAY, R. A.; JEWETT, J. W. *Physics for Scientists and Engineers, Volume 2*. [S.l.]: Cengage Learning, 2021.

SHIELDS, A. J. Semiconductor quantum light sources. *Nature photonics*, Nature Publishing Group UK London, v. 1, n. 4, p. 215–223, 2007.

SHLUGER, A. Defects in oxides in electronic devices. In: _____. *Handbook of Materials Modeling: Applications: Current and Emerging Materials*. Cham: Springer International Publishing, 2020. p. 1013–1034.

SHRIVASTAVA, A.; GUPTA, V. Methods for the determination of limit of detection and limit of quantitation of the analytical methods. *Chronicles of Young Scientists*, v. 2, p. 21–25, 2011.

SMITH, R. A. *Memoir of John Dalton: And History of the Atomic Theory Up to His Time*. [S.l.]: H. Bailliere, 1856. v. 13.

SUN, D.; MONAGHAN, P.; BRANTLEY, W.; JOHNSTON, W. Electrochemical impedance spectroscopy study of high-palladium dental alloys. part i: Behavior at open-circuit potential. *Journal of Materials Science: Materials in Medicine*, Springer, v. 13, p. 435–442, 2002.

THOMSON, G. P.; REID, A. Diffraction of cathode rays by a thin film. *Nature*, Nature Publishing Group UK London, v. 119, n. 3007, p. 890–890, 1927.

THOMSON, J. J. *On bodies smaller than atoms*. [S.l.]: US Government Printing Office, 1901.

TOBIAS, B. First-principles theory of electrochemical capacitance. *Electrochimica Acta*, v. 444, p. 142016, 2023.

TRIPATHY, N.; KIM, D.-H. Metal oxide modified zno nanomaterials for biosensor applications. *Nano Convergence*, v. 5, p. 27, 2018.

TRO, N. J.; FRIDGEN, T. D.; SHAW, L.; BOIKESS, R. S. *Chemistry: A molecular approach*. [S.l.]: Pearson Boston, 2017. v. 5.

TRUHLAR, D. G.; GARRETT, B. C.; KLIPPENSTEIN, S. J. Current status of transition-state theory. *The Journal of physical chemistry*, ACS Publications, v. 100, n. 31, p. 12771–12800, 1996.

VANMAEKELBERGH, D.; LILJEROTH, P. Electron-conducting quantum dot solids: novel materials based on colloidal semiconductor nanocrystals. *Chemical Society Reviews*, Royal Society of Chemistry, v. 34, n. 4, p. 299–312, 2005.

VENKATARAMAN, L.; KLARE, J. E.; TAM, I. W.; NUCKOLLS, C.; HYBERTSEN, M. S.; STEIGERWALD, M. L. Single-molecule circuits with well-defined molecular conductance. *Nano letters*, ACS Publications, v. 6, n. 3, p. 458–462, 2006.

WALLING, J. *Electrochemical kinetics, theoretical and experimental aspects (Vetter, Klaus J.)*. [S.l.]: ACS Publications, 1968.

WAN, Y.; ZHANG, Y.; WANG, X.; WANG, Q. Electrochemical formation and reduction of copper oxide nanostructures in alkaline media. *Electrochemistry Communications*, v. 36, p. 99–102, 2013.

WANG, M.; YIN, H.; ZHOU, Y.; SUI, C.; WANG, Y.; MENG, X.; WATERHOUSE, G. I. N.; AI, S. Photoelectrochemical biosensor for microrna detection based on a mos2/g-c3n4/black tio2 heterojunction with histostar@aunps for signal amplification. *Biosensors and Bioelectronics*, v. 128, p. 137–143, 2019.

WANG, S.; ZHANG, J.; GHARBI, O.; VIVIER, V.; GAO, M.; ORAZEM, M. E. Electrochemical impedance spectroscopy. *Nature Reviews Methods Primers*, Nature Publishing Group UK London, v. 1, n. 1, p. 41, 2021.

WANG, Y.; FAN, D.; ZHAO, G.; FENG, J.; WEI, D.; ZHANG, N.; CAO, W.; DU, B.; WEI, Q. Ultrasensitive photoelectrochemical immunosensor for the detection of amyloid β-protein based on sno2/sns2/ag2s nanocomposites. *Biosensors and Bioelectronics*, v. 120, p. 1–7, 2018.

WEBER, K.; CREAGER, S. E. Voltammetry of redox-active groups irreversibly adsorbed onto electrodes. treatment using the marcus relation between rate and overpotential. *Analytical Chemistry*, ACS Publications, v. 66, n. 19, p. 3164–3172, 1994.

WEES, B. V.; HOUTEN, H. V.; BEENAKKER, C.; WILLIAMSON, J. G.; KOUWENHOVEN, L.; MAREL, D. Van der; FOXON, C. Quantized conductance of point contacts in a two-dimensional electron gas. *Physical Review Letters*, APS, v. 60, n. 9, p. 848, 1988.

WELCH, M.; PHILLIPS, R. S. Improved syntheses of [3, 2-b]-and [2, 3-b]-fused selenolo- and thienopyrroles, and of furo [3, 2-b] pyrrole. *Heterocyclic Communications*, De Gruyter, v. 5, n. 4, p. 305–310, 1999.

WIERZBINSKI, E.; VENKATRAMANI, R.; DAVIS, K. L.; BEZER, S.; KONG, J.; XING, Y.; BORGUET, E.; ACHIM, C.; BERATAN, D. N.; WALDECK, D. H. The single-molecule conductance and electrochemical electron-transfer rate are related by a power law. *Acs Nano*, ACS Publications, v. 7, n. 6, p. 5391–5401, 2013.

WINKLER, J. R.; GRAY, H. B. Long-range electron tunneling. *Journal of the American Chemical Society*, ACS Publications, v. 136, n. 8, p. 2930–2939, 2014.

WU, X.; ZHANG, H.; HUANG, K.; ZENG, Y.; ZHU, Z. Rose petal and p123 dual-templated macro-mesoporous tio2 for a hydrogen peroxide biosensor. *Bioelectrochemistry*, v. 120, p. 150–156, 2018.

XIA, J. L.; CHEN, F.; LI, J. H.; TAO, N. J. Measurement of the quantum capacitance of graphene. *Nat. Nanotechnol.*, v. 4, n. 8, p. 505–509, 2009. ISSN 1748-3387. Disponível em: <<GotoISI>://WOS:000268942400014>.

ZALTA, E. N.; NODELMAN, U.; ALLEN, C.; PERRY, J. *Stanford encyclopedia of philosophy*. [S.l.]: Metaphysics Research Lab, Center for the Study of Language and Information ..., 1995.

ZETTILI, N. Quantum mechanics: concepts and applications. *John Wiley & Sons*, 2009.

ZHOU, Q.; YANG, L.; WANG, G.; YANG, Y. Acetylcholinesterase biosensor based on sno2 nanoparticles-carboxylic graphene-nafion modified electrode for detection of pesticides. *Biosensors and Bioelectronics*, v. 49, p. 25–31, 2013.

ZHU, M.; HUANG, Y.; HUANG, Y.; PEI, Z.; XUE, Q.; LI, H.; GENG, H.; ZHI, C. Capacitance enhancement in a semiconductor nanostructure-based supercapacitor by solar light and a self-powered supercapacitor-photodetector system. *Advanced Functional Materials*, v. 26, p. 4481–4490, 2016.

ZONG, X.; ZHU, R. Zno nanorod-based fet biosensor for continuous glucose monitoring. *Sensors and Actuators B: Chemical*, v. 255, p. 2448–2453, 2018.

ȘERBAN, I.; ENESCA, A. Metal oxides-based semiconductors for biosensors applications. *Frontiers in Chemistry*, v. 8, p. 354, 2020.